Raman spectroscopic analysis of normal, abnormal and irradiated oral mucosa: a tissue engineered and ex vivo approach

Salman Aziz Mian

Thesis submitted to the University of Sheffield for the degree of Doctor of Philosophy

Department of Materials Science and Engineering,
University of Sheffield.

November 2014

The University Of Sheffield.

Abstract

Head and neck cancer (HNC) is the sixth most common malignancy worldwide. Squamous cell carcinoma (SCC), the primary cause of HNC, evolves from normal epithelium through dysplasia before invading the connective tissue to form a carcinoma. However, less than 18% of dysplastic lesions progress to cancer with diagnosis currently relying on histopathological evaluation, which is invasive and time-consuming. A non-invasive, real-time, point-of-care method could overcome these problems and facilitate regular screening. The aim of this study was to use Raman spectroscopy to identify specific chemical moieties which can be identified to determine cancer progression and thereby investigate its use as a diagnostic tool.

Tissue-engineered models of normal, dysplastic and HNC squamous cell carcinoma (HNSCC) were constructed and their biochemical content determined by interpretation of spectral characteristics. Spectral features of normal models were mainly attributed to lipids, whereas, malignant models were observed to be protein dominant. Visible differences between the spectra of normal, dysplastic and cancerous models, specifically in the bands of amide I and III were observed. Principal component analysis, cluster analysis and linear discriminant analysis (LDA) were successful in identifying subtypes of dysplasia and cancer.

Patient biopsy samples were also analysed using Raman spectroscopy. Spectral data revealed biochemical variations associated with lipids, proteins and nucleic acids. LDA was utilised for tissue classification and achieved 99% specificity to normal and 97% sensitivity to cancer whereas between dysplasia and cancer a sensitivity of 80 and 92% was achieved respectively.

Finally, tissue-engineered models were irradiated and the post-irradiation effects were assessed. Chemometric data analysis revealed that nucleic acids and proteins were mainly targeted whilst increased incubation periods demonstrated cell repair and recovery mechanisms.

In summary, vibrational spectroscopy offers great potential in diagnosing, staging and designing treatments for HNSCC. This study has generated a wealth of spectral data, describing chemical structural changes associated with oral cancer progression and thereby building up a single comprehensive and standardised database for future studies.

Acknowledgements

In the name of Allah, the most beneficent, the most merciful!

I would like to pay sincere gratitude to my supervisor Dr. Ihtesham Ur Rehman and my co-supervisor Dr. Helen E. Colley for their extraordinary guidance, efforts and understanding towards my project. Their belief in me always kept me motivated whenever I felt low, which was certainly the key to success. I cherish their valuable advices that helped me overcome every single obstacle. It was truly a life time experience for me to work under their supervision. I thank them again for all the patience and hard work.

I would like to thank Dr. Keith Hunter for providing patient biopsy material for this project. I acknowledge Dr. Vanessa Hearnden for helping me out in the tissue culture and field labs for irradiation procedures. Thank you to Mathew Fisher for his technical support in field labs every time during my experiments. I specially thank technical staff in oral pathology lab for accommodating and assisting me with tissue sectioning and staining procedures.

Thank you to all my colleagues in the Raman group and in the department of materials science and engineering for their constant support. I am highly obliged to Ceyla Yorucu, a wonderful companion who helped me a lot in and outside the labs every time, especially with statistical analysis. I am grateful to my friends Abdullah C. S. Talari and Ahtasham Raza for their exceptional support every single day.

Most importantly my family, the love and support of my parents was priceless! Without them it would not have been possible for me to complete this work. I cannot thank them enough for what they have done throughout my entire life! Finally the understanding of my wife (Sara) and the love of my daughter (Eimaan) made it all happen! I thank them for standing by my side every hour of the day!

Abbreviations

^{o}C	degree celcius
λ	wavelength
µ	micro
3D	Three dimensional
a.u.	Arbitrary units
A	ampere
AFB	Autofluorescence Bronchoscopy
ALI	Air liquid interface
ATCC	American Type Culture Collection
BCC	Basal cell carcinoma
CA	Cluster Analysis
CARS	Coherent Anti-Stokes Raman Spectroscopy
CCD	Charged-coupled device
CIS	Carcinoma *in situ*
cm^{-1}	per centimetre
CSC	Cigarette Smoke Condensate
CT	Computed Tomography
DCIS	Ductal Carcinoma in Situ
DED	De-epidermised dermis
DMEM	Dulbecco's modified Eagle's Medium
DMSO	Dimethyl sulphoxide
DNA	Deoxyribonucleic acid
DPSS	Diode-pumped solid state
DSB	Double Strand Break
EBV	Epstein-Barr virus
ECACC	European Collection of Cell Culture
EDTA	Ethylenediaminetetraacetic acid
EGF	Epidermal growth factor
ESS	Elastic scattering spectroscopy
FAD	Flavin adenine dinucleotide
FCS	Fetal Calf Serum
fs	Femtosecond
FS	Fluorescence spectroscopy
FTIR	Fourier Transform Infrared spectroscopy
FCA	fussy c-means cluster analysis
g	gram
GI	Gastrointestinal
Gy	Gray
h	Hours
H&E	Hematoxylin and Eosin
Ham's F12	Nutrient Mixture F12
HCA	Hierarchical clustering analysis
HCL	Hydrochloric acid
HPV	Human Papilloma Virus
i3T3	Irradiated Swiss mouse fibroblasts
IMS	Industrial methylated spirits
IDC	Invasive Ductal Carcinoma
K	kilo
KMCA	k-mean cluster analysis
L	litre
LDA	Linear Discriminant Analysis

LDCT	Low-dose radiation computed tomography
LFS	Li Fraumeni Syndrome
LSPR	Localized surface Plasmon resonance
m	metre
m	milli-
M	molar
MM	malignant melanoma
MRI	Magnetic Resonance Imaging
NIR	near infra-red
N	nano
NAD^+	Nicotinamide Adenine Dinucleotide
NADH	Nicotinamide Adenine Dinucleotide
NaOH	Sodium hydroxide
NMSC	Nonmelanoma skin cancer
NOK	Normal oral keratinocytes
NOF	Normal oral fibroblasts
NOM	Normal oral mucosa
OCT	Optical Coherence Tomography
OSCC	Oral Squamous Cell Carcinoma
PARP1	Poly(ADP-ribose) polymerase-1
PBS	Phosphate buffered saline
PC	Principal Component
PCA	Principal Component analysis
PET	Positron Emission Tomography
pH	Potentiometric hydrogen ion concentration
PLS	Partial Least Squares
RB1	Retinoblastoma gene
RNA	Ribonucleic acid
rpm	Revolutions per minute
RPMI	Roswell Park Memorial Institute
RS	Raman spectroscopy
RSS	Resonance Raman Spectroscopy
SCC	Squamous Cell Carcinoma
SERS	Surface Enhance Raman Spectroscopy
SVM	Support Vector Machines
TB	Toluidine blue
TENOM	Tissue engineered normal oral mucosa
TSNA	Tobacco Specific Nitrosamines
UV	Ultra Violet
V	Volts
v	volume
W	Watt
w	weight

Contents

TABLE OF FIGURES

Chapter 1

Chapter 2

Chapter 3

List of Tables

Chapter 1

Introduction

1.1 Demographics of Oral Cancer

Worldwide Incidence

The incidence rate of oral cancer is increasing every year and together with pharyngeal cancers is now ranked as the sixth most common cancer worldwide (Argiris et al., 2008). In 2008, 263,900 new cases of oral cancer were reported worldwide, whereas, the number of mortalities reached 128,000 (Jemal et al., 2011). There are approximately 275,000 oral and 130,300 pharyngeal cancers diagnosed each year and these figures do not include nasopharyngeal cancers (Parkin et al., 2005). Developing countries account for two third of all diagnosed cases. According to the geographical aspect South and Southeast Asia (e.g. Pakistan, India, Sri Lanka and Taiwan), some areas of Western and Eastern Europe (e.g. France, Slovakia, Hungary and Slovenia), parts of Latin America and Caribbean (e.g. Brazil, Uruguay and Puerto Rico) and pacific regions (e.g. Papua New Guinea and Melanesia) have the higher incidence rates (figure 1.1) (Curado et al., 2009).

United Kingdom

In the UK 6,767 people were diagnosed with oral cancer in 2011. The numbers of new cases by anatomical site are presented in table 1.1. According to Cancer research UK, the prevalence of oral cancer is higher in men than women where male/female ratio in the UK is 2:1. According to the crude incidence rate, every 100,000 males there are approximately 15 new cases of oral cancer whereas there are 7 new cases in every 100,000 females (table 1.2). In both genders the average age of diagnosis is between 50 and 74 years of age (figure 1.2.).

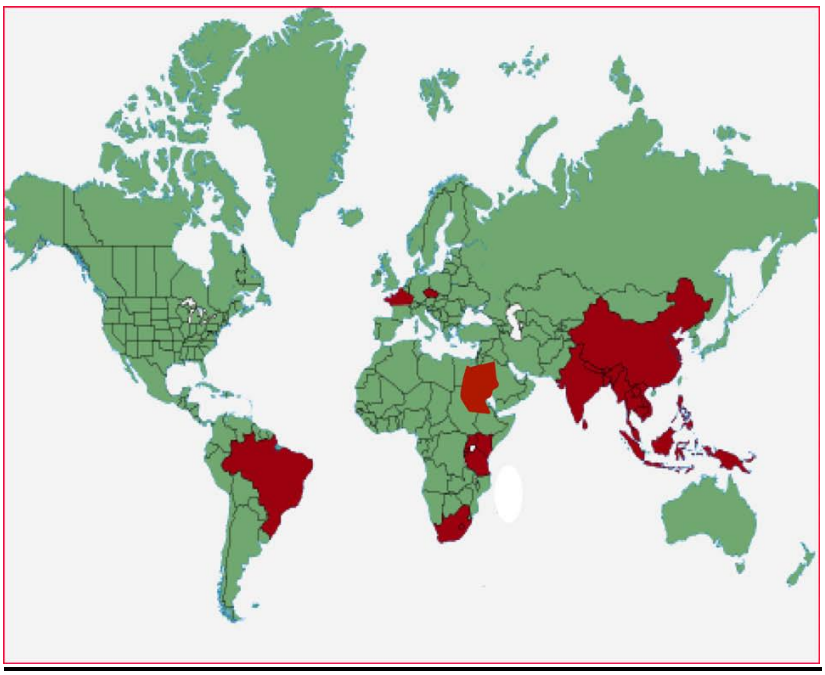

Figure 1. 1 Global map highlighting countries with high incidence and mortality from oral cancer

Table 1.1 Number of new cases by site in UK, 2011

Cancer site	Male	Female	Persons	Male: Female
Lip	248	133	381	1.9:1
Tongue	1336	692	2028	1.9:1
Mouth	1101	819	1920	1.3:1
Oropharynx	1065	391	1456	2.7:1
Piriform sinus	231	54	285	4.3:1
Hypopharynx	146	63	209	2.3:1
Others	180	80	260	2.3:1

Table 1.2 Number of Oral Cancer Cases, Crude and European Age-Standardized (AS) Incidence rate per 100,000 populations in 2011

		England	Wales	Scotland	Northern Ireland	UK
Male	Cases	3609	275	504	122	4510
	Crude rate	13.8	18.3	19.8	13.7	14.5
	AS rate	12.3	15.3	16.6	12.7	12.8
	AS rate -95% LCL	11.9	13.5	15.1	10.5	12.4
	AS rate -95% UCL	12.7	17.1	18	15	13.2
Female	Cases	1810	108	270	69	2257
	Crude rate	6.7	6.9	10	7.5	7
	AS rate	5.2	5.1	7.5	6.2	5.4
	AS rate -95% LCL	5	4.1	6.6	4.7	5.2
	AS rate -95% UCL	5.5	6	8.4	7.6	5.7

Persons	Cases	5419	383	774	191	6767
	Crude rate	10.2	12.5	14.7	10.5	10.7
	AS rate	8.6	10.1	11.8	9.3	9
	AS rate -95% LCL	8.4	9.1	10.9	8	8.8
	AS rate -95% UCL	8.9	11.1	12.6	10.6	9.2

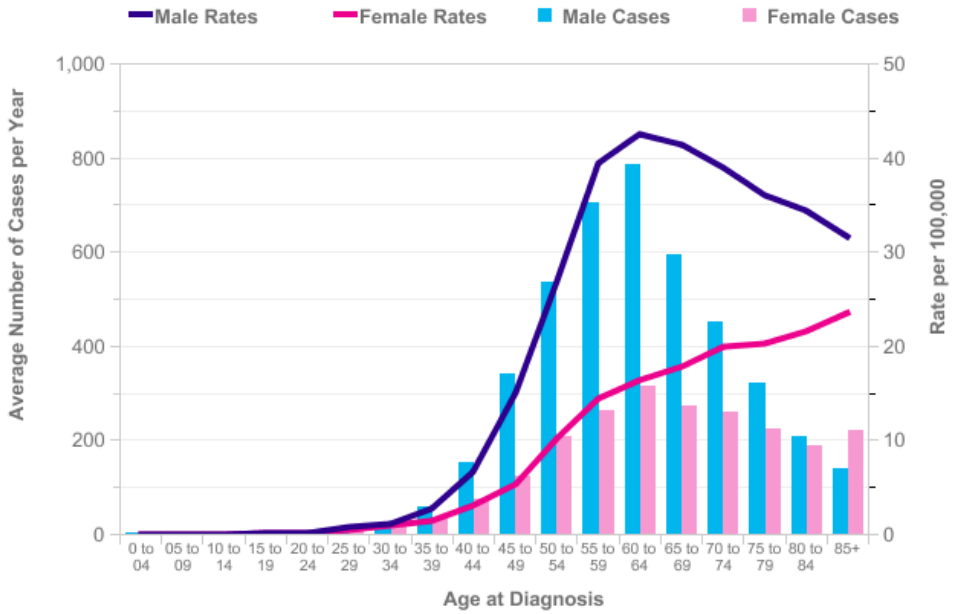

Figure 1. 2 Average Number of New Cases per Year and Age-Specific Incidence Rates per 100,000 Population, UK (Cancer research UK).

With the increase in age there is an increased risk of developing oral cancer. According to statistics produced by Cancer Research UK, 87% of cases are diagnosed in people over 50 years of age, however in high risk areas of the developing countries; oral cancer is relatively common in younger individuals.

1.2 Etiology

The most common risk factors for the development of oral squamous cell carcinoma (OSCC) are described below.

Tobacco

Tobacco consumption in the form of cigarette, cigar and pipe smoking is one of the major causes of oral cancer (Warnakulasuriya et al., 2005, Lee et al., 2009). In the early

era of the 1900's, use of pipe smoking was reduced because it was mainly associated with lip cancers. According to a study in Spain, the habit of leaving cigarette on the lip lead to increased incidence of lip cancer (Lopez et al., 2003).

Use of tobacco in the form of cigarettes is a common way of consumption in the United States (Tomar, 2003), whereas the consumption of smokeless tobacco (tobacco chewing) is relatively higher in the rest of the world. Tobacco, whether it is smokeless or in the form of cigarette smoking, consists of variety of carcinogens for instance, tobacco specific nitrosamines (TSNA), benzopyrenes, formaldehyde, crotonaldehyde, acetaldehyde, nickel, arsenic and nicotine (Reichart, 2001). Intake of smokeless tobacco is more commonly seen in young adults between the ages of 18-25 years (Tomar, 2003). Premalignant conditions like leukoplakia, erythroplakia and oral submucosal fibrosis (OSF) are generally caused by use of smokeless tobacco (Chakrabarti RN, 1991) (Shiu, February 2004). Deoxyribonucleic acid (DNA) double strand break (DSB) is initiated at the cellular level by cigarette smoke condensate (CSC), this breakdown is generated by reactive oxygen present in normal keratinocytes and fibroblasts. This breakdown is responsible for the establishment of micronuclei, anaphase bridges and disturbances in cells which leads to abnormal metabolic activities (Luo et al., 2004).

Alcohol

One of the major risk factors for developing cancer of the oral cavity, pharynx, larynx and oesophagus is the chronic intake of alcohol (Brown, 2005). Alcohol has the potential to induce carcinogenesis as the permeability of the oral mucosa is increased by ethyl alcohol which acts as a solvent. Due to this increase in permeability the influx of a number of carcinogens like nitrosamines, asbestos, polycyclic hydrocarbons and carcinogens of tobacco also increases (Seitz HK and PM., 2002, Seitz et al., 1998).

It has been reported that acetaldehyde is responsible for interfering in the process of DNA synthesis, promotes injuries to cells and enhances chromosomal imbalance. Therefore acetaldehyde derived from alcohol has a significant carcinogenic effect. Injury caused to DNA in a cell is a result of formation of toxic oxygen radicals and reactive oxygen species by alcohol (Seitz HK and PM., 2002).

Viral Infections

Use of tobacco and alcohol are considered to be the most important risk factors for squamous cell carcinoma of the head and neck region. Apart from these two factors, a lot of consideration has been made towards the potential role of Epstein-Barr virus (EBV) and the human papillomavirus (HPV) in the pathogenesis of head and neck cancers. The nasopharyngeal and lymphoepithelial carcinomas of the salivary glands are strongly related to Epstein-Bar virus (Niedobitek et al., 1993, Herrmann K and G., 2003), whereas, HPV is associated with squamous cell carcinoma of the tonsil (El-Moft y SK, 2003). Apart from these it appears that EBV and HPV may have a role in the pathogenesis of squamous cell carcinoma of the head and neck region (Herrmann K and G., 2003).

1.3 Current Diagnostic Options and their limitations

Histopathology

Histopathological evaluation of surgically excised suspected lesions is the current diagnostic option for cancer detection, which is known as the gold standard. This process involves surgical intervention to obtain a biopsy which is then processed in a laboratory for histological analysis. Processing includes fixation of the tissues followed by sectioning and mounting on glass slides for staining before it is forwarded to pathologists for microscopic examination. This evaluation is based on morphological appearance of tissues and any pathological condition is identified. These cytological or

morphological observations primarily appeared due to biochemical alterations in diseased tissues (Stone et al., 2004).

Limitations

- Surgical intervention is required to obtain the tissue for histopathological assessment. This procedure is technique sensitive, demands extremely skilled surgeons and causes anxiety and discomfort to the patients (Lau et al., 2003).
- Substantial sample preparation is needed before the tissue can be evaluated by pathologists. Sample preparation is a time consuming and a costly procedure which is associated with delays in diagnosis and treatment (Stefanuto et al., 2014, Upile T et al., 2007, Kendall et al., 2009).
- Inter and intra-observer variability is often associated with histopathological evaluations therefore pathologists may require consultation to reach a consensus diagnosis (Kujan et al., 2007, Kujan et al., 2006a).
- Errors in sample collection or preparation may require further surgical procedures to obtain biopsies which again delays the treatment and adds further anxiety and discomfort for the patient (Kendall et al., 2003, Lau et al., 2003).

Brush biopsy

Brush biopsy at present is frequently used in dental clinics to assess suspected lesions. It is a minimally invasive, low cost and only a mildly uncomfortable procedure for the patient. This practice has proved to be simple and efficient for dentists moreover sufficient sample can be collected for cytological assessments. A cytology brush is placed on the lesion and rotated 360° with gentle pressure. Once the rotation is complete, the brush is carefully rotated on the edge of a glass slide so that the sample material is transferred. A cytofixative spray is applied to preserve the sample for

cytological examinations. Fixation has to be done within a few seconds otherwise sample degradation may occur and result in lower diagnostic efficacy (Naugler, 2008).

Photosensitisers

The phenomenon of photosensitisers is to generate a strong fluorescent signal once they are topically applied within the oral cavity. Upon application they tend to quickly create higher fluorescent signals in areas where abnormal tissue is found and thereby help in the identification of abnormal cells. A specially designed and economical red diode laser is used to measure fluorescence. This technique benefits from being non-invasive and a less time consuming procedure. The limitations associated with photosensitisers are that the dye is unable to specify oral cancer as it stains any form of abnormal condition such as ulcers, inflammation, oral lichen planus and frictional keratosis etc. Secondly, minimum exposure of the red diode type laser is required in order to avoid tissue damage.

Toluidine Blue

Toluidine blue (TB) (Tolonium Chloride) is a metachromatic dye which is acidophilic in nature and has the ability to perform selective staining in tissues. TB attracts nucleic acids therefore it has the ability to make a bond with nuclear material of tissues which are rich in DNA and RNA (Sridharan and Shankar, 2012). TB has been widely used in dentistry as a stain for mucosal lesions for over 40 years (Ram and Siar, 2005). The oral cavity is rinsed with the stain and viable cells absorb it. The degree of absorption of the dye is directly proportional to the amount of metabolic activity in the cells and therefore more dye is absorbed into cells with a higher metabolic activity. Clinically, the technique is sensitive and requires experience to achieve good accuracy. This procedure is often associated with false positive results due to low specificity however clinicians

that regularly use the dye are able to achieve around 90% sensitivity (Wilder-Smith et al., 2009).

Chemi-luminescence

Chemi-luminescence can be described as a chemical reaction which emits light. The emitted light can differ in intensity and life time and show colours in a visible spectrum. Based on the mechanism of chemi-luminescence, ViziLite® has been introduced in the clinical settings to detect oral pre-cancer and cancer (Ram and Siar, 2005). This system can be used with both TB and acetic acid. The cytoplasm of the cell dehydrates once the patient rinses their mouth with these agents. Cancerous cells possess a higher nuclear to cytoplasmic ratio as compared to normal cells and therefore these agents amplify the difference in their properties. A ViziLite stick is then used to record chemi-luminescence which highlights suspected lesions as white patches. The benefits of using TB and ViziLite are ease of use, quick and relatively cost effective. The sensitivity of the test is still a matter of debate as it does not have the ability to differentiate between different grades of dysplasia and cancer as well as generating a high number of false positive results (Ram and Siar, 2005).

VELscope

VELscope is a commercially available light based device used to detect lesions of the oral cavity without any tissue staining. The mechanism is based on visualisation of fluorescence emerging as a result of intrinsic optical properties of normal or abnormal tissues. This system uses a blue light (400 – 460 nm) to excite stroma and epithelial cells. Excitation causes autofluorescence which varies in normal and pathological sites. Less autofluorescence is observed in pathological tissues due to increased metabolic activities and it is believed that VELscope utilises autofluorescence from nicotinamide adenine dinucleotides (NADH) and flavin adenine dinucleotides (FAD). VELscope has

demonstrated that normal and dysplasia/carcinoma can be successfully differentiated with a specificity and sensitivity of 98% and 100% respectively (Poh et al., 2007). The only concern is that the lesions of inflammation, ulcers, lichen planus or keratosis are not detected and will affect the accuracy of results.

Impedance spectroscopy

Impedance spectroscopy has the ability to measure bioimpedance of tissues non-invasively and in quick time. Tissues are exposed to sinusoidal current at different frequencies. Impedance of the tissues may result in voltage drop which is known as bioimpedance. Variations in bioimpedance are observed between different tissue types. Electrical impedance is present in all biological tissues because tissue structures possess both resistive and capacitive features. The tissue's electrical properties generate different signals of impedance at varying frequencies. The molecular structure can be determined at higher frequencies (> 1 GHz) whereas variations in the ionic environment around cells can be detected by frequencies less than 100 Hz (Sun et al., 2010). In cervical cancers, impedance spectroscopy has been employed to identify degree of intra epithelial neoplasia with sensitivity and specificity of 74% and 53% respectively (Abdul et al., 2006). It has also been used to distinguish between benign and malignant breast tissues however false positive results have also been reported due to limited depth of penetration in breast tissues (Zou and Guo, 2003, Murdoch et al., 2014).

1.4 Treatment of Oral cancer

Surgical resection along with radiation therapy is the treatment of choice for most of oral cancer cases (Argiris et al., 2008) but in recent years the concept of adjuvant therapy has been promoted which includes a combination of surgery, radiotherapy and chemotherapy.

Surgical resection

Surgical resections in oral cavity have always been a challenge for surgeons in order to maintain functions of speech and swallowing. Surgical advancements like trans-oral laser microsurgery have shown significant improvements to these challenges (Argiris et al., 2008). Despite these developments in surgical technologies, incomplete removal of tumours still remains a problem (Argiris et al., 2008).

Radiotherapy

Radiotherapy can be used in combination with surgery or alone in cases where vital organs are at severe risk of malfunctioning after surgical intervention. Cancer cells are exposed to ionising radiation which damages DNA directly or by free radical production from ionised water hence leading to cell death through restricted cell proliferation. The ability to repair damaged DNA is greater in normal cells but radiation affects both cancer and normal cells leading to severe side effects including mucositis and xerostomia (Argiris et al., 2008). In contrast to conventional radiotherapy, a fractionated method has been introduced in which overall exposure time is reduced by increasing dose intensities.

Chemotherapy

The use of chemotherapy in the treatment of oral cancer has reduced due to less effective results and highly toxic side effects. It is however used in advanced or cases where surgical intervention is contraindicated (Argiris et al., 2008). Amongst many, frequently used chemotherapeutic agents for oral cancer treatment are Cisplatin, 5-Fluorouracil (5-FU), Doxorubicin and Paclitaxel. Combination of drugs with intense but segmented delivery systems has been introduced to minimise toxicity and enhance efficacy.

1.5 Normal Oral mucosa

A basement membrane separates the connective tissue and stratified squamous epithelium of human oral mucosa. Basal keratinocytes are proliferative cells present next to the basement membrane and are responsible for repair and replacement of the epithelium. Supra-basal cells are partially differentiated, highly proliferative and located superficial to basal keratinocytes (figure 1.3). Prickle cell layer, also known as stratum spinosum lies over the supra-basal cells and is connected by desmosomes. During histological processing, desmosome attachment remains firm while cells shrink to produce a prickly appearance. Gingivae and hard palette are the keratinised areas of the oral cavity. In these regions terminally differentiated keratinocytes form the outer most epithelial layer (Salamat-Miller et al., 2005). Abundant keratin is present in keratinised layer with flattened cells having tiny or no nuclei. The term para-keratinised is used for non-keratinised regions such as buccal mucosa, where superficial layer is less keratinised. Fibroblasts are predominant cells in the connective tissue which play a vital role in the production of extracellular matrix proteins as well as releasing factors which are essential for the development of epithelium (Mackenzie and Fusenig, 1983).

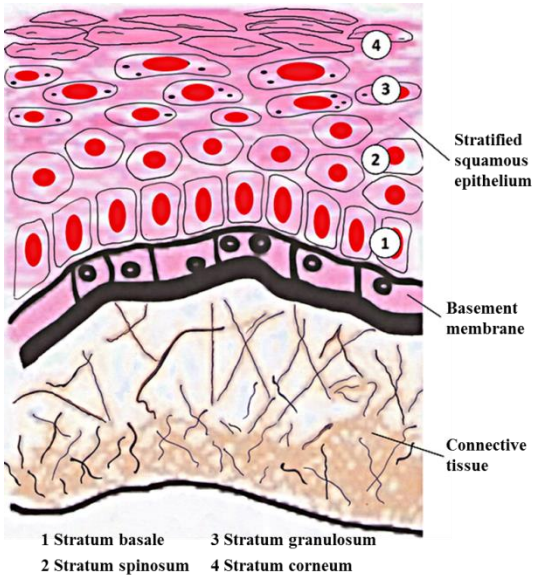

Figure 1. 3 Schematic illustration of normal oral mucosa

1.6 Pre-malignant transformation and grading criteria

The most common and potentially malignant lesions of the oral cavity are leukoplakia and erythroplakia however it is apparent that up to 50% of oral squamous cell carcinomas arise from clinically normal looking oral mucosa (Speight, 2007).

The criteria which are analysed by pathologists to diagnose oral epithelial dysplasia are presented in table 1.3.

Table 1.3. The architecture and cytology criteria used for grading oral epithelial dysplasia in the WHO classification 2005.

Architecture criteria	Cytology criteria
Irregular epithelial stratification	Abnormal variation in nuclear size
Loss of polarity of basal cells	Abnormal variation in nuclear shape
Drop-shaped rete ridges	Abnormal variation in cell size
Increased number of mitotic figures	Abnormal variation in cell shape
Abnormally superficial Mitoses	Increased nuclear–cytoplasmic ratio
Premature keratinisation in single cells	Increased nuclear size
Keratin pearls within rete ridges	Atypical mitotic figures
	Increased number and size of nucleoli
	Hyperchromatism

WHO System

The WHO system uses the criteria described above in relation to the thickness of the epithelium involved.

Mild Dysplasia (Grade I)

Mild dysplasia indicates minimal architectural alterations. Cells of the basal layer demonstrate proliferation but do not proceed beyond the lower third of the epithelium. Generally slight cytological atypia is observed with mild pleomorphism of cells and mitoses are not evident (Speight, 2007).

Moderate Dysplasia (Grade II)

Atypical cells proliferate into the middle one third of the epithelium in moderate or grade II dysplasia. Severe cytological changes such as hyperchromatism and prominent cellular or nuclear pleomorphism are observed as compared to mild dysplasia. Usually in the basal layers, abnormal and increased mitoses may be seen. In the lower half of the epithelium, architectural changes may be observed due to loss of basal polarity and hyperplasia resulting in bulbous rete pegs. At the same time, maturation and stratification are comparatively normal often with hyperkeratosis (Warnakulasuriya et al., 2008).

Severe Dysplasia (Grade III)

Severe dysplasia demonstrates abnormal proliferation of cells from the basal layer into the upper third of the epithelium. Obvious cytological and architectural alterations are observed. Along with changes seen in mild and moderate dysplasia, noticeable pleomorphism is present with either large nuclei or multiple nucleoli. Usually signs of prominent and suprabasal mitoses are evident along with apoptotic bodies. Severe

architectural changes are observed, showing thorough loss of stratification with abnormal keratinisation. Rete pegs are usually abnormal in shape with lateral extensions which are specifically significant in the detection of severe dysplasia. Rarely, prominent acantholysis may be observed in some lesions with severe disturbance in the architecture. Thickened epithelium is observed in severe dysplasia however in some cases marked epithelial atrophy may also be seen especially in erythroplakia or lesions from ventral tongue, floor of the mouth or soft palate (Speight, 2007).

Carcinoma *in situ*

The most severe form of epithelial dysplasia is carcinoma in situ which demonstrates full thickness cytological and architectural changes. Such alterations are rare in the oral cavity; keratinised surface layer is still intact even in the presence of severe atypia. Carcinoma in situ is regarded as a premalignant condition by some whereas a malignant change without invasion by others (Speight, 2007).

The current WHO dysplasia grading system does not offer an objective analysis of the morphological and cytological features of dysplasia. As a result, there is a lack in consistency with significant inter- and intra-observer variability in the presence and absence and/or grading of oral dysplasia.

Figure 1.4 shows the stages of transformation of normal oral mucosa through dysplasia and carcinoma *in situ* (CIS). Characteristic features of dysplasia and CIS are provided in table 1.4.

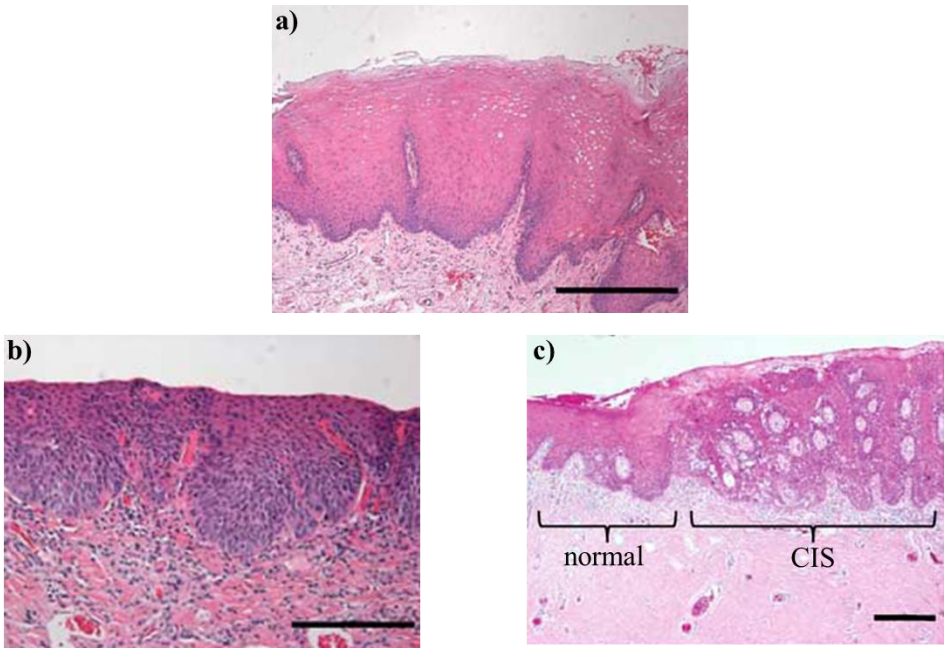

Figure 1. 4 H&E stained images of oral mucosa. a) normal oral mucosa, b) dysplastic oral mucosa and c) carcinoma in situ. Scale bars indicate 200 µm. Images from (Colley et al., 2011)

Table. 1.4 Characteristic features of transformation in moderate dysplasia and carcinoma *in situ* (Speight, 2007).

	Dysplasia (moderate)	**Carcinoma *in situ***
Proliferation	Atypical cells proliferate in basal 2/3rd of epithelium	Abnormal proliferation through entire epithelium
Cytological changes	Hyperchromatism Prominent nuclear pleomorphism Atypical mitotic figures in basal layers	Full thickness cytological alterations as observed in dysplasia
Structural changes	Atypical hyperplasia Loss of basal polarity Bulbous rete pegs Hyperkeratosis	Full thickness Structural alterations as observed in dysplasia

Binary System

Recently, a binary system for grading oral epithelial dysplasia has been reported (Kujan et al., 2006b, Kujan et al., 2007) . This system proposes a division between low risk and high risk lesions related to a lesion's potential to transform into SCC instead of the existing three grades. The binary grading system utilises the recommended cytological and architectural features of dysplasia (recommended by WHO) (Table 1.3).

Lesions showing less than four architectural and five cytological criteria are classified as 'low-risk' whereas those with exhibiting a higher number of criteria are deemed high-risk. The two studies undertaken so far show this system to be a good predictor for malignant changes in oral epithelial dysplasia with a significant improvement in intra-observer agreement compared to the existing WHO system (Kujan et al., 2006b). However, further work and validation is required before the binary system is considered to replace the existing method.

1.7 Tissue Engineering

Tissue engineering is a multidimensional area of science where biologists, material scientists and clinicians work in close collaboration with each other to generate organotypic tissues which can be used in research and repair or replacement of damaged tissues. Clinically, successful replacements of tissue engineered skin (Chakrabarty et al., 1999), urethra (Bhargava et al., 2008) and bladder (Atala et al., 2007) have been demonstrated in patients. Two dimensional monolayer cell cultures have been traditionally used in biological research as a tool to understand cell behaviour. The information obtained from monolayer cell cultures may be limited as they do not replicate three dimensional (3D) tissue behaviour and therefore do not ideally represent the *in vivo* environment. Cells cultured as monolayers show differences in behaviour when compared to those grown in a 3D microenvironment (MacNeil, 2007)

(Moharamzadeh et al., 2007). Tissue engineering of 3D tissues offers a more physiologically relevant model and its use as a tool in cancer research is becoming more and more prevalent.

Applications of Tissue engineered oral mucosa

Numerous tissue engineered models of oral mucosa have been introduced for *in vitro* studies and clinical applications (Moharamzadeh et al., 2007). They can be used for:

1) Replacement grafts for surgically excised or damaged tissues (Bhargava et al., 2004).
2) *In vitro* models to understand physiological and pathological conditions (Duong et al., 2005).
3) Replacement for animals when analysing toxicity of drugs, irradiation or consumer products.

3D Tissue engineered oral mucosa

Cell behaviour and proliferation is significantly different in 3D tissue engineered models as compared to monolayer cell cultures. A number of scaffold materials have been established as substitutes to connective tissue for cell seeding such as acellular skin (Bhargava et al., 2004), amniotic membranes, synthetic polymer materials (Moharamzadeh et al., 2007), gels made up of collagen, gelatine and fibrin (Moharamzadeh et al., 2007, Duong et al., 2005). Epithelial formation is influenced by fibroblasts and connective tissue moreover differentiation and proliferation of keratinocytes is also affected by factors released by fibroblasts (Mackenzie and Fusenig, 1983, MacNeil, 2007). Models produced using air-liquid interface (ALI) enhances differentiation of epithelial cells and allows them to stratify to mimic natural oral mucosa (Bhargava et al., 2004). Therefore 3D models produced at ALI using

keratinocytes, fibroblasts and connective tissue have maximum clinical relevance in order to understand tissue response against stimuli such as drugs and irradiation. These models have been assessed to understand the interaction between soft tissue and dental implants (Chai et al., 2010), safety of mouth washes (Moharamzadeh et al., 2009) and dental restorative composite resins (Moharamzadeh et al., 2008).

Investigations of cancer therapies are usually performed on monolayer cell cultures before animal studies however these 2 dimensional models have several limitations. For an effective cancer treatment, some of the important aspects which should be kept in consideration include tumour behaviour at different stages of cancer and effect of different microenvironments. Monolayer studies lack these properties and 3D models have this advantage where cancer progression can be monitored at different stages. Usually different results are achieved in drugs tested on 2D and 3D models which may possibly be a reason that promising results obtained from 2D models fail on animal studies (Knuchel et al., 1989). Therefore evaluation of treatment modalities on 3D models could potentially produce effective results and improve clinical outcomes. These 3D models of dysplasia and cancer provide a platform to understand progression of disease which may aid in early diagnosis. Moreover treatment technologies can also be tested on these models which closely resemble natural conditions.

1.8 Emerging Diagnostic Options: Optical Spectroscopy

In recent years, a lot of interest has been developed to explore biochemical contents present in the tissues using optical spectroscopic techniques which can detect early signs of neoplasia. In research, these techniques have shown great potential to successfully differentiate between various tissue types (Malini et al., 2006, Olivo et al., 2011, Devpura et al., 2011, Shafer-Peltier et al., 2002, Haka et al., 2006, Haka et al., 2005, Movasaghi et al., 2012, Rehman et al., 2007, Kendall et al., 2009, Old et al., 2014, Crow et al., 2005, Shetty G, 2006, Stone et al., 2004, Stone et al., 2000). These

promising advancements have indicated that optical spectroscopies can potentially be used in parallel to conventional histopathology as well as during surgical procedures to assist guided biopsies. *In vivo* investigations have demonstrated that with the help of a fibre optic probe, real time and non-invasive tissue evaluations are also possible to produce positive results (Singh et al., 2013, Singh et al., 2012a, Wu et al., 2011). There are several spectroscopic techniques employed in cancer studies, such as Raman spectroscopy, Fourier Transform Infrared spectroscopy (FTIR), Elastic Scattering spectroscopy (ESS) and Fluorescent spectroscopy (FS) (Swinson et al., 2006, Harris et al., 2010, **2**:26). All these systems follow same mode of action in which light comes in contact with the matter and measures scattering, absorption or fluorescence to generate a spectrum containing biochemical information of the sample (Movasaghi et al., 2013, Bigio IJ, 1997, Bigio and Bown, 2004).

Advantages of Optical spectroscopy

Various studies on the use of spectroscopic techniques in quest of cancer detection have demonstrated many benefits. Briefly the advantages which these techniques may offer are listed below;

- They can provide biochemical information non-invasively which could be of diagnostic significance. Surgical intervention can be limited to a minimum.
- Spectral data can be collected within few seconds hence leading to quick detection.
- They can be used to collect spectral data from vital organs where surgery is contraindicated.
- They can detect tumour margins in order to assist surgeons to perform precise resections.

- Dysplastic/premalignant or follow up lesions can be monitored non-invasively within no time.
- They can reduce the risk of inter observer variability which is associated with histopathological examination.
- During cancer treatment, they can be useful in evaluating cellular response to radiation or chemotherapeutic drugs.

1.8.1 Elastic Scattering Spectroscopy (ESS)

The mechanism of Elastic scattering spectroscopy is wavelength dependant and based on interaction of light with the sample where the energy of incident and reflected light remains the same (elastic scattering). The reflected light holds information regarding morphological appearance of the tissues (Swinson et al., 2006). There are two types of scattered photons, single and multiple which indicate morphological information of surface layer of the tissue and morphological information of deeply resided tissue structures respectively. Within biological tissues, the primary structures responsible for scattering are nucleus, subcellular organelles and concentration of chromatin (Swinson et al., 2006). The diagnostic criteria of ESS resemble histopathological assessment as it also relies on nuclear to cytoplasmic ratio, chromatin content, cellular crowding and size of the nucleus (Upile T et al., 2007, Swinson et al., 2006, Sharwani et al., 2006). The equipment is inexpensive and user friendly which makes it a strong candidate for *in vivo* tissue investigations but it only offers information regarding morphological state of the tissue with limited sample volume instead of biochemical finger printing (Kendall et al., 2009).

1.8.2 Fluorescence Spectroscopy (FS)

Cells are excited when a biological tissue is exposed to light which in response reflects light in different colours, known as fluorescence. Sensitive detectors are used to record re-emitted light and generate a spectrum. Fluorescence takes place as a result of

fluorescent chromophores present within biological tissues. Fluorescence either takes place naturally when light comes in contact with tissues or it can be induced by exogenous photosensitisers like 5-aminolevulinic acids (ALA) (Upile T et al., 2007, Swinson et al., 2006). These substances can be sensed by FS and a distinctive spectrum is produced which contains biochemical information of the tissue. Along with detection of fluorescence, FS also has the ability to record absorption of light in biological tissues (Swinson et al., 2006, Upile T et al., 2007). Alfano and his colleagues in 1984 for the first time demonstrated that during malignant transformation in animal tissues, the fluorophores which are likely to change are amino acids, elastin, prophyrins, collagen and co-enzymes (NADH and flavins). They observed significant spectral variances related to flavins and prophyrins in normal and malignant tissues (Alfano et al., 1984). Since then several research groups have investigated the potential of FS on human tissues to separate normal and abnormal tissues (Bigio IJ, 1997, Bigio and Bown, 2004). Research studies based on FS have shown encouraging results in discriminating normal from pathological tissues but the sensitivity of the technique has reduced when used to differentiate between pathological conditions. Moreover this technology is wavelength dependant therefore requires multiple excitation sources to stimulate different fluorophores and has also been associated with false positive results.

1.8.3 Fourier Transform Infra-red Spectroscopy (FTIR)

In spectroscopic techniques, chemical bonds present within samples can be identified by measuring the degree of scattering, absorption or emission of the incident light which is normally a laser. FTIR spectroscopy detects the change in dipole moment of molecules as a result of vibrations caused by interaction of incident light and the sample. A broad spectrum infra-red (IR) light is exposed in FTIR which consists of several wavelengths. FTIR is based on an absorption mechanism in which incident light is absorbed by different bonds present within the sample which result in less light transmitted to the

detector. In FTIR spectra each wavelength reflects different chemical bonds present within the samples. The spectral range which can be exposed by FTIR is between 400 to 4000 cm^{-1} wavenumbers and has the ability to excite strong polar bonds like C=O, C-O, O-H, and C-H which are mainly present in carbohydrates, lipids and proteins. This property of FTIR has shown promising results in identifying normal and pathological cells/tissues on the basis of molecular differences amongst them (Kendall et al., 2009). Several studies based on cancer detection using FTIR spectroscopy have been reported with encouraging results (Fukuyama et al., 1999, Pallua et al., 2012, Andrus, 2006). FTIR spectroscopy does not offer confocal imaging and requires sample preparation prior analysis. Strong water bands are absorbed in FTIR spectroscopy therefore non-aqueous samples can be easily analysed and unfortunately *in vivo* application of the technique for tissue analysis is limited (Conroy et al., 2005).

1.9 Raman Spectroscopy

In 1928, the phenomenon of inelastic scattering of light was first discovered by Sir Chandrashekhara Venkata Raman, which was known as the ‘’Raman Effect’’. He conducted this research at the University of Calcutta and Indian Association for the Cultivation of Science (IACS). Sunlight was used as an incident source in the experiment which was focused on to the sample by a telescopic lens. Beyond the sample, another lens and optical filters were positioned at an angle to the direction of sunlight. Scattered light was recorded by naked eye initially but later photographic plates were utilised. Raman effect is the shift in wavelength of a small fraction of radiation scattered by molecules which differs in frequency of that of the incident beam (Krishnan and Shankar, 1981, RAMAN and KRISHNAN, 1928). The shift in the wavelength relies on the chemical structure of the molecules which are accountable for scattering of the incident light. The scattered light is consumed by Raman spectroscopy to analyse molecular vibrations which provide statistics regarding structure, shape,

electronic environment and bonding of the molecules, therefore resulting in qualitative and quantitative analysis of each compound (Willard et al., 1949). All functional groups possess specific vibrational energies therefore a unique Raman spectrum is generated for every molecule (Haynes et al., 2005). Raman effect takes place when incident light interacts with the electron cloud and bonds of a molecule and according to the basic Raman phenomenon, there is a change in polarisability when atoms are displaced from an equilibrium state as a result of molecular vibrations. The magnitude of change in polarization is directly proportional to the intensity of Raman scattering (Haynes et al., 2005). Raman spectroscopy is a precise and sensitive technique but with very weak signals, in the order of one trillionth of the incident beam. When biological tissues are used as specimen, four main components that contribute to the Raman spectra are nucleic acids (DNA and RNA), proteins (isoenzymes, immunoglobulin, hormones and keratins), water and lipids (cell membranes). The spectra acquired from these components provide characteristic features of the tissue.

1.9.1 Principles of Raman spectroscopy

The exposure of a molecule to a monochromatic light leads to elastic or inelastic scattering of light. There is no change observed in the photon frequency or wavelength in elastic scattering. On the other hand, inelastic scattering is shift in the photon frequency as a result of excitation of molecular vibrations during which energy may be gained or lost by photons (Kaur H.S., 2006, Swinson et al., 2006, Mahadevan-Jansen and Richards-Kortum, 1996, Hanlon EB, 2000, Dukor, 2006, Conroy et al., 2005).

Rayleigh scattering (Elastic)

According to this phenomenon, when light comes in contact with a molecule and the net exchange of energy (E) is zero therefore the frequency of scattered light is equal to that of the incident light ($E = E_o$) (figure 1.5) (Das and Agrawal, 2011).

Raman scattering (In Elastic)

When light comes in contact with a molecule, energy transfer takes place between photons and molecules resulting in less or more energy in the scattered photons, this is known as Raman scattering (figure 1.5) (Movasaghi et al., 2013).

Molecules are excited by photons and are transferred to a different energy level from the ground state. When relaxed, these molecules emit a photon at a different vibrational state. The emitted photon has a different frequency than that of the excitation wavelength because of the difference between initial and final energy levels of the molecule.

Stokes Raman Scattering

If the molecule gains energy (more energetic final vibrational state) from the light photon then the scattered light (emitted photon) would exhibit lower frequency than that of the incident light ($E = E_o - E_v$). This frequency shift is known as Stokes shift or *red-shift* (Stokes Raman scattering) (figure 1.5) (Das and Agrawal, 2011).

Anti-Stokes Raman scattering

If the light photons gain vibrational energy (E_v) from the molecule (less energetic final vibrational state) then the scattered light (emitted photon) would exhibit higher frequency than that of incident light ($E = E_o + E_v$). This frequency shift is known as Anti-Stokes shift or *blue-shift* (Anti-Stokes Raman scattering) (figure 1.5) (Das and Agrawal, 2011).

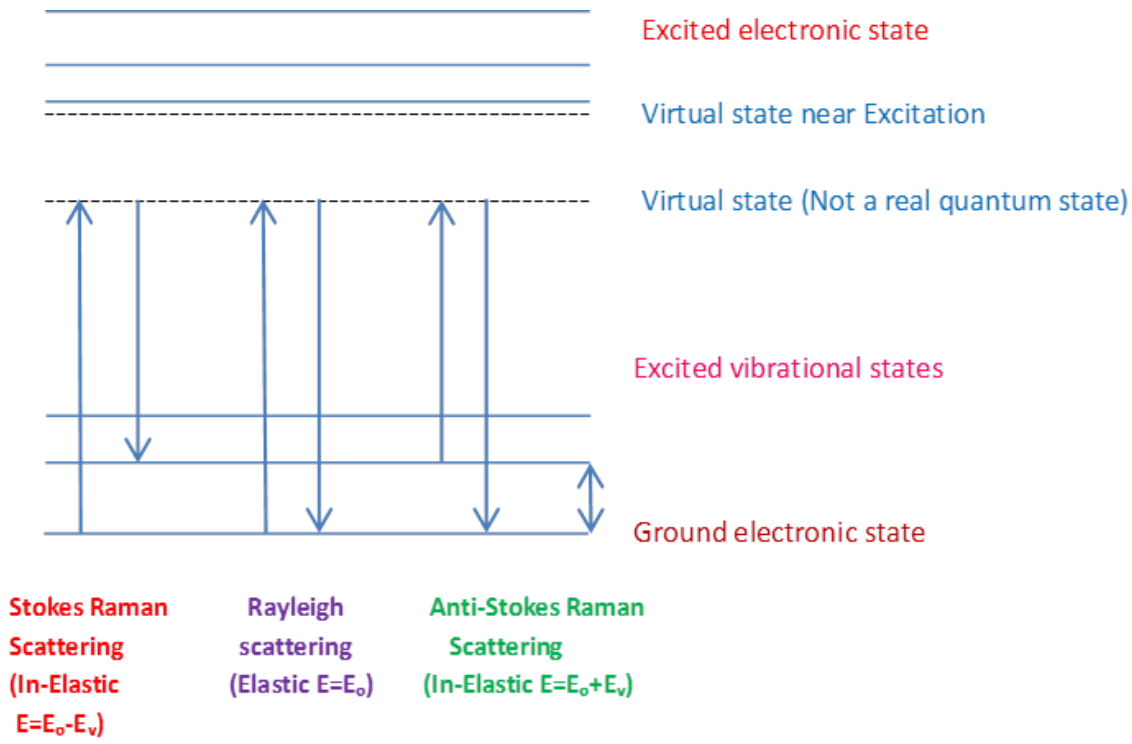

Figure 1. 5 Mechanism of Raman scattering

Vibrational modes of molecules

When molecules are excited with light source, there are two main types of vibrations that occur, namely stretching and bending vibrations.

Stretching vibrations

Stretching vibrations are those in which bond angles remain constant whereas change in bond length is observed. Further stretching vibrations are subdivided into two types known as **symmetric** and **asymmetric** vibrations. Symmetric vibrations are those in which bond lengths of functional groups change in the same direction and at the same time. These bond movements are opposite in asymmetric stretching (figure 1.6).

Bending vibrations

Bending vibrations differ from stretching in a sense that the bond lengths remain constant whereas change in bond angle is observed. Further bending vibrations are subdivided into four types known as **scissoring, rocking, wagging and twisting** vibrations. Bond movements are schematically described in (figure 1.6).

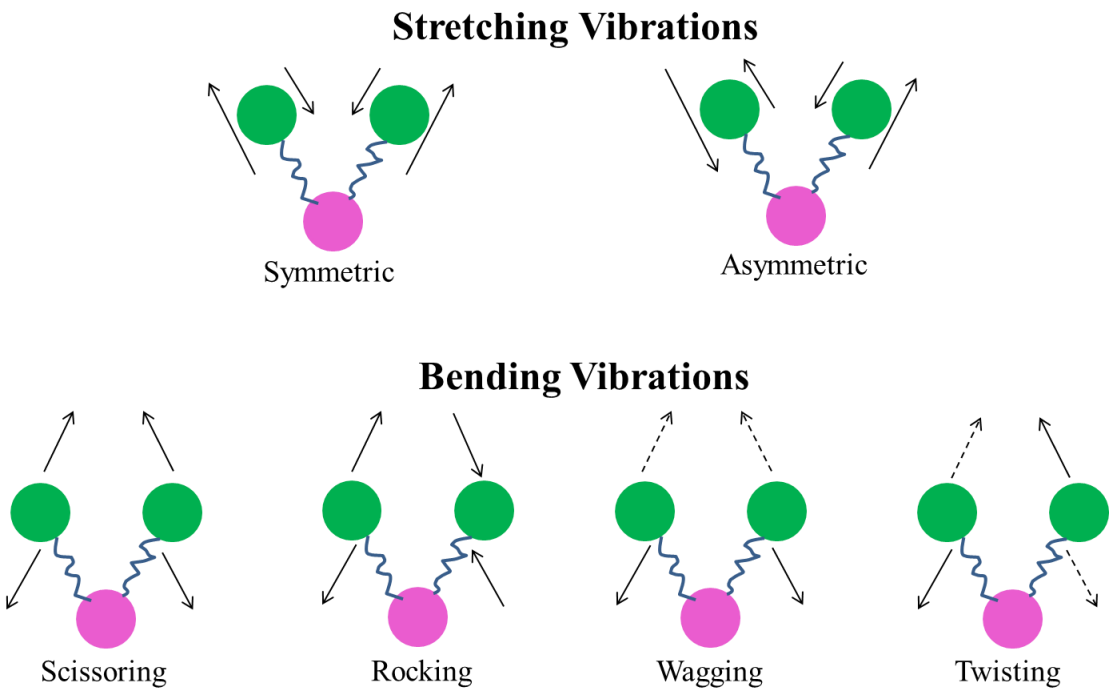

Figure 1. 6 Schematic descriptions of bond movements

A basic schematic illustration of a Raman system is shown in figure 1.7. Incident laser beam is deflected to the filter and then passes through an inverted microscope via an objective to shine on the sample. The objective collects the backscattered light and passes on to the filter which only allows Raman scattered light to proceed to the spectrograph. The stability of the instrument, sufficient resolution and high signal-to-noise ratio may affect the analysis on Raman spectra. The problems of fluorescence which disturbed Raman signals were resolved by the development of effective FT Raman spectrometers using near infrared (NIR) or red excitation lasers. Similarly, the ability of analysis was improved by extremely sensitive detectors in combination with optical fibres and microscopes (Parker and Tooke, 1997). Raman spectra can be collected by using two different technologies for instance Dispersive Raman spectroscopy and Fourier transform Raman spectroscopy. The difference between these two is the source of laser and the process by which Raman scattering is detected and analysed (McCreery R.L., 2000 , Hendra P. et al., 1991).

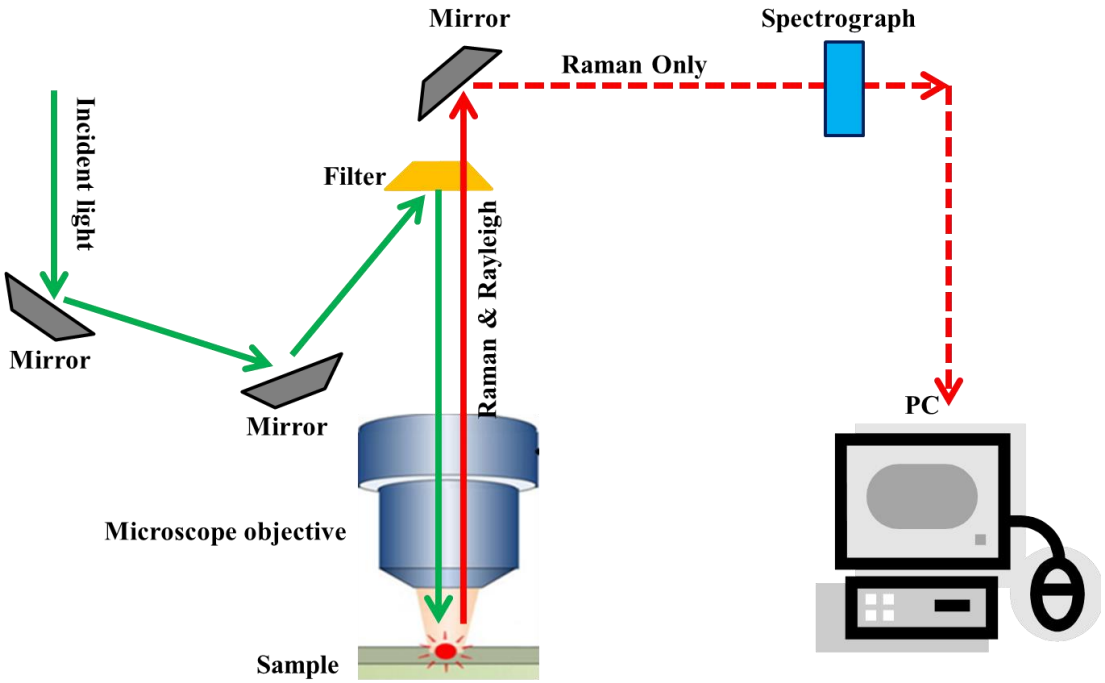

Figure 1. 7 Schematic illustration of a Raman system

1.9.2 Developments in Raman Systems

Raman spectroscopy has the ability to generate quantitative and qualitative information even though it has very weak signals which limit its chances to identify very low molecular concentrations (Petry et al., 2003). Improvements have been made especially from 1960's to enhance Raman signals which can lead to the production of high quality spectra with fine molecular details. Developments in Raman systems are discussed below in this section.

Surface Enhance Raman Spectroscopy (SERS)

In 1977, Jeanmaire and Van Duyne determined the fact that if the sample is placed on a roughened noble metal substrate, it has the ability to significantly increase Raman scattered signals (D.L. Jeanmaire and Duyne, 1977). Silver, gold or copper substrates produce strong electromagnetic fields when excited by visible light. These powerful electromagnetic fields increase the magnitude of dipole as well as intensity of inelastic scattered signals. Special resonators used in SERS allow the magnitude of Raman cross section to be 15 times more than that of basic Raman system which can produce spectra

even from extremely low concentrations (Kudelski, 2008). This advancement in Raman system is known as Surface Enhanced Raman Spectroscopy (SERS), which promotes the importance of noble metal substrates. SERS is extremely sensitive and can be applied in critical molecular identifications and in recent past it has been excessively used to explore areas of biological and chemical sensing such as trace analysis of pesticides (Weiβenbacher et al., 1997), antigens specific to prostate (Grubisha et al., 2003), nuclear waste (Bao et al., 2006), glucose (Shah et al., 2007) and several others. In this system, there are two ways to amplify Raman signals; 1) chemical enhancement, in which charge transfer takes place between the substrate and adsorbed molecules and 2) electromagnetic enhancement, where an electromagnetic field is created at the metal substrate resulting in amplified signals (Kudelski, 2008, Petry et al., 2003). Selection of substrate is the most important aspect when performing a SERS experiment. Excitation of localized surface Plasmon resonance (LSPR) is directly related to the SERS intensity therefore it is critical to control all factors that may influence LSPR in order to achieve maximum signal strength as well as reproducibility. Sensitive biological samples may get damaged when used with heavy metal surface but this can be resolved by using metal coated glass fibre tip.

SERS compatible lasers include gas, dye and solid-state lasers however Ultra Violet (UV) lasers have certain limitations because LSPR cannot be excited over a specific frequency threshold due to dielectric properties of noble metals (Haynes et al., 2005). A further advancement in SERS is the attachment of a fibre optic probe head with portable Raman system, this is named as tip-enhanced RS (Kudelski, 2008). This can be used for *in vivo* investigations to measure glucose levels in the body with the help of acquired Raman spectra (Lyandres et al., 2005).

Resonance Raman Spectroscopy (RSS)

In a classical Raman system, frequency of light which induces Raman Effect, determines the strength of scattered signals therefore the intensity of a scattered Raman signal varies according to the power of initial frequency. If this initial frequency becomes equal to the electronic transition of an irradiated molecule, Raman active modes are amplified up to 6 orders of magnitude. This phenomenon in Raman systems is known as resonance effect or resonance Raman spectroscopy (RSS). This effect has the ability to measure or target a specific molecule within a complex structure only if it has an absorption transition, which possesses same energy level as of the incoming photons (Robert, 2009). This specific property of RRS allows it to investigate particular molecules in biological tissues such as conformations or chromophores present in proteins can be assessed even though they are embedded in membranes. RRS has been extensively used in biological investigations of specific molecules such as iron-sulfer clusters, hemes and carotenoids (Ruban et al., 2007). Chromophoric biological samples like enzymes have been widely analysed by this technique. Electronic excitation of vibrational mode is generally increased where chromophores are present thus leading to enhanced signals (Kudelski, 2008). In living tissues, haemoglobin oxygen levels have also been measured using resonance effect by evaluating the intensity ratios of oxygenated and de-oxygenated haemoglobin (Ward et al., 2007). Fluorescence contamination can be significantly reduced by combining RRS and SERS, which can generate very sharp and precise spectra and can be extremely helpful in DNA identification (Faulds et al., 2003).

Coherent Anti-Stokes Raman Spectroscopy (CARS)

According to a traditional Raman system, the incident intensity of scattered Raman signals is linear however there is an involvement of two photons. One of these two photons is produced spontaneously. There is a vibrational transition which is obtained

by virtual excitation and de-excitation of higher energy states (Myers, 1997). The phenomenon of scattering can simply be defined as the energy exchange between incident photon and scattered molecule. Elastic or Rayleigh scattering takes place when there is no energy transfer between the incident photon and the molecule however in inelastic or Raman scattering there is a loss or gain in the energy of scattered photons which means that energy has been transferred (Myers, 1997). In contrast to traditional systems, CARS involve a non-linear Raman technique having two or more coherent monochromatic frequency waves as incident radiation. The overlapping of two monochromatic wave frequencies of the incident radiation is a characteristic feature of CARS. When the first frequency wave is higher than the second, the frequency difference between the two is the frequency of the molecule (Kudelski, 2008). Two special features that this technique offers are high spatial and temporal resolution and high signal generation capacity which allows measuring of the density difference between various levels of vibrational energies (S.A.J. Druet and Taran, 1981). Moreover, signals produced by CARS are generally five orders of magnitude stronger than those of a basic Raman system. According to Druet and Taran (1981), characteristic features of CARS are listed below;

- The dispersive mechanism produces enhanced and detailed spectroscopic measurements as compared to spontaneous Raman system.
- Excellent spectral and spatial resolution of 0.03 – 1 cm^{-1} and < 1mm respectively.
- Time resolution of approximately 100 fs.
- Much more luminous ($10^5 – 10^{10}$) as compared to basic Raman scattering.

Application of CARS is well documented in the fields of reactive media, plasma, gas laser amplifiers and cells (differentiation between cells) (El-Diasty, 2011, Konorov et al., 2007, Downes et al., 2011).

Confocal Raman Microscopy

The whole sample is uniformly illuminated in a typical Raman spectrometer whereas in confocal Raman system a specific point is illuminated and focused by adding a confocal microscope to the system. The incident light is focused onto the sample and the area of focus is dependent on the magnification of objective used (Petry et al., 2003). The objective which is connected to the spectrometer collects the scattered light from the sample which passes through a pinhole aperture and makes sure that only the reflected light from the focused area passes through and the additional light from any surrounding area is blocked (figure 1.8) (Petry et al., 2003). Fluorescence is difficult to control in these systems as compared to conventional Raman systems because the laser beam is targeted at a very small sample area. The advantage that this system offers is three dimensional measurement with extremely high spatial resolution of >1 μm which is capable of performing single cell investigations (James W. Chan et al., 2006, Zhang et al., 2008).

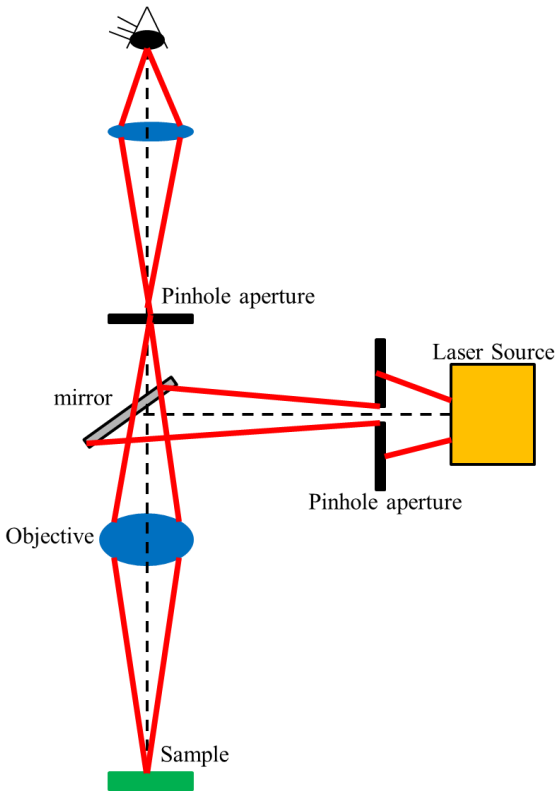

Figure 1. 8 Schematic illustration of a basic confocal Raman system

1.10 Data Analysis techniques

Spectral data can be analysed using several techniques after initial processing of the raw data such as normalisation, smoothing and baseline correction. Spectral data analysis can be performed by two main methods which include univariate and multivariate data analysis.

Univariate Data Analysis

Information present in spectral data is enormous and very complex however most of the times significant differences between spectra are visible. It is difficult to identify minute variations therefore there are chances that they may be overlooked (Kelly et al., 2011). Historically, several research groups have employed univariate data analysis methods such as peak ratios or peak intensities in order to determine possible biochemical markers (Mahadevan-Jansen et al., 1998, Stone et al., 2004, K.Teh et al., 2008). Univariate data analysis techniques can be applied on specific bands of different groups

which are of diagnostic significance. Various groups in the spectral data set can be compared by using simple calculations of peak ratios or intensities which have the potential to provide vital information. Univariate methods are restricted to specific areas of the spectral range therefore it may not be possible to explore complete spectral information with these techniques (Kendall et al., 2011). These methods cannot be ignored as they may be useful in analysing variations present in a single peak however they may have limitations as compared to multivariate data analysis techniques.

Multivariate Data Analysis

These techniques have the ability to extract important material from spectral data on the basis of computer sciences, statistics and mathematical calculations. There are two ways to utilise multivariate data analysis; unsupervised or supervised algorithms. ‘’Unsupervised algorithms’’ do not require any sample information before analysis whereas ‘’Supervised algorithms’’ do need prior knowledge regarding samples to classify them as normal or pathological in case of biological tissues (Wang and Mizaikoff, 2008).

Principal Component Analysis (PCA)

PCA is one of the most commonly used techniques for multivariate analysis of Raman spectral data. In biological tissues, numerous research groups have successfully demonstrated its use to differentiate between normal and pathological conditions (Mahadevan-Jansen et al., 1998, Malini et al., 2006, Stone et al., 2004, Murali Krishna et al., 2004, Teh et al., 2010). Apart from the constituents of a sample, there are possible factors such as equipment variation and errors in sample handling which may contribute to a Raman spectrum. PCA is an unsupervised algorithm which has the ability to compress the data set in order to eliminate irrelevant differences and at the same time restoring independent variations present in spectral features (Krishna et al., 2007). PCA

has the ability to generate a new set of variables from existing raw data, these new sets are known as principal components (PC's/factors) and scores. Each PC represents variations present in the spectral data where the first PC specifies maximum variance which decreases with every following PC therefore it is important to identify principal components that hold most useful information. PCA can be employed to analyse complete spectral range or desired regions of spectra which makes it more specific to a component in biological tissues.

Cluster Analysis

Cluster analysis generates classes or provides a trend present in the data set without having any prior knowledge (unsupervised method) (Kelly et al., 2011). The principle of cluster analysis is based on the degree of similarity and distance between groups; more similarities decreases the distance between groups (Wang and Mizaikoff, 2008). There are two types of clustering techniques; hierarchical clustering analysis (HCA), which do not need any information about the data before analysis, techniques that require prior knowledge are k-mean cluster analysis (KMCA) and fussy c-means cluster analysis (FCA). HCA is based on various linkage methods to produce clusters such as single linkage, complete linkage, average linkage and ward's method (Beebe and Kowalski, 1987).

- HCA Single-linkage

  According to this method, clusters are formed by using distance between nearest samples, as a result large clusters are formed and the separation between groups is not very good.

- HCA Complete-linkage

  Clusters are formed by using distance between farthest samples, as a result distinct clusters are formed and the separation between groups is much enhanced.

- HCA Average-linkage

  Clusters are formed by using average distance of single and complete linkage.

- Ward's method

  Ward's method has an added advantage over previously mentioned linkage systems that it not only forms clusters on the basis of similarities but it also measures the degree of homogeneity or heterogeneity within each cluster.

Linear Discriminant Analysis (LDA)

LDA is a commonly used supervised algorithm in which a linear combination of variables is created on the basis of variances between classes and the direction of variables in a spectral space is also determined. A number of unknown objects or samples are assigned a class membership through defined parameters. These defined parameters are the prior knowledge or training models of the data set which predict class memberships. Based on this information a linear discriminant function is calculated which differentiate between classes in the data set. Unknown samples are assigned to specific groups by these discriminant functions (Krafft et al., 2009). Discriminant functions minimises intra class variations and at the same time maximises variations between different classes. In quantitative data analysis the standard measure of distance between two classes is Mahalanobis distance. It relies on the relationship between variables which identify various trends for analysis. The distance between unknown samples and the centre of each identified group is usually determined by Mahalanobis distance (Wang and Mizaikoff, 2008, Krafft et al., 2009). LDA has been successfully used in several biological studies to classify different tissue types (K.Teh et al., 2008, Larraona-Puy et al., 2011, Larraona-Puy et al., 2009). Promising observations using LDA with spectral data sets have encouraged researchers to further explore this method.

Sensitivity and Specificity

To determine the strength of a diagnostic technique/algorithm is extremely essential in medical practice. The most commonly practiced tests are the calculation of sensitivity and specificity which predict normal or abnormal medical conditions (Stone et al., 2004). Sensitivity can be defined as the diagnostic ability of the test to determine the percentage of correctly identified diseased cases. Sensitivity of the test increases with increase in cases that are positively identified as a disease. Specificity on the other hand is used to calculate the percentage of cases which are positively classed as normal or no disease. Similarly the percentage of specificity increases with increase in correctly predicted normal subjects (Stone et al., 2004).

1.11 Raman spectroscopy in cancer research

Raman spectroscopy has been widely used in the field of chemistry and polymers to analyse various coatings on membranes and progression of several chemical reactions (Conroy et al., 2005, Laska and Widlarz, 2005, Quintas et al., 2004, Mazurek and Szostak, 2006, Baklanova et al., 2007, Hwang et al., 2005, Sacristan et al., 2002). Moreover, spectroscopy has been applied successfully in the fields of archaeology (Frost et al., 2002), forensic investigations (Thomas et al., 2005) and astronomy (Edwards et al., 2005)as well.

In recent years vibrational techniques and in particular Raman spectroscopy has gained a lot of interest in the field of biological sciences specially associated with diagnosis of pre-cancer and cancer (Malini et al., 2006, Olivo et al., 2011, Ana Paula Oliveira et al., 2006, Kendall et al., 2009, Stone et al., 2004, Stone et al., 2000, Stone et al., 2002b, Stone et al., 2002a). Within the last 10 years there has been a remarkable progress in biomedical imaging modalities for example Magnetic Resonance Imaging (MRI), Positron Emission Tomography (PET) and Computed Tomography (CT) for cancer diagnosis (Keereweer et al., 2011). The availability of these technologies has enabled

surgeons to perform surgical procedures with improved precision and accuracy leading to better prognosis. At the same time, drawbacks are also associated with these conventional technologies when used intraoperatively. This has shifted the focus of research a great deal towards optical imaging techniques in biomedical applications for oncology. These optical imaging techniques are called “Biophotonics”. These techniques could non-invasively provide real time imaging of cells and tissues which hold molecular level information and can be a useful tool to identify different types of tissues. Moreover these techniques may also aid in surgical procedures by detecting tumour margins with great precision and accuracy (Michael B. Fenn et al., 2011). The application of spectroscopic techniques have been reported on several biological tissues such as, teeth, pharynx, tongue, brain, breast, colon, lungs, skin, and heart etc.

Raman spectroscopy has been widely used in the field of biomedical applications. Different cancer types have been investigated in search of a real time, non-invasive and accurate diagnosis (Swinson et al., 2006, Krishna et al., 2004, Venkatakrishna et al., 2001, Sharwani et al., 2006, Deshmukh et al., 2011a, Singh et al., 2013, Singh et al., 2012a, Malini et al., 2006, Olivo et al., 2011).

Barr *et al*., (1998) published a review article aimed at early diagnosis of gastrointestinal cancer using optical spectroscopy. Their information suggested that fluorescence spectroscopy has the ability to detect malignancy at early stages and they also mentioned that this technique is currently under investigation. They also informed about optical coherence tomography (OCT) which can identify various layers of oesophageal wall whereas Raman spectroscopy has the potential to provide molecular level information and may be used in conjunction with endoscopes (Barr et al., 1998).

In 1999 Shaw and Mantsch published this novel review article which was focused on biological applications of vibrational spectroscopy. The main idea of this review paper

was to explore the role of NIR Raman spectroscopy in medical applications. This review also described the value of spectroscopic techniques in diagnostic applications where differentiation can be done on the basis of molecular alterations (Shaw and Mantsch, 1999).

Patrich *et al*., (2001) explored different aspects of medical diagnostics through mid-Infrared and Raman spectroscopy. This article provides evidence which support the ability of these techniques in the field of medical diagnostics. Their main focus was to explore internal medicine such as haematology, endocrinology, gastroenterology, angiology, rheumatology and nephrology. Moreover on the basis of literature they have also discussed *in vivo* applications of these techniques towards real time and non-invasive diagnosis.

Choo-Smith *et al*., (2002) published a review paper on biomedical applications of Raman spectroscopy. They provided an overview of biomedical avenues which are addressed by Raman spectroscopy, these areas included detection of pathogenic microorganisms, assessment of atherosclerotic plaque composition, evaluation of agents applied on skin and early diagnosis of cancer. Further in their discussion they focused on where Raman spectroscopy stands today and what are the limitations associated with it. They also identified the point in how to overcome practical limitations so that this technique is available in clinical set ups (Choo-Smith et al., 2002).

Review paper published by Zeng *et al*., (2004) was based on early diagnosis of lung cancer using various optical techniques and imaging systems. They provided detailed technical information regarding optical principles behind white light and Autofluorescence Bronchoscopy (AFB). Moreover this article also included the potential of AFB in terms of lung cancer diagnosis and management of patients. They mentioned that AFB has shown excellent results in detecting lung cancer and is

considered to be the most authentic and established technique at this time. In this article, Raman spectroscopy was also highlighted as a potent newly emerging technique (Zeng et al., 2004).

Swinson and colleagues explored the area of ‘’optical techniques used in diagnosis of head and neck malignancies’’ in their review article published in 2006. Three optical techniques, Fluorescence spectroscopy (FS), Elastic Scattering spectroscopy (ESS) and Raman spectroscopy were explained, compared and discussed in their article. They have presented that these techniques have the potential to differentiate between normal and pathological tissues on the basis of molecular level information obtained. Apart from tissue detection, they have also provided information regarding abilities of these techniques in determining drug levels during chemotherapy, surveillance of guided tissue biopsies and haemoglobin tissue perfusion in free flaps (Swinson et al., 2006).

Rehman and colleagues published a review article on Raman spectroscopy of biological tissues in 2007. The aim of this article was to provide a detailed background and establish a data base in terms of peak assignments of biological tissues. The idea was to generate comprehensive peak assignments of biological tissues which can represent molecular fingerprint and help other researchers to define chemical structure of biological tissues. This article was the first to provide detailed Raman peak frequencies of biological tissues and proved to be a great success and was cited by many research groups over the years (Movasaghi et al., 2007).

The potential of optical spectroscopy in cervical cancer was reviewed by Krishna *et al*., in 2008. A background of cervical cancer including anatomy, histology and etiology was also provided in the review article and they discussed the possibilities of cervical cancer detection through optical spectroscopy. Spectroscopic techniques, radiotherapy

and radiation resistance in relation to cervical cancers were also briefly included in this review paper (Murali Krishna et al., 2008).

Recent applications of Raman spectroscopy in diagnosis and biochemical evaluation were reported in a detailed review by Moreira et al., 2008. This review article provided detailed information about chemical identification and characterisation of biological compounds which may lead towards early, efficient and precise diagnosis of pathological conditions hence improving prognosis and eventually quality of life for patients. It was also mentioned in this study that Raman spectroscopy has a potential for sample characterisation which can be useful for in situ analysis of the disease.

Old et al., (2014) published a review article ‘’vibrational spectroscopy for cancer diagnostics’’. They provided a detailed explanation of Raman and FTIR spectroscopy and highlighted their ability to diagnose cancer on the basis of subtle biomolecular alterations. This article also provides a comprehensive comparison between the two techniques highlighting their pros and cons for various applications. They have discussed the application of these spectroscopic techniques in several medical applications such as diagnosis of oesophageal cancer, gastric cancer, colorectal cancer, lymphomas and breast cancer. Along with spectroscopic data, they have elaborated the significance of chemometric data analysis systems such as Principal Component Analysis (PCA), Linear Discriminant Analysis (LDA), Partial Least Squares (PLS), Support Vector Machines (SVM) and Cluster analysis. These multivariate data analysis techniques are capable of extracting relevant biochemical information out of huge spectral data sets and have shown extremely promising results. They have emphasized that a lot has been done in cancer detection using spectroscopic means but now it is time to move towards clinical application (Old et al., 2014).

The application of Raman spectroscopy in various cancers is summarised in table 1.5.

Table 1.5 Brief summary of application of Raman spectroscopy in various cancers

Research Group	Technique used	Investigated tissue/sample	Results	Ref.
Haka	**Raman spectroscopy** Spectra of breast tissue components (collagen, fat, cell nucleus, epithelial cell cytoplasm, calcium hydroxyapatite, calcium oxalate, cholesterol and β-Carotene were fitted against spectra of whole breast tissue.	**Breast tissue** 1) Normal tissue 2) Tissue with fibrocystic changes 3) Fibroadenoma 4) Infiltrating carcinoma	Increased collagen in abnormal breast tissues as a result of fibrosis	(Haka et al., 2005)
Haka	**Raman spectroscopy** Optical fibre probe	**Breast tissue** *In vivo* application during partial mastectomy.	sensitivity and specificity was 100% whereas accuracy was found to be 93.3%	(Haka et al., 2006)
Rehman	**Raman spectroscopy**	**Breast tissue** *In vitro* analysis of breast tissue samples.	Successfully differentiated between different grades of Invasive ductal carcinoma and ductal carcinoma *in situ.*	(Rehman et al., 2007)
Pichardo Molina	**Raman spectroscopy**	**Breast cancer** Analysed serum samples from healthy individuals and breast cancer patients.	Successfully discriminated between two serum types by achieving sensitivity and specificity of 97% and 78% respectively.	(Pichardo-Molina et al., 2007)
Kumar	**Raman spectroscopy**	**Breast tissue** 69 Frozen tissue samples from surgical resections	Promising relationship was observed in this study between pathological and Raman results to classify different tissue types.	(Kalyan Kumar et al., 2008)
Lieber	**Raman**	**Skin tissue**	Lesions were	(Lieber

	spectroscopy Portable fibre optic device was designed for this study to conduct in vivo investigation.	19 patients were selected and spectra were obtained from 21 lesions.	classified as normal, inflamed, Basal cell carcinoma (BCC) and Squamous cell carcinoma (SCC). Differentiation of inflamed and cancerous tissues showed an overall accuracy of 95%.	et al., 2008)
Larraona-Puy	**Raman spectroscopy**	**Skin tissue** Skin tissues excised during micrographic surgeries of 20 patients.	LDA classified tissues as BCC, dermis or epidermis. Collagen type I mainly contributed to differentiate between the dermis and BCC. DNA peaks provided evidences in discriminating BCC from epidermis. Over 85% sensitivity was recorded to distinguish BCC from dermis and epidermis.	(Larraona-Puy et al., 2009)
Larraona-Puy	**Raman spectroscopy**	**Skin tissue** Skin tissues excised during micrographic surgeries.	They were spectroscopically successful in differentiating hair follicle from BCC as they can be deceiving during diagnosis.	(Larraona-Puy et al., 2011)
Bodanese	**Raman spectroscopy**	**Skin tissue** Analysed normal skin tissues and BCC lesions. PCA and a biochemical model	The regions between 800-1000 cm^{-1} and 1200-1300 cm^{-1} showed the prominent	(Bodanese et al., 2010)

		were constructed based on the amounts of collagen and fat detected in Raman spectra.	differences which were related to vibrational bands from proteins and lipids.	
Beljebbar	**Raman spectroscopy** A portable Raman spectrometer coupled to a microprobe was used to obtained high quality spectra.	**Brain tissue** *Ex vivo* study was conducted on normal, invasive and tumour tissues. For their *in vivo* study, they implanted C6 glioblastoma cells in rat brain and monitored its growth from 0-20 days.	In ex vivo study normal, invasive and tumour tissues were discriminated with 100% accuracy. Raman spectral results not only differentiated between normal and tumour tissue but differences were also observed within tumour from 0 to 20 days during growth.	(Beljebbar et al., 2010)
Kirsch	**Raman spectroscopy** *In vivo* application using a fibre optic probe.	**Brain tissue** *In vivo* investigation for brain surface mapping to detect intracerebral tumours. Murine melanoma cells were injected in the carotid artery of mice, which in 14 days showed subcortical and cortical tumour growth.	Concentration of lipids in normal and cancerous tissues provides characteristic features that distinguish the tissue types. Raman results were co related with mass spectrometry analysis of the same tissue and was strongly supported.	(Kirsch et al., 2010)
Teh	**Raman spectroscopy**	**Gastrointestinal tissue** 76 gastric tissue samples from 44 patients who were experiencing endoscopy or gastrectomy.	Differentiated between normal and dysplastic tissues. PCA-LDA showed sensitivity and specificity of 95.2% and 90.9%	(K.Teh et al., 2008)

			respectively.	
Teh	**Raman spectroscopy**	**Gastrointestinal tissue** 100 tissue samples to differentiate between normal gastric epithelium and two subtypes of adenocarcinoma.	Clear differences were observed in normal stomach tissue and adenocarcinoma subtypes. PCA and multinomial logistic regression suggested that even more accurate discrimination can be achieved.	(Teh et al., 2010)
Lyng	**Raman spectroscopy**	**Cervical tissue** Tissue samples were obtained from 40 patients.	Spectra from nucleic acid, proteins, lipids and carbohydrates discriminated normal and abnormal tissues with the help of multivariate analysis.	(Lyng et al., 2007)
Robichaux-Viehoever	**Raman spectroscopy** *In vivo* study by introducing a portable Raman spectroscopic fiber-probe system	**Cervical tissue** 2 sets of patients, one undergoing hysterectomy (normal tissue) and second related to cervical dysplasia having abnormal Pap smear.	RS showed better sensitivity and specificity than colposcopic examination between high grade dysplasia and normal tissue.	(Robichaux-Viehoever et al., 2007)
Magee	**Raman spectroscopy**	**Lung tissue** Sputum analysis of 3 different groups. 1) Diagnosed lung cancer. 2) No lung cancer but having one risk factor. 3) Young healthy adults with no risk factors.	Lung cancer patient's sputum and at risk patient's sputum showed sensitivity and specificity of 90% and 62% respectively. At risk patients and healthy adults showed sensitivity and specificity of	(N. D. Magee et al., 2010)

			90% and 93% respectively.	

1.12 Raman Spectroscopy in Oral Cancer

It is extremely important to detect dysplastic and malignant lesions of the oral cavity accurately and at an early stage in order to improve prognosis of squamous cell carcinoma. Research has diverted a great deal towards Raman spectroscopy which is regarded as a potential tool for real time detection and surveillance of suspected lesions because of its ability to non-invasively provide biochemical information. Several studies have been reported in the literature regarding head and neck cancers but there is a need to further explore potentials of Raman spectroscopy in oral cancer exclusively.

Guze and co-workers conducted an *in vivo* study to assess the capabilities of Raman spectroscopy in differentiating normal or benign lesions from premalignant and malignant lesions. Cohort contained 18 patients between 20 to 65 years of age from both sexes, these treatment-naïve subjects were already diagnosed as benign hyperkeratosis, inflammation, fungal, dysplasia (mild, moderate and severe) or OSCC by histopathology. Raman probe was specially designed to collect spectra from 0 to 1800 cm^{-1} wavenumber with 1 second of acquisition time. One lesion was scanned within 5 minutes and no sign of discomfort was observed in patients. Two groups were formed, one containing premalignant and malignant lesions (MILD) and the second with normal and benign lesions (LEU). Spectral data revealed that there was no change in the intensity of phenylalanine peak centered at 1002 cm^{-1} in both groups. A broad

peak was observed between 1150 cm^{-1} and 1250 cm^{-1} containing several overlapping peaks at 1175 cm^{-1}, 1204 cm^{-1} and 1236 cm^{-1} which can be assigned to C – H bending mode of tyrosine, C – C_6H_5 stretching modes of tyrosine and phenylalanine and amide III C – N stretching mode respectively. An important finding was increased intensity of saturated fatty acids in LEU was observed at 1298 cm^{-1}. Similarly intense band at 1448 cm^{-1} (CH_2 bending mode of proteins and lipids) was present in LEU as compared to MILD group which was seen in difference spectra. Tryptophan is known to be an important amino acid in metabolic activities; it was present at 1618 cm^{-1} and difference spectra showed increased intensity in MILD group. Multivariate data analysis using linear discriminant analysis (LDA) was able to discriminate between MILD and LEU with 100% sensitivity and 77% specificity (Guze et al., 2014). Spectra from lesion border and within tumour showed subtle differences between them which might indicate heterogeneity or complex nature of malignant tissues. They also suggested that tumour margin might have a trend like normal tissue hence resulting in reduced specificity. They concluded by successfully demonstrating *in vivo* application of Raman spectroscopy in discrimination of premalignant/malignant and normal/benign oral tissues. They had a relatively small data set therefore in future a larger group of data set would certainly be helpful.

Aditi Sahu and colleagues performed their experiments on serum (blood) samples keeping in mind that these samples can be easy to collect, store and transported to those laboratories where Raman equipment is available. They selected 40 patients having OSCC of the tongue and 14 from buccal mucosa making a total of 54 samples. All these patients were already confirmed with OSCC by histopathological examination. DNA, proteins, amino acids and β-carotene contributions were observed in spectral data. Further when spectra of different samples were compared, variances in peak intensity and shifts were seen. β-carotene was present at 1155 and 1523 cm^{-1} showing highest

peak intensity in normal sera however decreased intensity was seen in tongue and buccal OSCC spectra. Difference spectra were calculated by subtracting normal from OSCC for further analysis. Buccal mucosa cancer serum spectra showed increased intensities of protein assignments at amide I (1660 cm^{-1}), amide III (1240 cm^{-1}), DNA (1340 cm^{-1}), CH_2 deformation (1445 cm^{-1}), tyrosine (830 cm^{-1}) and tryptophan (850 cm^{-1}). Negative bands indicated higher presence in normal samples which were seen in phenylalanine (1004 cm^{-1}) and β-carotene at (1155 cm^{-1} and1523 cm^{-1}). Tongue cancer serum samples showed similar features upon comparison with control normal sera spectra. Overall spectral data showed increased DNA and protein levels and decrease in β-carotene was associated with pathogenesis. They also supported that with decrease in β-carotene there was in increased risk of breast cancer in females. Based on their results they also concluded that proteins, DNA and decreased levels of β-carotene may be characteristic Raman markers associated with cancer. Two different approaches were adopted before performing multivariate analysis in order to identify heterogeneity within samples. 1) Spectra wise approach where each spectra was treated as an individual and 2) patient wise approach where average spectrum of 1 sample represented whole group. Their data concluded that PCA-LDA has shown encouraging separation between normal and cancer serum samples with an efficiency of approximately 85% in spectra wise approach and 78% in patient wise approach. Classification between cancer groups also showed promising results but a larger data set is required for further improvements and patient wise approach was proposed for prospective studies (Sahu et al., 2013).

Froukje Cals and colleagues (2013) conducted their work on oral tissue sections. Their results demonstrated that characteristic peaks of basal and supra-basal layers of the epithelium were monitored between 784 – 938 cm^{-1} and 1206 – 1370 cm^{-1}. Moreover they also observed peaks originating from epithelium at 526, 546, 784, 828, 942, 958,

1128, 1318 and 1340 cm^{-1} (Cals et al., 2013). The presence of collagen associated peaks at 570, 820, 858, 876, 922, 1248 cm^{-1} indicated existence of loose and dense connective tissue. The quantity of collagen in tissues is expressed in spectral data which discriminates between loose and dense connective tissue (Movasaghi et al., 2007). Further findings include distinct bands of adipose tissue (874, 972 1064, 1082, 1264, 1304, 1440, and 1746 cm^{-1}) and smooth muscle (488, 758, 904, 1046, 1104, 1278, 1304 and 1398 cm^{-1}) in spectral data. The focus of this study was to investigate different layers of oral mucosa and identify specific features of these layers which can be used as Raman markers. They suggested that in normal mucosa which is not sectioned, Raman spectrum may arise from deeper layers due to thinner epithelium as compared to malignant tissue. This was predominantly shown by two sharp bands at 1260 and 1300 cm^{-1} which were attributed to *cis* stretch C-H and CH_2 twist respectively, a sharp peak in the amide I region due to C=C stretch vibrations (1656 – 1660 cm^{-1}), a strong CH_2 bend (1440 – 1450 cm^{-1}), and ester bands (1740 – 1750 cm^{-1}) (Krishna et al., 2004, Malini et al., 2006, Wu et al., 2011, Singh et al., 2012b, Su et al., 2012b). Adipose tissue forms the deep underlying submucosal layer, since normal oral mucosa exhibits thinner epithelium as compared to cancer therefore it is likely that their spectra are lipid dominant however one cannot conclude that increased epithelial thickness is associated to cancer which may lead to incorrect classification. It is shown that normal tissue spectra have been associated with lipid dominant peaks as compared to protein dominancy in malignant conditions moreover it has also been claimed that malignant tissues originating from epithelial surfaces generally exhibit increased epithelial thickness (Mills and Morris, 1999, Mills, 2004).

Singh *et al*., (2013) demonstrated *in-vivo* application of Raman Spectroscopy to detect early changes in neoplastic transformation. *In-vivo* Raman spectra were collected from tumour adjacent mucosa (TAM) with and without tobacco related cancerous lesion and

from age-matched healthy controls with and without tobacco habits. Spectral results of healthy control individuals suggested high lipid content due to the dominance of δCH_2 band; amide III region, amide I and the ester band around 1744 cm^{-1}. However on the other hand, in tumour region spectra δCH_2 band was broad and shifted and amide I peak was broad which suggested protein dominant region. In healthy mucosa reticulin and collagen fibres are present in epithelium and lamina propria whereas submucosa consists of adipose tissue (Singh et al., 2013). Architectural arrangement or morphological appearance is lost during pathological conditions and in tumours which might result in mixing of different layers and loss of lipid content (Deshmukh et al., 2011a, Venkatakrishna et al., 2001, Malini et al., 2006). Large amounts of surface proteins, antibodies, antigens and enzymes are present in cells during abnormal or pathological conditions which may generate a protein enriched spectrum. They found minor differences between spectra of contralateral normal and habitués healthy controls although their spectra were dominated by lipid dominant bands. Healthy controls spectra showed subtle shift in amide III and δCH_2 along with broadening of amide I region hence suggesting alterations in secondary structure of proteins. Overall lipid loss was observed at 1440, 1300 and 1743 cm^{-1} in patients with tumours and increased contents of haemoglobin (1560 cm^{-1}) and DNA (1340, 1480 cm^{-1}) were recorded at the same time which may propose that number of dividing nuclei and process of angiogenesis is increased during cancer and are known indications of tumorogenesis. It was suggested that these changes may be as a result of long term consumption of tobacco which may lead to increased proliferation of epithelial cells in the upper aero-digestive track of smokers and therefore may play a role in preliminary genetic changes accounting for the development of SCC (Shin et al., 1993). Hyper cellularity as a result of tobacco consumption was also reported with spectral changes showing lipid loss (1300, 1440, 1743 cm^{-1}), major protein characteristics (broad 1660 cm^{-1}) and significant

DNA peaks (1340, 1480 cm^{-1}). Moreover they also found positive DNA bands with loss of lipid features (1300, 1440, 1650, 1743 cm^{-1}) in non-habitués contralateral patients. Overall the general trend observed was loss of lipids in most of the pathological conditions as compared to healthy controls (Singh et al., 2013). These findings were very promising however still there is a need to further explore Raman spectroscopy and generate a comprehensive database which can be used for chemometric modelling systems.

Su *et al*. (2012) examined normal and cancerous oral tissues as well as squamous cell carcinoma cell line (TCA8113) using Raman confocal micro-spectrometer. They observed that DNA and proteins were dominant in malignant tissues however amino acids were mainly associated to normal tissue spectra, these findings were also confirmed by Zinin *et al*., 2010 and Gelder *et al*., 2007. Strong peaks of tryptophan (molecular vibrational modes) were observed at 756 and 1546 cm^{-1} in normal oral tissue whereas vibrational band of phenylalanine of proteins at 1004 cm^{-1} was present in both tissue types. Strong bands at 1341 and 1655 cm^{-1} were observed in malignant tissue sections which were attributed to vibrational mode of adenine (A) and guanine (G) of DNA, and carbohydrate amide I in proteins, respectively (De Gelder et al., 2007, Zinin et al., 2010, Su et al., 2012a). Cell samples produced fewer Raman peaks as compared to tissue samples suggesting that tissues are more complex structures. Moreover differences between normal and cancer cells were relatively less as compared to normal and cancer tissues. Prominent and strong band observed at 1449 cm^{-1} may be attributed to CH_2 bending mode of lipids and long chain amino acids. Peak assigned to vibration of carbohydrate amide I was present at 1656 cm^{-1}. Strong peaks at 856 cm^{-1} were present in normal cells which may relate to molecular vibrational modes of tyrosine whereas cancer cells exhibit strong spectral contribution at 1266 cm^{-1} which can be associated with α-helix structure of proteins (amide III band). They suggested that

nucleic acid content was higher in malignant tissues and cells as compared to normal because of the fact that specific DNA associated peaks at 1341 and 1580 cm^{-1} had increased intensities in cancer. Furthermore, malignant cells and tissues also showed increase in intensities of peaks present at 1265 and 1655 cm^{-1} which were typical protein assignments. They also found that peaks associated with amino acids (756, 856, 1175, and 1606 cm^{-1}) were considerably stronger in normal cells and tissues as compared to malignancy and proposed that carcinogenesis might be related to amino acid metabolism. Study conducted by Tankiewicz Anna's 2006 also strongly suggested that patients with oral squamous cell carcinoma have increased concentrations of tryptophan (Tankiewicz et al., 2006).

Singh and colleagues (2012) conducted an *in vivo* study to investigated premalignant oral lesion using Raman spectroscopy. Spectral data revealed that contralateral normal, habitual tobacco users and healthy controls were dominated by lipids which was indicated by C=O ester bands, strong δCH2 bend and sharp amide I and III features however in contrast to this, they found out that tumour spectra are enhanced with broad proteins bands at amide I and III and broad and shifted δCH2 bend. These findings were consistent with earlier reports as well (Malini et al., 2006, Olivo et al., 2011, Deshmukh et al., 2011a). Lipid bands were also dominant in spectra of habitual tobacco users however subtle differences were present as compared to healthy controls, for example slight shift in amide III and δCH2 bend along with broader of amide I region, which might propose alterations in protein secondary structures. Similarly it was observed that spectra of premalignant lesions showed features like tumour spectra in the finger print region. They also suggested that long term use of tobacco can cause inflammation of upper-aero digestive tract due to increased proliferating cells; these changes may contribute towards development of OSCC. These epithelial changes may have differentiated between healthy controls, habitual tobacco users and contralateral normal

subjects. In normal oral mucosa, different layers such as, epithelium, lamina propria and submucosa can be easily identified however in pathological conditions all these layers are mixed and lead to loss of underlying lipid layers. PCA and LDA were performed which showed promising results where average of 94.7% classification efficiency was achieved between normal, pre-malignant and tumour sets. In second set of comparison which included healthy controls, tobacco users and pre-malignant cases, an average classification efficiency of 94.9% was achieved (Singh et al., 2012a). These results were very promising and encouraged the use of multivariate data analysis techniques like PCA and LDA for future studies with even larger and diverse data sets.

Atul Deshmukh and group (2011) designed this study to perform deep tissue analysis and collected Raman spectra from different surfaces of oral epithelium and connective tissue *ex vivo*. Predominant lipid features were observed in normal tissue spectra which were identified by ester bands, sharp peaks of amide III, strong δCH2 bend and sharp band at amide I, however in contrast tumour spectra revealed protein enriched features such as broad amide I and III and broadened δCH2 bend. They identified that strong lipid features were present in intact and separated connective tissue as compared to epithelium; moreover broad spectral features were seen in epithelial data at amide I and amide III. Average and standard deviation results showed fewer similarities in cancer tissue suggesting it has more complex and heterogenic nature as compared to normal. PCA results demonstrated that no clear separation was seen between all 4 groups of normal tissue and highly overlapping cluster formation was observed between intact epithelium and connective tissue. On further evaluation it was found that PCA was able to cleanly classify separated epithelium and connective tissue which suggested that more variations were present in spectral date of separated epithelium and connective tissue. Scatter plot of LDA showed the same trend where separated epithelium and connective tissue formed clusters far from one another and an overall accuracy of 94%

was achieved. They concluded that the morphology and structure of tissues are directly related to Raman spectral signatures. Spectra from intact tissue showed contributions from both lipids and proteins however same surface spectra were different after separation. This suggests overlapping of various spectral features in intact tissue and spectra recorded from surface does include features from underlying tissues which may be beneficial for depth profiling (Deshmukh et al., 2011a).

Li *et al*., 2009 conducted an *in vitro* study and used tissue samples of oral squamous cell carcinoma (SCC) for Raman analysis. Spectral data showed a general increase in intensities of SCC as compared to normal tissues, specifically peaks related to proteins and DNA which were present at 747, 897, 939, 1060, 1125 and 1610 cm^{-1} assigned to CH_2 rocking, C–C stretching, C–C skeletal stretching, amide I (α-helix), C–N stretching in phenylalanine and C—C bending in phenylalanine and tyrosine. Moreover, rise in DNA content was observed due to increased intensity at 1092 cm^{-1} which is an assignment of O–P–O backbone stretching in DNA. In general their work identified that malignant tissues have increased intensities at 751, 939, 1220, 1250 and 1344 cm^{-1} which are assignments of symmetric ring breathing of tryptophan, C–C stretching and amide III, β-sheet in protein and CH deformation of protein respectively. The ring-breathing modes of DNA and RNA were also increased in malignant tissues and observed at 780, 1250 and 1344 cm^{-1}. Other significant increases that they observed were at 1071 and 2850 cm^{-1} which were associated to skeletal C–C stretching and $\nu_{as}CH_2$ of lipids (Li et al., 2010). Their results mainly based on univariate data analysis whereas use of multivariate tools would have improved the accuracy of their results.

Malini and co-workers in 2006 performed their work on normal, premalignant, inflammatory and malignant oral tissues. Their spectral data revealed that significant differences were observed between normal and malignant tissues in the region 1200–1800-cm^{-1} however less variances were noticed between malignant, premalignant and

inflammatory tissues which were primarily in 900–1400-cm^{-1} region. In normal tissues, phospholipid peaks were pronounced with no involvement from proteins at 1750cm^{-1} (C¼¼O) ;sharp, weak peak at 1650 cm^{-1} (C¼¼C); strong CH_2 bend at 1440 cm^{-1} (C—O—C); two sharp peaks at 1330 cm^{-1} and 1270 cm^{-1} (¼¼CH); and the broad peak at 1080 cm^{-1}. Oral epithelium in normal condition is a bilayer membrane of squamous epithelial surface which generates a lipid dominant spectrum. In contrast, broad and strong amide I, CH_2 bend at 1450 cm^{-1}, broad peaks in the amide III between 1200–1350 cm^{-1} region, and the sharp phenylalanine peak at 1000 cm^{-1} were observed in protein enriched malignant tissue spectra. As the tissue changes its state from normal to inflammatory, premalignant or malignant, large amounts of proteins are built within cells such as enzymes, receptor proteins, antigens and antibodies which produce a protein dominant spectrum. Amide I band of proteins showed significant alterations between tissue types which may suggest disordered protein structure and conformational changes such as α-helix, β-plates. Promising results were obtained in their study which showed that inflammatory and malignant tissues were distinguished from normal and malignant which may lead to the possibility of detecting the lesions early (Malini et al., 2006). Metabolic activities are increased in malignant conditions which give rise to molecular species like NADH and FAD, moreover DNA content also increases as the proliferation rates of cells. Amide I and amide III regions showed substantial changes as the tissue changed its state from normal to inflammatory.

Blood flow has known to increase at the site of injury which is evident in inflammatory conditions. In response to any external or internal, injuries or pathogens these inflammatory responses take place. Albumin is a protein and present in blood plasma, it is suggested that protein peaks (1653, 1450, 1342, 1317, 1270, 1241, 1050–1160, and 943 cm^{-1}) in inflammatory tissues had their major contribution from proteins (Parker, 1983).

Oliveira and colleagues (2006) evaluated the potential of Fourier-Transform (FT)-Raman spectroscopy to differentiate between normal, dysplastic and oral squamous cell carcinoma tissues. In this study oral carcinogen was induced to 21 male Syrian Golden hamsters by applying 0.1 mL of 0.5% 7,12-dimethybenz[a]anthracene (DMBA) in mineral oil in right pouch whereas left pouch only contained mineral oil and served as a control. Exophytic and endophytic tumours developed at 14^{th} week and the animals were sacrificed. Both right and left mucosae were excised and all 42 samples were stored in liquid nitrogen until required for Raman analysis. Histological examination revealed that 2 out of 21 carcinogen induced samples developed dysplasia and the rest of 19 as OSCC. Significant spectral differences were observed in 800 – 1800 cm^{-1} region between normal and malignant tissues. Normal tissues presented higher intensities of lipids associated peaks as compared to OSCC. Similar pattern was seen in studies conducted by Venkatakrishna et al., (2001) and Yang et al., (1998) (Venkatakrishna et al., 2001, Yang et al., 1998). Variations in the intensity of phenylalanine band was observed at 1007 cm^{-1} where increased intensity was present in OSCC spectra which might suggest increased protein content in cancer tissues. They also suggested that the shift in nucleic acid band from 1555 – 1560 cm^{-1} may be due to increased nucleic acids in cells and might hold diagnostic significance between normal and malignancy. Though a small number of dysplastic cases were analysed, there was a shift observed at 1267 – 1337 cm^{-1} which was more intense as well than normal and malignant. PCA results showed encouraging separation between tissues and best results were observed at principal components 3 and 6. Clear separation between OSCC and normal clusters were seen and a sensitivity and specificity of 100% and 55% respectively was achieved. Overall they concluded that protein dominancy is observed in malignant tissues as compared to lipid enhanced normal mucosa spectrum (Ana Paula Oliveira et al., 2006).

1.13 Hypothesis

Raman spectroscopy can be used in the diagnosis and treatment of oral cancer to differentiate between normal and abnormal tissues as well as tissues undergoing radiotherapy on the basis of biochemical dissimilarities.

1.14 Aims

- To develop tissue engineered models of the oral mucosa for *in vitro* analysis using Raman Spectroscopy.
- To investigate the potential of Raman spectroscopy as an analytical tool to detect biochemical differences between tissue engineered models of normal, dysplastic and cancerous oral mucosa.
- To analyse tissue engineered dysplastic and cancer models to identify and differentiate their subtypes using Raman spectroscopy.
- To determine the use of Raman spectroscopy to probe patient biopsies of normal, dysplastic and cancerous oral lesions and differentiate them on the basis of biochemical variations.
- To investigate the effects of different doses of radiation and identify specific biomolecules that show significant variations both in tissue-engineered normal and cancer models using Raman spectroscopy. These biomolecules may act as Raman markers for targeted radiotherapy and reduce the side effects as well as improve treatment outcomes in future.

Chapter 2

Materials & Methods

Section 1 - Tissue Engineered Oral Mucosa

Healthy human tissue models have been developed and used as grafts in different parts of the body for repair and replacement purposes. Apart from their clinical application, these models along with dysplastic and cancer models provide an appropriate replication of *in vivo* events by facilitating understanding of disease progression *in vitro* leading to better diagnostic abilities and improved therapeutics.

We have developed and investigated three different types of tissue engineered oral mucosa models including normal, dysplastic and cancerous oral mucosa. Various cell lines were used to construct these models which consist of an epithelium along with underlying connective tissue (Colley et al., 2011). Understanding the variations present in biochemical pathways in different tissue types is extremely vital and could be achieved by these *in vitro* 3D models.

Raman spectral analysis of these models from normal to dysplastic and cancerous oral mucosa provided molecular level information helping in distinguishing between different tissue types.

2.1 Materials

All materials used in this study were purchased from Sigma-Aldrich (Poole, UK) unless otherwise stated and used as of the manufacturer's instructions.

2.1.1 Cell Culture basics

Class II laminar flow hoods (Walker Safety Cabinets, Glossop, Derbyshire, UK) were used for all aseptic cell culture work. 70% (v/v) industrial methylated spirit (IMS) (Fisher Scientific UK Ltd, Loughborough, UK) was used to sterilise laminar hoods and equipment prior to use. All plastic was purchased from Costar, (High Wycombe, Buckinghamshire, UK) and Greiner (Bio-one, Gloucestershire, UK).

- **Dulbecco's modified Eagle's Medium (DMEM)**

  DMEM (Gibco, Paisley, UK) came supplemented with 4500mg/l glucose GlutaMAX™ I and sodium pyruvate.

- **Nutrient Mixture F12 (Ham's F12)**

  Purchased from Biosera, East Sussex, UK, supplemented with L-glutamine and sodium bicarbonate.

- **Fetal Calf Serum (FCS)**

  FCS (heat inactivated) purchased from Biosera, East Sussex, UK was stored frozen. Prior to use, new batches were tested for cell growth and behaviour as compared to the previous batch.

- **Penicillin/Streptomycin**

- **Amphotericin B**

- **Adenine**

  Adenine powder (0.5g) was dissolved in 70ml of distilled water. 1M Hydrochloric acid (HCl) was added to completely dissolve the powder. 80ml solution was made with distilled water after filter sterilisation to achieve a final concentration of 6.25µg/ml.

- **Insulin**

  Bovine Insulin powder (10mg) was mixed in 1ml of 0.01M HCl. 9ml of distilled water was added once the powder was dissolved to achieve a final concentration of 1mg/ml.

- **3, 3, 5- Tri-iodothyronine (T3)/Apo-Transferrin**

  13.6mg T3 was dissolved in 0.02M sodium hydroxide (NaOH). 100ml solution was made with distilled water once the powder dissolved completely. Apo-transferrin (250mg) was added and dissolved in 30ml of phosphate buffered saline (PBS). A 50ml solution was prepared in PBS by adding 0.5ml of the T3 solution and 30ml of the apo-transferrin solution.

- **Hydrocortisone**

  1ml of distilled water was used to dissolve 25mg of hydrocortisone powder. Total volume 10ml was prepared using PBS.

- **Epidermal Growth Factor (Human Recombinant from E. Coli)**

  100µg of epidermal growth factor (EGF) was dissolved in 1ml of distilled water.

- **Cholera Toxin**

  1mg aliquot of Cholera toxin (from *Vibrio cholera)* was dissolved in 1.18ml distilled water, and stored at 4°C as stock solution. 10ml of media containing serum was used to dilute 100µl of stock solution.

- **RPMI 1640 AQ media**

  RPMI supplemented with sodium bicarbonate and L-glutamine.

- **Phosphate buffered saline**

  Phosphate buffered saline (PBS) was prepared by using tablets (Dulbecco A), purchased from Oxoid Ltd, Basingstoke, Hampshire, UK. 100ml of distilled water contained one PBS tablet which gave a concentration of 100mM. PBS was

prepared in autoclavable bottles and autoclaved for 10 minutes at 115°C. Sterile PBS was stored at room temperature.

- **Trypsin/EDTA (Ethylenediaminetetraacetic acid)**

  Trypsin 0.05%/ 0.02% EDTA w/v was stored at -20°C.

- **Cryopreservation Medium**

  Medium was prepared by 90% fetal calf serum (FCS) and 10% dimethyl sulphoxide (DMSO) (v/v).

- **Difco Trypsin**

  Difco trypsin 0.1% (w/v) was suspended as follows. 0.5g of D-glucose and 0.5g of Difco trypsin powder (Difco, West Molesey, Surrey, UK) were dissolved in 500ml PBS and the pH was adjusted to 7.4 using 2M NaOH. After sterilisation by filtering through a 0.22µm filter, 10ml aliquots were stored at -20°C. Before use, 100 IU ml^{-1} penicillin, 100 mg ml^{-1} streptomycin and 0.625 µg ml^{-1} amphotericin B were added in Difco trypsin solution.

- **Collagenase A**

  Collagenase A was dissolved in DMEM containing 10% FCS to a final concentration of 0.05% (w/v) and stored at -20 °C.

- **Scalpel blades, Syringes and Filters**

  Size 22 scalpel handles and blades were used and purchased from Swann-Morton, Sheffield, UK. Syringes and filters (BD Bioscience, Oxford, UK.) were used for sterilisation, with filters having pore size of 0.22µm which allowed them to eliminate contaminating bacteria or fungi.

2.1.2 Primary Cells

Details of primary oral cells isolated from buccal/gingival mucosa are given in table 2.1.

Table 2.1 Primary oral cells used to construct 3D tissue engineered models

Primary Cells	Origin	Source
Normal Oral Fibroblasts (NOF)	Buccal/Gingival mucosa	Waste tissue collection
Normal Oral Keratinocytes (NOK)	Buccal/Gingival mucosa	Waste tissue collection

2.1.3 Cell Lines

Six different cell lines were used to construct specific tissue engineered oral mucosa models. The details of these cell lines are outlined in the table 2.2.

Table 2.2 Details of cell lines used for development of 3D tissue engineered oral mucosa

CELLS	CELL TYPE	ORIGIN	SOURCE
DOK	Dysplastic (mild to moderate)	Isolated from the tongue of 57 years old male	European Collection of Cell Culture (ECACC)
D19	Dysplastic (Severe)	Buccal mucosa	Kindly donated by Dr. Keith Hunter, School of Clinical Dentistry, University of Sheffield (McGregor et al., 1997).
D20	Dysplastic (Moderate)	Lateral tongue	Kindly donated by Dr. Keith Hunter, School of Clinical Dentistry, University of Sheffield (McGregor et al., 2002).
CAL27	OSCC	Tongue	ATCC (Manassas, VA, USA) (Jiang et al., 2009).
FaDu	OSCC	Pharynx (male)	ATCC (Manassas, VA, USA)
SCC4	OSCC	Tongue (different patients)	ATCC (Manassas, VA, USA)

2.1.4 Cell culture media

Different ingredients and compositions were used to prepare cell culture media for specific cell lines or primary cells. Normal oral keratinocytes (NOK) are difficult to culture in conventional media as compared to cancer cell lines which have the ability to proliferate without added supplements. Green's media is more complex in its composition having additional supplements such as adenine, insulin, epidermal growth factor (EGF) and cholera toxin which enhances proliferation and culture lifespan of normal oral keratinocytes. By altering the conventionally used tissue culture medium, it is possible to grow disaggregated human keratinocytes in the absence of dermal cell products. Considering that NOK and dysplastic cell lines do not grow desirably in simple culture media therefore they were cultured in Green's medium whereas cancer cell lines proliferate easily without additional growth factors in the medium. The details of culture media used for specific cell lines or primary cells are provided later in this chapter.

10% DMEM for NOF AND Cal27

Cell culture medium used for NOF and Cal27 was supplemented DMEM (table 2.3). 500 ml media was prepared at a time and stored at 4° C for use up to a month. Table below explains the composition of 10% DMEM.

Table 2.3 Composition of 10% DMEM

Component	Final concentration	Storage
Dulbecco's modified Eagle's Medium	89%	4°C
Fetal Calf Serum	10%	-20°C
Penicillin/Streptomycin	100i.u./ml penicillin and 100µg/ml streptomycin	-20°C
Amphotericin B	0.625µg/ml	-20°C

GREEN'S media for NOK, D19 and D20

Green's media was used for culturing NOK, D19 and D20 cell lines. 500 ml media was prepared at a time and stored at 4° C for use up to a month. Table 2.4 explains the composition of Green's medium.

Table 2.4 Composition of Green's medium

Component	Final concentration	Storage
Dulbecco's modified Eagle's Medium	66%	4°C
Nutrient Mixture F12 (Ham's F12)	21.6%	4°C
Fetal Calf Serum	10%	-20°C
Penicillin/Streptomycin	100i.u./ml penicillin and 100µg/ml streptomycin	-20°C
Amphotericin B	0.625µg/ml	-20°C
Adenine	0.025µg/ml	-20°C
Insulin	5µg/ml	4°C
3, 3, 5- Tri-iodothyronine/ Apo-Transferrin	1.36ng/ml T3 and 5µg/ml apo-transferrin	-20°C
Hydrocortisone	4 µg/ml	4°C
Epidermal Growth Factor	5 ng/ml	-20°C
Cholera Toxin	8.47ng/ml	4°C

Medium for DOK

Cell culture medium used for DOK was 10% DMEM supplemented with hydrocortisone to enhance cell growth. 500ml media was prepared at a time and stored at 4° C for use up to a month. Table 2.5 explains the composition of medium.

Table 2.5 Cell culture medium for DOK

Component	Final concentration	Storage
Dulbecco's modified Eagle's Medium	89%	4°C
Fetal Calf Serum	10%	-20°C
Penicillin/Streptomycin	100i.u./ml penicillin and 100µg/ml streptomycin	-20°C
Amphotericin B	0.625µg/ml	-20°C
Hydrocortisone	5µg/ml	4°C

Medium for FaDu

Cell culture medium used for FaDu was 10% RPMI. 500ml media was prepared at a time and stored at 4° C for use up to a month. Table 2.6 explains the composition of 10% RPMI.

Table 2.6 Cell culture medium for FaDu

Component	Final concentration	Storage
RPMI 1640	89%	4°C
Fetal Calf Serum	10%	-20°C
Penicillin/Streptomycin	100i.u./ml penicillin and 100µg/ml streptomycin	-20°C
Amphotericin B	0.625µg/ml	-20°C

Medium for SCC4

SCC4 cells were cultured in the following medium.

Table 2.7 Cell culture medium for SCC4

Component	Final concentration	Storage
Dulbecco's modified Eagle's Medium	45%	4°C
Nutrient Mix F12 (Ham's F12)	45%	4°C
Fetal Calf Serum	10%	-20°C
Penicillin/Streptomycin	100i.u./ml penicillin and 100µg/ml streptomycin	-20°C
Amphotericin B	0.625µg/ml	-20°C
Hydrocortisone	0.4µg/ml	4°C

2.2 Methods

Passaging cell

Cells were passaged once they had reached 80% confluency which allowed cells to proliferate further. To passage, initially the cells were washed twice with 10ml PBS after removing culture media to eliminate any serum proteins. To detach the cells from the flask, 5ml trypsin/EDTA was added and incubated at 37°C for approximately 5 minutes. Once detached, the trypsin/EDTA was neutralised by the addition of 5 ml cell culture medium and the resultant solution centrifuged for 5 minutes at 1000 revolutions per minute (rpm) in a bench top centrifuge. After which the supernatant was removed and the cell pellet re-suspended in its respective culture medium and placed into a cell culture flask.

Cell counting

A modified Neubauer haemocytometer (Weber Scientific International, Middlesex, UK) was used for cell counting. Four $1mm^2$ squares (volume $1 \times 10^{-4}ml$) were counted and the average was used to calculate total cell number using the following formula;

$$\frac{\text{Mean number of cells / } 1mm^2 \text{ x dilution factor}}{\text{Volume counted } (1 \times 10^{-4}ml)} = \text{cells/ml}$$

Freezing cells

For cryopreservation cells were re-suspended in the cryopreservation medium (90% FCS, 10% DMSO) and 1ml was transferred into a cryovial (Cellstar cryovials from Greiner bio-one, Gloustershire, UK) with a cell concentration of between 0.5 to 3 million per ml and placed in a Nalgene™ Cryo 1°C freezing container (Nalgene Co., New York, USA), at -80°C for at least 4-8 hours before shifting to a liquid nitrogen dewar (-196°C).

Thawing cells

Appropriate safety measures were followed to remove cryovials from the liquid nitrogen. Cells in cryopreservation media were immediately thawed in 37°C water bath, re-suspended into cell culture medium and centrifuged at 1000 rpm for 5 mins. After centrifugation, the supernatant was discarded and the cell pellet re-suspended in respective cell culture medium before adding to a new culture flask.

2.2.1 Isolation of Primary Cells from Oral Biopsies

Surgical Removal of Oral Tissues

During third molar routine surgical extractions, gingival waste tissue was collected from dental surgeries at Charles Clifford Dental Hospital, Sheffield, UK under ethical approval number 09/H1308/66 from fully consenting patients by a dentist (ethical approval form presented in appendix). Removed waste tissues were kept in PBS containing 100 IU ml^{-1} penicillin, 100 mg ml^{-1} streptomycin and 0.625 µg ml^{-1}

amphotericin B and stored at 4°C prior to processing. Stored tissue was processed to isolate primary normal oral fibroblasts and keratinocytes for construction of 3D tissue engineered oral mucosa models. Tissue processing is detailed later in this chapter.

Irradiated 3T3 Feeder Layer

Keratinocytes were proliferated over a feeder layer of XCELLentis 3T3 murine fibroblast cells (XCELLentis, Gent, Belgium). These are mouse cells which were initially placed in culture flasks and later in CellSTACK® (Corning Life Sciences Inc, New York, USA) having a surface area of 6,360cm^2 which allowed large number of cells to proliferate. After achieving 80% confluency, cells were detached, pelleted and exposed to 60 Grays of irradiation using a cobalt-60 source irradiator. Irradiated cells (i3T3) were cryopreserved and resurrected immediately before use.

Isolation of Normal Oral Keratinocytes

Oral tissues were kept in 0.1% w/v Difco trypsin and incubated overnight at 4°C. The epithelium was then separated from the connective tissue followed by gentle scraping of keratinocytes from the top surface of the connective tissue and underside of the epithelium using a scalpel. The remaining connective tissue was stored in PBS containing 100 IU ml^{-1} penicillin, 100 mg ml^{-1} streptomycin and 0.625 µg ml^{-1} amphotericin B for extraction of fibroblasts later. A cellular pellet of scraped keratinocytes was achieved by centrifuging them along with Difco trypsin solution at 1200 rpm for 5 minutes. The supernatant was discarded in bleach and the cells were re-suspended in Green's medium (Table 2.4) and subsequently seeded in a T75 cell culture flask over i3T3 feeder layer.

Isolation of Normal Oral Fibroblasts

The remaining connective tissue was finely diced using a scalpel and placed in collagenase A (0.5%) solution and incubated at 37°C (5% CO_2) for 18 hours. After this

incubation period, the connective tissue was centrifuged at 2000 rpm for 10 mins. The supernatant along with undigested tissue was carefully removed and the cells re-suspended in 10% DMEM (table 2.3) and seeded in a T25 cell culture flask.

2.2.2 Culturing 3D Tissue Engineered Models of Oral Mucosa

Preparation of de-epidermised dermis (DED)

Cadaveric skin treated with glycerol was purchased from Euro Skin Bank (Beverwijk, Netherlands) and stored at 4°C until required. This was preferred over fresh skin obtained from surgery because the supply was reliable, adequate and from the same patient in order to maintain reproducibility and properties of scaffolds. Glycerol was removed from the skin by thorough washing in PBS for two days and subsequently placed in 1 M sodium chloride for 24 h at 37°C in order to de-cellularise the skin. After 24 hours, the epithelium was carefully scraped from the skin surface and remaining skin was washed thrice with PBS. This procedure was effective in removing the epidermis and at the same time maintaining the architectural integrity as well as basement membrane proteins. Processed DED was stored in DMEM at 4°C.

Cell Culture

Cell culture was performed in T75 tissue culture flasks. Culture media was changed after every 2-3 days. There was a routine testing for mycoplasma infection in the cells and any infected cells were discarded.

Culturing 3D models

Squares of processed DED with the dimensions of 2 cm x 2 cm were cut and placed into a 6 well plate. Surgical stainless steel chamfered rings (internal diameter 8 mm) were placed onto the DED and a liquid tight seal was achieved by applying gentle pressure.

For dysplastic and cancer models NOF and dysplastic (DOK, D19 OR D20)/OSCC cells (Cal27, SCC4 or FaDu) were seeded onto the DED within the steel rings at concentrations of $5x10^5$ and $2.5x10^5$ respectively.

For normal oral mucosa model, NOF and NOK were seeded onto the DED within the steel rings at a concentration of $5x10^5$ and 10 $x10^5$ respectively.

Three days post seeding, the models were raised to an air liquid interface (ALI). Specific cell culture media were used for each cell line. At the ALI, the bottom of the model was exposed to media whereas the top of the model was exposed to air (figure 2.1)

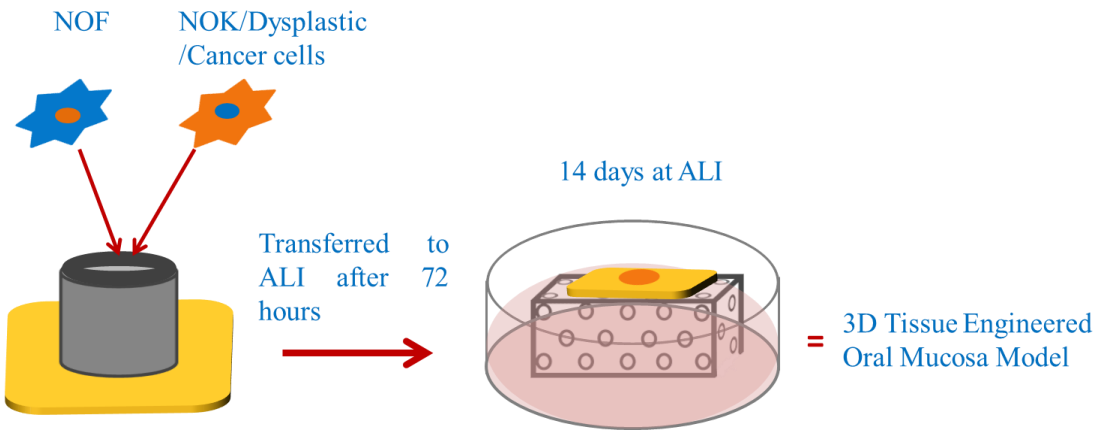

Figure 2. 1 Diagram showing cell seeding onto the DED and inside the chamfered surgical stainless steel ring followed by lifting the model to an air liquid interface (ALI)

Models were cultured for 14 days with the media changed every alternate day. At day 14 the models were washed with PBS and fixed in 3.7% formaldehyde and kept at room temperature for at least 24 h before histological processing.

2.2.3 Histological Processing of samples

Leica TP1020 benchtop tissue processor (Leica microsystems, Milton Keynes, UK.) was used to process the samples overnight. Table 2.8 explains sample processing steps.

Table 2.8 Scheme for histological processing

Solution	Exposure time
10% neutral buffered formalin	1 hour
70% alcohol	1 hour
70% alcohol	1 hour
90% alcohol	1 hour
90% alcohol	1 hour
100% alcohol	1 hour
100% alcohol	1 hour
100% alcohol	1 hour
Xylene	90 minutes
Xylene	90 minutes
Paraffin wax I	2 hours
Paraffin wax II	2 hours

To embed the sections, Leica EG1160 embedding centre, dispenser and hot plate (Leica microsystems, Milton Keynes UK) was employed.

2.2.4 Sample preparation

Sectioning

Wax embedded samples were cut to the desired thicknesses using a Leica RM2235 manual rotary microtome (Leica microsystems, Milton Keynes UK) with a S35 microtome blades (Feather, Osaka, Japan) and mounted onto VFM microscope glass slides (CellPath Ltd. Newtown, UK).

Sample thicknesses

Sections were cut at two different thicknesses 4 µm and 20 µm. SuperFrost® Plus glass slides (Thermo Scientific) were used for tissue sections of 4 µm thickness. These sections were hematoxylin and eosin (H&E) stained followed by histological examination. H&E staining of these slides was performed using a Shandon linear staining machine.

For the 20 µm tissue sections, VFM microscope slides (Cell Path Ltd. Newtown, UK) were used. These tissue sections were de-waxed for analysis by Raman spectroscopy.

2.2.5 Raman spectroscopic measurements

Spectra were acquired using a DXR Raman microscope (Thermo Scientific, Madison, WI, USA) fitted with a 532 nm diode-pumped solid state (DPSS) laser with a laser power of 10 mW. The microscope was equipped with X50 long working distance objective lens. The confocal aperture of the system was set to 50 µm pinhole and estimated spectral and spatial resolutions (spot size) were 5.5 - 8.3 cm^{-1} and 1.1 µm respectively. Scattered light was detected using a CCD detector with an average 2 cm^{-1} per CCD pixel element. The scattered Raman signal was measured over complete spectral range (400 to 3400 cm^{-1}). Exposure time was set to 30 seconds and 5 sample exposures (2 minutes 30 seconds) were accumulated to improve the signal to noise ratio. The spectra obtained were analysed and processed using OMNIC Atlµs™ software suit (Thermo Scientific, Madison, WI, USA).

2.2.6 Raman Data Processing

Raman data between 600 to 3400 cm^{-1} region was analysed. Seven different samples were analysed using Raman spectroscopy. The samples included tissue engineered normal oral mucosa, three different tissue engineered models of dysplastic oral mucosa and three different tissue engineered models of cancerous oral mucosa. A total of 302 spectra were collected for this study (D20 = 47, DOK = 39, D19 = 30, Cal27 = 55,

SCC4 = 51, FaDu = 45 and normal oral mucosa NOM = 35). Additional spectra were collected from thick dysplastic and cancer epithelia in order to acquire maximum biochemical information. A mean spectrum for each of the seven samples was produced for the purpose of evaluation and comparison. Smoothing and base line correction for the spectra was performed using OMNIC Atlμs™ software suit (Thermo Scientific, Madison, WI, USA).

2.2.7 Data Analysis

Chemo-metric methods were used to quantify the spectral differences of various groups present in the data. These methods were performed usimg Unscrambler X 10.2 software, purchased from Camo software (Oslo, Norway). Principal component analysis (PCA) was performed over the complete spectral range (600 to 3400 cm^{-1}), amide I (1550 to 1750 cm^{-1}**)** and amide III (1200 to 1400 cm^{-1}**)** regions of normal, dysplastic and cancerous data set. The maximum variance between the data was observed within first three principal components (PC's). Cluster analysis (CA) was performed over complete spectral range (600 to 3400 cm^{-1}) by Ward's method using squared Euclidean distance.

Linear Discriminant Analysis (LDA) was also performed over the entire spectral range. Pre-processing comprised of baseline correction and Unit Vector Normalisation. 4 samples from each group were left out at each pass for prediction until the total number of spectra were predicted (table 2.9).

Table 2.9 LDA model set up for tissue engineered oral mucosa models

Tissue Type	No. of spectra used to build up LDA model at each pass	No. of spectra assumed unknown at each pass
Normal	31	4
D19	26	4
D20	43	4
DOK	35	4
FaDu	41	4
SCC4	47	4
Cal27	51	4

Sensitivity and Specificity

Sensitivity of a test is calculated to determine correctly classified ‘’diseased’’ individuals in a data set. On the other hand specificity of a test correctly determines ‘’disease-free or healthy’’ individuals in a data set.

The following formulas are used to calculate sensitivity and specificity of a data set;

Sensitivity = a / a + c **Specificity** = d / b + d

Where **a =** True Positive, **b =** False Positive, **c** = False Negative and **d** = True Negative

2.3 Materials & Methods

Section 2 - Patient biopsy work

In this study we have examined three different tissue types including normal, dysplastic and cancerous oral mucosa. All tissue samples were obtained from Department of Oral Pathology, Charles Clifford Dental Hospital, University of Sheffield under ethical approval number 08/S0709/70 (ethical approval form presented in appendix). The selection criteria for sample selection was based on anatomical location of the lesion therefore all samples used were originating from different areas of the tongue. Prior to spectroscopic analysis, these tissue sections were histologically classified as normal, dysplastic and cancer by expert pathologists.

2.3.1 Sample Quantity

A total of 45 different cases were employed in this study which included 15 normal, 15 dysplastic and 15 cancers, between the age ranges from 36 to 91 years (table 2.10).

Our study was based on samples collected from one anatomical location so that minimum inter region variations were encountered. There are studies which have shown that Raman spectral differences were observed with various anatomical locations within the oral cavity (Bergholt et al., 2012).

Table 2.10 Details of patient biopsies used for spectroscopic analysis

Type	Grade	Age	Gender	Smoking	Alcohol	Site
Normal	-	60	male	Y	Y	Ventral/lateral tongue
Normal	-	45	male	Y	Y	Ventral tongue
Normal	-	53	male	Y	Y	Ventral tongue
Normal	-	42	female	Y	N	Ventral/lateral tongue
Normal	-	55	male	Y	Y	Ventral/lateral tongue

Normal	-	64	female	Y	N	Ventral/lateral tongue
Normal	-	56	female	N	N	Ventral tongue
Normal	-	52	male	N	N	Ventral/lateral tongue
Normal	-	39	male	Y	N	Ventral tongue
Normal	-	45	male	N	N	Ventral tongue
Normal	-	59	male	N	N	Ventral tongue
Normal	-	42	female	Y	Y	Ventral/lateral tongue
Normal	-	73	male	Y	Y	Ventral tongue
Normal	-	59	female	N	N	Ventral tongue
Normal	-	66	male	Y	N	Ventral/lateral tongue
Dysplastic	severe	90	male	Y	Y	Ventral/lateral tongue
Dysplastic	mild	75	female	10/day	Y	Ventral tongue
Dysplastic	mild	63	male	Y Excessive	Y Limited	Ventral tongue
Dysplastic	mild-mod	72	female	N	Y Limited	Ventral/lateral tongue
Dysplastic	focal mild	45	male	N	N	Ventral/lateral tongue
Dysplastic	moderate	74	male	Y	Y Excessive	Ventral/lateral tongue
Dysplastic	moderate	76	female	N	N	Ventral tongue
Dysplastic	moderate	42	male	10/day	Y Limited	Ventral/lateral tongue
Dysplastic	severe	49	male	Y	Y Limited	Ventral tongue
Dysplastic	mild	75	female	N	Y Limited	Ventral tongue
Dysplastic	mild-mod	59	male	20/day	Y Excessive	Ventral tongue
Dysplastic	moderate	62	female		N	Ventral/lateral tongue
Dysplastic	severe	63	male	40/day	N	Ventral tongue
Dysplastic	severe	59	male	Y	N	Ventral tongue
Dysplastic	severe	91	female	Y	Y	Ventral/lateral

						tongue
Cancer	well diff	62	male	Y	Y	Anterior dorsum tongue
Cancer	mod diff	36	female	N	Y Limited	Lateral tongue
Cancer	mod diff	38	male	N	N	Lateral tongue
Cancer	mod diff	71	male	N	N	Lateral tongue
Cancer	mod diff	50	female	Y	Y	Lateral tongue
Cancer	mod diff	72	male	Y	N	Lateral tongue
Cancer	mod diff	76	male	Y	Y	Lateral tongue
Cancer	mod diff	91	male	Y	N	Lateral tongue
Cancer	mod diff	56	male	Y	Y	Ventral tongue
Cancer	mod diff	62	female	Y	Y	Lateral tongue
Cancer	mod diff	79	male	Y	Y	Lateral + ventral tongue
Cancer	mod diff	84	female	N	N	Lateral border of tongue
Cancer	mod diff	46	male	Y	Y	Ventral tongue
Cancer	mod diff	68	male	Y	Y	Lateral tongue
Cancer	mod diff	67	female	N	N	Lateral tongue

2.3.2 Spectral quantity

A total number of 900 good quality spectra were acquired from 45 different tissue samples. Each group i.e. normal, dysplastic and cancer, had 15 samples and 20 spectra were collected from every single tissue section. For each group, 300 spectra were collected from 15 cases (table 2.11).

Table 2.11 Total numbers of cases and acquired Raman spectra

Tissue Type	Number of cases	Number of spectra from each case	Total number of spectra
Normal	15	20	300
Dysplastic	15	20	300
Cancer	15	20	300
Total	**45**		**900**

2.3.3 Experimental procedures

Sectioning of samples, sample thickness, Raman spectroscopic measurements, data processing and data analysis, were kept constant throughout this project as described in section 1 of materials and methods, unless otherwise stated.

Linear Discriminant Analysis Set up

LDA was performed over the entire spectral range (600 to 3400 cm^{-1}). Pre-processing comprised of baseline correction and Unit Vector Normalisation. 50 samples from each group were left out at each pass for prediction until a total number of 150 spectra were predicted (table 2.12).

Table 2.12 LDA model set up for patient biopsies

Tissue Type	No. of spectra used to build up LDA model at each pass	No. of spectra assumed unknown at each pass
Normal	150	50
Dysplasia	150	50
Cancer	150	50

2.4 Materials & Methods

Section 3 - Irradiated Tissue Engineered Oral Mucosa

In this study we have investigated the effects of radiations on tissue engineered normal and cancerous oral mucosa.

Tissue engineered models were constructed using the same protocol as described in section 1, unless otherwise stated.

2.4.1 Radiation equipment

AGO HS 320 3.2w x-ray system (AGO x-ray Ltd. Yeovil, UK) was used for the purpose of irradiation of tissue engineered models. This system offered a maximum capacity of 250 kV at 15 mA. The actual source of radiation used was metal ceramic 320 x-ray tube model MXR 321 (COMET SA, Switzerland). 5 Gy models were exposed for 9 minutes at 200 kV and 12.8 mA whereas 10 and 15 Gy models were exposed for 18 and 27 minutes respectively.

2.4.2 Culturing and Irradiation of T.E. Oral Mucosa Models with 5, 10 and 15 Gy

Squares of processed DED with the dimensions of 2 cm x 2 cm were cut and placed into a 6 well plate. Surgical stainless steel chamfered rings (internal diameter 8 mm) were placed onto the DED and a liquid tight seal achieved applying gentle pressure.

For cancer models NOF and OSCC cells (Cal27, SCC4 or FaDu) were seeded onto the DED within the steel rings at concentrations of $5x10^5$ and $2.5x10^5$ respectively.

For normal oral mucosa model, NOF and NOK were seeded onto the DED within the steel rings at a concentration of $5x10^5$ and $10\ x10^5$ respectively.

Three days post seeding, the models were raised to an air to liquid interface (ALI). Specific cell culture media was used according to the cell line used. At the ALI, the bottom of the model was exposed to media whereas the top of the model was exposed to air (figure 2.2).

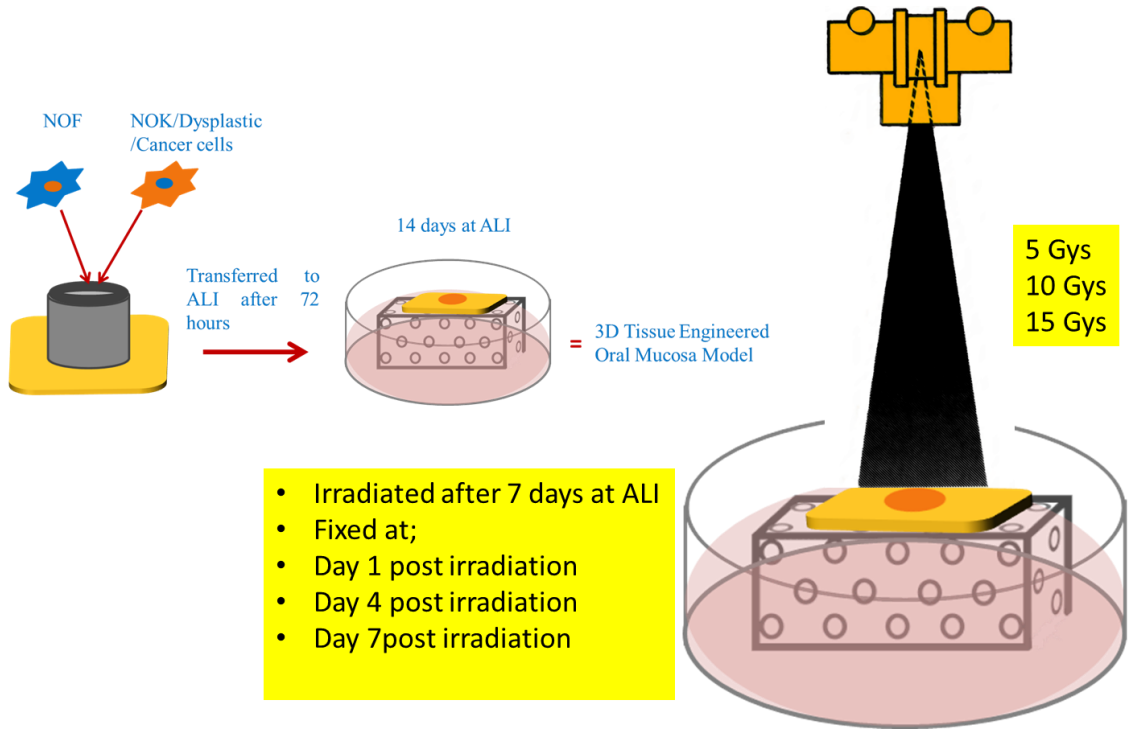

Figure 2. 2 Diagram showing cell seeding onto the DED and inside the chamfered surgical stainless steel ring followed ALI and irradiation with 5, 10 and 15 Gy

Models were cultured for 7 days at the ALI with the media changed every alternate day. After 7 days at the ALI, models were irradiated to 5, 10 and 15 Gy. Control models were also constructed alongside for comparison with irradiated ones. 24 h after irradiation, the first set of normal and cancer models was washed in PBS and fixed in 3.7% formaldehyde, referred to as ‘’Day 1’’ in results, including controls. 4 days after irradiation, the second set of normal, cancer and their controls was washed in PBS and fixed in 3.7% formaldehyde, referred to as ‘’Day 4’’. 7 days after irradiation, the third set of normal, cancer and their controls was washed in PBS and fixed in 3.7% formaldehyde, referred to as ‘’Day 7’’. Post fixation, the models were kept at room temperature for at least 24 h before histological processing.

Sectioning procedures, sample thickness, Raman spectroscopic measurements, data processing and data analysis, were kept constant throughout the project as described in section 1 of materials and methods chapter, unless otherwise stated.

2.4.3 Sample and spectral quantity

A total of 480 spectra were collected from 24 tissue engineered normal and cancerous oral mucosa models. The details of these models are provided in table 2.13 and 2.14. Average spectra of these models were carefully analysed during peak identification. Mean spectra of all the tissue engineered oral mucosa samples including control and irradiated were used for comparison and statistical analysis.

Table 2.13 Number of samples along with collected spectra from tissue engineered normal oral mucosa (control and irradiated)

Model	Day 1 (spectra)	Day 4 (spectra)	Day 7 (spectra)
Control	20	20	20
5 Gy	20	20	20
10 Gy	20	20	20
15 Gy	20	20	20
	80	80	80
Total			**240**

Table 2.14 Number of samples along with collected spectra from tissue engineered cancerous oral mucosa (control and irradiated)

Model	Day 1 (spectra)	Day 4 (spectra)	Day 7 (spectra)
Control	20	20	20
5 Gy	20	20	20
10 Gy	20	20	20
15 Gy	20	20	20
	80	80	80
Total			**240**

2.4.4 Data Analysis

Principal component analysis (PCA) was performed over the complete spectral range (600 to 3400 cm^{-1}), amide I (1550 to 1750 cm^{-1}**)**, amide III (1200 to 1400 cm^{-1}**)** and 800 to 1200 cm^{-1} regions of tissue engineered normal and cancerous data set including controls and irradiated models, however Cluster analysis (CA) was performed over the entire spectral range. PCA and CA were performed at day 1, 4 and 7 post radiation treatment. Pre-processing comprised of baseline correction and Unit Vector

Normalisation. The maximum variance between the data was observed within first three principal components (PC's). CA was performed by Ward's method using squared Euclidean distance.

2.5 De-wax protocol for RS analysis

It is essential to establish a standard and authentic experimental protocol before commencing research work. Spectroscopic investigations of paraffin embedded tissues may be challenging as wax may contribute to the Raman spectrum if not completely eliminated. In order to acquire wax free biochemical information from the tissues, a standard protocol for de-waxing 20 µm thick tissue sections was established and published (Mian at. al., 2014 presented in appendix).

Sample Thickness

Microscope glass slide can contribute to the Raman spectrum when thin tissue sections (less than 10-15 µm) are analysed and can influence the fingerprint region. It was therefore necessary to mount 20 µm thick tissue sections onto the glass slides to obtain a spectrum free from glass background.

De-waxing of 20µm thick sections

Tissue engineered oral mucosa models as well as patient biopsies used in this project were wax embedded therefore complete removal of wax was mandatory in order to collect pure biological information. Contamination of the tissue sections significantly affects vital evidence present in Raman spectral data which may lead to false and discouraging results. As wax contributes to the fingerprint region of the Raman spectra, it interferes with amide I, amide III, nucleic acid and keratin compartments and prevents their expression (Faoláin et al., 2005). Therefore, in spectroscopic studies it is extremely important to completely eliminate wax in order to acquire comprehensive expression of vital components, which are of diagnostic significance. A standard protocol was

established for de-waxing of tissue sections using xylene in order to eliminate residual wax contribution from Raman spectrum (Mian et al., 2014).

Established Protocol

Tissue engineered models of the oral mucosa were prepared, fixed and paraffin embedded as previously described (Colley et al., 2011). 20 µm tissue sections were cut and mounted onto glass slides. Mounted sections were oven dried for 30 minutes at 60 °C. For wax removal the slides were placed in xylene for increasing lengths of time (2-45 minutes). Xylene treatment was followed by dehydration of the tissue sections in 50%, 70% and 100% ethanol for 5 minutes each as well as to eliminate xylene from the tissue sections. 18 sections were prepared for Raman analysis and the experiment was performed in duplicate. Steps followed for de-waxing of tissue sections are explained in table 2.15.

Table 2.15 De-waxing protocol of tissues mounted on glass slides for RS analysis

STEPS	PURPOSE
Heat (60°C)	To dry the slides completely and make sure the section is firmly attached.
Xylene (30 minutes)	To eliminate wax from tissue section and slide.
50% alcohol (5 minutes)	For dehydration of tissue
70% alcohol (5 minutes)	For dehydration of tissue
100% alcohol (5 minutes)	For dehydration of tissue

Chapter 3

Results and Discussion

Section 1 - Tissue Engineered work

This section contains work conducted on 3D tissue engineered models of normal, dysplastic and cancerous oral mucosa. Raman spectroscopy was employed to investigate different types of oral mucosa on the basis of biochemical variances present between them. Spectral data was also analysed by unsupervised and supervised algorithms which demonstrated accurate results in order to recognise subtypes of dysplastic and cancer models. These 3D tissue engineered models closely resemble *in vivo* conditions; since human tissue is scarce therefore these models provide an ideal platform to understand the progression of disease outside human body. Biochemical information obtained by Raman spectra can be extremely sensitive and may identify specific biomolecules which can be used as Raman markers for cancer detection non-invasively and in no time.

3.1 Results

3.1.1 Tissue Engineered Normal Oral Mucosa

Primary human NOK's and primary human NOF's were cultured on acellular skin scaffold to construct tissue engineered normal oral mucosa (TENOM).

A stratified epithelium was produced by culturing TENOM models at an air to liquid interface (ALI) (figure 2.1). The epithelium showed clear differentiation and was approximately 10 cells thick. A well-formed basal cell layer was seen in the epithelium underlying an organised prickle cell layer. Cells present at the most superficial layer showed evidence of maturation with flattened cells and very few nuclei giving the epithelium a smooth flat surface. TENOM models also show rete ridges, which is a unique rounded feature of epithelial connective tissue junction. Fibroblasts were well

differentiated and evenly populated in the underlying connective tissue (highlighted by arrows in figure 3.1).

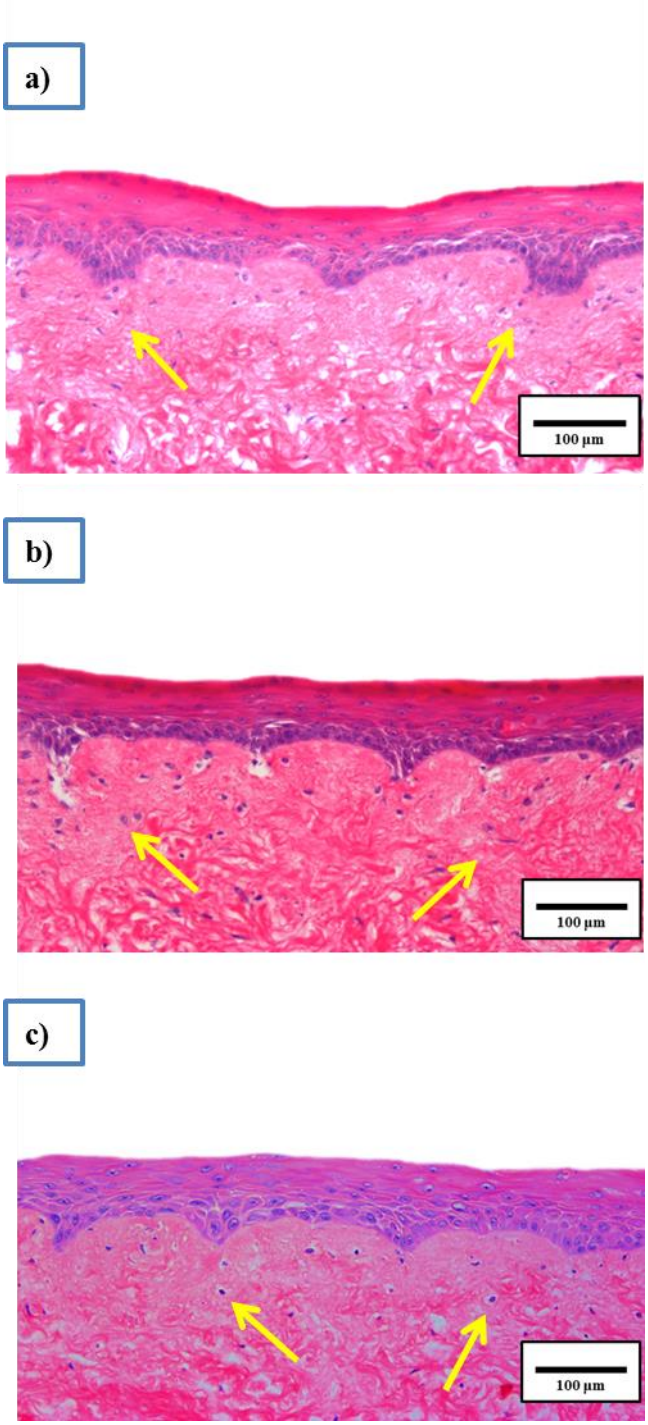

Figure 3. 1 TENOM were produced by seeding NOK and NOF (1x 106 and 5x105, respectively) on to DED and culturing at an ALI for 14 days. Three different batches of primary cells were used. a) TENOM1, b) TENOM2, c) TENOM3

3.1.2 Tissue Engineered Dysplastic Oral Mucosa

DOK

Compared to the normal mucosa model, the epithelium showed variable thickness with fewer flattened cells in the superficial layer suggesting disordered maturation. Variable degrees of dysplasia were seen which in places extended through the full thickness of the epithelium. The hallmark signs of dysplasia were noted which included hyperchromatism, nuclear and cellular pleomorphism, individual/deep cell keratinisation and a disorganized prickle cell layer. Basal cells showed significant cytological atypia (figure 3.2a).

D19

D19 cells were cultured with NOF on a DED scaffold for 14 days to obtain a 3D tissue engineered D19 dysplastic model. After 14 days in culture at ALI, a multi-layered epithelium was formed. D19 cells were more proliferative as they penetrated well on top and underneath the model. In addition to full thickness dysplasia, micro/early invasion was seen focally with individual cell invasion in the superficial connective tissue. Morphologically, these cells appear to be spindle shaped and discohesive, invading into the connective tissue as isolated cells instead of forming tumour islands (highlighted by arrows in figure 3.2b whereas yellow boxes indicate the site of spectral acquisition). Epithelium detachment from the connective tissue in areas may have occurred as an artefact to histological processing (highlighted by circles in figure 3.2b).

D20

D20 cells were cultured with NOF on a DED scaffold for 14 days to obtain a 3D tissue engineered D20 dysplastic model. The epithelium formed by D20 cells after being at ALI in culture for 14 days was approximately 10 cells thick and showed some signs of

stratification as well as focal areas of surface keratinisation. Full thickness dysplasia and drop shaped rete pegs were seen in the connective tissue after 14 days culture. The epithelium showed disordered maturation with hyperkeratosis, basal cell hyperplasia as well as nuclear and cellular pleomorphism amounting to carcinoma *in situ* in places (figure 3.2c). The extent of epithelial cell invasion into the connective tissue was less than D19 and DOK.

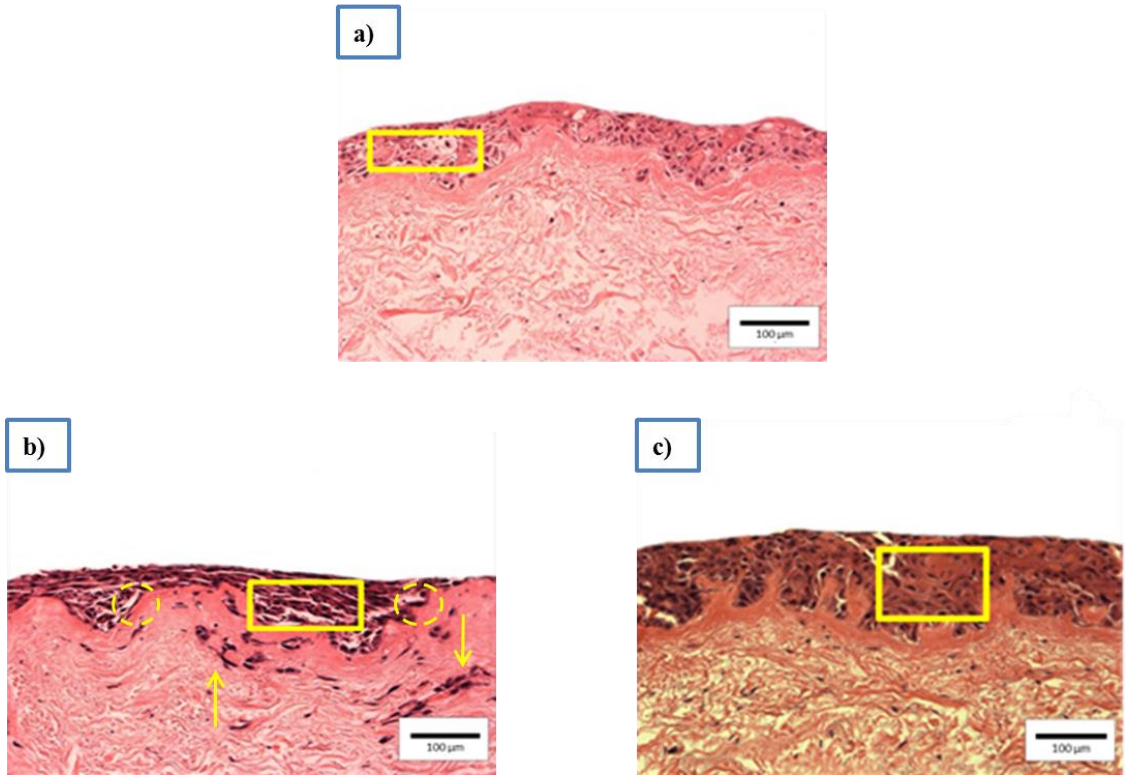

Figure 3. 2 Dysplastic models were produced by seeding D19/D20/DOK and NOF (2.5x 105 and 5x105, respectively) on to DED and culturing at an ALI for 14 days. a) DOK, b) D19 and c) D20

3.1.3 Tissue Engineered Cancerous Oral Mucosa

Cal27

Bulbous rete processes, abnormal keratinocyte maturation and a fibroblasts populated dermis was seen in Cal27 models. The pleomorphism was much more pronounced compared to the dysplastic models with prominent hyperchromatic nuclei, basal cell hyperplasia, dyskeratosis and full thickness dysplasia. Focally, epithelial penetration suggests early invasion of OSCC in the connective tissue (highlighted by arrows in figure 3.3a).

FaDu

This model showed marked pleomorphism with widespread features of carcinoma *in situ* and a complete absence of stratification. There was abundant pleomorphism, abnormal mitotic figures as well as signs of acantholysis, and necrosis (highlighted by arrows in figure 3.3b). High levels of cell death were noticed in these models after 14 days of culture at ALI. Clinically in deeply invaded cancerous tissues, such high levels of cell deaths are suggestive of a very aggressive and invasive cancer.

SCC4

SCC4 cells were cultured with NOF on a DED scaffold for 14 days to obtain a 3D tissue engineered SCC4 OSCC model. These models appeared similar to FaDu morphologically, with unorganized cell proliferation. Acantholysis, necrosis and apoptosis were evident which again indicated aggressive proliferation of cells. Tumour islands and invasion of epithelium into the connective tissue was also observed which is highlighted by circle and arrow respectively in figure 3.3c.

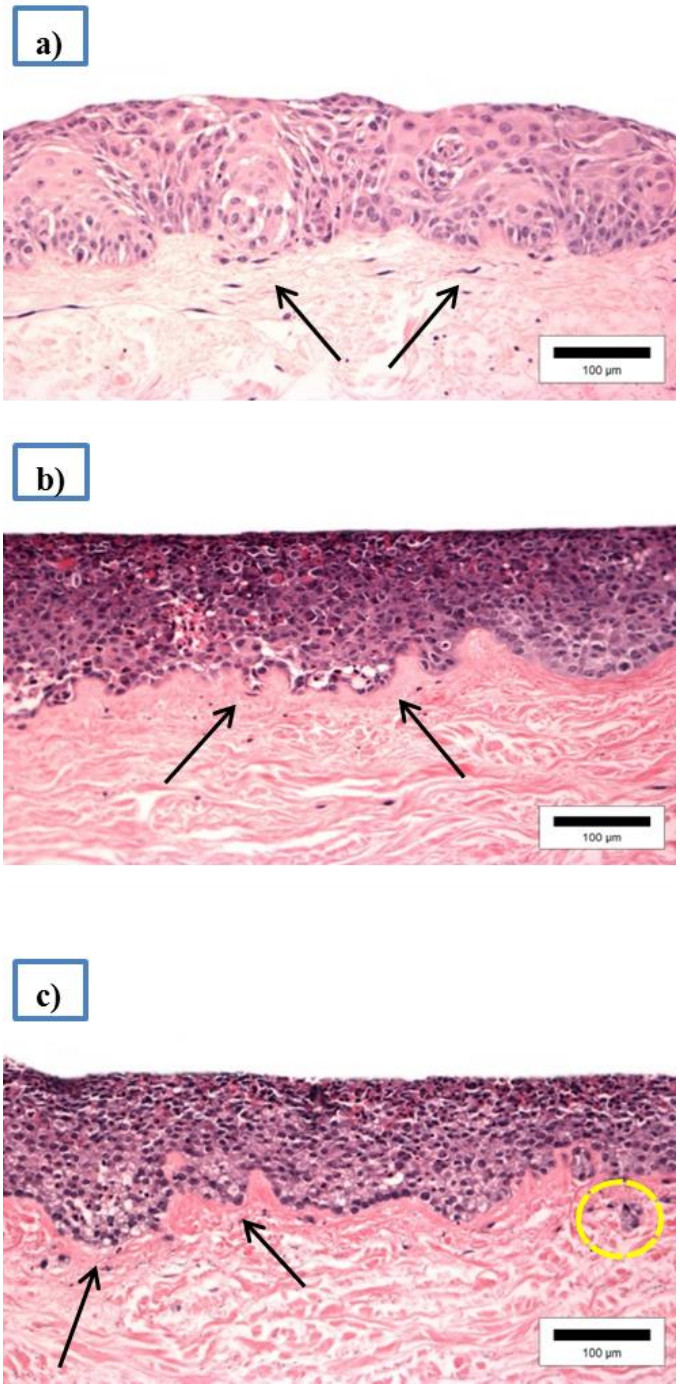

Figure 3. 3 Cancer models were produced by seeding Cal27/FaDu/SCC4 and NOF (2.5x 105 and 5x105, respectively) on to DED and culturing at an ALI for 14 days. a) Cal27, b) FaDu and c) SCC4

3.2 Raman spectroscopic results

3.2.1 3D Tissue Engineered Normal Oral Mucosa (TENOM)

A total of 150 spectra were collected from 3D TENOM models. Mean spectra of three different TENOM models were carefully analysed during peak identification, which revealed that they possess similar peaks throughout the complete spectral range (400 cm^{-1} to 3400 cm^{-1}) as shown in figure 3.4.

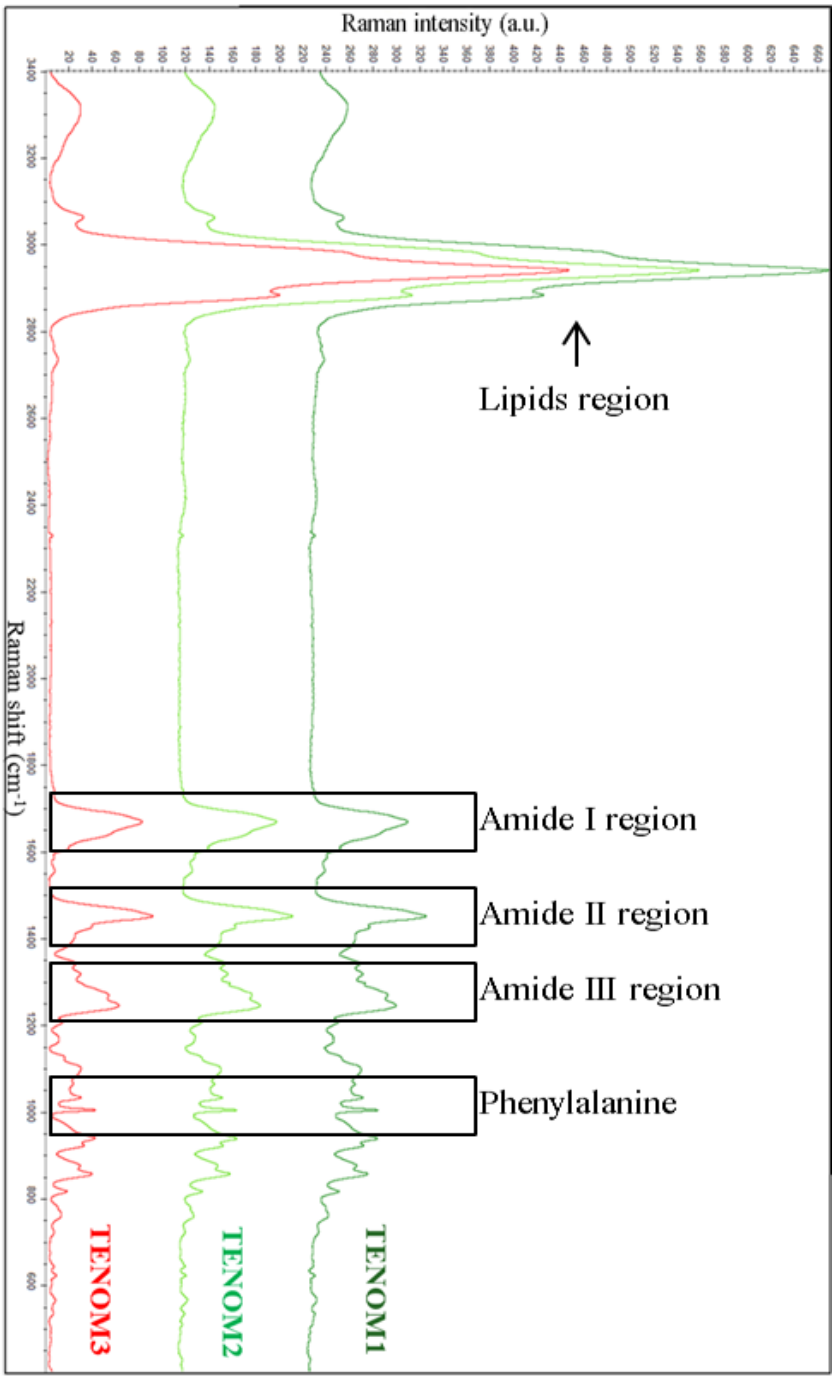

Figure 3. 4 Mean spectra of 3 different tissue engineered normal oral mucosa models

All the peaks were examined and assigned to their respective molecular groups. As mentioned previously that TENOM showed similar peaks, therefore we acquired mean spectrum of all three models for further comparison with dysplastic and cancerous tissue engineered oral mucosa models. Figure 3.5 shows mean spectrum of 3 tissue engineered normal oral mucosa models (TENOM) and table 3.1 details peak assignments of normal, dysplastic and cancerous oral mucosa models along with references.

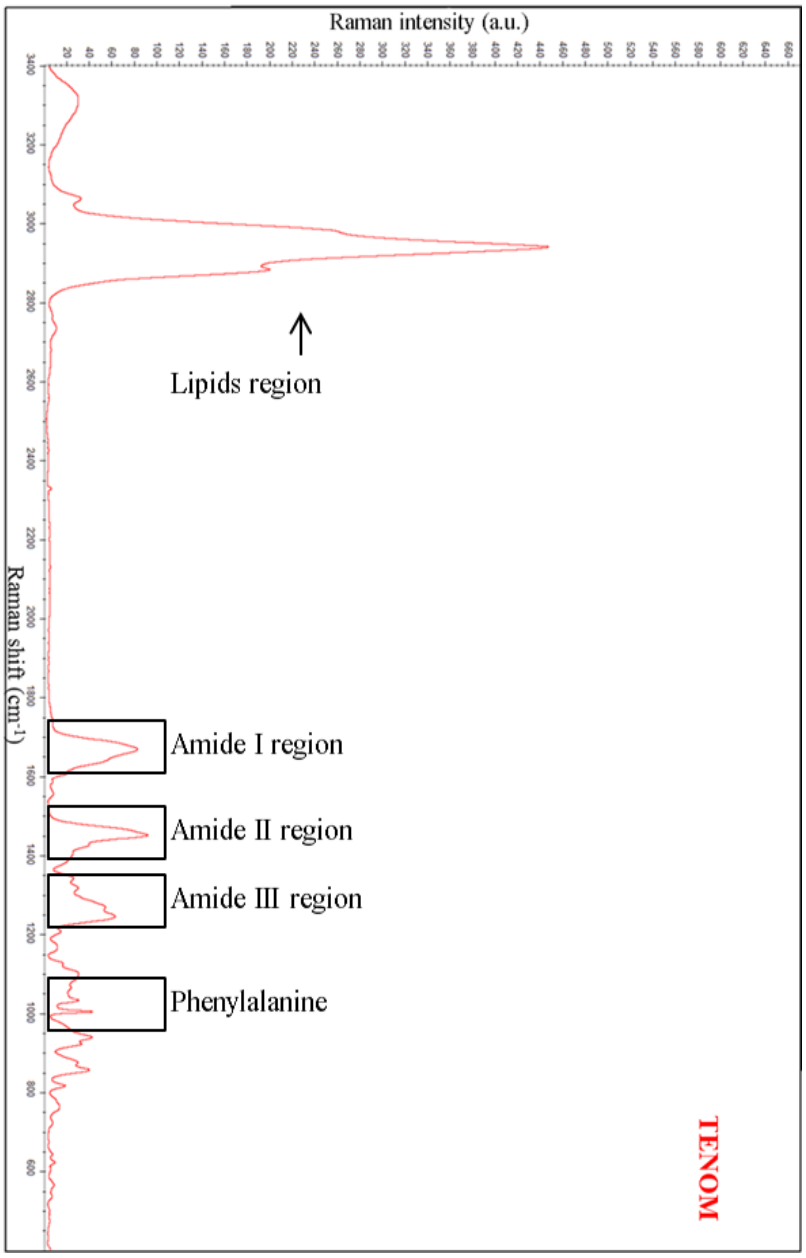

Figure 3. 5 TENOM, mean spectrum of tissue engineered normal oral mucosa models

Table 3.1 Details of peak assignments, comparison and references of tissue engineered normal, dysplastic and cancerous oral mucosa

Peak No. (cm^{-1})	Assignment	N	D19	D20	DOK	Cal27	SCC4	FaDu	Ref.
621	C-C twisting mode of phenylalanine (protein assignment)		✓	✓	✓	✓	✓	✓	(Stone et al., 2002b) (Notingher et al., 2004b)
622	C-C twisting mode of phenylalanine (protein assignment)	✓							(Stone et al., 2002b) (Stone et al., 2004)
642	C-C twisting mode of tyrosine	✓	✓	✓	✓				(Cheng et al., 2005) (Stone et al., 2004)
643	C-C twisting mode of tyrosine					✓	✓	✓	(Stone et al., 2004, Cheng et al., 2005)
721	DNA	✓							(Binoy et al., 2004) (IU. Rehman et al., 2012)
724	Ring breathing modes of DNA/RNA bases		✓	✓	✓	✓	✓	✓	(Binoy et al., 2004) (James W. Chan et al., 2006) (IU. Rehman et al., 2012)
759	Tryptophan	✓	✓	✓	✓	✓	✓	✓	(Stone et al., 2004) (Krafft et al., 2005)
780	Uracil based ring breathing		✓			✓	✓	✓	(Farquharson et al., 2005)

	mode								
815	Proline, hydroxyproline, tyrosine, υ PO_2^- stretch of nucleic acid	✓							(Cheng et al., 2005)
817	C-C stretching (collagen assignment)				✓				(Frank et al., 1995)
828	Ring breathing mode of tyrosine Phosphodiesters Tyrosine/O-P-O stretch DNA		✓	✓		✓	✓	✓	(Notingher et al., 2004a) (Ruiz-Chica et al., 2004) (Stone et al., 2002b)
853	Proline, hydroxyproline, tyrosine, tyrosine ring breathing mode Glycogen		✓	✓	✓	✓	✓	✓	(Cheng et al., 2005) (James W. Chan et al., 2006) (Binoy et al., 2004)
855	Proline, tyrosine, υ(C-C) proline + δ(CCH) ring breathing, tyrosine (protein assignment) Amino acid side chain vibration of proline and hydroxyl proline	✓							(Stone et al., 2002b) (Huang et al., 2003a) (Cheng et al., 2005)
874	Hydroxyproline (C-C), tryptophan C-C stretching	✓							(Frank et al., 1995) (Gniadecka et al.,

									1997) (Krishna et al., 2004)
875	Asymmetric stretch vibration of choline group $N^+(CH_3)_3$ characteristic for phospholipids				✓				(Krafft et al., 2005)
900	Monosaccharide (β-glucose) (C-O-C) skeletal mode			✓				✓	(Shetty G, 2006)
921	C-C stretch of proline ring/glucose /lactic acid	✓			✓				(Stone et al., 2002b) (Kendall et al., 2003) (Stone et al., 2004) (Kendall et al., 2011)
935	C-C stretch backbone (protein α-helix conformation) (protein assignment)		✓	✓	✓	✓	✓	✓	(Huang et al., 2003a) (Stone et al., 2002b)
938	C-C stretch backbone (protein α-helix conformation)	✓							
958	Carotenoids, cholesterol		✓	✓		✓	✓	✓	(Stone et al., 2004)
1002	Symmetric ring breathing mode of phenylalanine, C-C		✓			✓	✓	✓	(Puppels et al., 1991) (Mahadevan-Jansen and Richard

	skeletal stretch								s-Kortum, 1996) (Stone et al., 2004) (Krishna et al., 2004) (Seballos et al., 2005) (Malini et al., 2006) (Jess et al., 2006) (James W. Chan et al., 2006) (Zhang et al., 2008)
1003	Symmetric ring breathing mode of phenylalanine, C-C skeletal stretch	✓		✓	✓				
1031	CH_3 CH_2 bending modes of collagen and phospholipids, phenylalanine of collagen, proline (collagen assignment) C-H in-plane bending mode of phenylalanine C-H stretching of proteins		✓	✓	✓	✓	✓	✓	(Frank et al., 1995) (Huang et al., 2003a) (Cheng et al., 2005) (Stone et al., 2002b) (James W. Chan et al., 2006)

1032	CH_3 CH_2 bending modes of collagen and phospholipids, phenylalanine of collagen, proline (collagen assignment)	✓							(Frank et al., 1995) (Huang et al., 2003a) (Cheng et al., 2005)
1062	C-C skeletal stretch lipids		✓		✓		✓		(Faoláin et al., 2005, Mian et al., 2014)
1063	C-C skeletal stretch lipids	✓							
1097	Phosphodioxy groups in nucleic acids	✓							(Krafft et al., 2005)
1100	C-C vibration mode of the gauche-bonded chain		✓	✓	✓	✓	✓	✓	(Huang et al., 2005) (Cheng et al., 2005)
1124	υ(C-C) skeletal of acyl backbone in lipids	✓							(Cheng et al., 2005)
1127	υ (C-C) skeletal of acyl backbone in lipids		✓	✓	✓	✓	✓	✓	
1157	Carotenoids (absent in normal tissue) C-C, C-N stretching (protein)		✓	✓		✓	✓	✓	(Mahadevan-Jansen and Richards-Kortum, 1996) (James W. Chan et al.,

									2006)
1163	Tyrosine C-H in-plane bending of tyrosine	✓							(Krishna et al., 2004) (Cheng et al., 2005)
1173	Cytosine, guanine Tyrosine (collagen type I)		✓	✓	✓	✓	✓	✓	(Ruiz-Chica et al., 2004) (Cheng et al., 2005)
1206	Hydroxyproline, tyrosine (collagen assignment)	✓							(Frank et al., 1995) (Stone et al., 2004)
1208	Tryptophan, phenylalanine (protein assignment)		✓	✓	✓	✓	✓	✓	(Frank et al., 1995) (Stone et al., 2004)
1244	Amide III, asymmetric phosphate stretching modes originating from phosphodiester groups of nucleic acids	✓	✓		✓				(Lakshmi et al., 2002) (Cheng et al., 2005) (Shetty G, 2006) (Dukor, 2006) (Movasaghi et al., 2007)
1246	Amide III, asymmetric phosphate stretching modes originating from phosphodiester groups of nucleic acids					✓	✓	✓	(Lakshmi et al., 2002) (Cheng et al., 2005) (Shetty G, 2006) (Dukor, 2006) (Movasaghi et al., 2007)
1266	Amide III (protein in α-helix	✓							(Huang et al., 2003a) (Laksh

	conformation) Tryptophan (protein assignment)								mi et al., 2002) (Cheng et al., 2005)
1267	Amide III (protein in α-helix conformation) Tryptophan (protein assignment)		✓		✓				(Huang et al., 2003b, Lakshmi et al., 2002)
1295	Methylene twisting		✓				✓		(Huang et al., 2005) (Rehman et al., 2007)
1317	Guanine ring breathing modes of DNA/RNA bases, C-H deformation (protein)	✓	✓	✓	✓	✓	✓	✓	(Ruiz-Chica et al., 2004) (Movasaghi et al., 2007)
1337	Polynucleotide chain (DNA purine bases)(protein assignment) Nucleic acid mode which indicate amount of content in tissue Tryptophan					✓	✓	✓	(Stone et al., 2004) (Mahadevan-Jansen and Richards-Kortum, 1996) (Notingher et al., 2004a) (Dukor, 2006) (Cheng et al., 2005)
1338	Polynucleotide chain (DNA purine bases)(prote		✓	✓	✓				(Stone et al., 2004) (Mahadevan-Jansen

	in assignment) Nucleic acid mode which indicate amount of content in tissue Tryptophan								and Richards-Kortum, 1996) (Notingher et al., 2004a) (Dukor, 2006) (Cheng et al., 2005)
1341	Nucleic acid mode which indicate amount of content in tissue G (DNA/RNA)	✓							(Mahadevan-Jansen and Richards-Kortum, 1996) (Notingher et al., 2004a) (Dukor, 2006)
1425	Deoxyribose (B,Z markers)	✓							(Ruiz-Chica et al., 2004)
1448	CH_2 CH_3 bending mode in malignant tissues CH_2 bending (proteins)		✓	✓		✓	✓	✓	(Shafer-Peltier et al., 2002) (Yi-Yong et al., 2003) (Cheng et al., 2005) (Malini et al., 2006)
1450	CH_2 bending (proteins)	✓			✓				
1554	Protein bands CH_2 stretching/CH_3 asymmetric deformation	✓							(Hanlon EB, 2000, Dukor, 2006) (Faoláin et al., 2005)

1558	Tryptophan (protein assignment)		✓	✓	✓				(Cheng et al., 2005)
1583	C=C bending mode of Phenylalanine Tryptophan		✓	✓	✓	✓	✓	✓	(Lau et al., 2003) (Huang et al., 2003a) (Devpura et al., 2011)
1585	C=C Olefinic stretch C=C Olefinic stretch (protein assignment)	✓							(Faoláin et al., 2005) (IU. Rehman et al., 2012)
1607	Tyrosine, phenylalanine ring vibration C=C phenylalanine, tyrosine Cytosine	✓							(Lakshmi et al., 2002) (Notingher et al., 2004a)
1605	Tyrosine, phenylalanine ring vibration (proteins) Ring C-C stretch of phenylalanine		✓	✓	✓	✓	✓	✓	(James W. Chan et al., 2006)
1615	Tyrosine, tryptophan, C=C (protein)		✓	✓	✓				(James W. Chan et al., 2006)
1655	Amide I of proteins Amide I (α-helix)			✓					(Huang et al., 2003a) (Shetty G, 2006)
1658	Amide I of proteins Amide I (α-helix)					✓			(Huang et al., 2003a) (Shetty G, 2006)

1662	Protein band α-helix structure of amide I C=O carbonyl stretch Nucleic acid modes		✓						(Dukor, 2006, Hanlon EB, 2000) (Huang et al., 2003a, Mahadevan-Jansen and Richards-Kortum, 1996) (Farquharson et al., 2005) (Mahadevan-Jansen and Richards-Kortum, 1996) (Barr et al., 1998)
1665	Protein band C=C stretching band α- helix structure of amide I Structural protein mode of tumours						✓	✓	(Hanlon EB, 2000, Dukor, 2006) (Mahadevan-Jansen and Richards-Kortum, 1996) (Huang et al., 2003a)
1667	Protein band α-helix structure of amide I C=O carbonyl	✓			✓				(Dukor, 2006, Hanlon EB, 2000) (Huang et al., 2003a, Mahadevan-Jansen and

	stretch								Richards-Kortum, 1996) (Farquharson et al., 2005)
2726	C-H stretches					✓	✓	✓	(Krafft et al., 2005)
2727	C-H stretches		✓	✓	✓				(Krafft et al., 2005)
2733	C-H stretches	✓							(Krafft et al., 2005)
2881	CH_2 asymmetric stretch of lipids and proteins		✓	✓	✓		✓		(Koljenović et al., 2005) (IU. Rehman et al., 2012)
2882	CH_2 asymmetric stretch of lipids and proteins	✓							(Koljenović et al., 2005)
2933	C-H vibrations in lipids and proteins $\upsilon_{as}CH_2$, lipids and fatty acids		✓	✓		✓	✓	✓	(Rehman et al., 2007) (Shetty G, 2006)
2937	Chain end CH_3 symmetric band				✓				(Krafft et al., 2005)
2939	C-H vibrations in lipids and proteins $\upsilon_{as}CH_2$, lipids and fatty acids	✓							(Rehman et al., 2007) (Shetty G, 2006)
3061	CH stretching	✓	✓	✓	✓	✓	✓	✓	(Movasaghi et al., 2012)

Tryptophan and 622 to 938 cm^{-1} region

Peaks present at 622 and 642 cm^{-1} are typical assignments of C-C twisting modes of phenylalanine and tyrosine in biological tissues, respectively. Peak existing at 721 cm^{-1} is attributed to deoxyribonucleic acid (DNA). These three peaks exhibit relatively less intensities as compared to the rest of peaks in the normal tissue spectra. The fingerprint region (600 to 1800 cm^{-1}) in biological tissues is rich in proteins, nucleic acids and lipids where peaks present at 759, 874, 1266 and 1554 cm^{-1} are specific assignments of tryptophan (C-C stretching). Peaks observed at 815, 855 and 874 cm^{-1} are attributed to υ PO_2^- stretch of nucleic acid and proline, hydroxyproline, ring breathing of tyrosine, amino acid side chain vibration of proline and C-C hydroxyproline (protein assignment) respectively. C-C stretch of proline ring/glucose/lactic acid and C-C stretch backbone (protein α-helix conformation) are assigned to 921 and 938 cm^{-1} respectively.

1003 to 1667 cm^{-1} region

A sharp, intense and typical peak at 1003 cm^{-1} is attributed to symmetric ring breathing mode of phenylalanine (C-C skeletal stretch). Phenylalanine is a protein assignment which was also observed at 1032 (phenylalanine of collagen) and 1607 cm^{-1} (shoulder) (C=C and ring vibration of phenylalanine). Minor peaks at 1063 and 1124 cm^{-1} are assignments of C-C skeletal stretch in lipids. A broad peak at 1097 cm^{-1} is attributed to Phosphodioxy groups in nucleic acids. Weak contributions at 1163 and 1206 cm^{-1} are attributed to C-H in-plane bending of tyrosine and hydroxyproline (collagen assignment).

1244 to 1266 cm^{-1} (amide III) region

Bands present at 1244 and 1266 cm^{-1} are characteristic assignments of amide III (protein in α-helix conformation) in biological tissues, where strong spectral contribution was observed. Peaks originating at 1244 cm^{-1} are also attributed to

asymmetric phosphate stretching modes arising from phosphodiester groups of nucleic acids.

1317 to 1667 cm^{-1} region

The peaks arising at 1317 and 1341cm^{-1} can be attributed to ring breathing modes of nucleic acid (DNA/RNA) bases or C-H deformation in proteins. A shoulder was observed at 1425 cm^{-1} which is an assignment of Deoxyribose (nucleic acid). A strong and sharp band was present at 1450 cm^{-1}**,** referring to CH_2 bending modes in proteins. Weak spectral contributions were noticed at 1554 and 1585 cm^{-1}**,** which are attributed to CH_2 stretching/CH_3 asymmetric deformation in protein bands and C=C Olefinic acids respectively, both are protein assignments. Intense and strong band originated at 1667 cm^{-1} is a specific protein assignment of α-helix structure of amide I.

2733 to 3061 cm^{-1} region

A weak band at 2733 cm^{-1} is an assignment of C-H stretching vibrations in lipids. A shoulder was observed at 2882 cm^{-1}, attributed to CH_2 asymmetric stretch of lipids and proteins whereas the strong band arising at 2939 cm^{-1} is assigned to C-H vibrations in lipids and proteins as well as CH_2 asymmetric stretch in lipids/fatty acids. CH stretching vibrations were present at band originating at 3061 cm^{-1}.

3.2.2 3D Tissue Engineered Dysplastic Oral Mucosa

A total of 150 spectra were collected from 3D tissue engineered dysplastic oral mucosa models namely D19, D20 and DOK. Mean spectra of these models were analysed which showed several spectral differences amongst them (figure 3.6). Peak assignments with references are given in table 3.1.

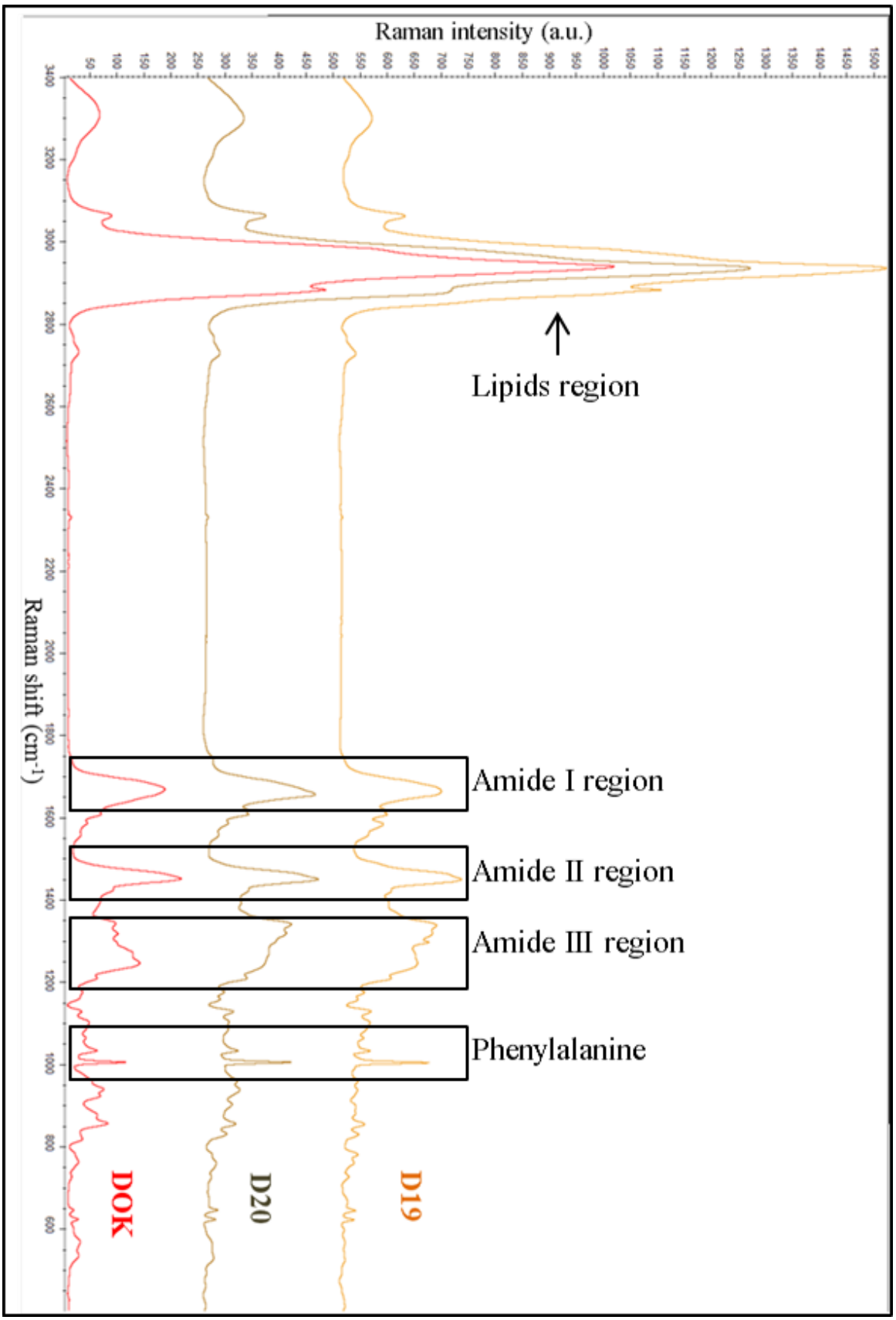

Figure 3. 6 Mean spectra of 3D tissue engineered dysplastic oral mucosa models (D19, D20 and DOK)

Tryptophan and 621 to 958 cm^{-1} region

The bands present at 621 and 642 cm^{-1} are assigned to C-C twisting modes of phenylalanine and tyrosine in D19, D20 and DOK, respectively. A weak band was observed in all three dysplastic tissues with slightly higher intensity in D19 at 724 cm^{-1} and is attributed to DNA. Peaks present at 759, 1208, 1267 (absent in D20), 1338, 1583 and 1558 cm^{-1} are specific assignments C-C stretching modes of tryptophan. There is a short and weak band at 724 cm^{-1} which only appeared in the D19 tissue spectrum and is attributed to ring breathing mode of nucleic acid (uracil based). Band observed at 817 cm^{-1} is a C-C stretching and is a collagen assignment which only appeared in DOK. The Peak originating at 828 cm^{-1} in D19 and D20 models was assigned to ring breathing mode of tyrosine, Phosphodiesters and O-P-O stretching of DNA, this band did not appear in the DOK model. The Peak appearing at 853 cm^{-1} was intense in DOK as compared to the other models and was attributed to proline, hydroxyproline, and ring breathing mode of tyrosine. A unique shoulder appeared in DOK model spectrum at 875 cm^{-1} which is an assignment of asymmetric stretch vibration of choline group $N^+ (CH_3)_3$ which is specific for phospholipids. A shoulder appeared at 921 cm^{-1} only in DOK spectrum which can be attributed to C-C stretch of proline ring/glucose/lactic acid. Bands arising at 935 cm^{-1} in all three models are assignment of C-C stretch backbone (α-helix conformation of protein) with highest peak intensity seen in DOK. The weak and short peak at 958 cm^{-1} is attributed to carotenoids and cholesterol which was missing in DOK.

1002 to 1208 cm^{-1} region

A sharp and intense peak originated at 1002 cm^{-1} (only in D19), whereas it was shifted to 1003 cm^{-1} in the rest of the dysplastic models, is a typical assignment of symmetric ring breathing mode of phenylalanine, D19 possessed highest intensity compared to

D20 and DOK. A band appeared at 1031 cm^{-1} and was present in all dysplastic models with D20 having the most intense peak. This peak can be assigned to CH_3 CH_2 bending modes of collagen and phospholipids, C-H in-plane bending mode of phenylalanine and C-H stretch of proteins. A very weak band was present in the spectra of D19 and D20 at 1062 cm^{-1} which can be attributed to C-C skeletal stretch of lipids. Only the D20 data set showed weak contribution at 1084 cm^{-1} which is an assignment of phosphodiester groups present in nucleic acids. C-C vibration mode of the gauche bonded chains was observed in all three dysplastic models at 1100 cm^{-1} where D20 had the lowest peak intensity. A small peak at 1127 cm^{-1} is an assignment of C-C skeletal stretch in lipids. A weak and short band at 1157 cm^{-1} is attributed to carotenoids, appearing in spectra of D19 and D20. All dysplastic model spectra showed a weak contribution at 1173 cm^{-1} which can be associated to cytosine, guanine or tyrosine (collagen type I). Band appearing at 1208 cm^{-1} is a protein assignment and attributed to phenylalanine.

1244 to 1267 cm^{-1} region

Bands appearing in this region (1244 – 1267 cm^{-1}) are characteristic assignments of proteins in biological tissues which can be attributed to Amide III (protein in α-helix conformation) and tryptophan. Peak appearing at 1244 cm^{-1} can also be recognised as asymmetric phosphate stretching modes originating from phosphodiester groups of nucleic acids.

1295 to 1615 cm^{-1} region

A band arising at 1295 cm^{-1} was only observed in D19 model spectrum which was attributed to methylene twisting. Peaks present at 1317 and 1338 cm^{-1} appeared in all dysplastic tissue models which were assigned to guanine ring breathing modes of DNA/RNA bases, C-H deformation of proteins and nucleic acids respectively. CH_2 bending in proteins is assigned to the band present at 1450 cm^{-1} in DOK tissue models

which has shown a shift to 1448 cm^{-1} in D19 and D20. A peak present at 1583 cm^{-1} was intense in the spectrum of D19 as compared to D20 and DOK, which was attributed to C=C bending mode of phenylalanine (protein assignment). Band at 1605 cm^{-1} is an assignment of tyrosine, ring vibration of phenylalanine or C-C of phenylalanine whereas 1615 cm^{-1} (missing in DOK) is attributed to C=C of tyrosine or tryptophan (proteins assignment).

1655 to 1667 cm^{-1} region

The bands present at 1655 (D20), 1662 (D19) and 1667 cm^{-1} (DOK) are characteristic assignments of proteins in α-helix structure of amide I, which showed strong spectral contribution. Band shift was significantly noticed in the amide I region of these dysplastic tissue engineered model spectra.

2727 to 3061 cm^{-1}region

A weak band at 2727 cm^{-1} was observed, which can be assigned to C-H stretching vibrations in lipids. A shoulder in D20 spectrum and peaks in D19 and DOK were present at 2881 cm^{-1}**,** attributed to CH_2 asymmetric stretch of lipids and proteins, whereas the strong band arising at 2933 cm^{-1} (D19 and D20 only) is assigned to C-H vibrations in lipids and proteins as well as CH_2 asymmetric stretch in lipids/fatty acids. Peak arising at 2937 cm^{-1} is attributed to chain end CH_3 asymmetric band of lipids which was shifted in DOK. CH stretching vibrations were present at band originating at 3061 cm^{-1}.

3.2.3 3D Tissue Engineered Cancerous Oral Mucosa

A total of 150 spectra were collected from 3D tissue engineered cancerous oral mucosa models (Cal27, SCC4 and FaDu). Average spectra of these models are shown in figure 3.7 and peak assignments with references are detailed in table 3.1.

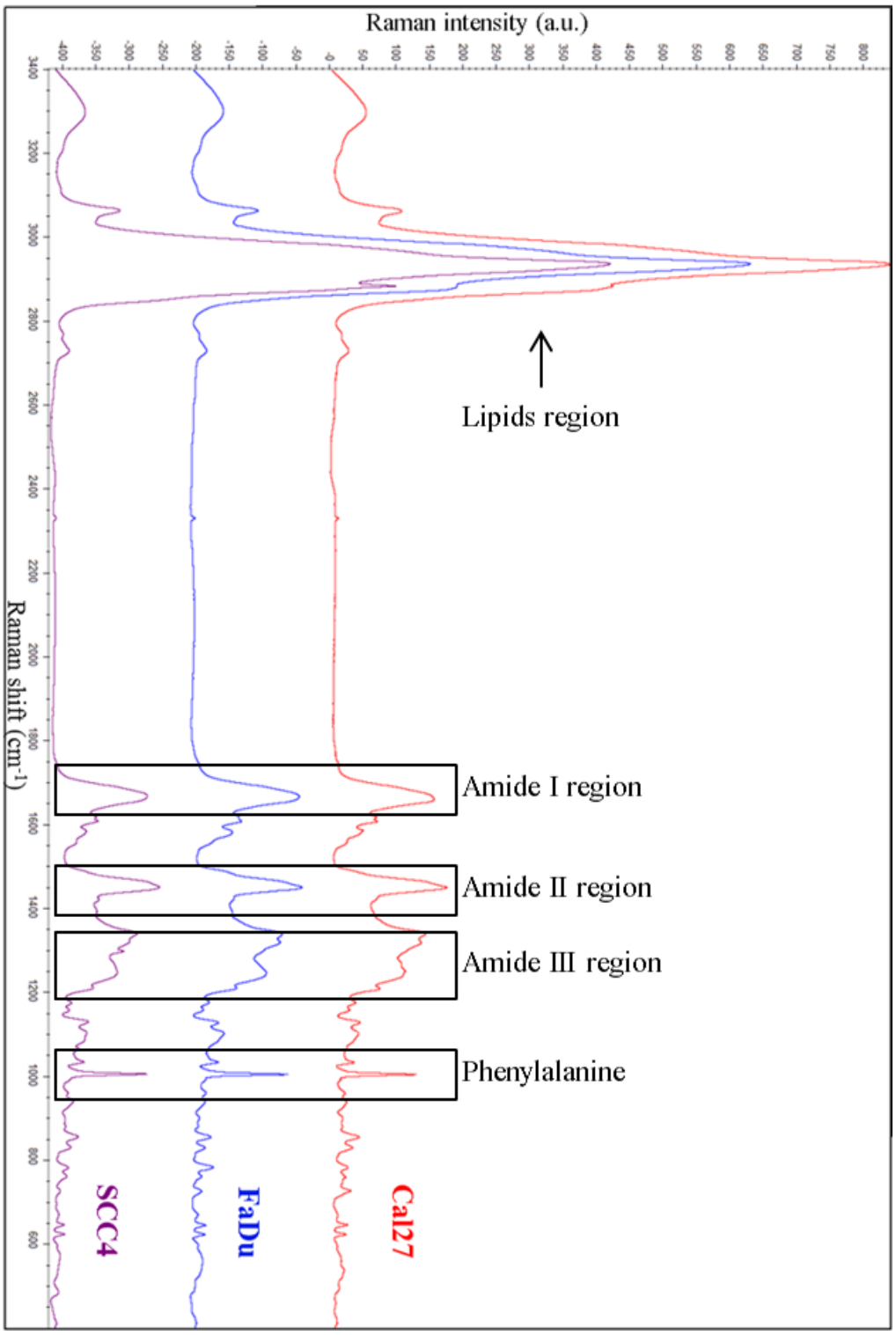

Figure 3. 7 Mean spectra of tissue engineered cancerous oral mucosa models (Cal27, SCC4 and FaDu)

Tryptophan and 621 to 958 cm^{-1} region

The bands present at 621 and 643 cm^{-1} are assigned to C-C twisting modes of phenylalanine and tyrosine in Cal27, SCC4 and FaDu, respectively. A weak band was observed in all three cancer tissues with slightly higher intensity in Cal27 at 724 cm^{-1} and is attributed to ring breathing modes of DNA/RNA bases. Peaks present at 759, 1208, 1337, 1583 and 1615 cm^{-1} are specific assignments of C-C/C=C stretching modes of tryptophan.

The band observed at 780 cm^{-1} is uracil based ring breathing mode in DNA/RNA where FaDu models showed highest peak intensity. The Peak originating at 828 cm^{-1} can be assigned to ring breathing mode of tyrosine, Phosphodiesters and O-P-O stretching of DNA. Peak appearing at 853 cm^{-1} was intense in Cal27 as compared to the rest of models and was attributed to proline, hydroxyproline, and ring breathing mode of tyrosine. Cal27 spectrum showed a band at 900 cm^{-1} which was absent in the rest of cancer models and can be assigned to monosaccharide (β-glucose), C-O-C skeletal mode. The band arising at 935 cm^{-1} in all three models is an assignment of C-C stretch backbone (α-helix conformation of protein) with the highest peak intensity seen in SCC4 models. A weak and short peak at 958 cm^{-1} is attributed to carotenoids and cholesterol and was present in all three cancer models.

1002 to 1208 cm^{-1} region

A sharp and intense peak originated at 1002 cm^{-1} in all three of the dysplastic models which is a typical assignment of symmetric ring breathing mode of phenylalanine where increased peak intensity was seen in FaDu as compared to Cal27 and SCC4. A band appeared at 1031 cm^{-1} and was present in all cancer models with SCC4 models having the most intense peak. This peak may be assigned to CH_3 CH_2 bending modes of collagen and phospholipids, C-H in-plane bending mode of phenylalanine and C-H

stretch of proteins. A short and weak band was present only in the spectrum of SCC4 models at 1062 cm^{-1} and was attributed to C-C skeletal stretch of lipids. C-C vibration mode of the gauche bonded chains was observed in all three cancer models at 1100 cm^{-1} with SCC4 showing the lowest peak intensity. A small peak at 1127 cm^{-1} can be an assignment of C-C skeletal stretch in lipids. A weak and short band at 1157 cm^{-1} is attributed to carotenoids, appearing in spectra of all cancer models. All cancer model spectra showed weak spectral contribution at 1173 cm^{-1} which can be associated to cytosine, guanine or tyrosine (collagen type I). The band appearing at 1208 cm^{-1} is a protein assignment and attributed to phenylalanine.

1246 to 1266 cm^{-1} region

Bands appearing in this region are characteristic assignments of proteins in biological tissues which can be attributed to Amide III (protein in α-helix conformation) and tryptophan. Peak appearing at 1244 cm^{-1} can also be recognised as asymmetric phosphate stretching modes originating from phosphodiester groups of nucleic acids.

1295 to 1615 cm^{-1} region

Peak at 1295 cm^{-1} was only observed in the spectrum of SCC4 models and can be attributed to methylene twisting. Peaks present at 1317 and 1337 cm^{-1} appeared in all cancer tissue models can be assigned to guanine ring breathing modes of DNA/RNA bases, C-H deformation of proteins and nucleic acids respectively. CH_2 bending in proteins is assigned to the band present at 1448 cm^{-1} in all cancer tissue models. Peak present at 1583 cm^{-1} was intense in the spectrum of FaDu as compare to Cal27 and SCC4, which may be attributed to C=C bending mode of phenylalanine (protein assignment). The band at 1605 cm^{-1} is an assignment of tyrosine, ring vibration of phenylalanine or C-C of phenylalanine whereas 1615 cm^{-1} is attributed to C=C of tyrosine or tryptophan (proteins assignment).

1658 to 1665 cm^{-1} region

A broad and strong band present at 1658 (Cal27) and 1665 cm^{-1} (SCC4 and FaDu) is a characteristic assignment of proteins in α-helix structure of amide I. Band shift was significantly noticed in the amide I region of these tissue engineered cancer models.

2726 to 3061 cm^{-1} region

A weak band at 2726 cm^{-1} was observed, which can be assigned to C-H stretching vibrations in lipids. A shoulder appeared in Cal27 and FaDu spectra as compared to a peak in SCC4 at 2881 cm^{-1}**,** which are attributed to CH_2 asymmetric stretch of lipids and proteins, whereas the strong band arising at 2933 cm^{-1} is assigned to C-H vibrations in lipids and proteins as well as CH_2 asymmetric stretch in lipids/fatty acids. CH stretching vibrations were present at 3061 cm^{-1} in all cancer model spectra.

3.2.4 Peak Height Analysis

Peak height analysis was performed to compare various peak intensities of tissue engineered normal, dysplastic and cancer models. Important contributions from phenylalanine, tryptophan, amide I, amide II and nucleic acid were analysed which demonstrated increased peak intensities in dysplastic and cancer models (Figure 3.8).

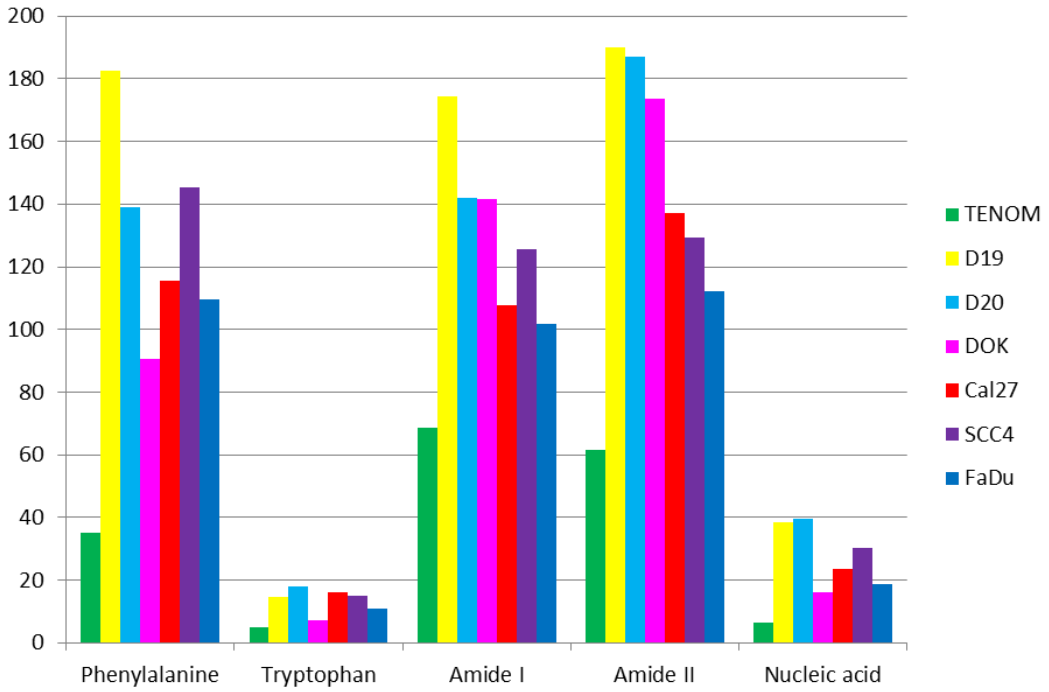

	1003 cm^{-1} Phenylalanine	1208 cm^{-1} Tryptophan	Amide I	Amide II	1338 cm^{-1} Nucleic acid
TENOM	35.26	5.06	68.52	61.58	6.44
D19	182.62	14.71	174.33	190.05	38.31
D20	138.95	18.10	141.97	187.00	39.51
DOK	90.61	7.37	141.43	173.65	16.28
Cal27	115.51	16.01	107.87	137.06	23.69
SCC4	145.23	14.90	125.65	129.44	30.35
FaDu	109.51	10.84	101.69	112.01	18.89

Figure 3. 8 Peak Height Analysis of major proteins and nucleic acid bands (tissue engineered models) in the finger print region of average Raman spectra

3.3 Multivariate Data Analysis

In this study supervised and unsupervised algorithms were employed to categorise different tissue engineered models on the basis of their spectral variances.

Principal Component Analysis (PCA)

PCA was performed over complete spectral range (400 to 3400 cm^{-1}), 1550 to 1750 cm^{-1} (amide I) and 1200 to 1400 cm^{-1} (amide III) region. The comparison was conducted between normal-dysplastic, normal-cancer and dysplastic-cancer tissue engineered models.

Normal-Dysplastics

Over the complete spectral range, PC1 discriminated normal from D19 and DOK as well as it differentiated D20 from D19 and DOK (figure 3.9). The second PC distinguished D19 from DOK and D20 and to a lesser extent with normal models (figure 3.9). In the amide I region, PC1 discriminated normal as well as D20 from D19 and DOK, whereas the variation described by PC2 differentiates D20 and DOK from normal and to a lower extent normal from D20 (figure 3.10). Amide III region shows a different trend as PC1 differentiates normal and DOK from D19 and D20 while PC2 separates DOK from normal, D20 and to a lesser extent D19 (figure 3.11). 3D plot shows a clearer separation of DOK from the normal and dysplastic models at PC2 (figure 3.11b).

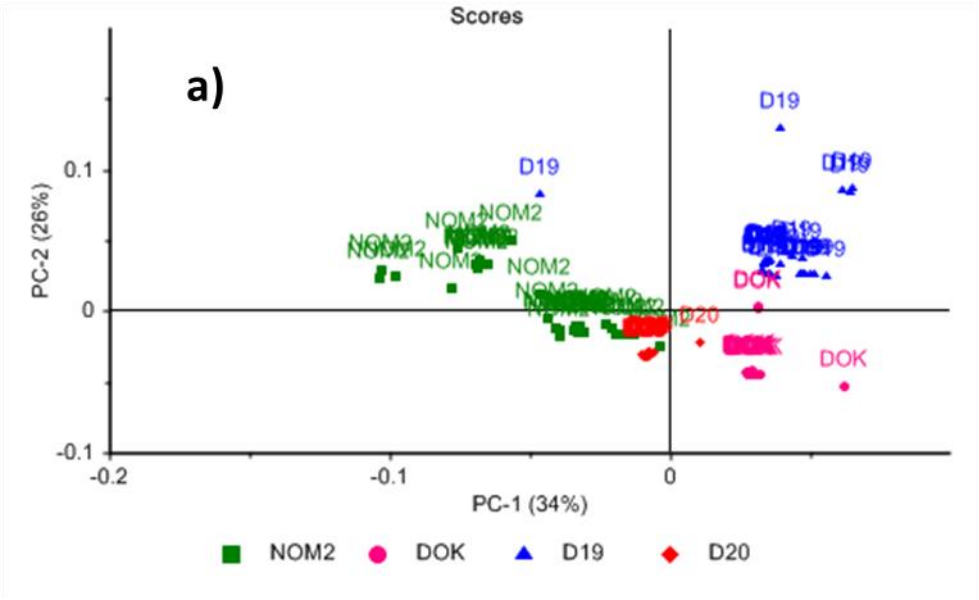

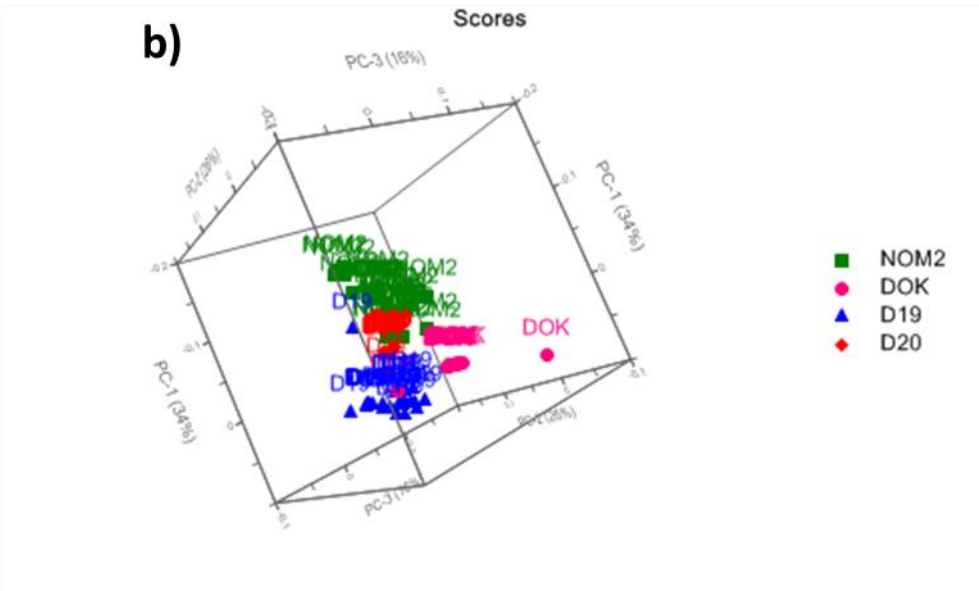

Figure 3. 9 a) PCA plot over complete spectral range between normal and dysplastic models showing PC1 and PC2, b) PCA 3D plot showing PC1, PC2 and PC3

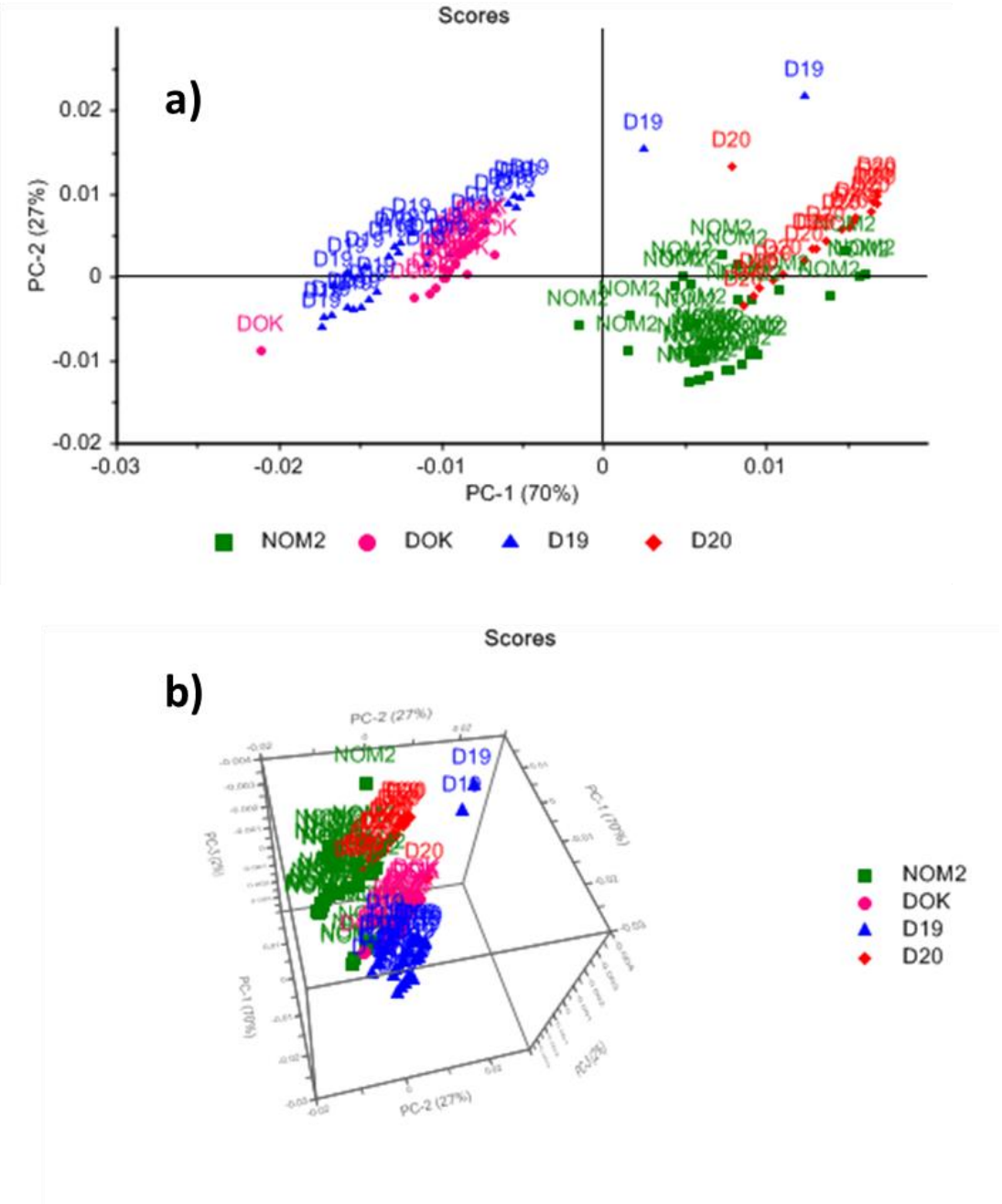

Figure 3. 10 a) PCA plot over amide I region between normal and dysplastic models showing PC1 and PC2, b) PCA 3D plot showing PC1, PC2 and PC3

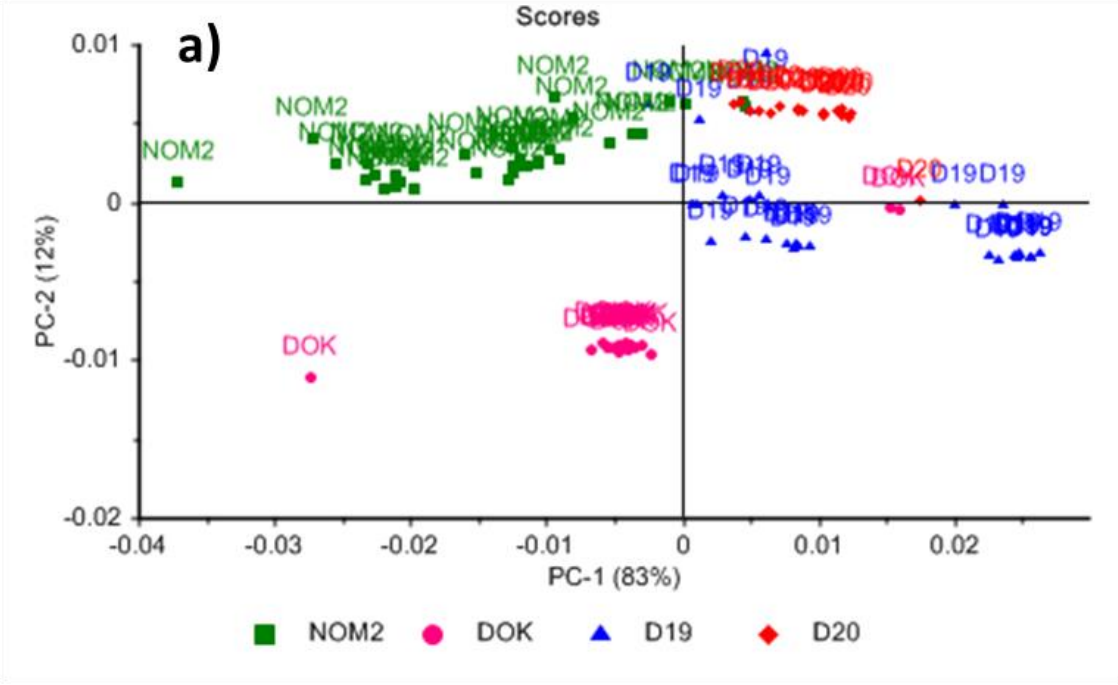

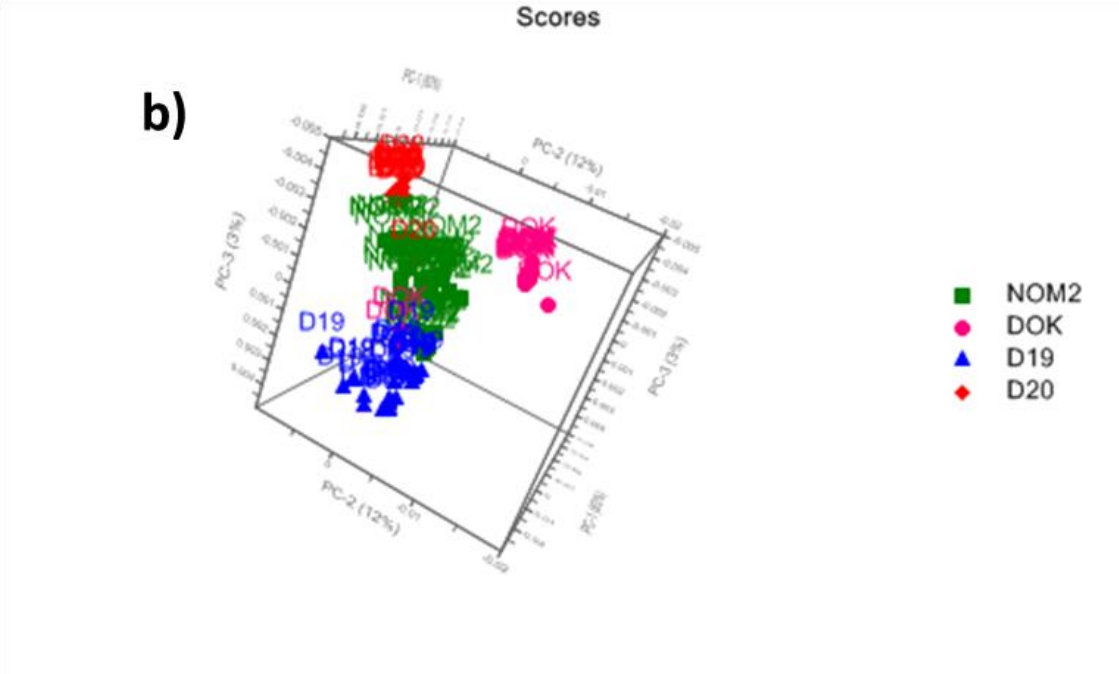

Figure 3. 11 a) PCA plot over amide III region between normal and dysplastic models showing PC1 and PC2, b) PCA 3D plot showing PC1, PC2 and PC3

Normal-Cancer

The complete range PCA analysis of normal and cancer models showed that PC1 differentiated Cal27 models from SCC4 and FaDu models significantly whereas to a lesser extent with normal (figure 3.12a). PC2 separated normal from FaDu models considerably but to a minor extent with SCC4 and Cal27 models (figure 3.12b). The third component was able to differentiate normal from the rest of three cancer models (figure 3.12c). Amongst normal and cancer models, PC1 differentiated normal and FaDu models from SCC4 models in the amide I region (figure 3.13a). The variations described by PC2 discriminates FaDu and SCC4 models from Cal27 and normal models and shows clearer separation between normal and Cal27 (figure 3.13a). In the Amide III region PC1 differentiates FaDu from the rest having a few similarities with SCC4 (figure 3.14). On the other hand PC2 differentiates SCC4 models from normal and Cal27 models and to a slightly lesser extent with FaDu models (figure 3.14).

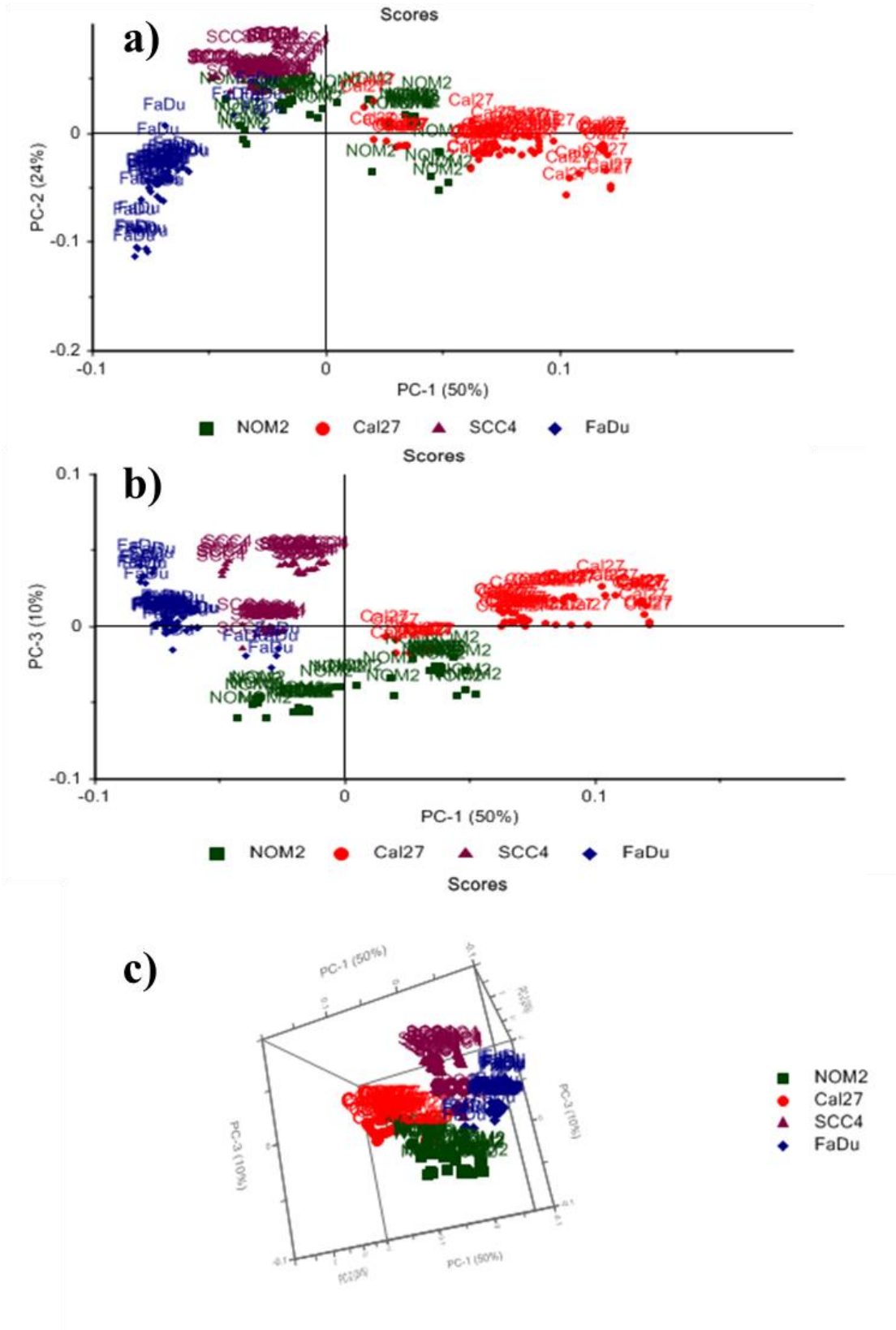

Figure 3. 12 a) PCA plot over complete spectral range between normal and cancer models showing PC1 and PC2, b) showing PC1 and PC3, c) PCA 3D plot showing PC1, PC2 and PC3

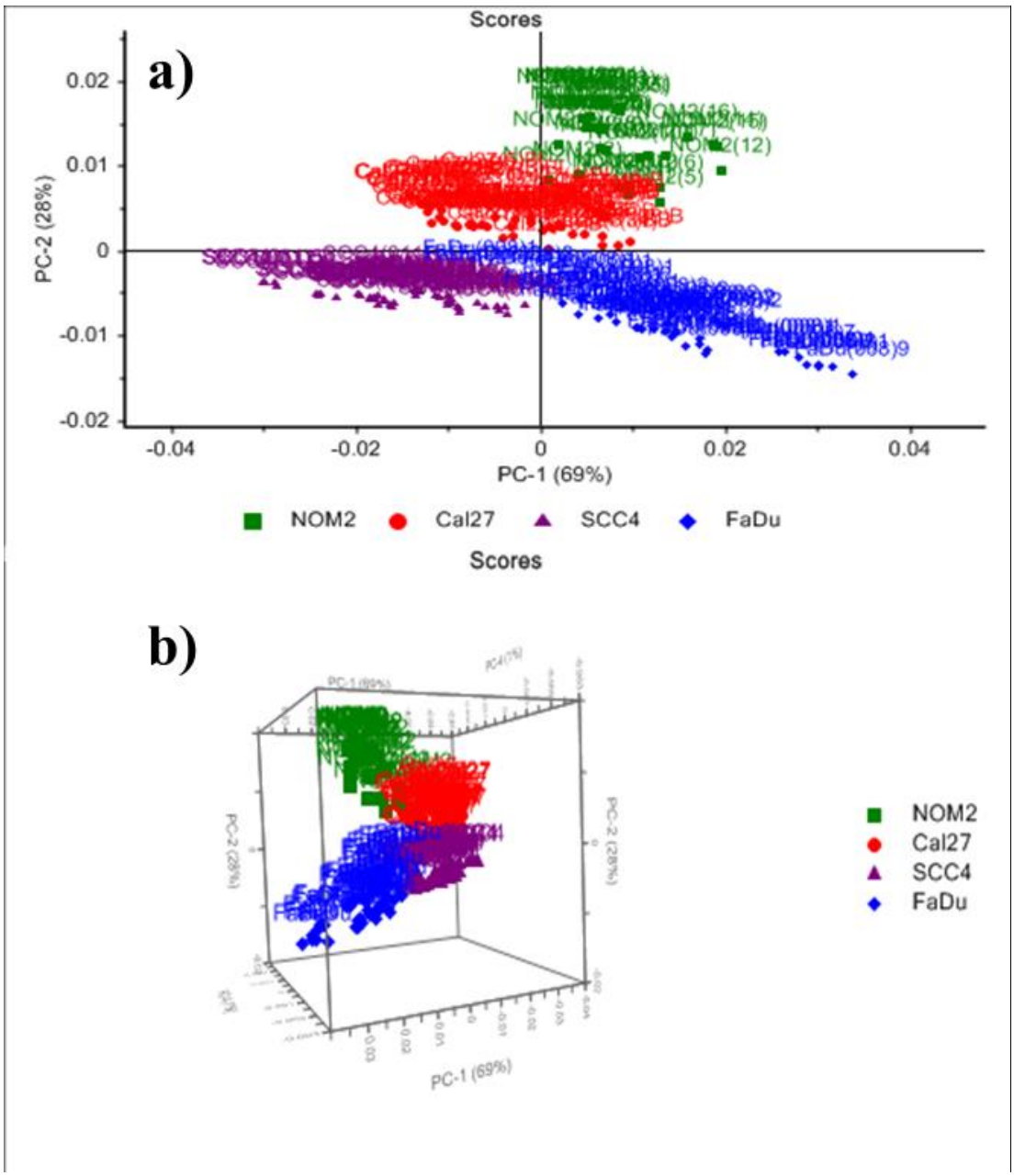

Figure 3. 13 a) PCA plot over amide I region between normal and cancer models showing PC1 and PC2, b) PCA 3D plot showing PC1, PC2 and PC3

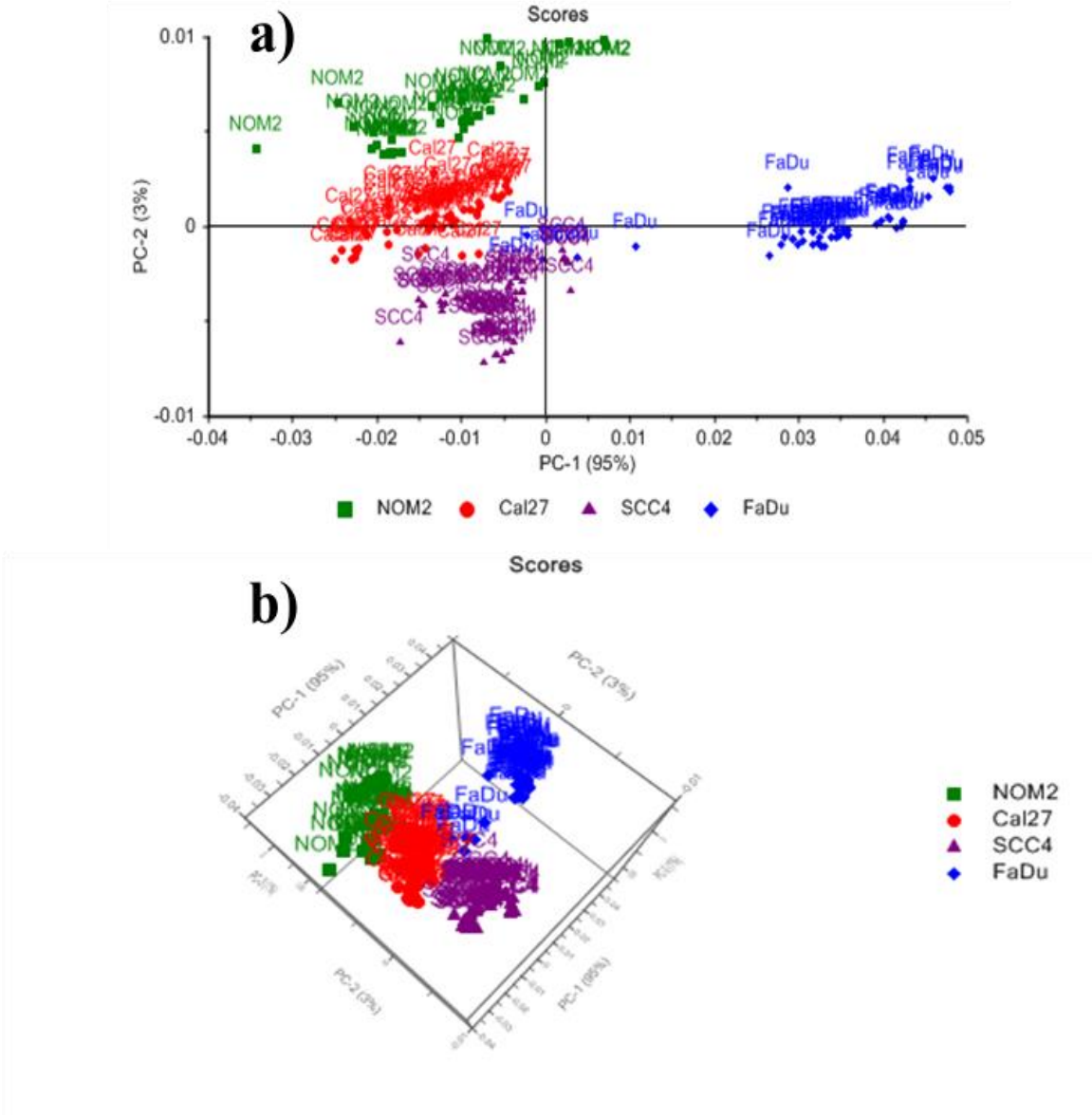

Figure 3. 14 a) PCA plot over amide III region between normal and cancer models showing PC1 and PC2, b) PCA 3D plot showing PC1, PC2 and PC3

Dysplastic-Cancer

In the PC1 of complete spectral range Cal27 were separated from the rest of dysplastic and cancer models whereas PC2 showed differentiation between FaDu and the rest of cancer and dysplastic models (figure 3.15a). PC3 has shown discrimination between D20 and DOK from the rest of the cancer and dysplastic models; however D19 has shown more similarities with the cancer data set (figure 3.15b). PC1 of the amide I region separates FaDu from DOK, Cal27 and SCC4; whereas PC2 differentiates D20, DOK and Cal27 from FaDu, D19 and SCC4 (figure 3.16). Amide III region showed

differentiation of FaDu, D20 and D19 (to a lesser extent) from DOK, Cal27 and SCC4 in the first component whereas PC2 distinguished DOK from D19, D20 and Cal27 (figure 3.17a). PC3 of the amide III region was able to differentiate DOK and D20 from the rest of cancers and dysplastic model (figure 3.17b).

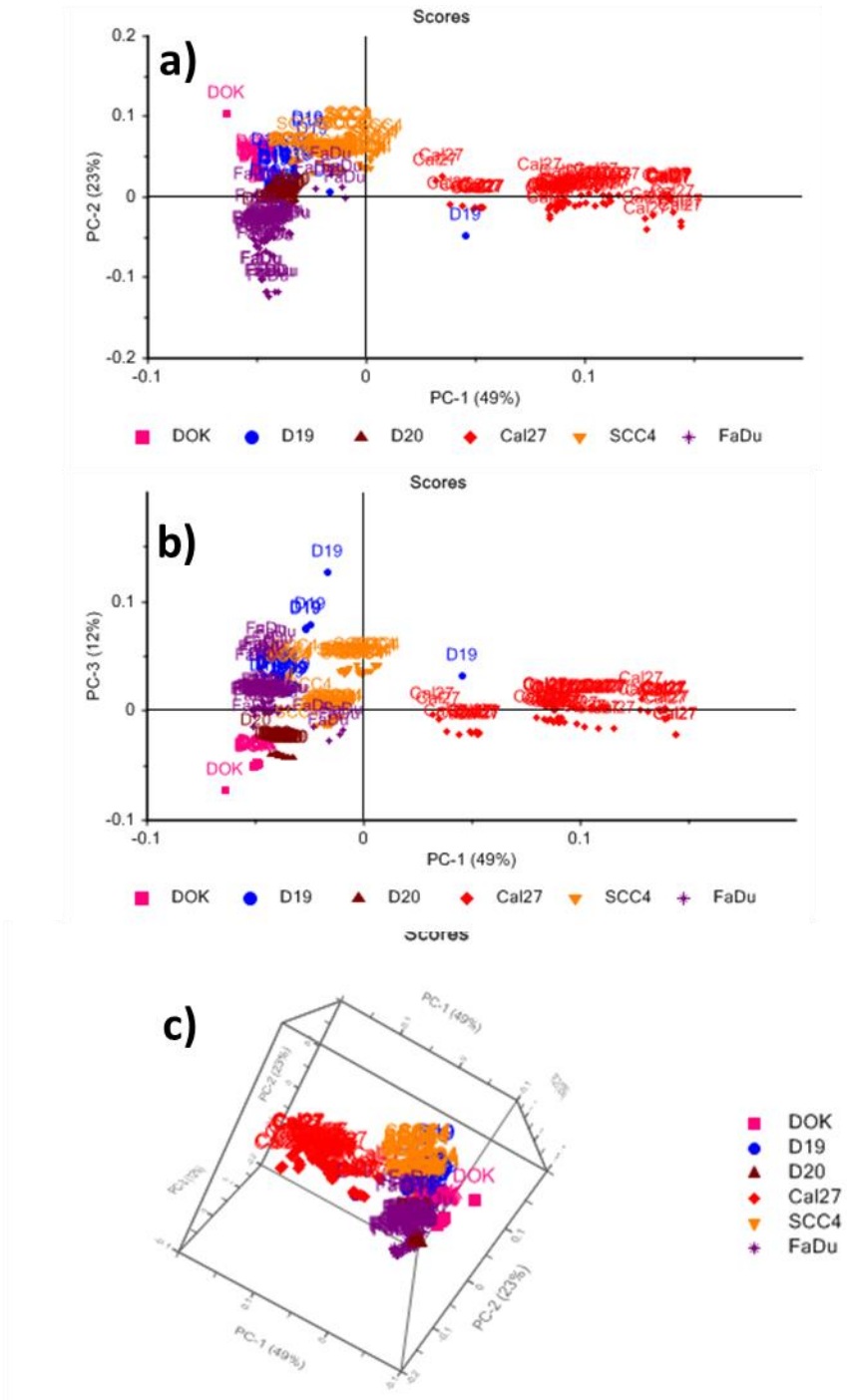

Figure 3. 15 a) PCA plot over complete spectral range between dysplastic and cancer models showing PC1 and PC2, b) showing PC1 and PC3, c) PCA 3D plot showing PC1, PC2 and PC3

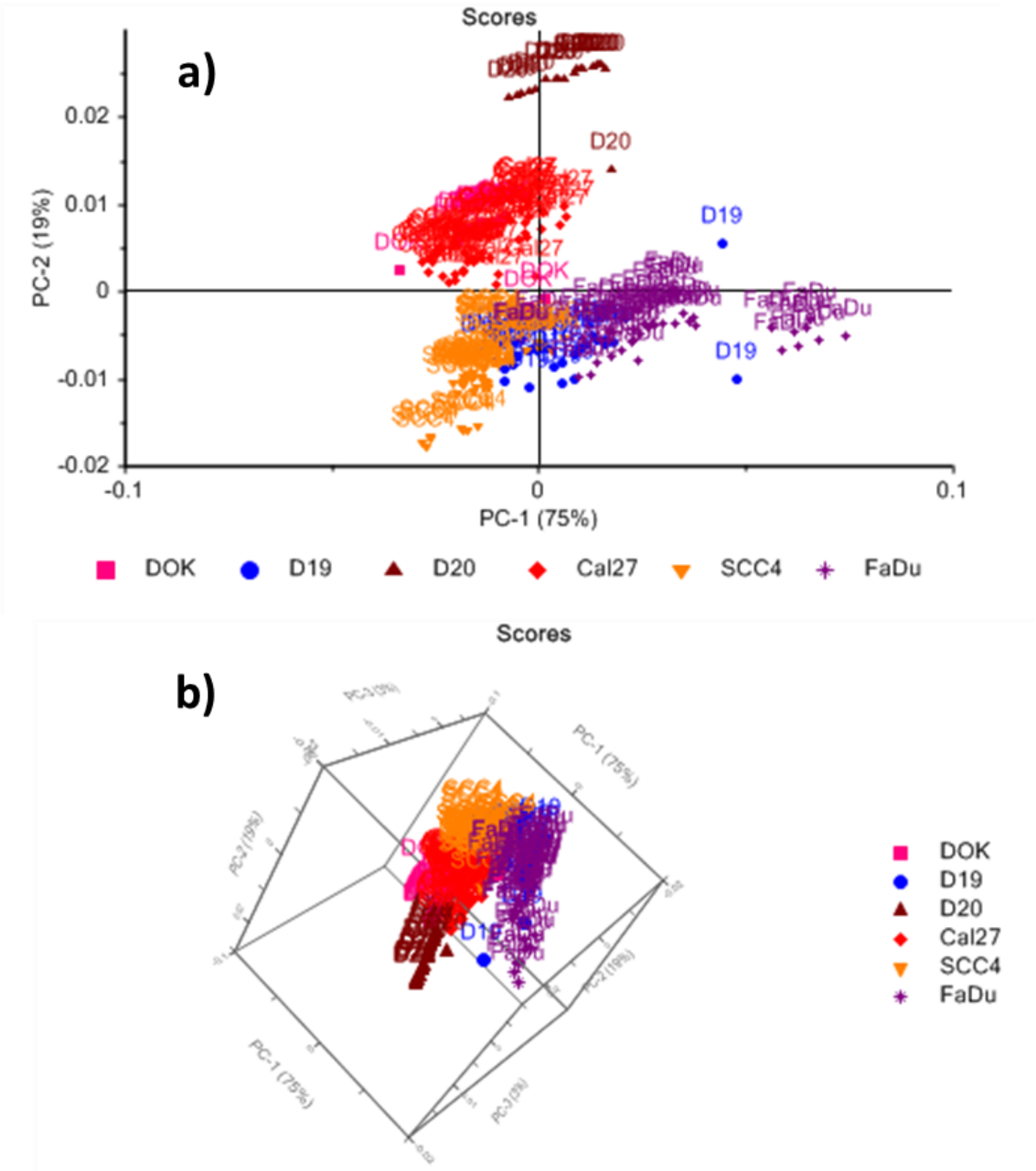

Figure 3. 16 a) PCA plot over amide I region between dysplastic and cancer models showing PC1 and PC2, b) PCA 3D plot showing PC1, PC2 and PC3

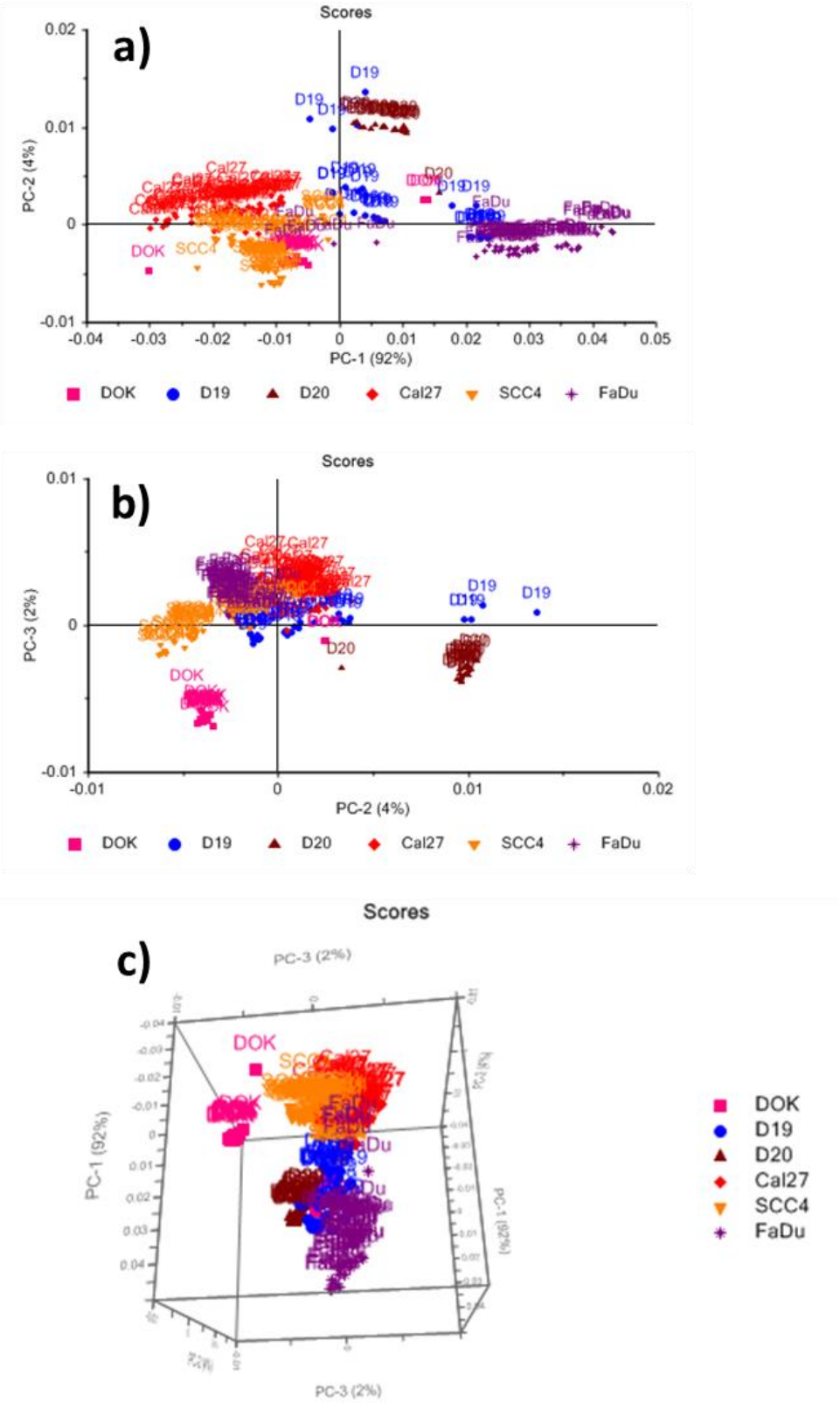

Figure 3. 17 a) PCA plot over amide III region between dysplastic and cancer models showing PC1 and PC2, b) showing PC2 and PC3, c) PCA 3D plot showing PC1, PC2 and PC3

Cluster Analysis (CA)

Figure 3.18 shows cluster classifications of normal and dysplastic models in the complete spectral range. Two main clusters are formed, one exclusively contains dysplastic models and a clear separation to normal models is observed. D19 is as dissimilar to normals as the other dysplastics but not as close to D20 and DOK as the latter two are to each other.

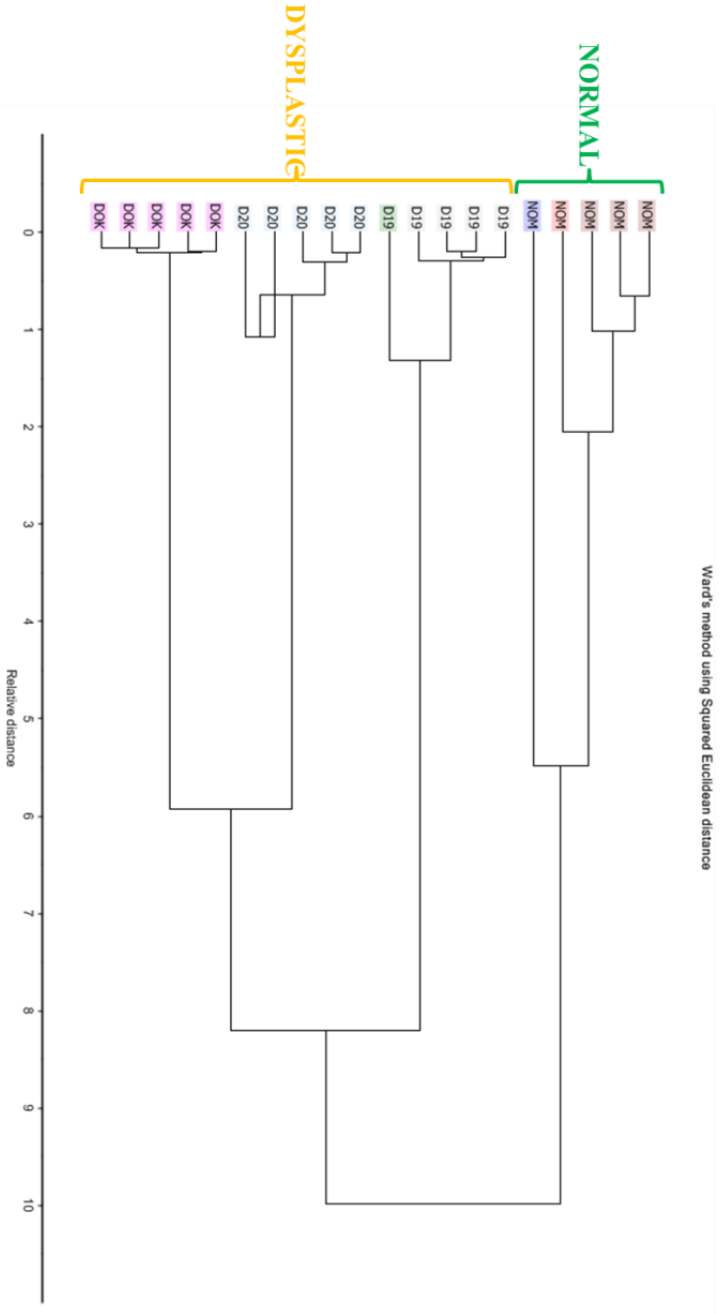

Figure 3. 18 Dendogram showing classification between normal and dysplastic tissue models over complete spectral range

Cluster analysis of normal and cancer models is shown in figure 3.19. FaDu is dissimilar to normal, Cal27 and SCC4. FaDu is squamous cell carcinoma cell line from the pharynx whereas the rest of the cancer cells originate from tongue. Cal27 is equally distant to normal models as to SCC4.

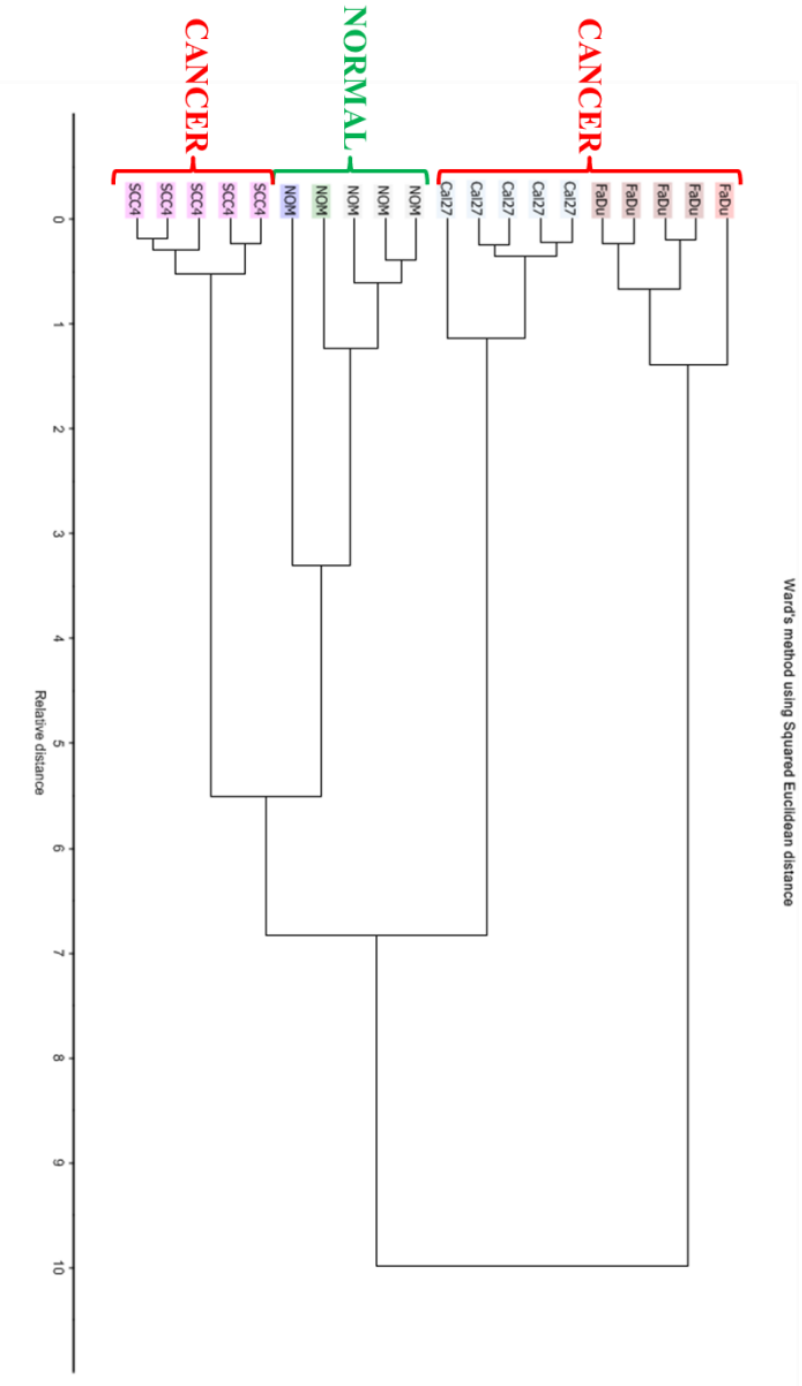

Figure 3. 19 Dendogram showing classification between normal and cancer tissue models over complete spectral range

Figure 3.20 shows the cluster analysis of dysplastic and cancer models. FaDu and SCC4 are more close to the dysplastics than the Cal27. This suggests that FaDu and SCC4 cause similar pathway changes as the dysplastics as compared to Cal27.

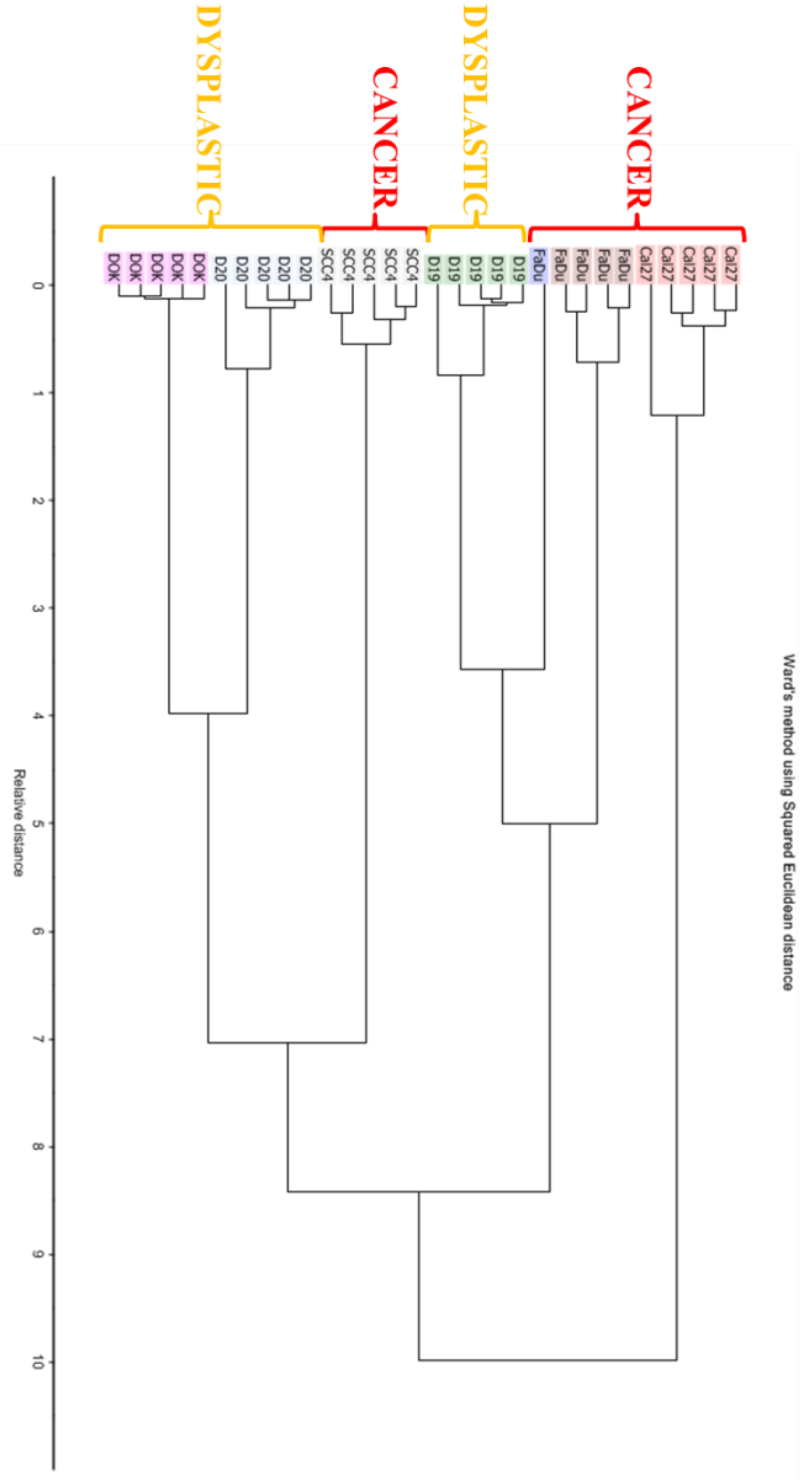

Figure 3. 20 Dendogram showing classification between dysplastic and cancer tissue models over the complete spectral range

Figure 3.21 shows cluster analysis for all models. Normal is clearly more similar to dysplastics than cancers. Cal27 and FaDu are very different to the averages of all other groups.

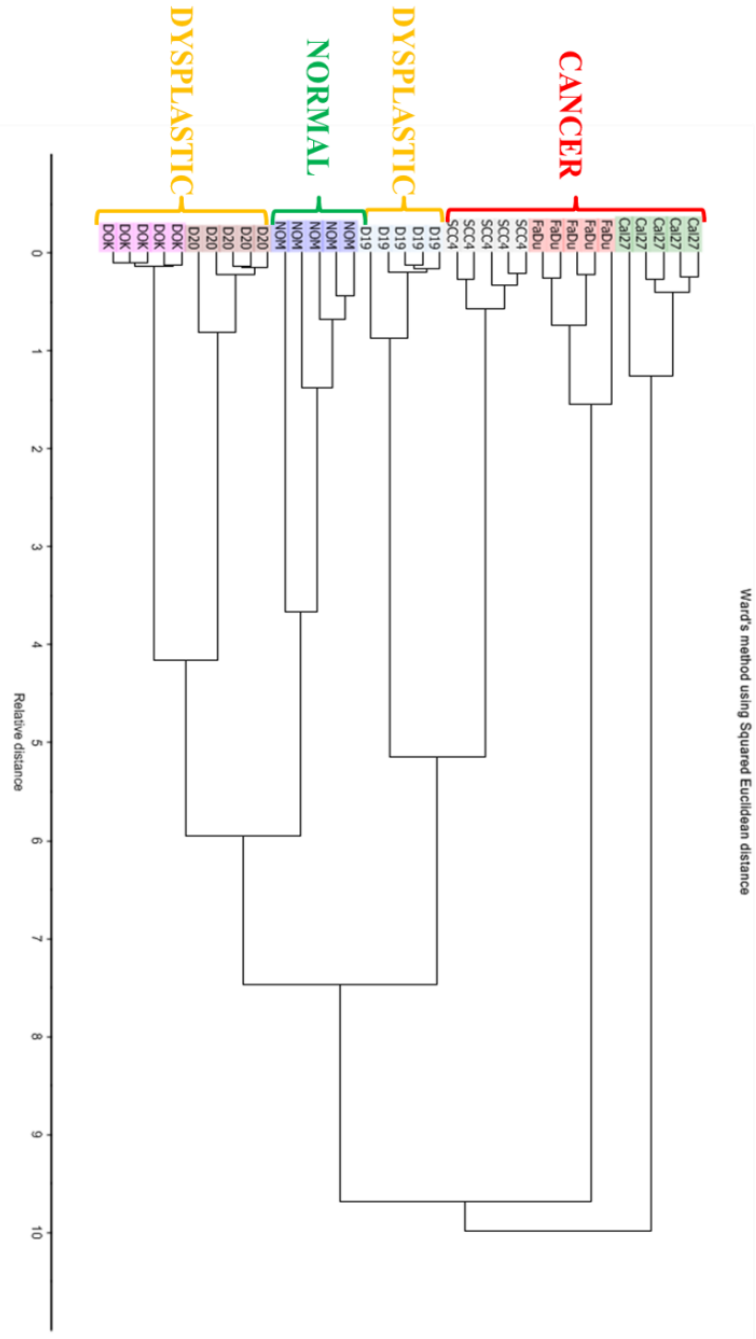

Figure 3. 21 Dendogram showing classification between normal, dysplastic and cancer tissue models over complete spectral range

Linear Discriminant Analysis (LDA

LDA was set up in two different ways to assess its accuracy in order to;

1) Predict the broad tissue state i.e. normal, dysplastic or cancer.
2) Predict down to the subtypes i.e. D19, D20, DOK, Cal27, SCC4 and FaDu.

Prediction as broad tissue state

Normal vs. Cancer

14 out of 20 normal mucosa models were classed as normals whereas 6 were misclassified as cancers with a specificity of 70%. Cancer models were classed as cancers with a sensitivity of 100% as shown in figure 3.22a.

Dysplastic vs. Cancer

54 out of 60 dysplastic mucosa models were grouped as dysplastic, out of which 6 were misclassified as cancer resulting in a sensitivity of 90% whereas 98.3% sensitivity was recorded for cancer models as described in figure 3.22b.

Normal vs. Dysplastic vs. Cancer

Normal models were predicted with a specificity of 75% whereas 55 out of 60 dysplastic mucosa models were grouped as dysplastics and 6 cancers with a sensitivity of 91%. Only 1 cancer model was misclassified as dysplastic whereas the rest of 59 were predicted correctly with a sensitivity of 98.3% (figure 3.22c).

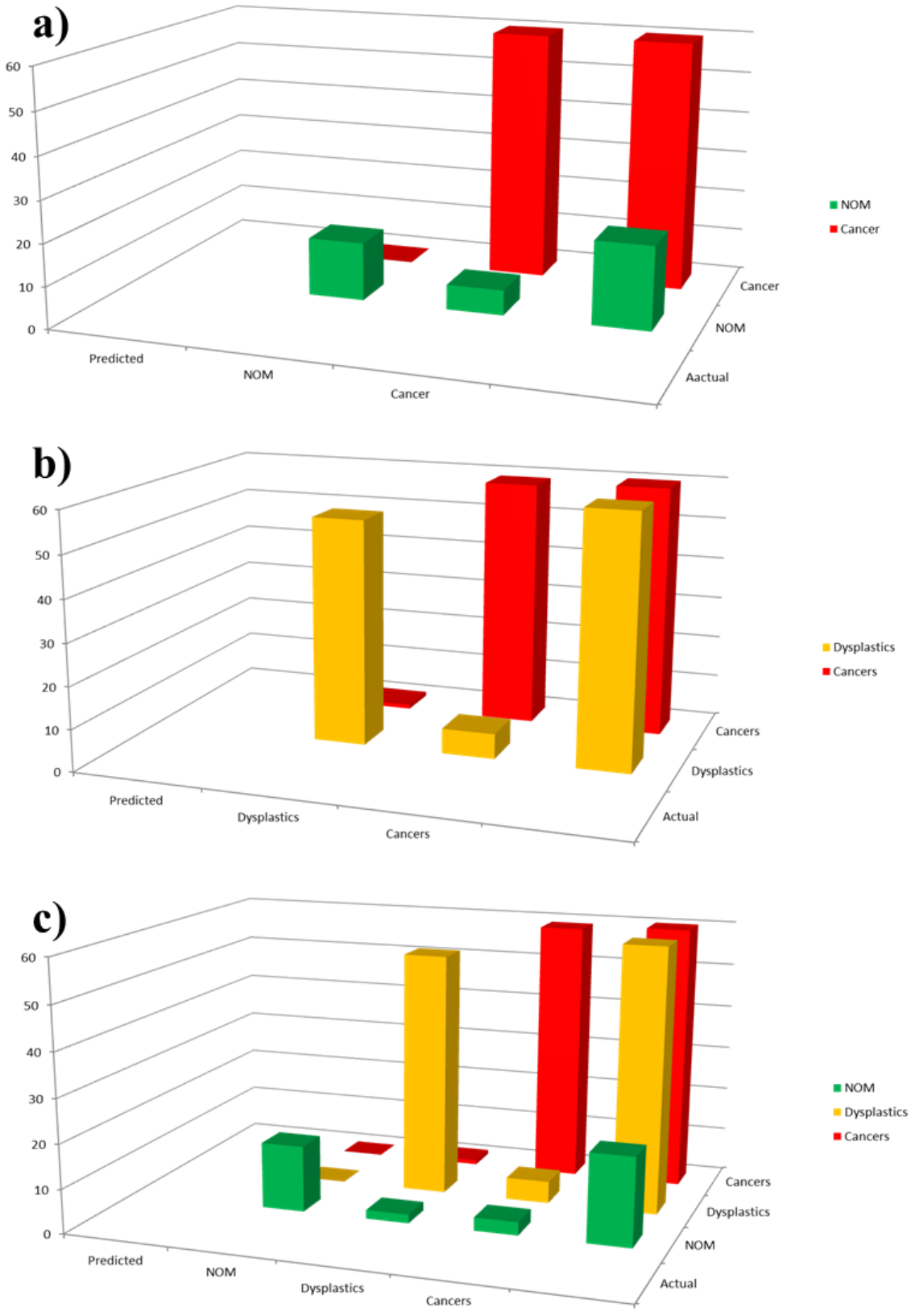

Figure 3. 22 LDA prediction as broad tissue state a) normal and cancer, b) dysplastic and cancer and c) normal, dysplastic and cancer

Prediction as subtypes

Normal vs. cancer

LDA performed over individual groups were predicted with exceptional accuracy and 100% sensitivity and specificity for normal and cancer models were achieved (Cal27, SCC4 and FaDu). Not only was normal discriminated from cancer but various cancer models were also successfully separated from one another (figure 3.23a).

Dysplastic vs. Cancer

Analysis between each model of dysplasia and cancer predicted 100% sensitivity to D19, Cal27 and SCC4 models whereas 70%, 85% and 90% sensitivity was achieved for FaDu, D20 and DOK respectively. A few FaDu, D20 and DOK were misclassified as D19 moreover only 1 model of D20 was grouped as Cal27 (figure 3.23b).

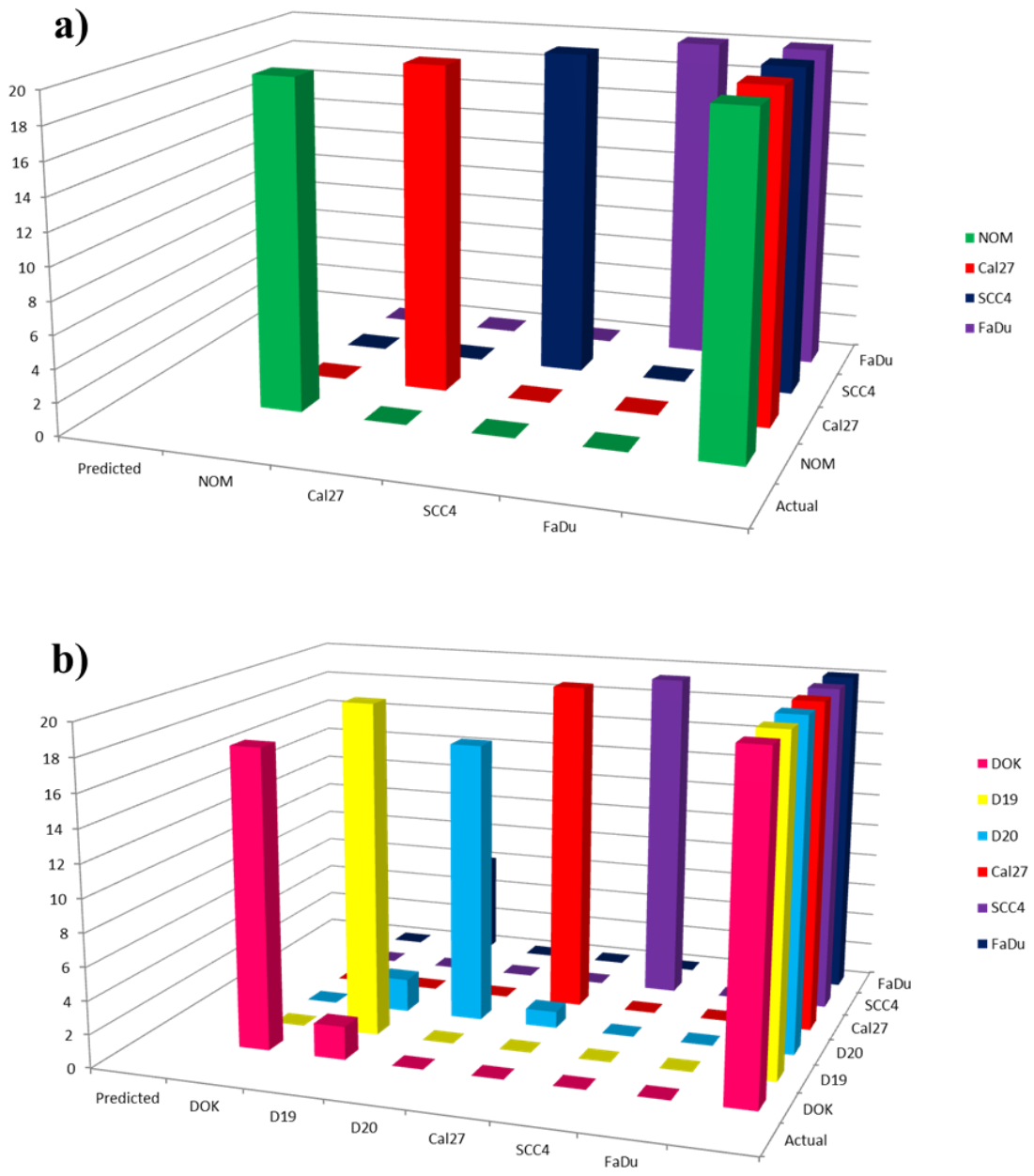

Figure 3. 23 LDA prediction as subtypes of dysplastic and cancer models a) normal, Cal27, SCC4 and FaDu, b) D19, D20, DOK, Cal27, SCC4 and FaDu

3.4 Discussion (Section 1 - Tissue Engineered work)

Histopathological evaluation of patient biopsy material is the gold standard for cancer diagnosis. Despite being the most dependable and established source for detection of cancers, it is associated with certain limitations, such as, surgical intervention, time delays, lack of frequent biopsies, inter observer variability and anxiety to the patients. These limitations have shifted the research towards spectroscopy and in particular Raman spectroscopy, which is capable of providing real time biochemical information of the tissues non-invasively. Raman spectrum can be collected in a very short time (few seconds to minutes) and it can also eradicate the element of inter observer variability, which is associated with histopathological evaluation (Singh et al., 2012b, Rastogi et al., 2013).

In our study, for the first time, we have employed Raman spectroscopy to investigate 3D tissue engineered models of normal, dysplastic and cancerous oral mucosa. Characteristic Raman spectral features were used to differentiate between different tissue types instead of morphological appearance. We were able to identify characteristic Raman spectral features associated with normal, dysplasia and cancerous tissues.

Dysplasia is a transitional phase and histologically subtle changes in the cells are observed which are reversible and at present it is not possible to predict which dysplastic lesion will transform to cancer based on current methods (Rastogi et al., 2013). The percentage of lesions proceeding from premalignant to malignant is very small which makes it difficult to detect cancers that originate from dysplastic lesions at an early stage. Spectral variations particularly at the high wavenumber region, amide I and amide III, clearly distinguished between normal, dysplastic and cancer models furthermore subtypes were also identified with multivariate algorithms.

Normal vs. Dysplasia

Significant spectral variances between tissue engineered normal and dysplastic oral mucosa are shown in figure 3.24, moreover differences amongst dysplastic models (D19, D20 and DOK) can also be observed.

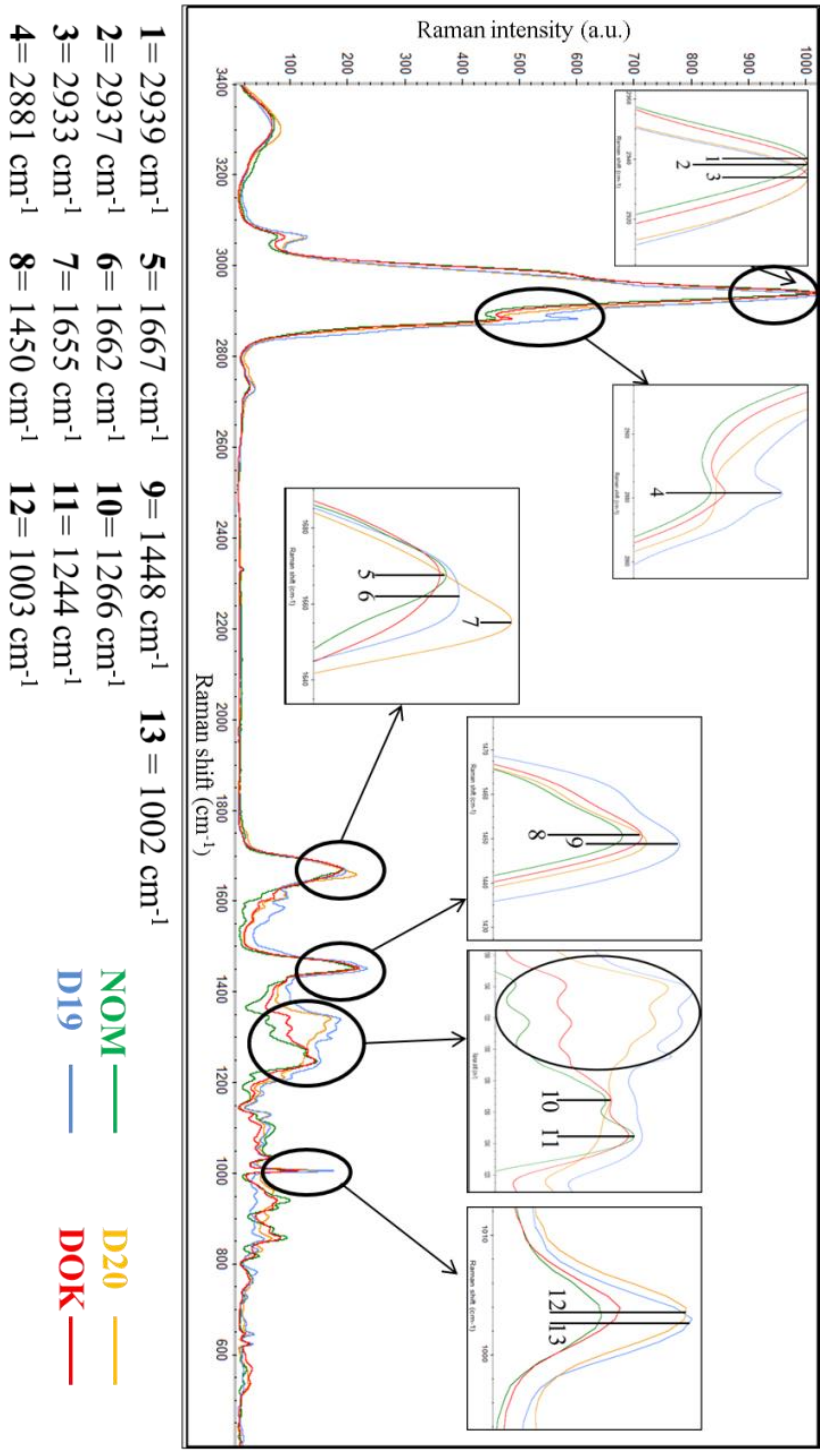

Figure 3. 24 Overlay Raman spectra of tissue engineered normal and dysplastic oral mucosa models (D19, D20 and DOK)

Stretching vibrations of lipids and proteins are primarily present at the higher wavenumber region (2800 to 3100 cm^{-1}). These bands appear as a result of molecular vibrations such as, CH_3, CH_2 and CH=CH. Lipid peaks are expressed by both normal and abnormal tissues at 2939, 2937, 2933 and 2881 cm^{-1} with variations observed in peak positioning and intensities which might be as a result of differences in lipid structural changes and concentrations amongst them. High wavenumber region of the Raman spectra of biological tissues offer unique information about lipids, which may be exceptionally beneficial for lipid peroxidation assessments. In biological tissues such as oral mucosa, vital information regarding lipid saturation can be obtained through spectroscopic means which may lead to potential Raman markers for lipid metabolism. The concentration of unsaturated fatty acids increases in the cells with the progression of disease resulting in variations in peak positioning and intensities. Low lipid synthesis rate might express some effects on the lipid metabolism of cells hence resulting in decreased number of saturated fatty acids moreover, increased level of lipid degradation may be caused due to excessive lipid peroxidation. Research studies have investigated and revealed that increased concentrations of polyunsaturated fatty acids significantly affect signalling pathways as well as cell shape and metastatic behaviour of cancer (Mylonas and Kouretas, 1999).

Band present at 2939 cm^{-1} in the normal mucosa model is shifted to 2937 and 2933 cm^{-1} in DOK and the rest of two dysplastic models respectively. This shift in DOK, D19 and D20 shows variations in the CH stretching vibrations of lipids which not only differentiates normal from dysplasia but also separates DOK from D19 and D20. Peaks present at 2881 cm^{-1} which are assignments of CH_2 asymmetric stretch of lipids, have shown variations in intensities which might indicate varying amounts of unsaturated fatty acids present in normal and dysplastic tissue models. Increased amounts of

unsaturated fatty acids might be associated with the progression of disease (Ayala et al., 2014, Mylonas and Kouretas, 1999). The lowest peak intensity in this region is observed in normal tissue model whereas D19 possesses highest intensity. These spectral features observed in the high wavenumber region have shown significant variances between normal and dysplastic tissue engineered models, furthermore variances amongst dysplastic tissues are also evident. These features also indicate differences between various subtypes or grades of dysplasia in terms of mild, moderate of severe.

Amide I, II and III regions showed major contribution in the Raman spectra of tissue engineered oral mucosa models. These contributions were as a result of stretching and bending vibrations of biomolecules such as carbonyl (C=O) stretching, O-P-O vibrations, C-H bending, asymmetric phosphate stretching of nucleic acids, C=C bending mode of Phenylalanine, Tyrosine, C-C stretching, CH_2 twisting, CH_2 deformations and C=C stretching of lipids (Deshmukh et al., 2011b, Venkatakrishna et al., 2001, Malini et al., 2006). Raman spectral information in the fingerprint region also identified nucleic acid bases such as thymine, adenine, guanine, uracil and ring breathing mode of cytosine (Stone et al., 2004, Movasaghi et al., 2012, Rehman et al., 2007).

Proteins play a vital role in terms of differentiation between normal and pathological conditions as well as it can be used as a potential molecular marker in cancer biology. Protein metabolism in relation to metastasis, which includes transcription (RNA synthesis) and translation (protein synthesis), can be obtained by biochemical information acquired by Raman spectrum. Tryptophan is an essential amino acid required for different metabolic processes and is needed for rapidly dividing malignant cells. Malignant tissue samples possess relative increase in peak intensities of

tryptophan (Devpura et al., 2011, Tankiewicz et al., 2006). In our study, similar patterns regarding peak intensities for tryptophan can also be observed. One of the peaks attributed to tryptophan is observed at 1583 cm^{-1} (Devpura et al., 2011, Movasaghi et al., 2007) which shows significant increase in its intensity in pathological state. Raman spectrum observes characteristic peaks of tryptophan in biological tissues; these bands are specific and have been reported repeatedly in the literature in association with cancer and its progression (Malini et al., 2006, Venkatakrishna et al., 2001, Singh et al., 2013). We have used three different dysplastic cell lines (D19, D20 and DOK) in our study, spectral data reveals that not only normal oral mucosa model differs from dysplasia but within dysplastic models variations could also be observed. D19 has shown the most intense tryptophan peak at 1583 cm^{-1}, suggesting that it contains most tryptophan as compared to the rest of the dysplastic and normal models. Different intensity levels of tryptophan in normal and dysplastic oral mucosa models demonstrate the sensitivity of Raman spectroscopy. Clinically speaking, this might aid in determining different grades of dysplasia such as mild, moderate or severe, hence leading to surveillance of these lesions and early detection of cancer.

Amide bands occurred as a result of vibrations of the amide bonds of polypeptide backbones where amide I represents carbonyl stretching (C=O) vibrations of amide group and indicating α-helical structure of proteins. Amide II region show bending vibrations of N-H and CH_2 of amide group whereas amide III discloses C-N-H in-plane bending modes hence representing β sheets and random coils of proteins. Peak positioning, intensity and area in a Raman spectrum provide wealth of information regarding biochemical composition and the conformational structure of biological tissues. The amide I region of the normal and dysplastic oral mucosa models (figure 3.24) has shown significant variations in terms of broadness, positioning and intensity of the peaks. Peak present in the Amide I region at 1667 cm^{-1} in normal oral mucosa

spectrum could be differentiated from the rest of dysplastic models in terms of area, positioning and intensity. This band was broader and shifted to 1662 cm^{-1} in the spectra of D19 whereas D20 showed the highest intensity at 1655 cm^{-1}. Normal tissues possess sharp bands as compared to broad and strong bands in premalignant and malignant conditions (Malini et al., 2006). The surface layer is a lipid bilayer membrane of squamous epithelium in normal conditions therefore the acquired Raman spectrum is lipid dominant however in dysplasia or malignancy, the surface layer is replaced with huge amounts of surface proteins for instance receptor proteins, enzymes, antigens and antibodies etc. which generate a protein dominant Raman spectrum (Malini et al., 2006). Our results have shown similar spectral trends in the amide I region where normal can be differentiated from dysplasia and different types of dysplastic models can also be clearly separated. D19 has shown the broadest band which might indicate severe conformational differences such as α-helix, β plates and disordered structure. Several research groups (Malini et al., 2006, Olivo et al., 2011, Venkatakrishna et al., 2001) have identified in their work that broadness of the peak is increased when the tissue changes its state from normal to premalignant and then malignant which might be due to structural changes occurring in proteins. Amongst dysplastic tissue engineered models, D19 has shown the broadest peak at 1662 cm^{-1} (amide I) which may suggest the severity of dysplasia on the basis of extreme alterations in protein structure. According to such findings, it may be the case that not only normal could be separated from dysplasia but different stages (mild, moderate and severe) could also be identified on the basis of biochemical variations present in tissues.

Significant spectral variations were observed in the fingerprint region especially in the amide I and amide III regions and therefore PCA was performed over the complete spectral range. There are several studies in which these classification systems have been successfully used to differentiate normal tissue from dysplasia such as work done on

cervical cancer (Mahadevan-Jansen et al., 1998, Utzinger et al., 2001, Lyng et al., 2007), stomach (Teh et al., 2008), oesophagus (Kendall et al., 2003) and oral cancer (Malini et al., 2006). Most of the studies have found to discriminate normal tissue from malignant whereas less work has been completed on identifying different grades of dysplasia. Malini *et al*., 2006, successfully differentiated normal oral mucosa from different types of premalignant conditions however they were less successful whilst trying to identify differences between different graded of dysplasia. PCA of the amide I region has also shown encouraging separation between normal and dysplastic models. Since dysplasia is a transitional phase between normal and cancer, it is difficult to draw a line which can isolate dysplastic models however cluster formation of PC1 (1^{st} principal component) was able to differentiate normal and D20 from D19 and DOK whereas PC2 (2^{nd} principal component) differentiated normal from dysplastic models with D20 showing more similarities with normal model. The overall percentage of explained variance in the amide I region was recorded to be 97% (figure 3.10). These classifications suggest the possibility of identifying different types of tissues on the basis of biochemical differences amongst them. The amide I region has shown that substantial amount of biochemical alterations occur in this region as the tissue changes its state from normal to dysplasia, even within dysplastic models we could observe separate cluster formations which might be suggesting different grades of dysplasia. These modelling systems can be extremely beneficial in identifying the state of the tissue and these spectral regions may be used as Raman markers in identifying the progression of the disease.

The peaks present at 1448 and 1450 cm^{-1} are assignments of CH_2, CH_3 bending modes of proteins (amide II), here too D19 shows a broad and strong peak at 1448 cm^{-1} as compared to normal and the rest of the dysplastic models. This shift in the wavenumber might also suggest the amount of stress and strain present in the tissue due to increased

metabolic activities as well as increased amounts of proteins (Movasaghi et al., 2012). D20 and DOK has shown similar peak behaviours in terms of positioning however, peak area and intensity has differed which suggests biochemical differences in the amide II region between the tissue types. An increase or decrease in relative intensity suggests that the quantity or amount of any specific component changes, in this case spectral results have clearly demonstrated that with the progression of the oral mucosa from normal to dysplasia (and even within dysplasia), an increased concentration of proteins is observed.

Spectral features at the amide III region (1200 to 1350 cm^{-1}) have shown significant variances between normal and dysplastic tissue engineered models. In normal tissue spectra, the peak present at 1244 cm^{-1} is assigned to amide III of proteins, which was intense and also observed in the DOK model spectra with subtle variation. However, in D19, a broad band was observed instead of a sharp peak whereas in D20 this peak was not present. This decrease in intensity of the amide III of D20 was unexpected which might indicate degradation or/and disordered proteins with the progression of disease which was also found in the work carried out by Donfack *et al*. according to their work, neoplastic skin cells possess degraded and disordered protein structures in comparison to normal cells (Donfack et al., 2010).

The amide III region produced significant differences compared to the remaining wavenumbers of the Raman spectra, this might be due to the fact that this region not only contains proteins but also provides biochemical information regarding the nucleic acid compartment (1317, 1337, 1338 and 1341 cm^{-1}) and can be assigned to the polynucleotide chain (DNA purine bases), nucleic acid modes indicating the amount of DNA in tissues and guanine ring breathing mode of DNA/RNA (Dukor, 2006, Rehman et al., 2007, Ruiz-Chica et al., 2004, Notingher et al., 2004a, Stone et al., 2004,

Mahadevan-Jansen and Richards-Kortum, 1996). Intensity levels were clearly increased from normal to dysplastic as well as within different types of dysplasia. When tissue changes its state from normal to dysplastic or malignant, cell proliferation takes place in an abnormal pattern which suggest that the amount of proteins and nucleic acids have increased (Short et al., 2005). Moreover, there is an increase in the nuclear/cytoplasmic ratio which is related to cellular transformation during premalignant conditions (Stone et al., 2002a). According to histopathological evaluation, different grades of dysplasia can be identified by nucleic acid to cytoplasmic ratios (Huang et al., 2003b). Our results show the same trend in which dysplastic tissue models has the highest peak intensity as compared to normal, suggesting that an increased DNA activity is present in dysplasia. Raman spectroscopic results show a high level of consistency with histopathological results and therefore the amide III region, especially the nucleic acid compartment, might be used as a biochemical Raman marker for identification and grading of dysplasia or malignancy.

PCA of the amide III region has shown encouraging separation between normal and dysplastic models with an overall explained variance of 95% (figure 3.11). PC1 was able to differentiate normal and DOK from D19 and D20 whereas PC2 differentiated normal, D20 and D19 (to a lesser extent) from DOK. Interesting cluster formation was observed between DOK and D19 in the amide III region which contains biochemical information regarding proteins and nucleic acids (DNA/RNA). The amide I region could not be used to separate DOK and D19 significantly though two separate clusters were formed. Despite this the amide III region clearly separated the two different types of dysplastic models. This may indicate the importance of the amide III region as a potential Raman marker which can identify differences within dysplasia on the basis of protein and nucleic acid variations.

Phenylalanine is an essential amino acid, which was observed at 1003 cm^{-1} in normal, D20 and DOK whereas in D19 tissue model it was shifted to 1002 cm^{-1}. Several studies have demonstrated that patients with malignancy, HIV infections, trauma, burn and sepsis, the blood concentration level of phenylalanine is increased (Chang et al., 1983, Roth et al., 1985, Rath et al., 1987, Ollenschläger et al., 1988). An increased intensity of phenylalanine was significant in dyaplastic tissue models and reflects an increased amount of protein associated with dysplasia. It was found that the intensity of protein dominant peaks increased as the tissue changes from normal to dysplastic or malignant. These finding were consistent with previous studies (Venkatakrishna *et al*., 2001; Krishna *et al*., 2004; Malini *et al*., 2006) suggesting that in normal oral mucosa, Raman spectrum arise from a lipid dominant surface bilayer whereas in dysplasia or malignancy the oral epithelium is rich in proteins hence delivering a protein dominant spectrum (Krishna et al., 2004, Venkatakrishna et al., 2001, Malini et al., 2006).

CA showed two main branches one entirely contained tissue engineered normal oral mucosa whereas the second branch represented dysplastic tissue only (figure 3.18). These clusters were formed on the basis of differences between the data set. Within dysplastics, three sub-sets were created which represent D19, D20 and DOK moreover, none of the dysplastic model mixed with other dysplastic data set which might suggest high sensitivity of the technique. It was possible to not only separate normal from dysplasia but cluster analysis proved to be a vital algorithm in identifying different groups of dysplastic models.

Normal vs. Cancer

Significant spectral variances between tissue engineered normal and cancerous oral mucosa are shown in figure 3.25, differences amongst cancer models (Cal27, SCC4 and FaDu) can also be observed.

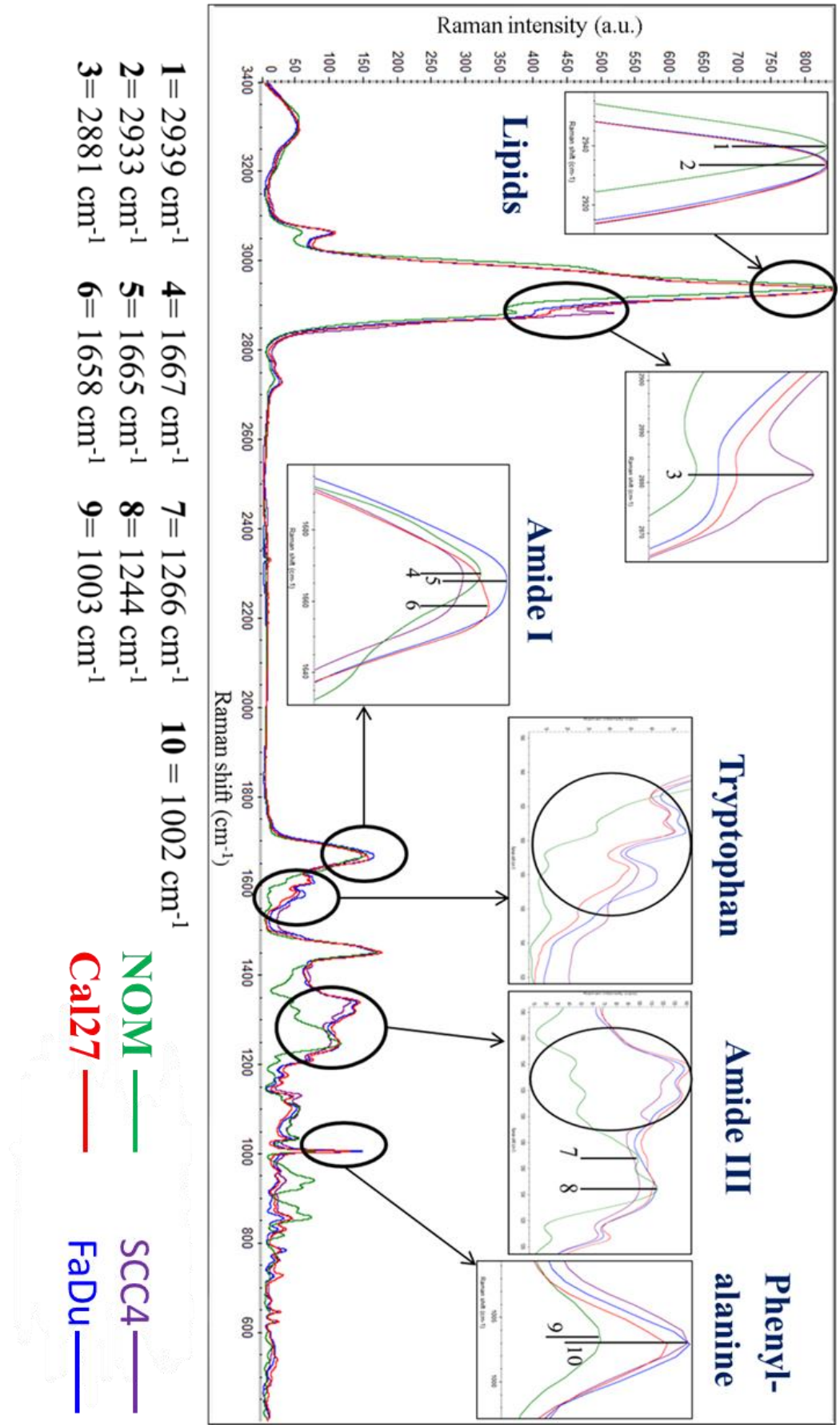

Figure 3. 25 Overlay Raman spectra of tissue engineered normal and cancerous oral mucosa models (FaDu, SCC4 and Cal27)

Molecular vibrations such as, CH_3, CH_2 and CH=CH, produce these bands which are known to be unique spectral markers for identification of different tissue types. Lipid peaks expressed by both normal and abnormal tissues at 2939, 2933 and 2881 cm^{-1} with variations observed in peak positioning and intensities might be as a result of differences in lipid structural changes and concentrations amongst them. Lipid peroxidation provides vital information regarding the state of tissue therefore this region of the Raman spectrum might be extremely useful in detecting such changes. Signalling pathways, cell shape and metastatic behaviour of cancer is seriously affected by increased concentrations of polyunsaturated fatty acids (Mylonas and Kouretas, 1999).

The band present at 2939 cm^{-1} in the normal mucosa model had shifted to 2933 cm^{-1} in all cancer models. This shift shows variations in the CH stretching vibrations of lipids and differentiates normal from cancer; moreover we can also distinguish DOK from cancer models as well in this region. Peaks present at 2881 cm^{-1} in normal and SCC4, are assignments of CH_2 asymmetric stretch of lipids and show variations in intensities which might indicate varying amounts of unsaturated fatty acids present in normal and cancer tissue models. Progression of cancer might be associated with increased amounts of unsaturated fatty acids. SCC4 spectra showed the highest peak intensity as compared to normal whereas a shoulder was observed in Cal27 and FaDu spectra. Spectral variances in the high wavenumber region have differentiated normal from cancer as well as differences within cancer models were also noticeable. These characteristics may be able to identify different grades of cancer hence can be extremely useful in terms of early detection.

Tankiewicz *et al.,* (2006) also concluded in their studies that malignancy might be associated with increased amounts of tryptophan (Tankiewicz et al., 2006). Similar patterns of increased tryptophan intensities were also observed in our study. Peaks

attributed to tryptophan (observed at 1208, 1558 and 1583 cm^{-1}) (Devpura et al., 2011, Movasaghi et al., 2007) shows significant increase in intensity as the tissue changes from normal to cancer hence suggesting an increased amount of tryptophan and increased metabolic activities in cancer cells. Raman spectrum observes characteristic C=C bending mode of tryptophan in biological tissues; these bands are specific and have been reported repeatedly in the literature in association with cancer and its progression (Malini et al., 2006, Tankiewicz et al., 2006). Similar to dysplastic spectral data, differences within different cancer models were also observed which may suggest different type or stages of cancer and might be a useful Raman marker for identification and surveillance of the disease.

Different anatomical locations in the oral cavity show differences in Raman spectra despite the tissue all being normal (Bergholt et al., 2012). This suggests that Raman spectroscopy is not only sensitive enough to detect variances between different types of tissues such as normal, premalignant or malignant but it also observes anatomical variances within one tissue type (Bergholt et al., 2012). FaDu model spectra have shown significant differences in the finger print and C-H region as compared to Cal27 and SCC4. On the basis of evidence in the literature regarding spectral variances being observed at different anatomical sites, it may suggest that the FaDu cell line was squamous cell carcinoma from the pharynx whereas Cal27 and SCC4 were obtained from tongue, hence the reason why we have detected spectral differences between these cancer models. This was one of the considerations that we only isolated normal oral fibroblasts and keratinocytes from buccal mucosa tissue to construct normal models in order to limit anatomical variations.

The peak present in the Amide I region at 1667 cm^{-1} (C=O stretching mode of amide group) in normal oral mucosa spectrum could be differentiated from the rest of cancer

models in terms of peak area, positioning and intensity (figure 3.25). This band was broader and shifted to 1665 (SCC4 and FaDu) and 1658 cm^{-1} (Cal27) suggesting molecular conformational differences between normal and cancer as well as within cancer models. Broad peaks are characteristic features observed in premalignant and malignant conditions indicating protein dominancy in tissues whereas in normal oral mucosa lipids are dominant and express sharp bands. Oral mucosa is a stratified epithelium and in malignant conditions cells present in all layers proliferates, which may express surface proteins from antibodies, signalling agents and enzymes hence indicating increased nucleic acid and protein content in such tissues which is consistent with histopathology (Malini et al., 2006, Murali Krishna et al., 2004). FaDu has shown the broadest band which might indicate severe conformational differences such as α-helix, β plates and disordered structure. Several research groups (Malini et al., 2006, Olivo et al., 2011, Venkatakrishna et al., 2001) have identified in their work that broadness of the peak is increased when the tissue changes its state from normal to premalignant and malignant which might be due to structural changes occurring in proteins.

PCA results have shown promising separation between normal and cancer tissue models of the oral mucosa in amide I region with 97% of explained variance. Clusters were nicely separated from one another and PC1 differentiated normal, FaDu and Cal27 (lesser extent) from SCC4 whereas PC2 discriminated normal and Cal27 from the rest of two cancer models. In relation to our previous PCA results of dysplastic models, again we found that all three cancer models were different from one another showing differences in their chemical structure, this could be a step forward in determining the type of cancer which might lead to a better treatment outcome for patients. These modelling systems can be extremely useful in identifying state of the tissue and these spectral regions may be used as Raman markers to identify disease.

In normal tissue spectra, peak present at 1244 cm^{-1} can be assigned to amide III of proteins, however, in cancer models, a broad band was observed instead of a sharp peak. Significant spectral differences were observed in the amide III region as compared to the remaining wavenumbers of Raman spectra, this might be due to the fact that this region also contains biochemical information regarding nucleic acids (1317, 1337, 1338 and 1341 cm^{-1}) and can be assigned to polynucleotide chain (DNA purine bases), nucleic acid modes indicating mount of DNA in tissues and Guanine ring breathing mode of DNA/RNA (Stone et al., 2004, Mahadevan-Jansen and Richards-Kortum, 1996, Dukor, 2006). The biochemistry of cancer progression has also been linked with abnormal nucleic acid metabolism (Heimann et al., 1991). Increased metabolism of nucleotides and amino acids have been associated with abnormal nucleic acid synthesis (Deberardinis et al., 2008). Intensity levels were clearly raised from normal to dysplastic and cancer as well as within different types of cancers. When tissue changes its state from normal to dysplastic or malignant, cell proliferation takes place in an abnormal pattern which may suggest that there is increased amount of proteins and nucleic acids (Short et al., 2005). Moreover, there is an increase in the nuclear/cytoplasmic ratio which is related to cellular transformation during premalignant conditions (Stone et al., 2002a). According to histopathological evaluation, different grades of dysplasia and cancer can be identified by nucleic acid to cytoplasmic ratios, Moreover, Huang *et al*. observed Raman bands associated with cellular components of nucleic acids that were relatively broad and intense in malignant tissues indicating an increase in their levels (Huang et al., 2003b). Our results show the same tendency in which dysplastic and cancer tissue models have higher peak intensities as compared to normal, suggesting increased metabolic activities. It is important to mention that differentiation between dysplasia and cancer was also recorded in acquired Raman spectral data (figure 3.26), which is encouraging and may

aid in surveillance of dysplastic lesions. PCA results of dysplastic vs. caner at amide I region separated D20 (dysplastic) from FaDu and SCC4 (cancer) in PC1 however the second PC differentiated DOK from Cal27 (figure 3.16). In the amide III region PC1 differentiated D19 and D20 from Cal27 and SCC4, on the other hand it also distinguished between DOK and FaDu. The second PC was able to separate DOK from Cal27. These findings could lead to an area of interest where dysplasia might be monitored non-invasively in order to detect the malignant lesion at an early stage.

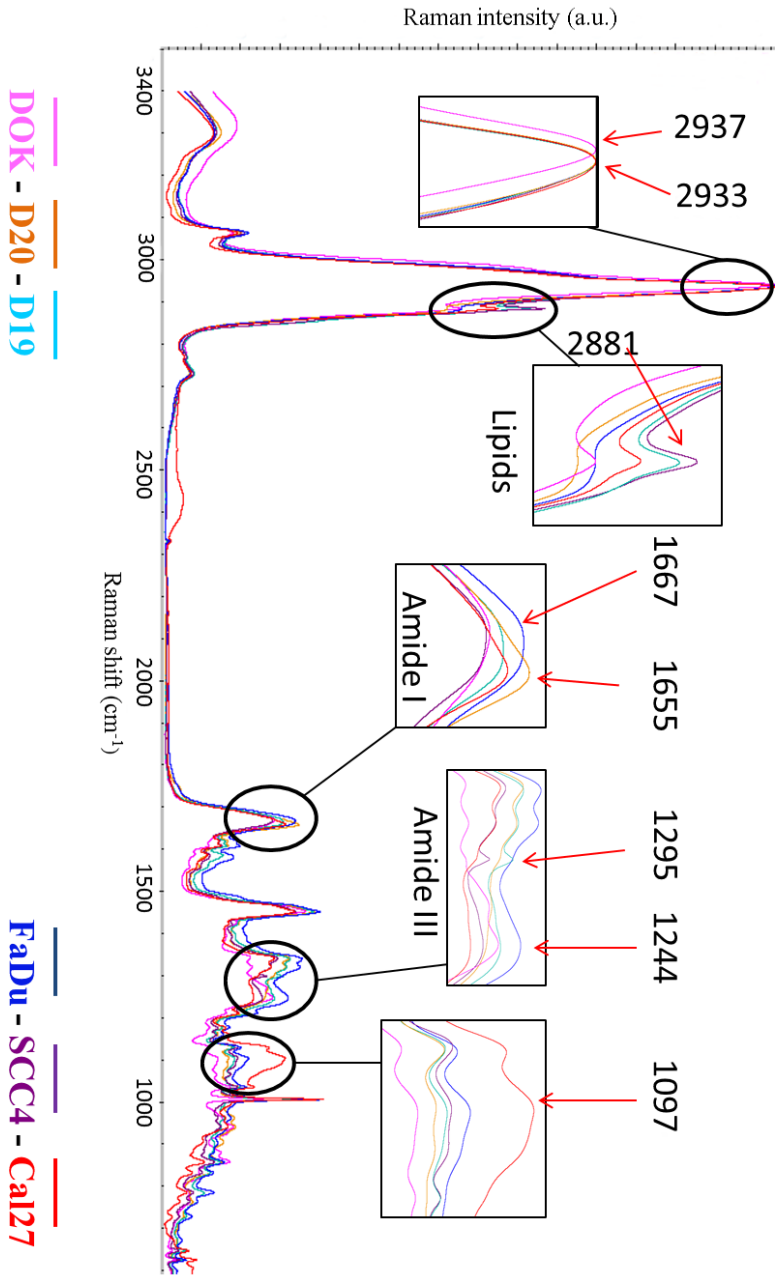

Figure 3. 26 Overlay Raman spectra of tissue engineered dysplastic (D19, D20 and DOK) and cancerous oral mucosa models (FaDu, SCC4 and Cal27)

Raman spectroscopic results show consistency with histopathological findings in this regard therefore it may suggest that the amide III region especially nucleic acid compartment might be a potential biochemical Raman marker for identification and grading of dysplasia or cancer.

Throughout our data sets we have observed that amide III region shows the maximum amount of variances due to the fact that along with proteins, nucleic acids (DNA/RNA) are also present in this region. It is believed that with the progression of disease, metabolic activities are increased within cells and as a result increased amounts of nucleic acids are also observed. In amide III region PC1 was able to differentiate FaDu from the rest of cancer models as well as normal mucosa whereas PC2 differentiated normal and Cal27 from SCC4. Unlike amide I region, it was possible to separate all three cancer models in amide III region. PCA results in the amide III region have clearly separated FaDu from the rest of data set which might be suggesting that along with amide III variations; anatomical location has also played a significant role in this separation.

Phenylalanine was observed at 1003 cm^{-1} in normal whereas in cancer tissue models it was shifted to 1002 cm^{-1}. Increased intensity of phenylalanine was significant in dyaplastic and cancer tissue models which reflects increased amount of protein associated with abnormal tissues. This was expected that the intensity of protein dominant peaks may increase as the tissue changes from normal to dysplastic or malignant (Venkatakrishna *et al*., 2001; Krishna *et al*., 2004; Malini *et al*., 2006). In normal oral mucosa, Raman spectrum arise from a lipid dominant surface bilayer whereas in dysplasia or malignancy the oral epithelium is rich in proteins hence delivering a protein dominant spectrum (Krishna et al., 2004, Venkatakrishna et al., 2001, Malini et al., 2006).

In CA, two main branches were formed as shown in the dendogram (figure 3.19), one exclusively contained FaDu model whereas the second branch represented normal, Cal27 and SCC4. It is important to mention that all the normal model data set was in a separate sub-branch of dendogram. Cluster analysis also confirmed the importance of anatomical location and showed the sensitivity of Raman spectroscopy by grouping FaDu in entirely a different branch. All tissue models, including normal were separately grouped and none of them mixed with the other.

LDA Classification

Past research of spectroscopic analysis of oral tissues has focused on the differentiation between normal and cancerous tissues (Venkatakrishna et al., 2001, Krishna et al., 2004), however Malini *et al*. 2006 not only discriminated normal from cancer but also extended the data set by including inflammatory and premalignant lesions. Their PCA results were able to separate normal from cancer but poor discrimination was recorded amongst abnormal tissues.

In our study, we constructed 3D tissue engineered models of normal, dysplastic and cancerous oral mucosa for Raman spectroscopic analysis. These models mimic natural conditions closely and provide an opportunity to understand the mechanism of disease progression. PCA models were built and used for LDA predictions. We used these models in two different ways;

1) Predict the broad tissue state i.e. normal, dysplastic or cancer.

2) Predict down to the subtypes i.e. D19, D20, DOK, Cal27, SCC4 and FaDu.

Raman prediction against known models of normal, dysplasia or cancer showed encouraging results with higher percentage of accurately categorized models and less misclassification such as 75% specificity to normal models and 91% and 98%

sensitivity was achieved in dysplastic and cancer models as a whole group respectively. In the entire group classification, promising results were obtained between dysplastic and cancer models where we achieved sensitivity of 90% and 98%, respectively. This supports the potential of Raman spectroscopy and proposes that the technique may provide clinical assistance for surveillance of suspected dysplastic lesions. Dysplastic lesions have always been a challenge in terms diagnosis. Raman being a non-invasive technique has the abilities to assist surveillance of such suspected lesions. The support of these algorithms has produced promising results in terms of sensitivity and accuracy to identify various tissue types.

In further investigations, we observed that Raman's ability was enhanced in terms of identifying subtypes of dysplastic and cancer models. LDA results showed 100% sensitivity and specificity for normal and all cancer models namely Cal27, SCC4 and FaDu indicating that Raman might be more sensitive to pick differences within sub types. RS has the potential to come up as a powerful tool along with multivariate data analysis techniques to classify different grades, stages or types of tumours.

D19, Cal27 and SCC4 models produced 100% sensitivity however a few misclassifications were also seen between FaDu, D20 and DOK. As we know that FaDu although is a squamous cell carcinoma cell line it is derived from a different anatomical location, the pharynx. Amongst the cancer models Cal27 showed the most consistency in tissue classification which might suggest that they have relatively homogenous nature as compared to SCC4 and FaDu. FaDu was misclassified as D19 for up to 30% however it did not show any similarities with the other two cancer models. This might suggest that D19 belongs to the severe case of dysplasia which is why it has shown more similarities with FaDu.

Our results have demonstrated that RS proved to be extremely accurate in identifying subtypes of tissue engineered models and has the potential to overcome limitations associated with histopathology. In comparison with histopathology, RS is very easy to use and *in vivo* studies have already demonstrated its clinical applications (Singh et al., 2013, Singh et al., 2012a, Wu et al., 2011). Good quality spectrum was collected in under 3 minutes which could be significantly reduced by changing spectroscopic parameters and the non-invasive nature of the technique offers promising future in cancer diagnosis as well as monitoring of dysplastic tissues.

3.5 Summary of tissue engineered work

- In this study for the first time 3D Tissue engineered models of normal, dysplastic and cancerous oral mucosa were analysed using Raman spectroscopy.
- 302 high quality Raman spectra were acquired for analysis.
- Sample acquisition took 2 minutes and 30 seconds which is practical for *in vivo* application. This time could be reduced to less than a minute.
- Visual spectral differences were evident in the lipid region (high wavenumber), proteins and nucleic acid regions (finger print).
- Amide III region contains nucleic acid compartments as well and showed encouraging separation between normal and abnormal tissues. This may suggest that this region might have the potential to be recognised as a Raman marker for the identification of disease.
- Chemometric analysis based on PCA, Cluster Analysis and LDA successfully differentiated between various tissue models on the basis of biochemical differences amongst them.

- Raman not only identified normal, dysplasia and cancer models but it was also able to discriminate between subtypes of dysplasia and cancer which might suggest that different grades or stages of tumours can also be detected.
- FaDu, a squamous cell carcinoma cell line from pharynx was isolated from the other two models of oral cancer which are both derived from tongue. This supports the fact that even the same cell type with different anatomical location can be detected by Raman spectroscopy.
- LDA results demonstrated a classification between tissue engineered models. High percentage of sensitivity and specificity was achieved and we observed that the percentage of correctly predicted models was enhanced when employed on individual tissue constructs (D19, D20, DOK, Cal27, SCC4 and FaDu) instead of using them as a whole group (dysplasia and cancer).
- Tissue engineered models closely resemble *in vivo* conditions but patient biopsy material would certainly be more complex in nature therefore it would be very interesting to investigate oral mucosa samples *ex vivo* and explore further potentials of RS.

Chapter 3:

Section 2 - Patient Biopsy work

This section contains work conducted on normal, dysplastic and cancer patient biopsies from oral mucosa. Raman spectroscopic investigations were carried out to separate different types of oral mucosa on the basis of biochemical variances observed between them. Use of unsupervised and supervised algorithms have also been demonstrated which proved to be easily compatible with spectral data to produce accurate results. Biochemical information obtained by Raman spectra can be extremely sensitive to predict normal and abnormal tissues which can play a vital role in clinical set ups for the early detection of cancers. At this time and age there is a need to introduce a vibrational technique in clinical settings which is capable of identifying pathology non-invasively and in no time. Moreover they may detect tumour margins and assist surgeons to perform precise guided biopsy procedures.

3.6 Oral mucosa samples

A total of 45 cases were selected for this *ex vivo* study which included 15 samples each of normal oral mucosa (NOM), oral dysplasia and oral squamous cell carcinoma (OSCC). All specimens were selected from tongue tissue in order to keep the anatomical site constant. Raman spectra were acquired from epithelia of all tissues; representative H&E images are given in figure 3.27.

Normal oral mucosa

NOM shows parakeratinised stratified squamous epithelium overlying connective tissue. The epithelium possesses normal morphological and cytological features and an organised architecture. Epithelium shows clear epithelial differentiation with a well formed basal layer (figure 3.27a).

Oral Dysplasia

Representative H&E image of oral dysplasia shows severely dysplastic epithelium with drop shaped rete pegs, nuclear and cellular pleomorphism, hyperchromatism and abnormal mitoses involving most of the epithelial thickness. There is no evidence of invasion into the underlying connective tissue (figure 3.27b).

Oral squamous cell carcinoma

Ulcerated and dysplastic epithelium giving rise to islands and strands of moderately differentiated squamous cell carcinoma infiltrating the connective tissue. The tumour cells show nuclear and cellular pleomorphism, abnormal mitoses, hyperchromatism and focal areas of keratinisation (figure 3.27c).

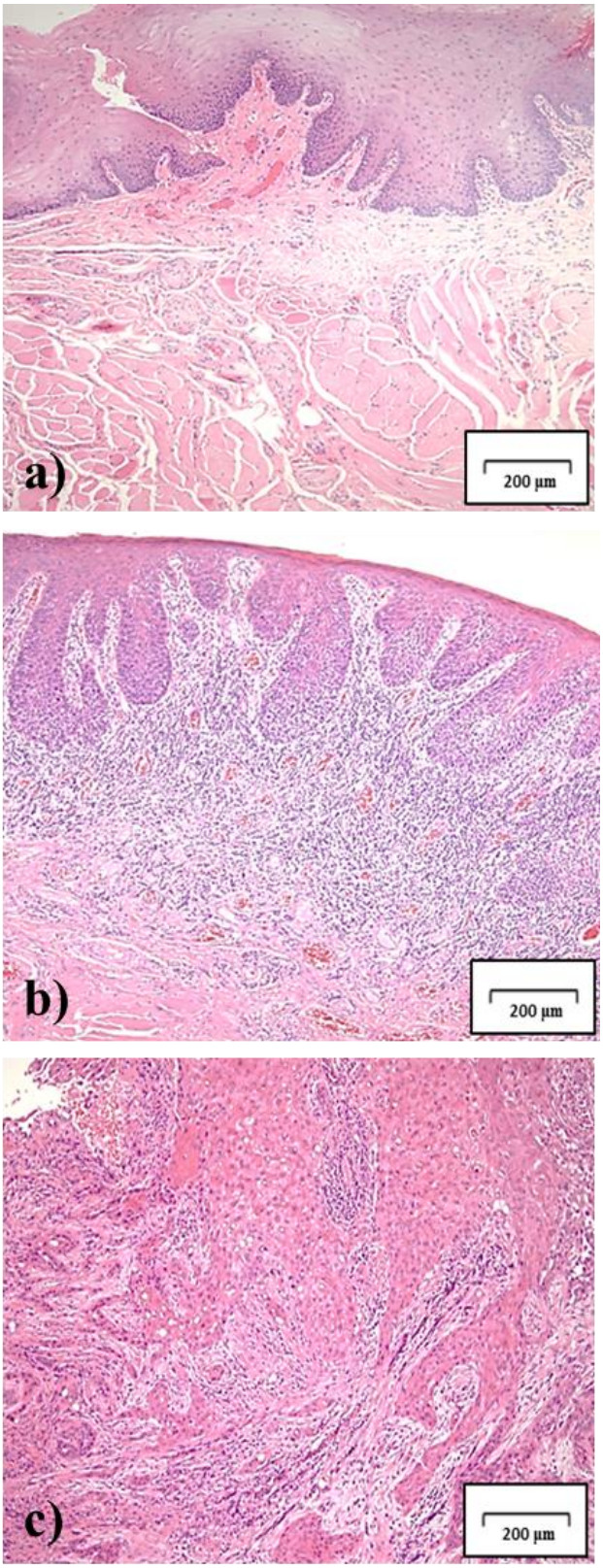

Figure 3. 27 Representative H and E images of oral mucosa samples from tongue, a) normal oral mucosa, b) oral dysplasia and c) oral squamous cell carcinoma

3.7 Raman spectroscopic results

3.7.1 Normal Oral Mucosa

A total of 300 spectra were collected from 15 normal oral mucosa (NOM) samples. Average spectra of these NOM samples are shown in figure 3.28. Average spectrum of all the NOM samples is shown in figure 3.29 and peak assignments along with comparison and references are detailed in table 3.2.

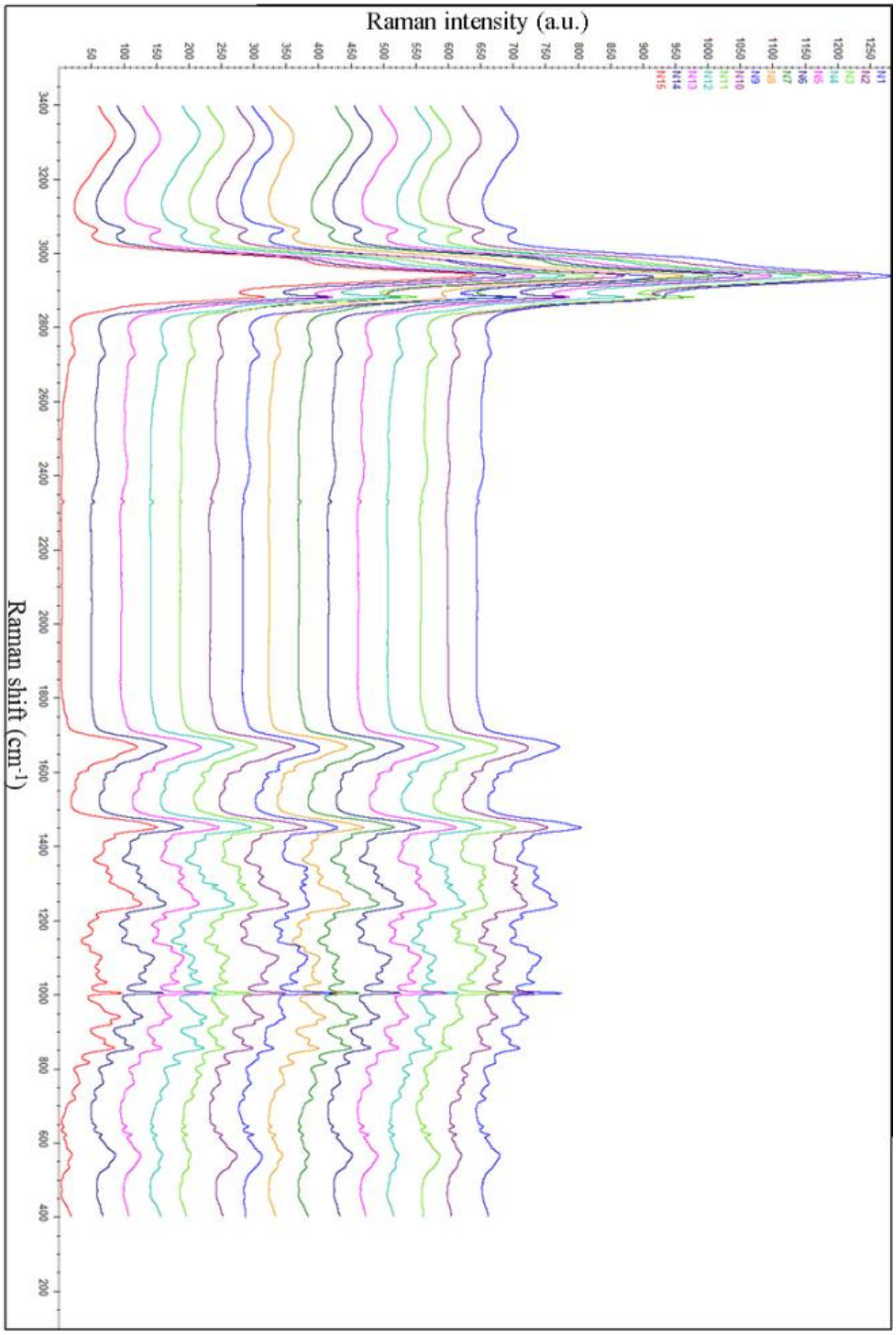

Figure 3. 28 Average spectra of 15 different normal oral mucosa samples

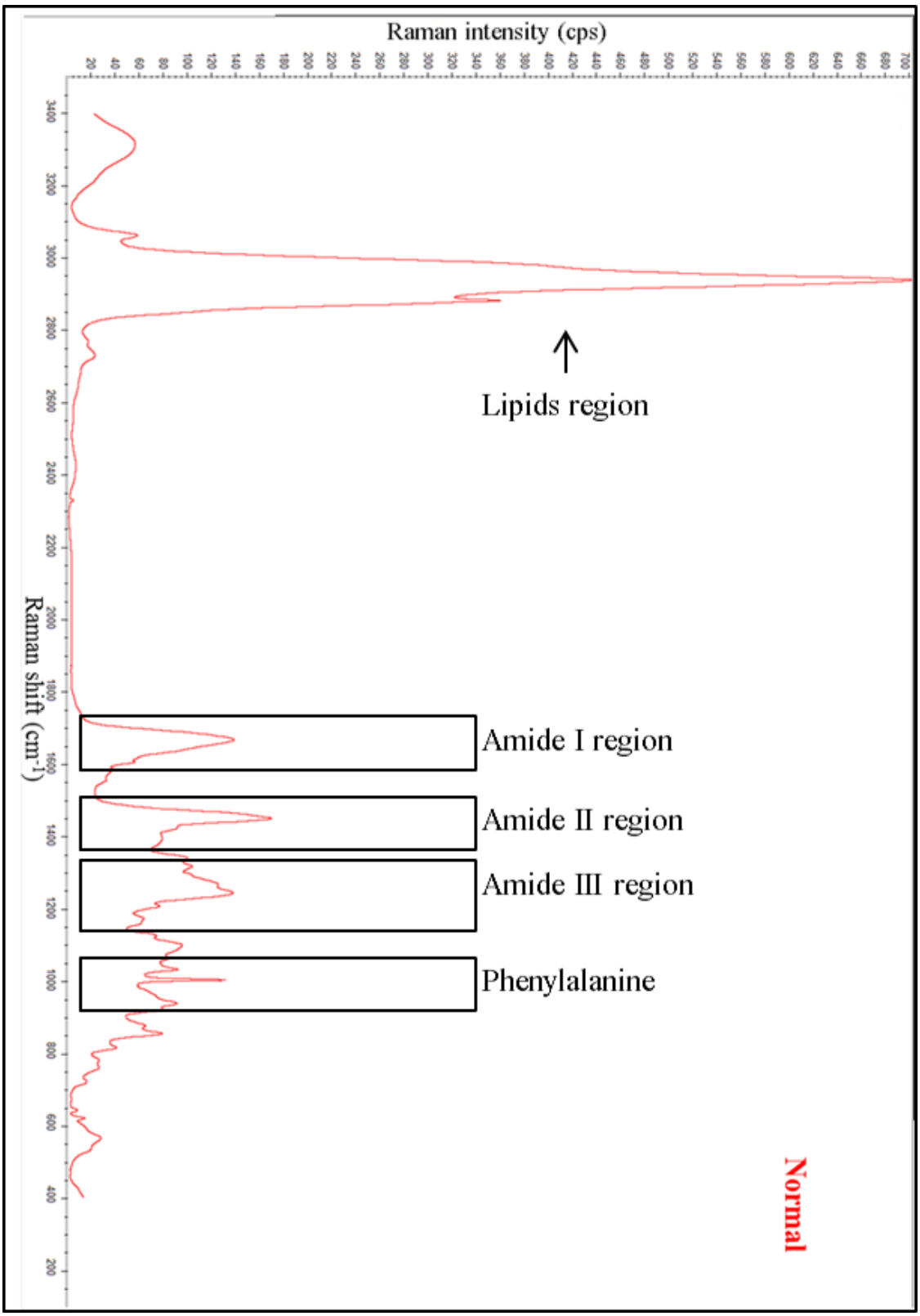

Figure 3. 29 Average spectrum of all normal oral mucosa samples

Tryptophan and 621 to 938 cm^{-1}region

Peaks present at 642 and 622 cm^{-1} are typical assignments of C-C twisting modes of phenylalanine and tyrosine in biological tissues respectively. Peak at 721 cm^{-1} can be

attributed to deoxyribonucleic acid (DNA). The spectral band centered at 780 cm^{-1} is attributed to uracil based ring breathing mode. Peaks present at 759, 874, 1266, and 1554cm^{-1} are specific assignments of tryptophan (C-C stretching). Peaks observed at 815, 855 cm^{-1} and 874 cm^{-1} can be attributed to υPO_2^- stretch of nucleic acid and proline, hydroxyproline, ring breathing of tyrosine, amino acid side chain vibration of proline and C-C hydroxyproline (protein assignments). C-C stretch of proline ring/glucose/lactic acid and C-C stretch backbone (protein α-helix conformation) can be assigned to 921 cm^{-1} and 938 cm^{-1} respectively.

1003 to 1667 cm^{-1} region

A sharp, intense and typical peak at 1003 cm^{-1} can be attributed to symmetric ring breathing mode of phenylalanine (C-C skeletal stretch). Phenylalanine is a protein assignment which was also observed at 1032 (phenylalanine of collagen) and 1607 cm^{-1} (shoulder) (C=C and ring vibration of phenylalanine). Minor peaks at 1063 and 1124 cm^{-1} can be assigned to C-C skeletal stretch in lipids. A broad peak at 1097 cm^{-1} can be attributed to Phosphodioxy groups in nucleic acids. Weak contributions at 1163, 1172 and 1206 cm^{-1} are attributed to C-H in-plane bending of tyrosine and hydroxyproline (collagen assignment).

1244 to 1266 cm^{-1} region

Bands present at 1244 and 1266 cm^{-1} are characteristic assignments of amide III (protein in α-helix conformation) in biological tissues, where strong spectral contributions were observed. Peaks originating at 1244 cm^{-1} can also be attributed to asymmetric phosphate stretching modes arising from phosphodiester groups of nucleic acids.

1317 to 1667 cm^{-1} region

Peaks arising at 1317 and 1341cm^{-1} can be attributed to ring breathing modes of nucleic acid (DNA/RNA) bases or C-H deformation in proteins. A shoulder was observed at 1425 cm^{-1}**,** which can be assigned to Deoxyribose (nucleic acid). A strong and sharp band was present at 1450 cm^{-1}, which can be attributed to CH_2 bending modes in proteins. Weak spectral contributions were noticed at 1554 and 1585 cm^{-1}**,** which are attributed to CH_2 stretching/CH_3 asymmetric deformation in protein bands and C=C Olefinic acid respectively. Intense and strong band originated at 1667 cm^{-1}, which is a specific protein assignment of α-helix structure of amide I.

2730 to 3061 cm^{-1} region

A weak band present at 2733 cm^{-1} can be assigned to C-H stretching vibrations in lipids. A shoulder was observed at 2882 cm^{-1} which can be attributed to CH_2 asymmetric stretch of lipids and proteins, whereas the strong band arising at 2939 cm^{-1} is assigned to C-H vibrations in lipids and proteins as well as CH_2 asymmetric stretch in lipids/fatty acids. CH stretching vibrations were present at band originating at 3061 cm^{-1}.

3.7.2 Dysplastic Oral Mucosa

A total of 300 spectra were collected from 15 dysplastic oral mucosa samples. Average spectra of these samples are shown in figure 3.30. Average spectrum of all the dysplastic samples is shown in figure 3.31 and peak assignments along with comparison and references are detailed in table 3.2.

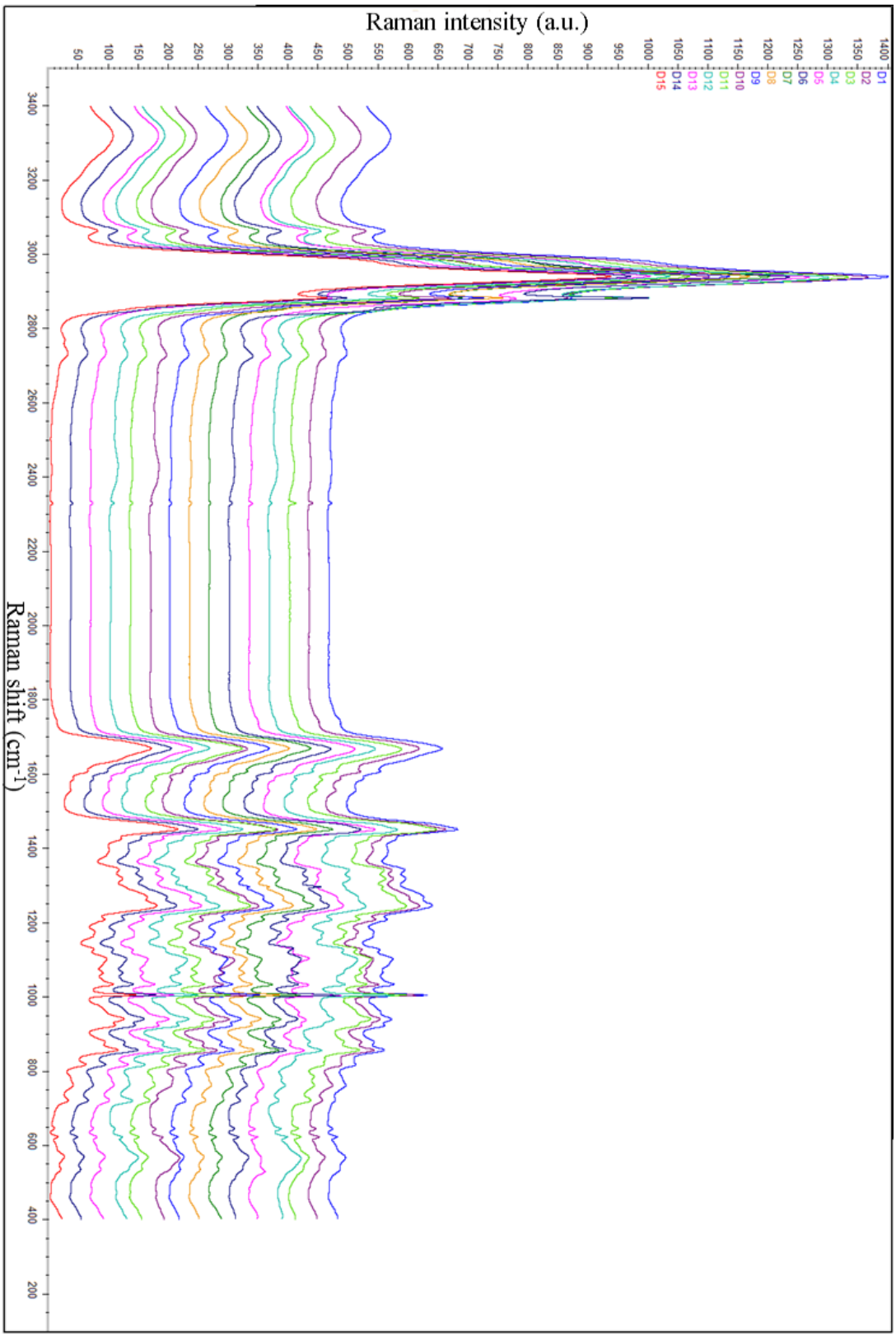

Figure 3. 30 Average spectra of 15 different dysplastic oral mucosa samples

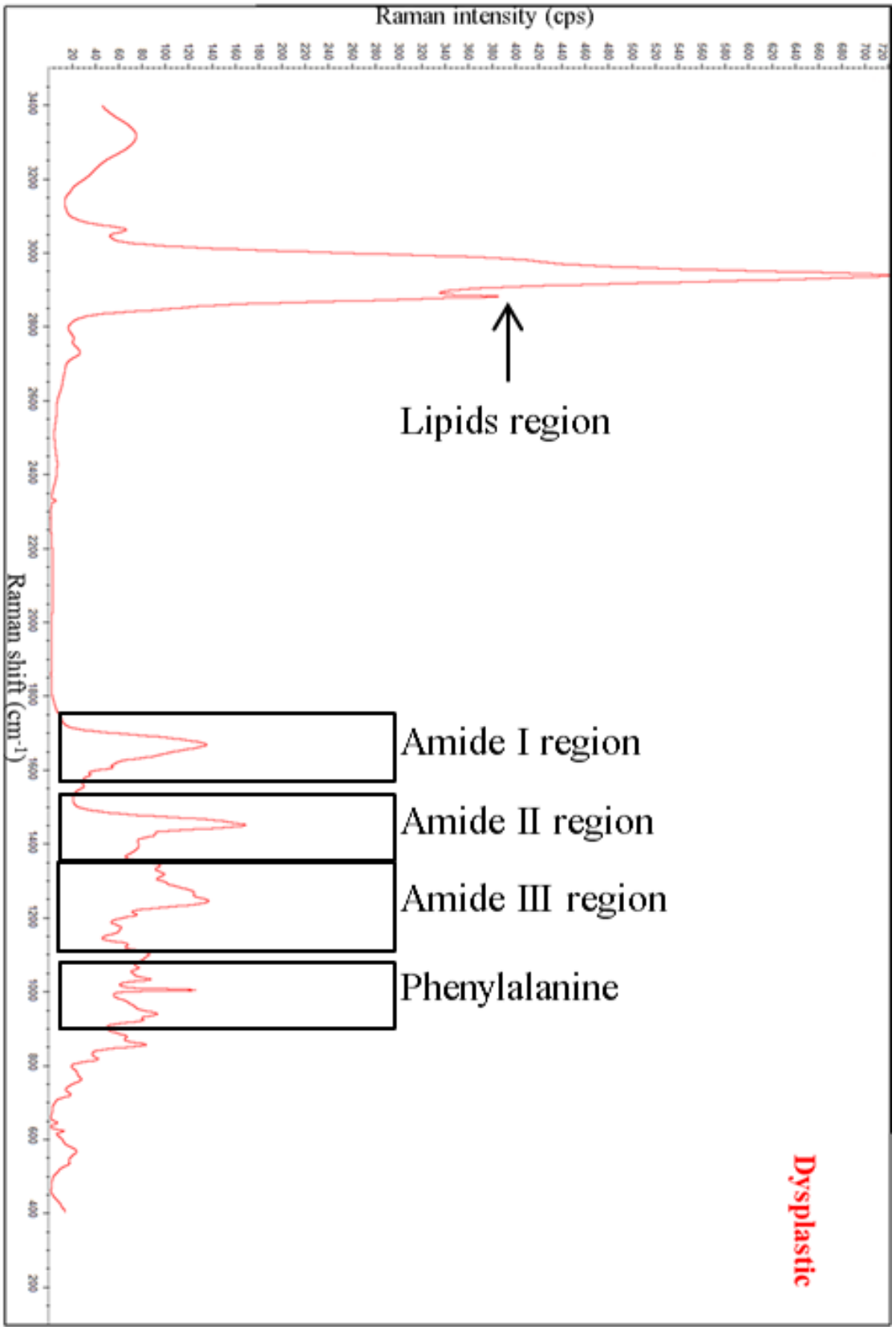

Figure 3. 31 Average spectrum of all dysplastic oral mucosa samples

Tryptophan and 621 to 935 cm^{-1} region

The bands present at 642 and 621 cm^{-1} can be assigned to C-C twisting modes of phenylalanine and tyrosine in dysplastic oral mucosa respectively. A weak band was observed 724 cm^{-1} and is attributed to deoxyribonucleic acid (DNA). Peaks present at 759, 1208, 1267, 1338 and 1558 cm^{-1} are specific assignments C-C stretching modes of tryptophan. The band observed at 817 cm^{-1} is a C-C stretching and is a collagen assignment. The peak appearing at 853 cm^{-1} can be attributed to proline, hydroxyproline, and ring breathing mode of tyrosine. A unique shoulder appeared at 875 cm^{-1} can be asymmetric stretch vibration of choline group N^+ $(CH_3)_3$ which is specific for phospholipids. A shoulder appeared at 921 cm^{-1}, which can be attributed to C-C stretch of proline ring/glucose/lactic acid. Band arising at 935 cm^{-1} is an assignment of C-C stretch backbone (α-helix conformation of protein).

1002 to 1208 cm^{-1} region

A sharp peak at 1002 cm^{-1} can be assigned to symmetric ring breathing mode of phenylalanine. A spectral band at 1031 cm^{-1} was present in all dysplastic models, which can be assigned to CH_3 and CH_2 bending modes of collagen and phospholipids, C-H in-plane bending mode of phenylalanine and C-H stretch of proteins. A very weak band was present at 1062 cm^{-1} that can be attributed to C-C skeletal stretch of lipids. At 1100 cm^{-1}, C-C vibrational mode of the gauche bonded chains was observed in dysplastic samples. A small peak at 1127 cm^{-1} can be assigned to C-C skeletal stretch in lipids. All dysplastic spectra showed a weak contribution at 1173 cm^{-1}, which can be associated with cytosine, guanine or tyrosine (collagen type I). Spectral band at 1208 cm^{-1} is also a protein assignment and may be attributed to phenylalanine.

1244 to 1267 cm^{-1} region

Spectral bands appearing in this region (1244 – 1267 cm^{-1}) are characteristic assignments of proteins in biological tissues, which can be attributed to Amide III (protein in α-helix conformation) and tryptophan. A peak appearing at 1244 cm^{-1} can also be recognised as asymmetric phosphate stretching modes originating from phosphodiester groups of nucleic acids.

1317 to 1667 cm^{-1} region

Peaks present at 1317 and 1338 cm^{-1} appeared in all dysplastic tissue spectra can be assigned to guanine ring breathing modes of DNA/RNA bases and C-H deformation of proteins and nucleic acid. A shoulder was present at 1424 cm^{-1}, which can be attributed to Deoxyribose, (B, Z markers). CH_2 bending in proteins is assigned to the band present at 1450 cm^{-1}. A peak present at 1583 cm^{-1} was attributed to C=C bending mode of phenylalanine (protein assignment). A spectral band at 1605 cm^{-1} can be an assignment of tyrosine, ring vibration of phenylalanine or C-C of phenylalanine. A spectral band at 1667 cm^{-1} is a characteristic assignment of proteins in α-helix structure of amide I.

2727 to 3061 cm^{-1} region

A weak spectral band at 2727 cm^{-1} was observed, which can be assigned to C-H stretching vibrations in lipids. A sharp peak present at 2881 cm^{-1} is attributed to CH_2 asymmetric stretch of lipids and proteins, whereas the strong band arising at 2937 cm^{-1} is attributed to chain end CH_3 asymmetric band of lipids. CH stretching vibrations were present at spectral band originating at 3061 cm^{-1}.

3.7.3 Cancerous Oral Mucosa

A total of 300 spectra were collected from 15 cancerous oral mucosa samples. Average spectra of these samples are shown in figure 3.32. Average spectrum of all the cancer samples is shown in figure 3.33 and peak assignments along with comparison and references are detailed in table 3.2.

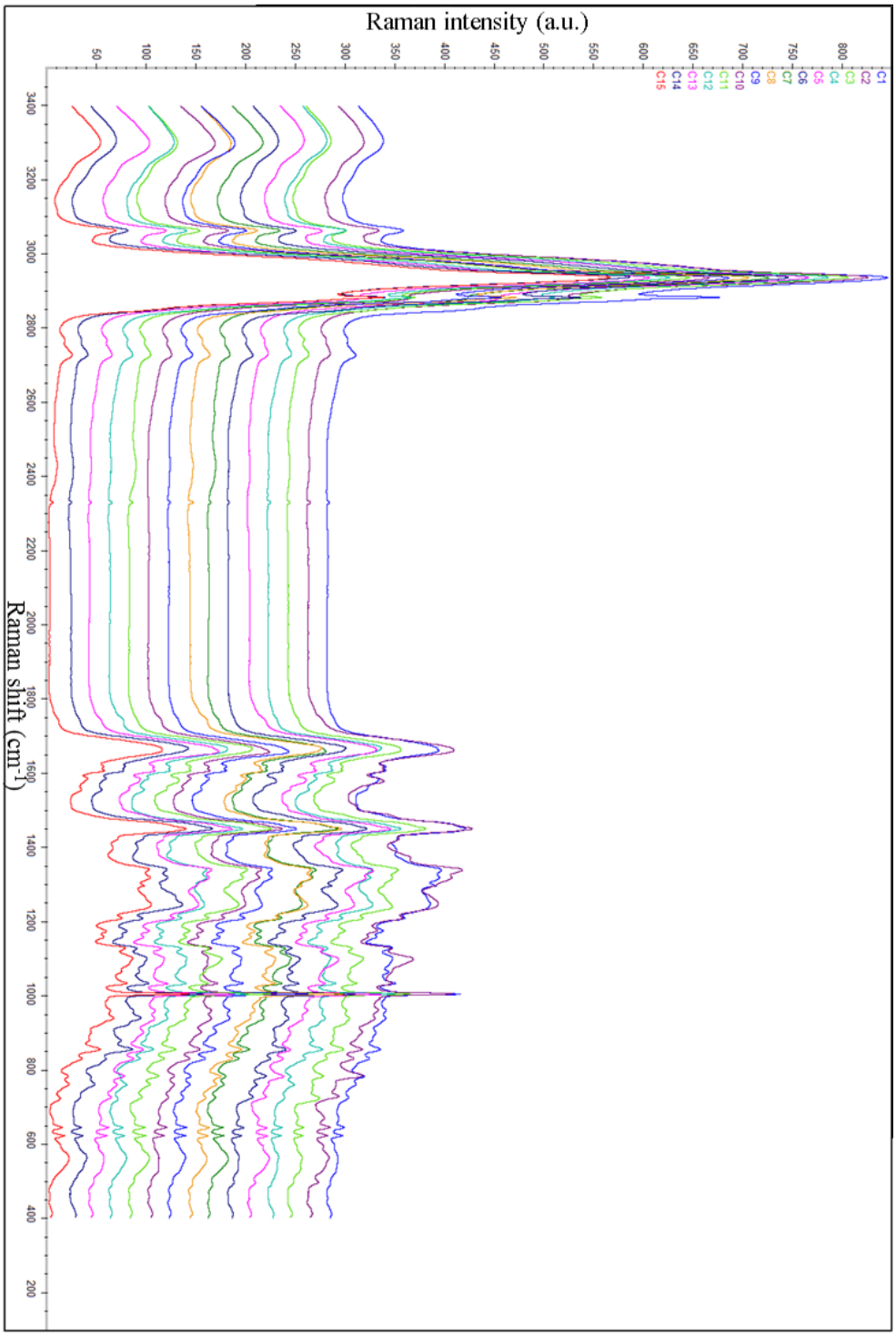

Figure 3. 32 Average spectra of 15 different cancerous oral mucosa samples

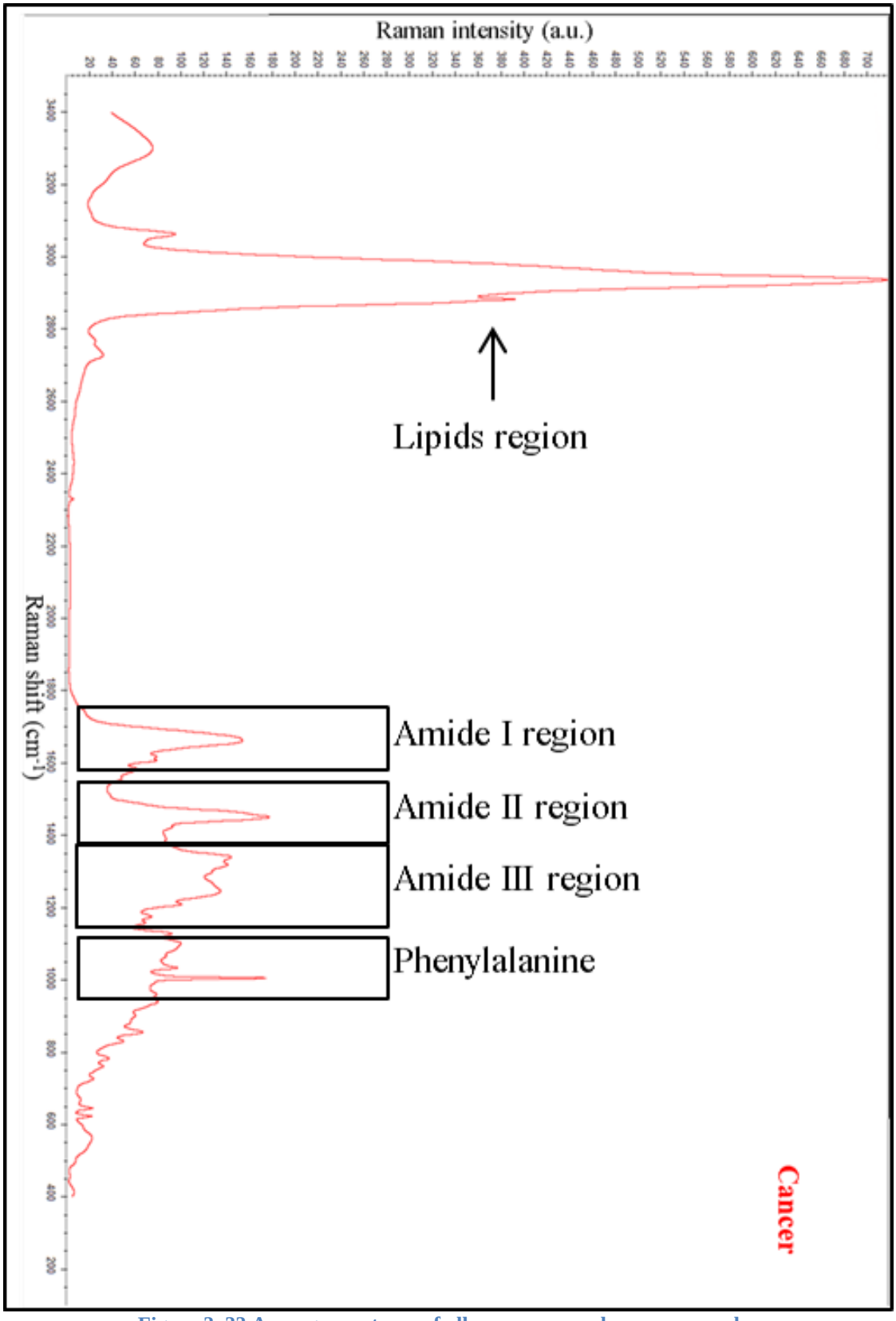

Figure 3. 33 Average spectrum of all cancerous oral mucosa samples

Tryptophan and 621 to 958 cm^{-1} region

Spectral bands present at 621 and 642 cm^{-1} can be assigned to C-C twisting modes of phenylalanine and tyrosine respectively. A weak band was observed in cancer tissues at 724 cm^{-1} and is attributed to ring breathing modes of DNA/RNA bases. Peaks present at 759, 1208, 1337, 1554 and 1615 cm^{-1} are specific assignments of C-C/C=C stretching modes of tryptophan. The band observed at 780 cm^{-1} is attributed to uracil based ring breathing mode in DNA/RNA. The Peak originating at 828 cm^{-1} can be assigned to ring breathing mode of tyrosine, Phosphodiesters and O-P-O stretching of DNA. Peak appearing at 853 cm^{-1} was attributed to proline, hydroxyproline, and ring breathing mode of tyrosine. The band present at 900 cm^{-1} can be assigned to C-O-C skeletal mode of monosaccharide (β-glucose). Bands arising at 935 cm^{-1} in all three models are assignment of C-C stretch backbone (α-helix conformation of protein). A weak and small peak at 958 cm^{-1} is attributed to carotenoids and cholesterol.

1002 to 1208 cm^{-1} region

A sharp band at 1002 cm^{-1} is a typical assignment of symmetric ring breathing mode of phenylalanine. Spectral band at 1031 cm^{-1} can be assigned to CH_3 and CH_2 bending modes of collagen and phospholipids, C-H in-plane bending mode of phenylalanine and C-H stretch of proteins. A short and weak band was present at 1062 cm^{-1}, which can be attributed to C-C skeletal stretch of lipids. C-C vibration mode of the gauche bonded chains was observed at 1100 cm^{-1}. A small peak at 1127 cm^{-1} can be an assignment of C-C skeletal stretch in lipids. A weak and small spectral band at 1157 cm^{-1} is attributed to carotenoids, appearing in spectra of all cancer tissues. Weak spectral contribution at 1173 cm^{-1} can be associated with cytosine, guanine or tyrosine (collagen type I). The band appearing at 1208 cm^{-1} is a protein assignment and attributed to phenylalanine.

1244 to 1266 cm^{-1} region

Spectral bands appearing in this region can be attributed to Amide III (protein in α-helix conformation) and tryptophan. The peak at 1244 cm^{-1} can also be recognised as asymmetric phosphate stretching modes originating from phosphodiester groups of nucleic acids.

1317 to 1615 cm^{-1} region

Peaks present at 1317 and 1337 cm^{-1} can be assigned to guanine ring breathing modes of DNA/RNA bases, C-H deformation of proteins and nucleic acid modes. CH_2 bending in proteins is assigned to the band present at 1448 cm^{-1}. A band present at 1583 cm^{-1} was attributed to C=C bending mode of phenylalanine (protein assignment). Spectral band at 1605 cm^{-1} is an assignment of tyrosine, ring vibration of phenylalanine or C-C of phenylalanine, whereas 1615 cm^{-1} can be attributed to C=C of tyrosine or tryptophan (proteins assignment).

1570 to 1670 cm^{-1} region

A broad and strong spectral band present at 1660 cm^{-1} is a characteristic assignment of proteins in α-helix structure of amide I. Spectral band shift was significantly noticed in the amide I region between normal, dysplastic and cancer tissues.

2726 to 3061 cm^{-1} region

A weak and broad spectral band centred at 2726 cm^{-1} was observed, which can be assigned to C-H stretching vibrations in lipids. Peaks present at 2881 cm^{-1} are attributed to CH_2 asymmetric stretch of lipids and proteins, whereas the strong band arising at 2935 cm^{-1} is assigned to C-H vibrations in lipids and proteins as well as CH_2 asymmetric stretch in lipids/fatty acids. CH stretching vibrations were present at peaks originating at 3061 cm^{-1} in all cancer tissue spectra.

Peak assignments and references of normal, dysplastic and cancer data set are presented in table 3.2.

Table 3.2 Details of peak assignments, comparison and references of normal, dysplastic and cancerous oral mucosa (patient biopsies)

Peak Number (cm^{-1})	Assignment	Normal	Dysplastic	Cancer	References
621	C-C twisting mode of phenylalanine (protein assignment)	✓	✓	✓	(Stone et al., 2002b) (Stone et al., 2004) (Notingher et al., 2004b)
642	C-C twisting mode of tyrosine	✓	✓		(Stone et al., 2004, Cheng et al., 2005)
643	C-C twisting mode of tyrosine			✓	(Stone et al., 2004, Cheng et al., 2005)
721	DNA	✓			(Binoy et al., 2004) (James W. Chan et al., 2006) (IU. Rehman et al., 2012)
724	Ring breathing modes of DNA/RNA bases		✓	✓	(Binoy et al., 2004) (James W. Chan et al., 2006) (IU. Rehman et al., 2012)
759	Tryptophan	✓	✓	✓	(Stone et al., 2004) (Krafft et al., 2005)
780	Uracil based ring breathing mode	✓		✓	(Farquharson et al., 2005)

815	Proline, hydroxyproline, tyrosine, υ PO_2^- stretch of nucleic acid	✓			(Cheng et al., 2005)
817	C-C stretching (collagen assignment)		✓		(Frank et al., 1995)
828	Ring breathing mode of tyrosine Phosphodiesters Tyrosine/O-P-O stretch DNA			✓	(Notingher et al., 2004a) (Ruiz-Chica et al., 2004) (Stone et al., 2002b)
853	Proline, hydroxyproline, tyrosine, tyrosine ring breathing mode Glycogen		✓	✓	(Cheng et al., 2005) (James W. Chan et al., 2006) (Binoy et al., 2004)
855	Proline, tyrosine, υ(C-C) proline + δ(CCH) ring breathing, tyrosine (protein assignment) Amino acid side chain vibration of proline and hydroxyl proline	✓			(Stone et al., 2002b) (Huang et al., 2003a) (Cheng et al., 2005)
874	Hydroxyproline (C-C), tryptophan C-C stretching	✓			(Frank et al., 1995) (Gniadecka et al., 1997) (Krishna et al., 2004)
875	Asymmetric stretch vibration of choline group $N^+(CH_3)_3$ characteristic for phospholipids		✓		(Krafft et al., 2005)
900	Monosaccharide (β-glucose) (C-O-C) skeletal mode			✓	(Shetty G, 2006)
921	C-C stretch of proline ring/glucose/lactic acid	✓	✓		(Stone et al., 2002b) (Kendall et al., 2003) (Stone et al., 2004)

					(Kendall et al., 2011)
935	C-C stretch backbone (protein α-helix conformation) (protein assignment)		✓	✓	(Huang et al., 2003a) (Stone et al., 2002b)
938	C-C stretch backbone (protein α-helix conformation)	✓			(Stone et al., 2004) (Cheng et al., 2005)
958	Carotenoids, cholesterol			✓	(Stone et al., 2004)
1002	Symmetric ring breathing mode of phenylalanine, C-C skeletal stretch		✓	✓	(Puppels et al., 1991) (Mahadevan-Jansen and Richards-Kortum, 1996) (Stone et al., 2004) (Krishna et al., 2004) (Seballos et al., 2005) (Malini et al., 2006) (Jess et al., 2006) (James W. Chan et al., 2006) (Zhang et al., 2008)
1003	Symmetric ring breathing mode of phenylalanine, C-C skeletal stretch	✓			(Puppels et al., 1991) (Mahadevan-Jansen and Richards-Kortum, 1996) (Stone et al., 2004) (Krishna et al., 2004)

					(Seballos et al., 2005) (Malini et al., 2006) (Jess et al., 2006) (James W. Chan et al., 2006) (Zhang et al., 2008)
1031	CH_3 CH_2 bending modes of collagen and phospholipids, phenylalanine of collagen, proline (collagen assignment) C-H in-plane bending mode of phenylalanine C-H stretching of proteins		✓	✓	(Frank et al., 1995) (Huang et al., 2003a) (Cheng et al., 2005) (Stone et al., 2002b) (James W. Chan et al., 2006)
1032	CH_3 CH_2 bending modes of collagen and phospholipids, phenylalanine of collagen, proline (collagen assignment)	✓			(Frank et al., 1995) (Huang et al., 2003a) (Cheng et al., 2005)
1062-3	C-C skeletal stretch lipids	✓	✓	✓	(Faoláin et al., 2005)
1097	Phosphodioxy groups in nucleic acids	✓			(Krafft et al., 2005)
1100	C-C vibration mode of the gauche-bonded chain		✓	✓	(Huang et al., 2005) (Cheng et al., 2005)
1124	υ (C-C) skeletal of acyl backbone in lipids	✓			(Cheng et al., 2005)

1127	υ (C-C) skeletal of acyl backbone in lipids		✓	✓	(Cheng et al., 2005)
1157	Carotenoids C-C, C-N stretching (protein)			✓	(Mahadevan-Jansen and Richards-Kortum, 1996) (James W. Chan et al., 2006)
1163	C-C skeletal stretch lipids	✓			(Stone et al., 2004)
1173	Cytosine, guanine Tyrosine (collagen type I)		✓	✓	(Ruiz-Chica et al., 2004) (Cheng et al., 2005)
1206	Hydroxyproline, tyrosine (collagen assignment)	✓			(Frank et al., 1995) (Stone et al., 2004)
1208	Tryptophan, phenylalanine (protein assignment)		✓	✓	(Cheng et al., 2005) (IU. Rehman et al., 2012)
1244	Amide III, asymmetric phosphate stretching modes originating from phosphodiester groups of nucleic acids	✓	✓	✓	(Lakshmi et al., 2002) (Cheng et al., 2005) (Shetty G, 2006) (Dukor, 2006) (Movasaghi et al., 2007)
1266-7	Amide III (protein in α-helix conformation) Tryptophan (protein assignment)	✓	✓		(Huang et al., 2003a) (Lakshmi et al., 2002) (Cheng et al., 2005)
1317	Guanine ring breathing modes of DNA/RNA bases, C-H deformation (protein)	✓	✓	✓	(Ruiz-Chica et al., 2004) (Movasaghi et al., 2007)

1337-8	Polynucleotide chain (DNA purine bases)(protein assignment) Nucleic acid mode which indicate amount of content in tissue Tryptophan		✓	✓	(Stone et al., 2004) (Mahadevan-Jansen and Richards-Kortum, 1996) (Notingher et al., 2004a) (Dukor, 2006) (Cheng et al., 2005)
1341	Nucleic acid mode which indicate amount of content in tissue G (DNA/RNA)	✓			(Mahadevan-Jansen and Richards-Kortum, 1996) (Notingher et al., 2004a) (Dukor, 2006)
1424-5	Deoxyribose (B,Z markers)	✓	✓		(Ruiz-Chica et al., 2004)
1448	CH_2 CH_3 bending mode in malignant tissues CH_2 bending (proteins) Amide II			✓	(Shafer-Peltier et al., 2002) (Yi-Yong et al., 2003) (Cheng et al., 2005) (Malini et al., 2006)
1450	CH_2 bending (proteins) Amide II	✓	✓		
1554-8	Tryptophan (protein assignment)	✓	✓	✓	(Cheng et al., 2005)

1583	C=C bending mode of Phenylalanine Tryptophan	✓	✓	✓	(Lau et al., 2003) (Huang et al., 2003a)
1585	C=C Olefinic stretch C=C Olefinic stretch (protein assignment)	✓			(Faoláin et al., 2005) (IU. Rehman et al., 2012)
1605	Tyrosine, phenylalanine ring vibration (proteins) Ring C-C stretch of phenylalanine		✓	✓	(James W. Chan et al., 2006)
1607	Tyrosine, phenylalanine ring vibration C=C phenylalanine, tyrosine Cytosine	✓			(Lakshmi et al., 2002) (Notingher et al., 2004a)
1615	Tyrosine, tryptophan, C=C (protein)	✓	✓	✓	(James W. Chan et al., 2006)
1660	Protein band C=C stretching band α- helix structure of amide I Structural protein mode of tumours			✓	(Hanlon EB, 2000, Dukor, 2006) (Mahadevan-Jansen and Richards-Kortum, 1996) (Huang et al., 2003a)
1667	Protein band α-helix structure of amide I C=O carbonyl stretch	✓	✓		(Dukor, 2006, Hanlon EB, 2000) (Huang et al., 2003a, Mahadevan-Jansen and Richards-Kortum, 1996) (Farquharson et al., 2005)

2726-30	C-H stretches	✓	✓	✓	(Krafft et al., 2005)
2881-2	CH_2 asymmetric stretch of lipids and proteins	✓	✓	✓	(Koljenović et al., 2005) (IU. Rehman et al., 2012)
2935-7	C-H vibrations in lipids and proteins $\upsilon_{as} CH_2$, lipids and fatty acids		✓	✓	(Rehman et al., 2007) (Shetty G, 2006)
2939	C-H vibrations in lipids and proteins $\upsilon_{as} CH_2$, lipids and fatty acids	✓			(Rehman et al., 2007) (Shetty G, 2006)
3061	CH stretching	✓	✓	✓	(Movasaghi et al., 2012)

3.7.4 Peak Height Analysis

Peak height analysis was performed to compare various peak intensities of normal, dysplastic and cancer tissues. Important contributions from phenylalanine, tryptophan, amide I, amide II and nucleic acid were analysed which demonstrated increase in peak intensities as the tissue changes its state from normal to dysplasia and cancer (figure 3.34).

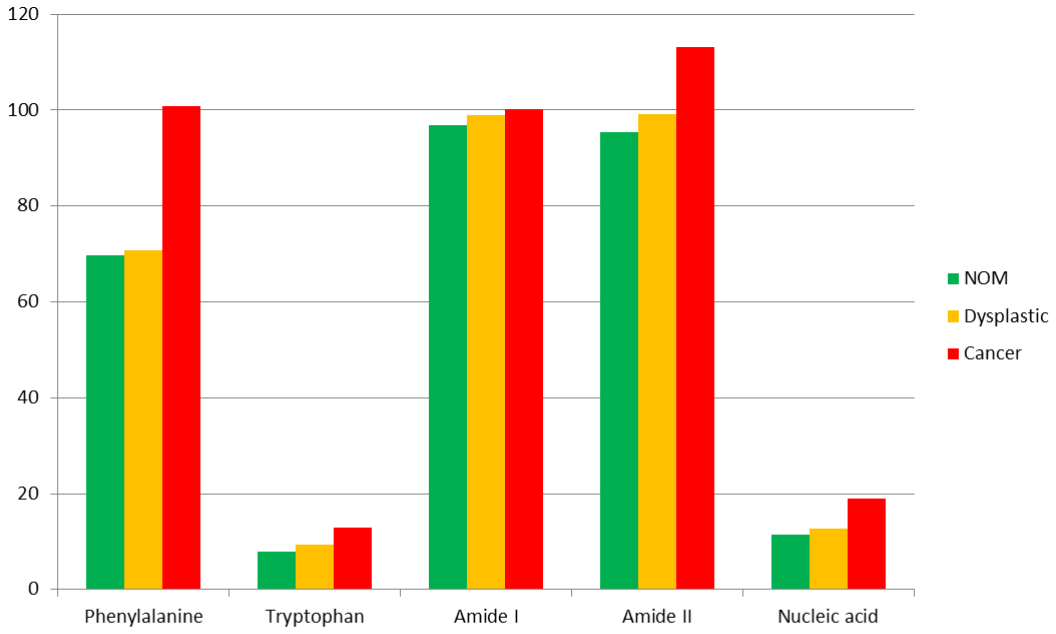

	1003 cm^{-1} Phenylalanine	1208 cm^{-1} Tryptophan	Amide I	Amide II	1338-41 cm^{-1} Nucleic acid
NOM	69.77	7.94	96.77	95.43	11.39
Dysplastic	70.75	9.41	98.99	99.12	12.77
Cancer	100.82	12.95	100.26	113.23	19.04

Figure 3. 34 Peak Height Analysis of major proteins and nucleic acid bands (patient biopsies) in the finger print region of average Raman spectra

3.7.5 Multivariate Data Analysis

Principal Component Analysis

PCA was performed over complete spectral range (400 to 3400 cm^{-1}), 2700 to 3100 cm^{-1} (Lipids/proteins), 1550 to 1750 cm^{-1} (amide I), 1200 to 1400 cm^{-1} (amide III) and 800 to 1200 cm^{-1} (DNA/Proteins) region. The comparison was conducted between normal, dysplastic and cancerous patient biopsies.

Complete Spectral Range (400 to 3400 cm^{-1})

PCA results of normal and cancerous oral mucosa over the complete spectral range showed 89% of variance with clear separation between the two tissue types. PC1 separated most of the normal tissue from cancers where the rest were discriminated by the second component (figure 3.35a & b). Analysis of dysplastic and cancer tissues showed an overall variance of 79% over complete spectral range, where two distinct clusters separated the two tissue types. The first component was able to distinguish most of the dysplastics from cancers (figure 3.35c & d). PCA between all three tissue types resulted in an overall variance of 87% amongst them, where cancer tissue was distinguished from normal and dysplastic (figure 3.35e & f).

Lipids/Proteins (2700 to 3100 cm^{-1})

PCA results between normal and cancer over 2700 to 3100 cm^{-1} spectral range showed 90% of variance, as clear separation between the two was observed. PC1 separated most of the normal tissue from the cancers, whereas the rest were differentiated by the second component (figure 3.36a & b). Dysplastic and cancer tissues showed an overall variance of 83%, where two distinct clusters separated them. The first component was able to distinguish most of the dysplastics from cancers (figure 3.36c & d). PCA between all three tissue types resulted in an overall variance of 88% amongst them, where PC1 showed highest variance between normal and cancer as well as dysplastic and cancer. The rest of the normal and dysplastics were distinguished from cancers in the second component (figure 3.36e & f).

Amide I (1550 to 1750 cm^{-1})

A higher variance percentage was recorded in this region where PCA results between normal and cancer showed 93% of variance with distinct separation between the two tissue types. PC1 separated most of the normal tissues from the cancerous tissue and

lesser variability was observed within normal tissue as the cluster appeared more compact (figure 3.37a & b). Analysis of dysplastic and cancer tissues showed an overall variance of 93%, where two distinct clusters separated the two tissue types. The first component was able to distinguish most of the dysplastics from cancers (figure 3.37c & d). PCA of all three tissue types showed an overall variance of 94% where PC1 showed maximum variance between normal and cancer as well as dysplastic and cancer. PC2 differentiated between the remaining normal and dysplastics from cancers (figure 3.37e & f). Less separation was observed between normal and dysplastic tissues.

Amide III (1200 to 1400 cm^{-1})

Maximum amount of variance (99%) was recorded in the Amide III (1200 to 1400 cm^{-1}) region. PCA results between normal and cancer showed 98% of variance with clear separation between the two tissue types. Two distinct clusters were formed, separating both the tissue types where PC1 and PC2 resulted in 73% and 25% variance respectively (figure 3.38a & b). Dysplastic and cancer tissues showed an overall variance of 98%. The first component was able to distinguish most of the dysplastics from cancers (figure 3.38c & d). PCA of all three tissue types showed an overall variance of 99% where PC1 showed 75%, variance between normal and cancer as well as dysplastic and cancer. PC2 differentiated between the remaining normal and dysplastics from cancers with 24% variance (figure 3.38e & f).

DNA/Proteins (800 to 1200 cm^{-1})

The amount of variance recorded in this region, between all three tissue types was between 84-86%. PCA results between normal and cancer showed 84% of variance with distinct separation between the two tissue types (figure 3.39a & b). Dysplastic and cancer tissues showed an overall variance of 84% where the first component distinguished most of the dysplastics from cancers (figure 3.39c & d). PCA of all three

tissue types showed an overall variance of 86% where PC1 showed 46% and PC2 resulted in 40% of variance amongst them (figure 3.39e & f).

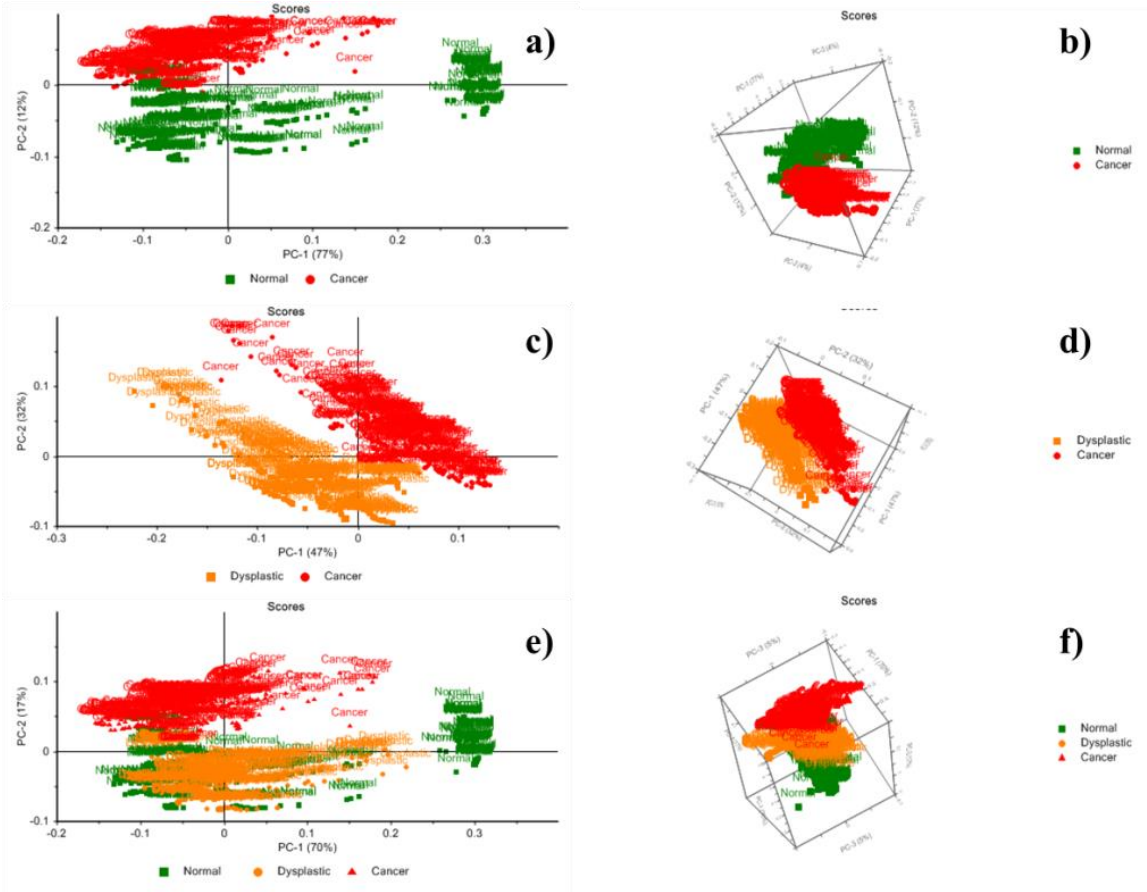

Figure 3. 35 PCA results over complete spectral range, (a, c and e) showing PC1 and PC2 of normal, dysplastic and cancer, (b, d and f) showing respective 3D plots.

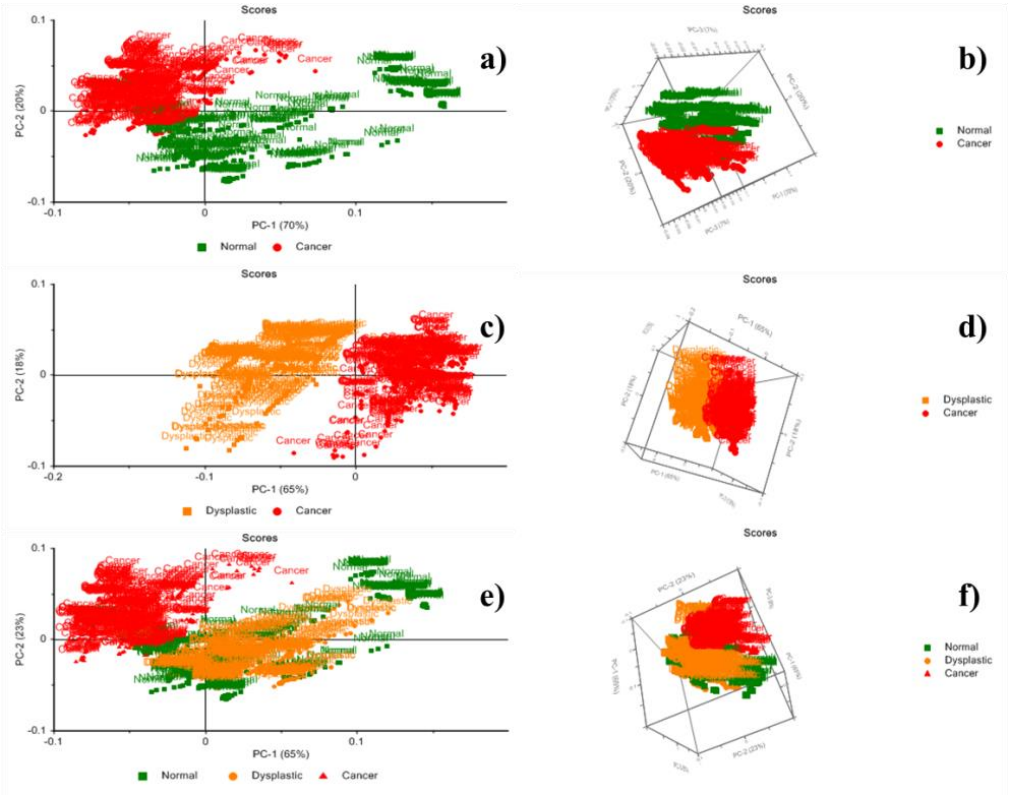

Figure 3. 36 PCA results over 2700 to 3100 cm-1 region, (a, c and e) showing PC1 and PC2 of normal, dysplastic and cancer, (b, d and f) showing respective 3D plots.

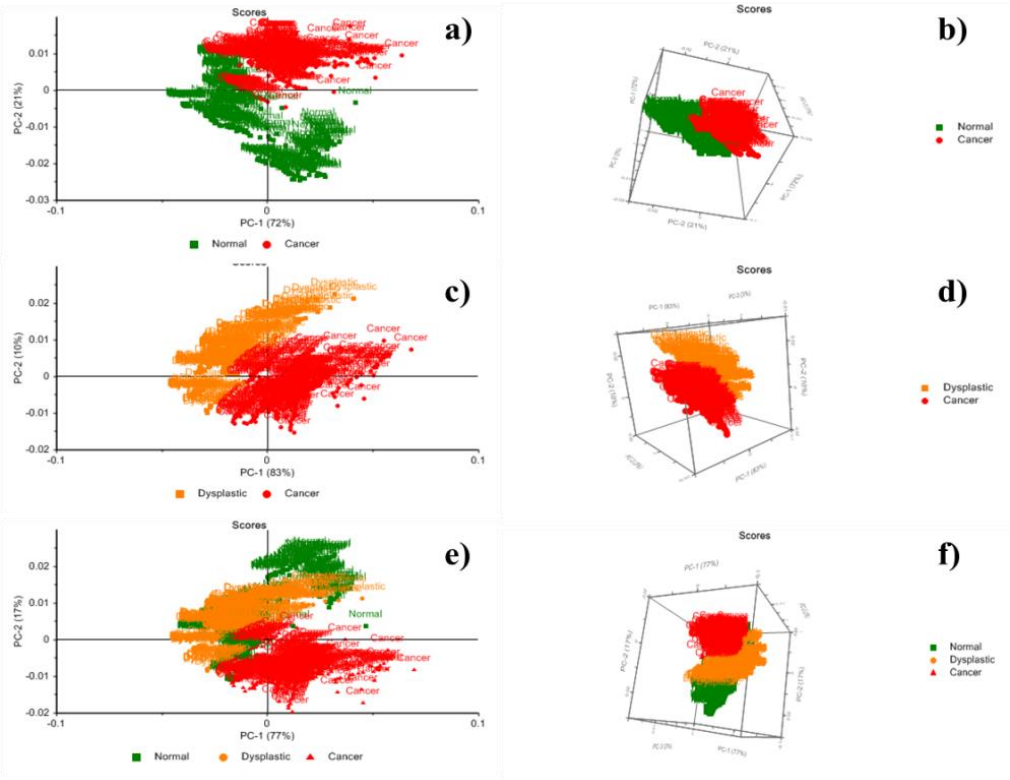

Figure 3. 37 PCA results over 1550 to 1750 cm-1 (amide I) region, (a, c and e) showing PC1 and PC2 of normal, dysplastic and cancer, (b, d and f) showing respective 3D plots.

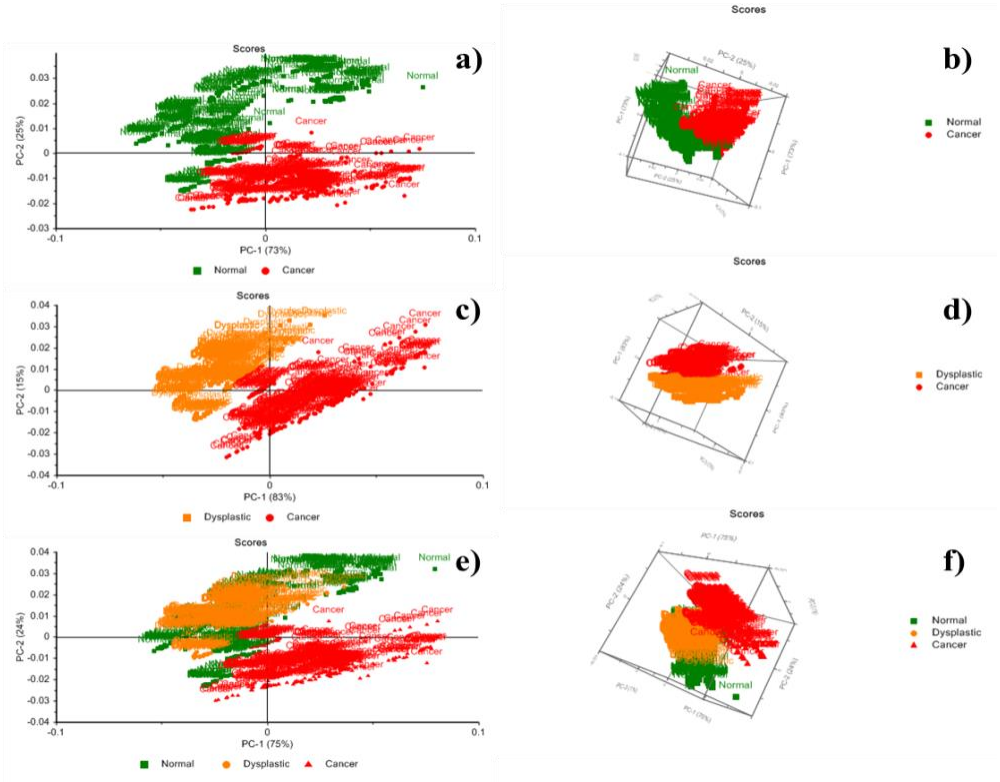

Figure 3. 38 PCA results over 1200 to 1400 cm-1 (amide III) region, (a, c and e) showing PC1 and PC2 of normal, dysplastic and cancer, (b, d and f) showing respective 3D plots.

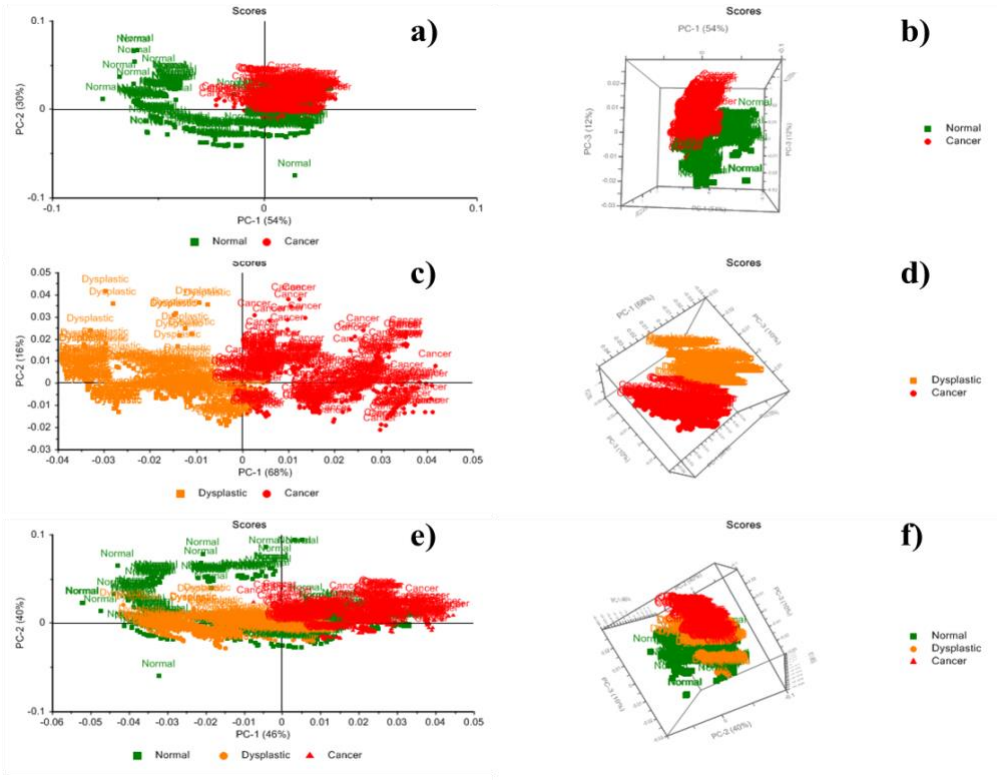

Figure 3. 39 PCA results over 800 to 1200 cm-1 (DNA/Proteins) Region, (a, c and e) showing PC1 and PC2 of normal, dysplastic and cancer, (b, d and f) showing respective 3D plots.

Cluster Analysis

Normal-Cancer

Figure 3.40 shows a dendogram of normal and cancer patient biopsies over the complete spectral range. Two main clusters are formed; one exclusively contains normal tissues whereas the second cluster primarily possesses cancer tissues with two normal outliers. Overall a clear separation of normal from cancer is observed.

Cancer-Dysplastic

Figure 3.41 shows a dendogram of dysplastic and cancer tissues. They have shown similar classification as normal to cancer. In this case again two distinct clusters are formed where one exclusively contains dysplastic and the second contains cancers with a few dysplastics invading them.

Normal-Dysplastic-Cancer

Figure 3.42 shows a dendogram of normal, dysplastic and cancer tissues. Two main clusters are formed where normal and dysplastics are grouped together in one cluster and the second cluster mainly contains cancer tissue. Clear separation of cancer from normal and dysplastic tissues is observed.

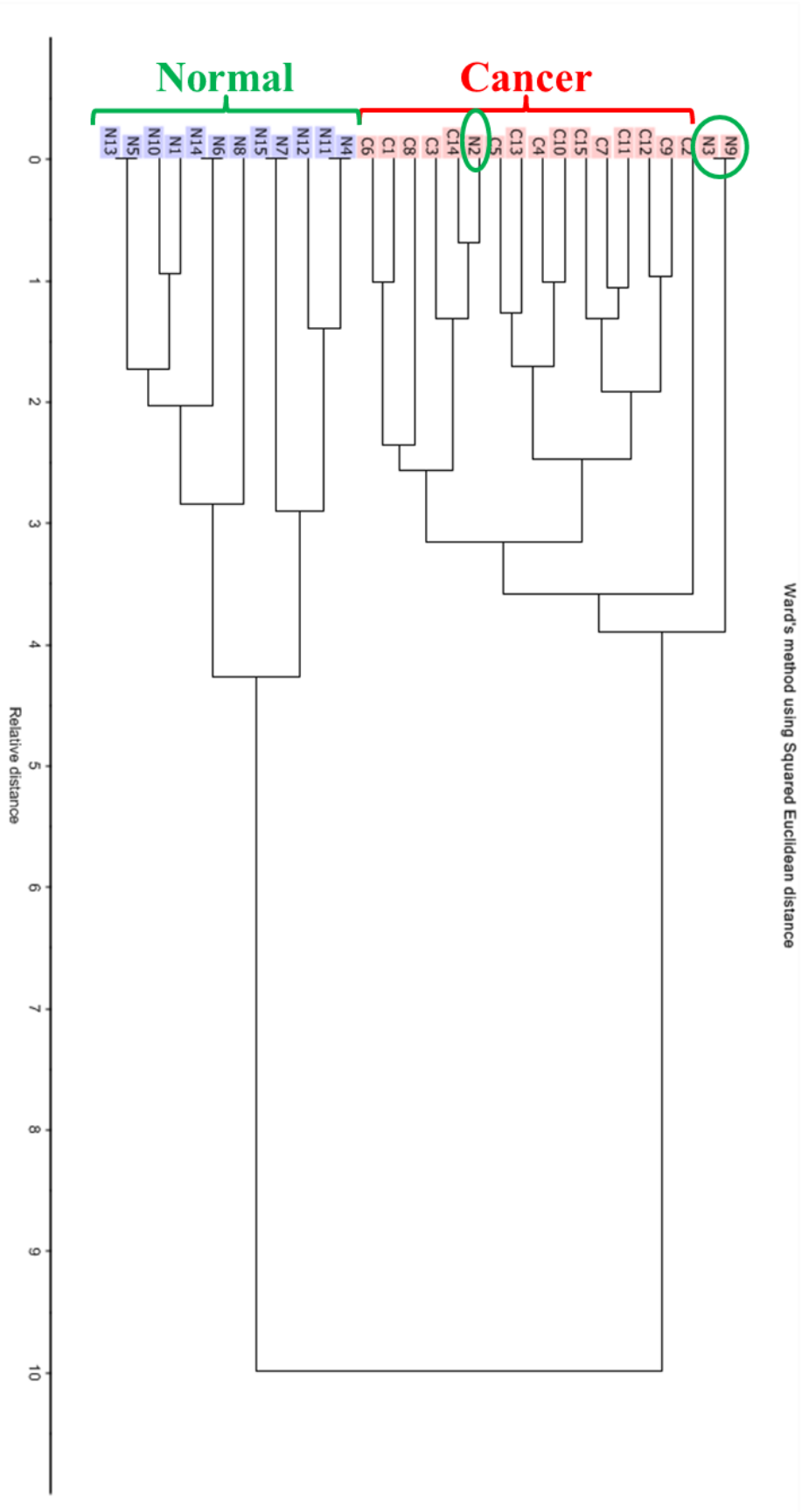

Figure 3. 40 Dendogram showing classification between normal and cancer tissues over complete spectral range.

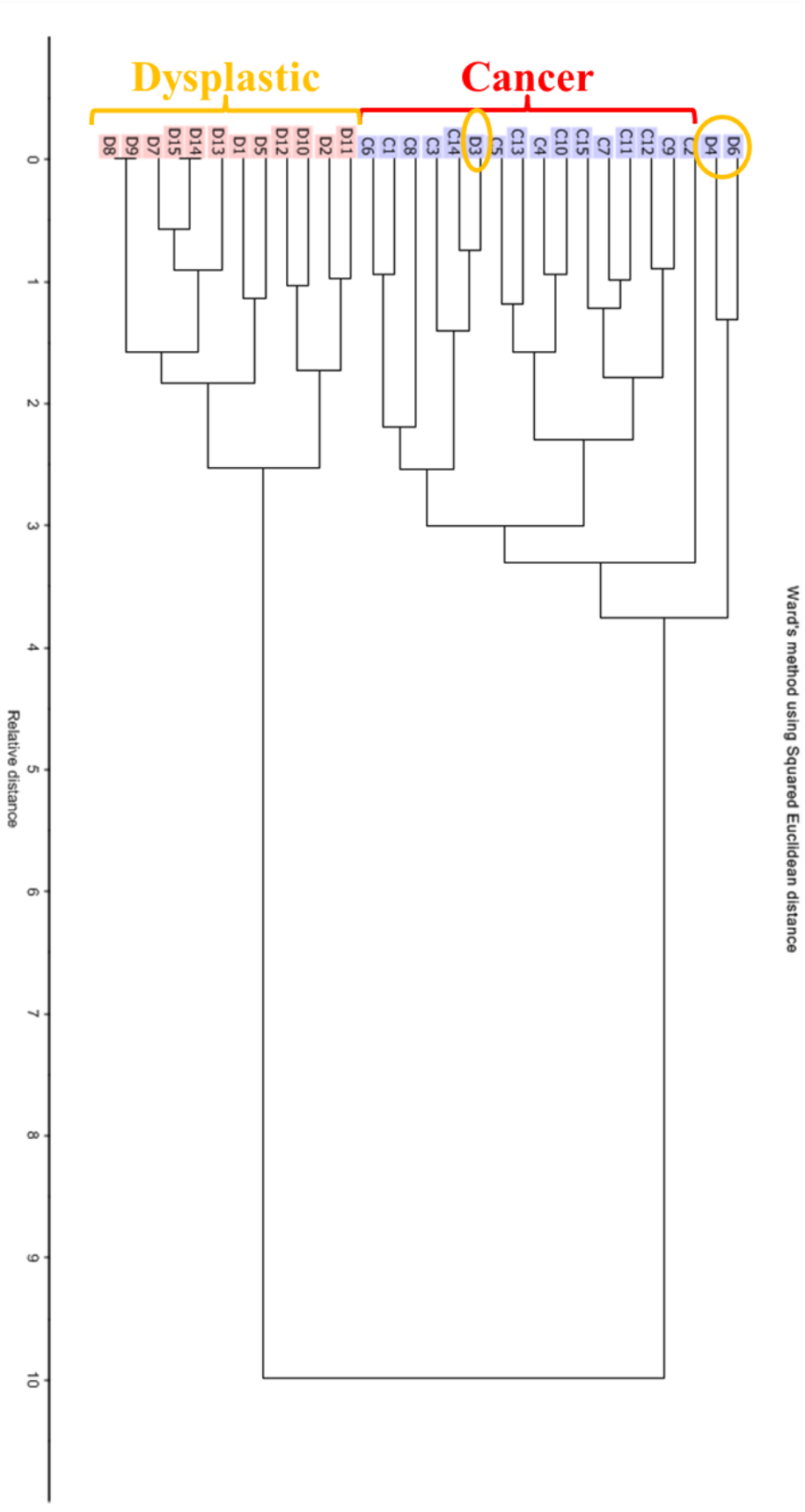

Figure 3. 41 Dendogram showing classification between dysplastic and cancer tissues over complete spectral range.

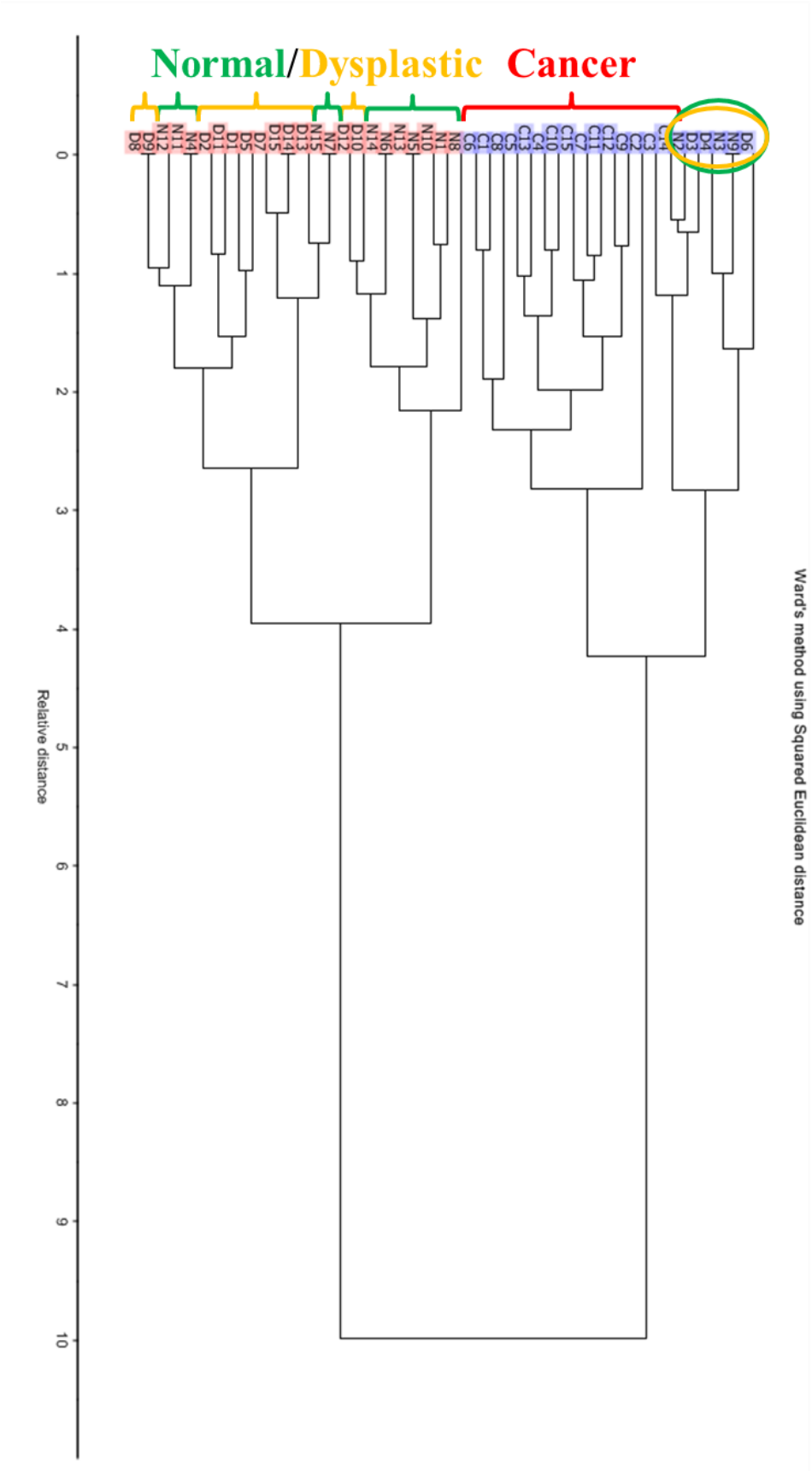

Figure 3. 42 Dendogram showing classification between normal dysplastic and cancer tissues over complete spectral range.

Linear Discriminant Analysis (LDA)

We used prior histopathological knowledge of 45 cases including normal, dysplasia and cancer from tongue and evaluated the potential of RS with tissue classification. LDA was employed over processed Raman spectra of all three tissue types. Randomly picked 150 spectra out of 300 from each tissue type were used for LDA, 100 spectra were classified as training data set and the remaining 50 were utilised as test sets.

LDA was performed over the complete spectral range to classify normal, dysplastic and cancerous tissues. LDA models were constructed and predicted in three different ways such as 1) normal against cancer, 2) dysplasia against cancer and 3) between normal, dysplasia and cancer.

Normal vs. Cancer

149 out of 150 normal oral mucosa samples were classified as normal and only 1 sample was misclassified as cancer with a specificity of 99% whereas sensitivity of 97.3% was achieved for cancer samples as shown in Figure 3.43a.

Dysplastic vs. Cancer

121 out of 150 samples of oral dysplasia were correctly grouped as dysplasia with a sensitivity of 80% whereas 92% sensitivity was recorded for cancer models as described in Figure 3.43b.

Normal vs. Dysplastic vs. Cancer

When all three LDA models were predicted together, normal mucosa samples achieved a specificity of 68% whereas 48% and 99% sensitivity was recorded for dysplasia and cancer respectively Figure 3.43c.

a)

	Actual	Normal	Cancer
Predicted			
Normal		149	4
Cancer		1	146
		150	150

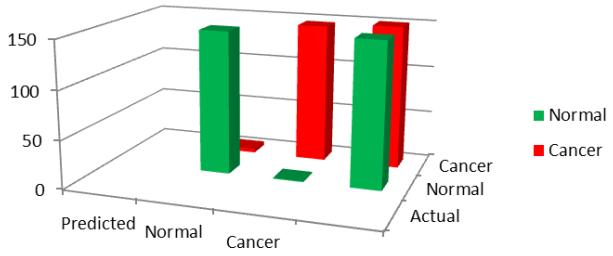

b)

	Actual	Dysplasia	Cancer
Predicted			
Dysplasia		121	12
Cancer		29	138
		150	150

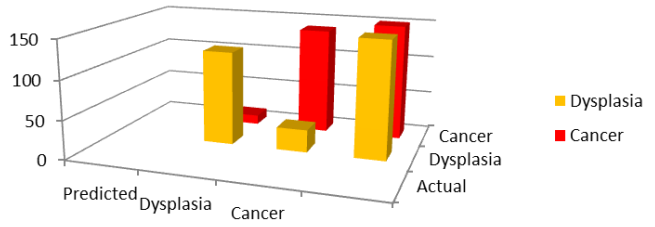

c)

	Actual	Normal	Dysplasia	Cancer
Predicted				
Normal		102	77	0
Dysplasia		47	72	1
Cancer		1	1	149
		150	150	150

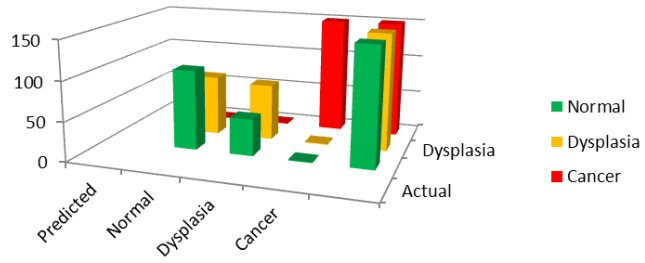

Figure 3. 43 LDA classification a) normal vs. cancer, b) dysplasia vs. cancer and c) normal vs. dysplasia vs. cancer

3.8 Discussion (Section 2 – Patient Biopsy work)

Histopathological investigation of cytological and morphological abnormalities of oral epithelia is the current gold standard of diagnosis (Muller et al., 2003). The diagnosis completely depends upon the experience of pathologist because the assessment is based on cellular and nuclear morphology which may have chances of inter and intra observer variability. The amount of workload on experienced pathologists certainly influences their efficacy and raises chances of diagnostic variability. Furthermore, the analysis is time consuming and the procedure requires histological processing which inhibit immediate diagnostic possibilities. Surgical intervention to obtain a biopsy and longer waiting times associated with histopathological evaluation increases anxiety for the patients as well as risk of post-operative metastasis in some cases (Bird et al., 2008).

These limitations have shifted the research towards spectroscopy and in particular Raman spectroscopy, which is capable of providing real time biochemical image of the tissues non-invasively. It offers several advantages such as increased frequency with which lesions may be monitored, comfort to the patients and no risk of metastasis is involved with the procedure. Raman spectrum can be collected in a very short time (few seconds to minutes) and it can also eradicate inter observer variability, which is associated with histopathological evaluations.

In our study, we have employed Raman spectroscopy to investigate normal, dysplastic and cancerous oral mucosa. A total of 45 patient samples (15 normal, 15 dysplasia and 15 cancers) were obtained from the Department of Oral Pathology, School of Clinical Dentistry, University of Sheffield, UK. We conducted this study to investigate the potential of Raman spectroscopy to discriminate normal and dysplastic oral mucosa from cancer. This study is different from the others because we only collected the oral mucosa samples from one anatomical site, which is tongue. There is evidence in the

literature suggesting that different anatomical sites show differences in Raman spectra (Bergholt et al., 2012) however different ethnic groups and gender does not influence Raman spectra (Guze et al., 2009). Characteristic Raman spectral features were used to differentiate between different tissue types instead of morphological appearance. We were able to identify distinctive Raman spectral features associated with normal, dysplasia and cancerous oral mucosal tissues. Significant spectral variances between normal and abnormal oral mucosa were seen and are shown in Figure 3.44.

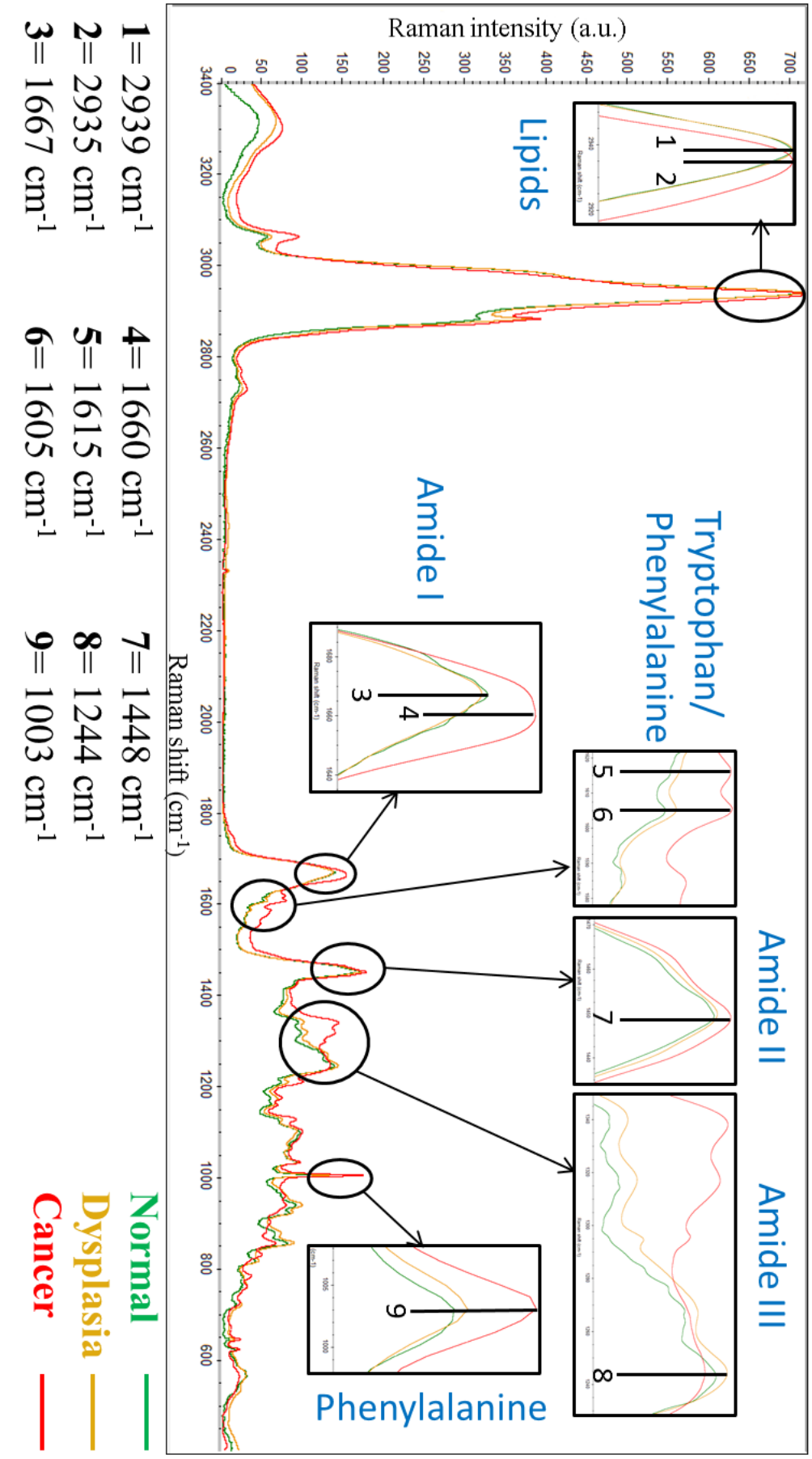

Figure 3. 44 Overlay Raman spectra of normal, dysplastic and cancerous oral mucosa

The high wavenumber region (2700 to 3100 cm^{-1}) of a Raman spectrum primarily contains stretching vibrations of lipids and proteins. These bands occur as a result of molecular vibrations such as, CH_3, CH_2 and CH=CH. Lipid peaks are expressed by both normal and abnormal tissues at 2939, 2935 and 2881cm^{-1} which showed variations in peak positioning and intensities suggesting that they might be as a result of differences in lipid structural changes and concentrations amongst them. Useful and significant information can be collected regarding lipid peroxidation assessments from high wavenumber region of the Raman spectra of biological tissues. Moreover, lipid saturation can also be evaluated through spectroscopic means which may lead to potential Raman markers for lipid metabolism. Studies in recent years have shown that lipid peroxidation is a critical step associated with pathogenesis or progression of disease (Mylonas and Kouretas, 1999). This process occurs naturally in the body in small amounts primarily due to various reactive oxygen species such as hydrogen peroxide and hydroxyl radical however there is another possibility that it may also trigger by actions of some phagocytes. The polyunsaturated fatty acids are attacked by these reactive oxygen species which begins a self-propagating chain reaction. This process of lipids destruction extremely effects cell viability despite the presence of natural antioxidant defence mechanism (Mylonas and Kouretas, 1999, Ayala et al., 2014). The concentration of unsaturated fatty acids increase in the cells with the progression of disease which may result in variations in Raman peak positioning and intensities which shows degree degradation of lipids as a result of lipid peroxidation, which is also known to be an indicator for aggressive cell proliferation. Low lipid synthesis rate might express some effects on the lipid metabolism of cells hence resulting in decreased number of saturated fatty acids moreover, increased level of lipid degradation may be caused due to excessive lipid peroxidation. Research studies have investigated and revealed that increased concentrations of polyunsaturated fatty acids

significantly affect signalling pathways as well as cell shape and metastatic behaviour of cancer (Mylonas and Kouretas, 1999).

The band present at 2939 cm^{-1} in the normal and dysplasia had shifted to 2935 cm^{-1} in cancer. This shift shows variations in the CH stretching vibrations of lipids suggesting differences between normal and dysplasia from cancer. Peaks present at 2881 cm^{-1}, which are assignments of CH_2 asymmetric stretch of lipids, have shown variations in intensities which might indicate varying amounts of unsaturated fatty acids present in normal, dysplastic and cancer tissues. Increased amounts of unsaturated fatty acids are a characteristic feature that might be associated with the progression of disease. Normal oral mucosa spectrum shows a shoulder as compared to increased peak intensities in dysplasia and cancer respective. These spectral features have shown significant variances between normal and abnormal tissues and can be extremely useful and may be of diagnostic significance in terms of early detection. PCA results over the high wavenumber region have shown a minimum variance of 83% in the first two principal components (figure 3.36). Normal and dysplastic tissues were distinctly separated by cancer in the lipid region; these results were consistent with the spectral observations and can be related to increased number of polyunsaturated fatty acids present in cancerous oral mucosa.

The fingerprint region (600 to 1800 cm^{-1}) of Raman spectra holds information regarding proteins, nucleic acids and lipids in biological tissues where amide I, II and III regions showed major contribution. Stretching and bending vibrations of biomolecules such as carbonyl (C=O) stretching, O-P-O vibrations, C-H bending, asymmetric phosphate stretching of nucleic acids, C=C bending mode of Phenylalanine, Tyrosine, C-C stretching, CH_2 twisting, CH_2 deformations and C=C stretching of lipids were observed in Raman bands (Mahadevan-Jansen et al., 1998, James W. Chan et al., 2006). Raman

spectral information in the fingerprint region also identified nucleic acid bases such as thymine, adenine, guanine, uracil and ring breathing mode of cytosine (Dukor, 2006, Hanlon EB, 2000, Mahadevan-Jansen and Richards-Kortum, 1996). Various metabolic processes and rapidly dividing malignant cells consume higher amounts of tryptophan, which is an essential amino acid and plays a vital role in cell proliferation. Increased levels of these compounds may suggest that during pathological conditions their quantity is raised as a result of aggressive cell division and peaks attributed to tryptophan show a relative increase in their intensities (Devpura et al., 2011, Tankiewicz et al., 2006). In our study, similar patterns regarding increased peak intensities for tryptophan can also be observed which indicates raised tryptophan levels as the tissue moves from normal to cancer. As shown in figure 3.44, peaks attributed to tryptophan are observed at 1583 and 1615 cm^{-1} (Devpura et al., 2011, Movasaghi et al., 2007), showing significant increase in intensities as the tissue changes from normal to cancer hence suggesting increased amount of tryptophan and increased metabolic activities at cellular level. Characteristic peaks of tryptophan observed in biological tissues are specific and have been reported frequently in the literature in association with cancer and its progression. Different intensity levels of tryptophan in normal, dysplasia and cancer demonstrate quantitative sensitivity of Raman spectroscopy. According to the clinical aspect, this might assist in determining different grades of dysplasia such as mild, moderate and severe or different stages of cancer which may help in early detection and improved prognosis of cancer.

The amide bands occur as a result of molecular vibrations of the amide bonds of polypeptide backbones where amide I represents carbonyl stretching (C=O) vibrations of amide group and indicating α-helical structure of proteins. Amide II region show bending vibrations of N-H and CH_2 of amide group whereas amide III discloses C-N-H in-plane bending modes hence representing β sheets and random coils of proteins. The

peak present in the Amide I region at 1667 cm^{-1} in normal and dysplastic tissue spectra could be differentiated from cancer in terms of area, positioning and intensity (figure 3.44). This band was broader and shifted to 1660 cm^{-1} in the cancer tissue which might suggest conformational changes due to altered metabolic activities at the cellular level. In normal oral mucosa the surface layer is a bilayer lipid membrane of squamous epithelium therefore the acquired Raman spectrum is primarily lipid dominant. Normal tissues possess sharp bands as compared to broad and strong bands in premalignant and malignant conditions (Malini et al., 2006). In dysplasia or malignancy, the surface layer is replaced with huge amounts of surface proteins for instance receptor proteins, enzymes, antigens and antibodies etc. which leads to a protein dominant Raman spectrum with broader peaks as compared to normal (Malini et al., 2006). Cancer tissues have shown broader band which might indicate severe conformational differences such as α-helix, β plates and disordered structure. Several research groups (Malini et al., 2006, Olivo et al., 2011, Venkatakrishna et al., 2001) have identified in their work that broadness of the peak is increased when the tissue changes its state from normal to premalignant and malignant which might be due to structural changes occurring in proteins.

Generally it is difficult to distinguish normal from dysplasia because the biochemical changes present in dysplastic tissues are subtle and take place gradually therefore it is not possible to draw a clear separation between the two (Stone et al., 2004). A probable clarification to this might be the existence of normal tissue within dysplastic during its transformation phase moreover there is another possibility as well that the spectra might be collected from clear margins of tissues, free of dysplasia.

PCA of the amide I region has also shown encouraging separation between normal and cancer as well as cancer and dysplasia. Since dysplasia is a transitional phase between

normal and cancer, it is difficult to draw a line which can isolate dysplastic tissue completely however cluster formation of PC1 was able to differentiate most of normal tissue from dysplastic whereas the majority of remaining were separated in PC2 (figure 3.37). The overall minimum percentage of explained variance in the amide I region was recorded to be 93%. These classifications suggest the possibility of identifying different types of tissues and amide I region has shown considerable amount of biochemical differences. These modelling systems can be extremely beneficial in identifying state of the tissue and amide I region may be used as Raman markers to detect diseased tissues.

The peak present at 1448 cm^{-1} is an assignment of CH_2, CH_3 bending modes of proteins (amide II), where a gradual increase in the intensity and broadness of the peak is observed as the tissue changes from normal to dysplasia and then caner. In this case spectral results have revealed that with the progression of disease protein content has risen quite significantly. In context to previous studies conducted on oral mucosa, it has been reported that normal oral mucosa is a lipid dominant surface whereas in pathological conditions the surface bilayer of oral mucosa is rich with proteins hence leading to a protein dominant Raman spectrum (Singh et al., 2012b, Singh et al., 2013, Deshmukh et al., 2011a). Increased protein intensities as well as broadening of peaks are recorded from normal to dysplasia and cancer which may suggest alteration in proteins in the abnormal state.

The amide III region (1200 to 1350 cm^{-1}) has shown significant variances between different oral tissues. In normal tissue spectra, peak present at 1244 cm^{-1} is assigned to amide III of proteins, which was also observed in dysplastic tissue spectra with subtle variation and increased intensity. However, in cancer, a broad band was observed instead of a sharp peak. Neoplastic skin cells possess degraded and disordered protein structures in comparison to normal cells (Donfack et al., 2010, Gniadecka et al., 1997).

This decrease in intensity of the amide III in cancer was unexpected in our results which might indicate degradation or/and disordered proteins with the progression of disease. Amide III region also contains biochemical information regarding nucleic acids (1317, 1337, 1338 and 1341 cm^{-1}) and can be assigned to polynucleotide chain (DNA purine bases), nucleic acid modes indicating mount of DNA in tissues and Guanine ring breathing mode of DNA/RNA (Stone et al., 2004, Stone et al., 2002b, Mahadevan-Jansen and Richards-Kortum, 1996, Mahadevan-Jansen et al., 1998, Notingher et al., 2004a, Ruiz-Chica et al., 2004, Movasaghi et al., 2013, Rehman et al., 2007, Dukor, 2006). This might be the reason that significant spectral differences as are observed between normal, dysplastic and cancerous oral mucosa.

Increased proteins and nucleic acid levels were observed in dysplasia and cancer. It might be suggested that proteins and nucleic acids are involved in metabolic activities during abnormal cell proliferation (Short et al., 2005). Histopathologically it is observed that during cellular transformation in premalignant and malignant conditions there is an increase in the nuclear/cytoplasmic ratio (Stone et al., 2002b). Moreover, it is also believed that, different grades of dysplasia can also be identified by nucleic acid to cytoplasmic ratios (Huang et al., 2003a). Our results show the same trend with cancer tissue having the highest peak intensity compared to normal and dysplastic hence suggesting that an increased DNA content is present in cancerous tissue. Living cells contain an enzyme called Nicotinamide Adenine Dinucleotide (NAD^+), which has two nucleotides held together by phosphate groups. Adenine and nicotinamide are the two bases to which one nucleotide is attached. NAD^+ plays a vital role in redox reactions during metabolic activities and is responsible for electron transfer between reactions. Previous studies have shown that in malignant conditions, due to increased metabolic activities there is an increase in NADH molecular species. During pathological conditions there is an increase in cell proliferation which leads to increased amounts of

DNA, in addition to this cell surface proteins, enzymes and hormones also show an increase in such conditions (Robbins et al., 1994 , Clark and Hester, 1993). Furthermore, there is strong evidence in the literature to suggest that during malignancy DNA structure undergoes significant alterations such as changes in DNA hydrogen bonding pattern due to change in degree of DNA methylation (Fukuyama et al., 1999, Banyay et al., 2003, Ci et al., 1999, Pallua et al., 2012, Petibois and Déléris, 2006). PCA of the amide III region has shown clear separation between normal, dysplasia and cancer with minimum overall explained variance of 98% (figure 3.38). It is believed that with the progression of disease, metabolic activities are increased within cells and as a result amount of nucleic acids is also increased. This may indicate the importance of amide III region as a potential Raman marker which can identify various tissue types.

Peak at 1003 cm^{-1} can be attributed to phenylalanine, an essential amino acid. In relation to the existing literature, oral mucosa is a lipid dominant tissue in normal conditions therefore we expect increased levels of proteins when tissue transforms from normal to dysplastic and cancer. Blood flow is increased at the site of injury, inflammation, infection, sepsis burn and malignancy, which is because of the immune response. In any of these conditions, increased amounts of amino acids (phenylalanine) are accumulated at the site due to increased blood flow (Chang et al., 1983, Rath et al., 1987, Roth et al., 1985, Ollenschläger et al., 1988). An increased intensity of phenylalanine was significant in dysplasia and cancer which may suggest increased amount of protein (Venkatakrishna et al., 2001, Krishna et al., 2004, Malini et al., 2006, Olivo et al., 2011, Singh et al., 2013).

Cluster analysis (CA) showed two main branches (figure 3.42), one entirely contained cancer tissue with a sub-branch containing few normal and dysplastics, however within the cancer group there was no normal or dysplasia found which might suggest the

sensitivity of cluster analysis in isolating cancers. As mentioned earlier that it is hard to draw a definitive line between normal and dysplasia because there are subtle changes that occur in tissues when they transform from normal to premalignant. This is also one of the reasons why it is difficult to diagnose cancer at an early stage. Cluster analysis not only groups different types of tissues but it also explains the relative distance within one tissue type based on intra tissue variability. We have also observed that due to the complex nature of cancer tissues, variability within cancer was higher than normal and dysplasia. This might suggest that in malignancy there is an increase in metabolic activities which are different in various cancers and it may vary in individuals.

LDA Classification

Classification systems have been widely explored in the past to differentiate between tissue types. Different cancers such as cervical (Mahadevan-Jansen et al., 1998), stomach (Teh et al., 2010), larynx (Stone et al., 2000), gastrointestinal (Stone et al., 2002a) and oral (Singh et al., 2013, Singh et al., 2012a, Venkatakrishna et al., 2001, Malini et al., 2006) have been successfully investigated using multivariate data analysis techniques. Most of the work was aimed to isolate cancer from normal tissues using different algorithms and promising results from previous studies have encouraged researchers to further explore the potential of Raman spectroscopy in the field of oncology.

In this study we have investigated normal, dysplastic and cancerous oral tissues with an aim to spectroscopically evaluate their biochemical differences. LDA classification between normal and cancer showed more than 95% sensitivity and specificity (figure 3.43a). These results suggested that Raman spectroscopy along with multivariate analytical tools is extremely sensitive to discriminate between normal and cancer tissues. Similarly over 80% sensitivity was recorded between dysplastic and cancer

tissue (figure 3.43b) however there was a drop in sensitivity and specificity of normal and dysplastic tissues (figure 3.43c). Overall the percentage of correctly classified tissues was higher than misclassifications which support the abilities of Raman spectroscopy as a potential diagnostic tool. Classifications between normal and cancer have proved to be highly accurate and suggest that cancer detection through Raman spectroscopy has a promising future alongside conventional histopathological techniques. Surveillance of dysplasia is the key for early cancer detection, 80% and 92% sensitivity was achieved in this study between dysplastic and cancer tissues respectively. These results suggest that in future RS may play a vital role non-invasively for the monitoring of dysplastic lesions. Classification results between dysplasia and cancer have demonstrated positive findings which indicate the potential of RS as an addition to the armoury of diagnostic tools and pathologists. Dysplastic conditions need to be kept under regular and non-invasive screenings in order to detect early cancerous changes which would improve prognosis and quality of life for the patients.

Sensitivity and specificity between normal and dysplasia was reduced as compared to cancer. These results show that similarities have been found between normal and dysplastic tissues. Dysplasia is a transitional phase which can proceed to cancer or revert to normal. Gradual biochemical changes take place during the transition of normal tissue to dysplasia therefore it is not possible to accurately separate these tissues (Stone et al., 2004). A possible explanation to this may be the presence of some normal tissue areas existing within dysplasia and they might have come under spectroscopic examination. In this case it should also be considered that the measurement might have been taken from the resection margin which may have normal or dysplastic tissue. Another possible explanation to this may be the phenomenon of field change cancerisation in which the morphology of normal tissue within field change zone

remains unchanged but biochemical changes do take place which might have been sensed by Raman spectroscopy (Keller et al., 2008).

3.9 Summary of patient biopsy work

- In this study we have analysed normal, dysplastic and cancerous tongue tissues from 45 different patients using Raman spectroscopy.
- 300 good quality spectra were collected from each case, making a total of 900 Raman spectra for investigations. Visual spectral differences were obvious in the lipids, proteins and nucleic acid regions.
- On the basis of biochemical variations, unsupervised algorithms such as PCA and CA were able to differentiate between normal and abnormal oral tissues.
- Increased intensities were observed in phenylalanine, tryptophan, nucleic acids, amide I and amide II as the tissue changed its state from normal to dysplasia and cancer. These biomolecules may act as potential Raman markers for cancer detection.
- LDA was used as a supervised algorithm which successfully differentiated between normal and cancer by achieving a sensitivity and specificity of over 95%.
- Sensitivity of more than 80% was achieved between dysplastic and cancer tissue samples. These results were very promising in terms of surveillance of dysplasia and early detection of cancer which may have a positive impact in future to improve prognosis for the patients.

Chapter 3:

Section 3 - Irradiated Tissue Engineered models

This section includes work conducted on irradiated 3D tissue engineered models of normal and cancerous oral mucosa. Raman spectral data was collected from control and irradiated models for biochemical comparison. PCA and CA were used to differentiate between control, 5, 10 and 15 Gy at day 1, 4 and 7 post radiations. Biochemical information obtained by Raman spectra can be particularly sensitive to predict which biological components get affected by radiotherapy and how the recovery mechanism takes place with increasing incubation times.

The biochemical pathway associated with radiotherapy is not very well established therefore the aim of this work is to extract chemical information from control and irradiated models of normal and cancerous oral mucosa to identify specific biomolecules which are more radiosensitive and may well be used as Raman markers for targeted treatments in future.

Vibrational spectroscopic techniques may offer non-invasive tissue assessments in clinical settings during radiotherapy procedures to minimise the associated side effects. Moreover they may be very useful in understanding tissue response to radiation on *in vitro* models which may aid in a better understanding of cancer treatment and eventually improve prognosis.

3.10 Tissue Engineered Normal Oral Mucosa

3.10.1 Control models

Primary human NOK's and primary human NOF's were cultured on acellular skin scaffold to construct TENOM.

The control models (not exposed to radiation) showed that a stratified epithelium was produced by culturing TENOM models at an ALI for 2 weeks (figure 3.45). A single layer of cells was seen at day 1 whereas the epithelium showed clear differentiation and was approximately 10 cells thick by day 4 and 7. At day 7, a well-formed basal cell layer was seen in the epithelium underlying an organised prickle cell layer, this feature gradually developed as it was not clearly seen at day 1 and 4. Cells present at the most superficial layer showed evidence of maturation with flattened cells and very few nuclei giving the epithelium a smooth flat surface. TENOM models also show rete ridges, which is a unique rounded feature of epithelial connective tissue junction. Fibroblasts were present and evenly populated in the underlying connective tissue.

3.10.2 Irradiated models

Effects of irradiation with 5, 10 and 15 Gy could clearly be seen in the TENOM models at day 1, 4 and 7 (figures 3.46 – 3.48). In contrast to the control models, epithelial maturation was severely disturbed by the different dosages of radiation which inhibited formation of a stratified epithelium. At day 1, all three radiated models showed a single cell layer in the epithelium however at day 4 and 7 signs of epithelial maturation were slightly improved. Fibroblast invasion in the connective tissue was also restricted in the day 1 irradiated models which improved at day 4 and 7 showing that the cells were not killed by the radiation exposure. Epithelial development and architecture was seriously challenged in the 15 Gy models as compared to the other doses. The maximum amount of fibroblast penetration in to the connective tissue was seen in the 5 Gy model at day 4. These irradiated models showed a lack of well-formed basal cell layer and rete ridges.

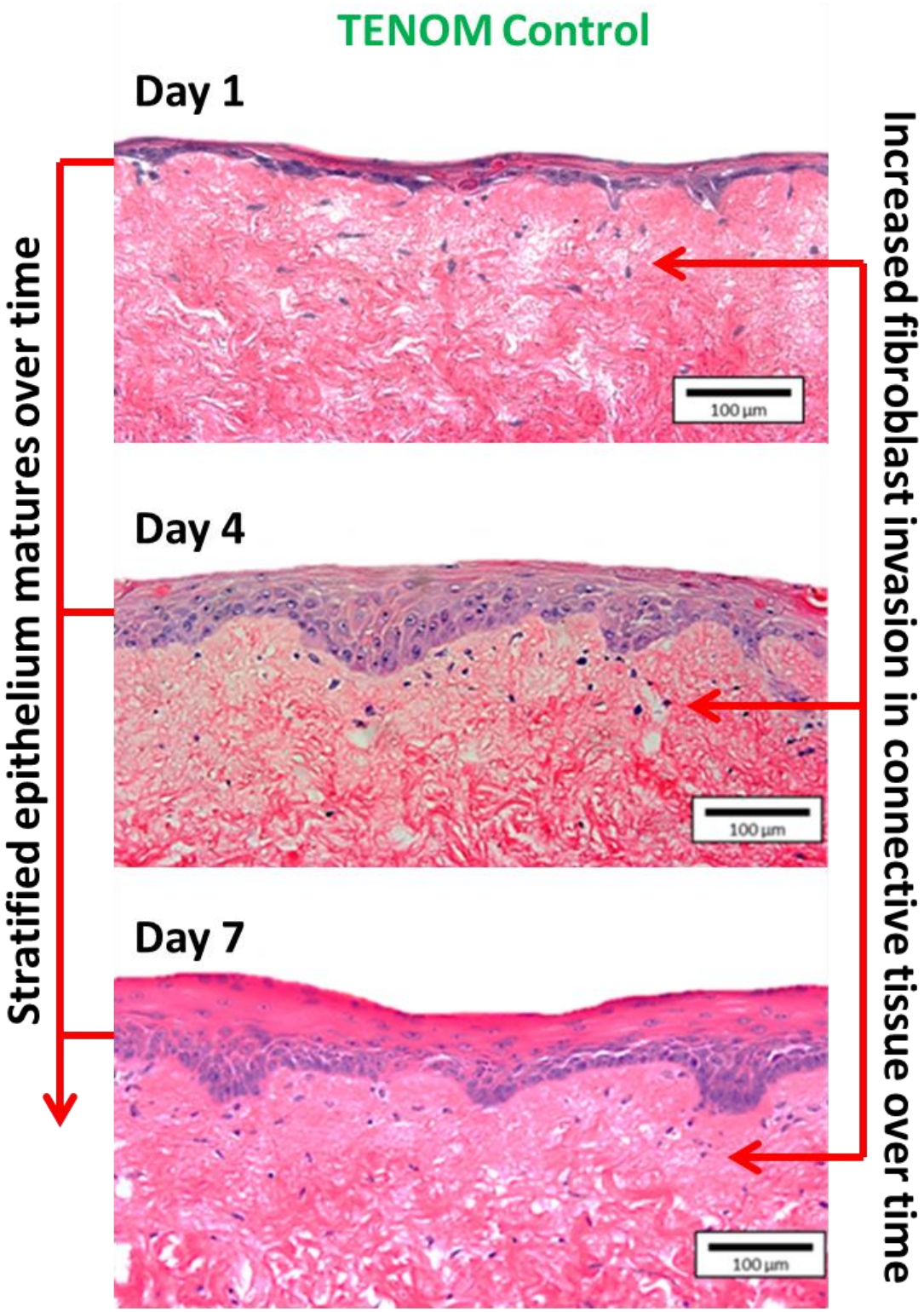

Figure 3. 45 H&E images of controlled tissue engineered normal oral mucosa at day 1, 4 and 7.

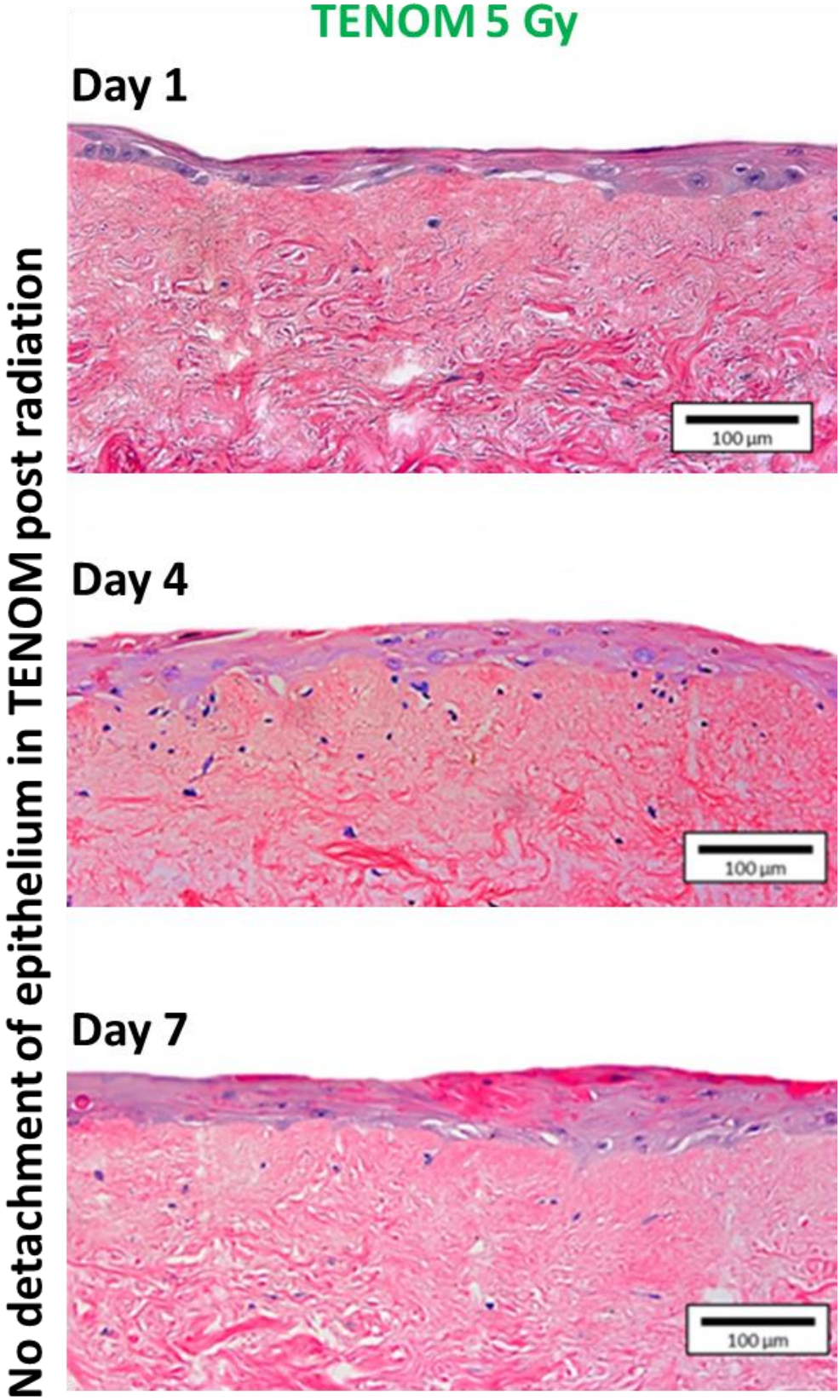

Figure 3. 46 H&E images of tissue engineered normal oral mucosa irradiated with 5 Gy (day 1, 4 and 7).

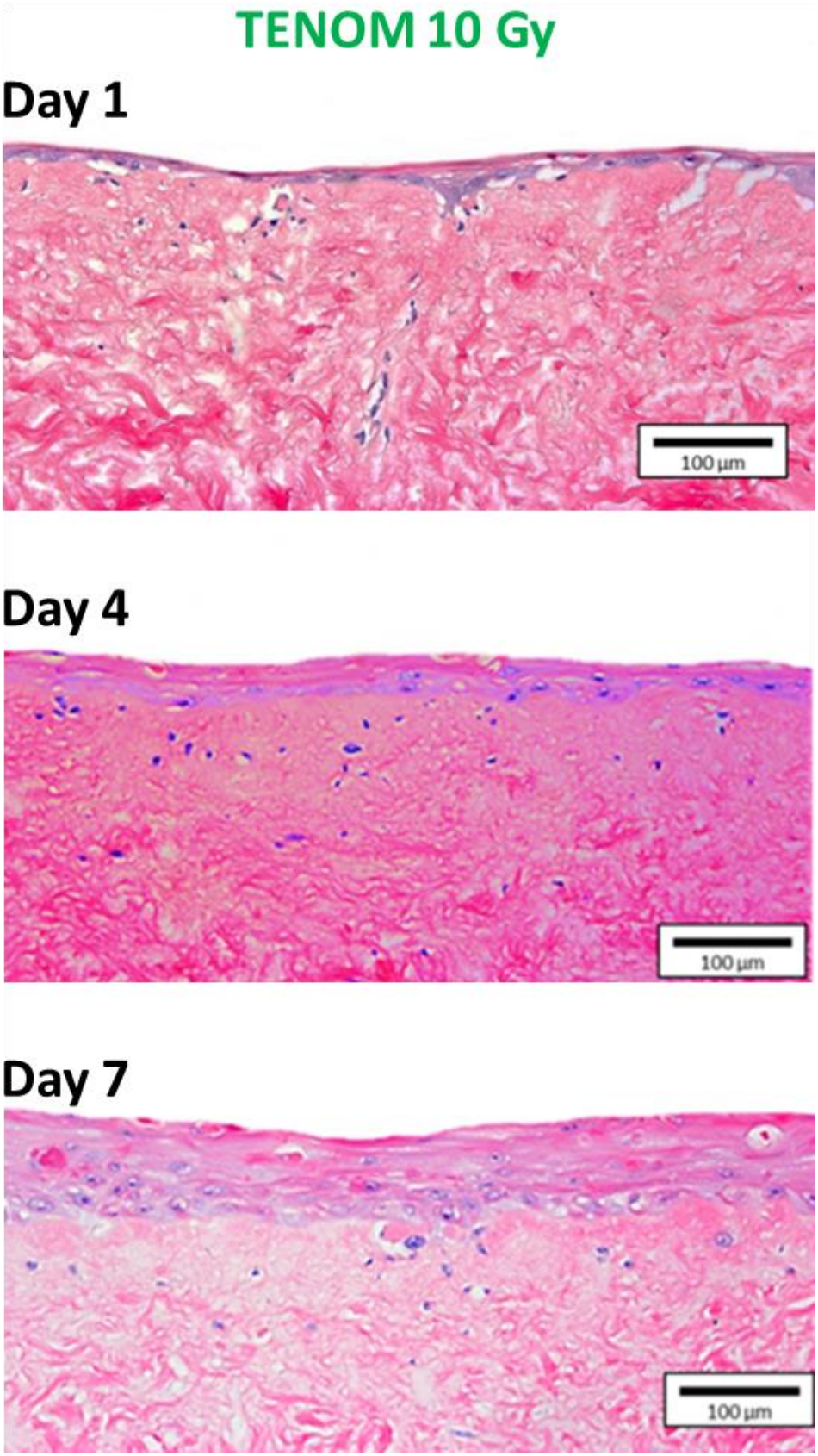

Figure 3. 47 H&E images of tissue engineered normal oral mucosa irradiated with 10 Gy (day 1, 4 and 7).

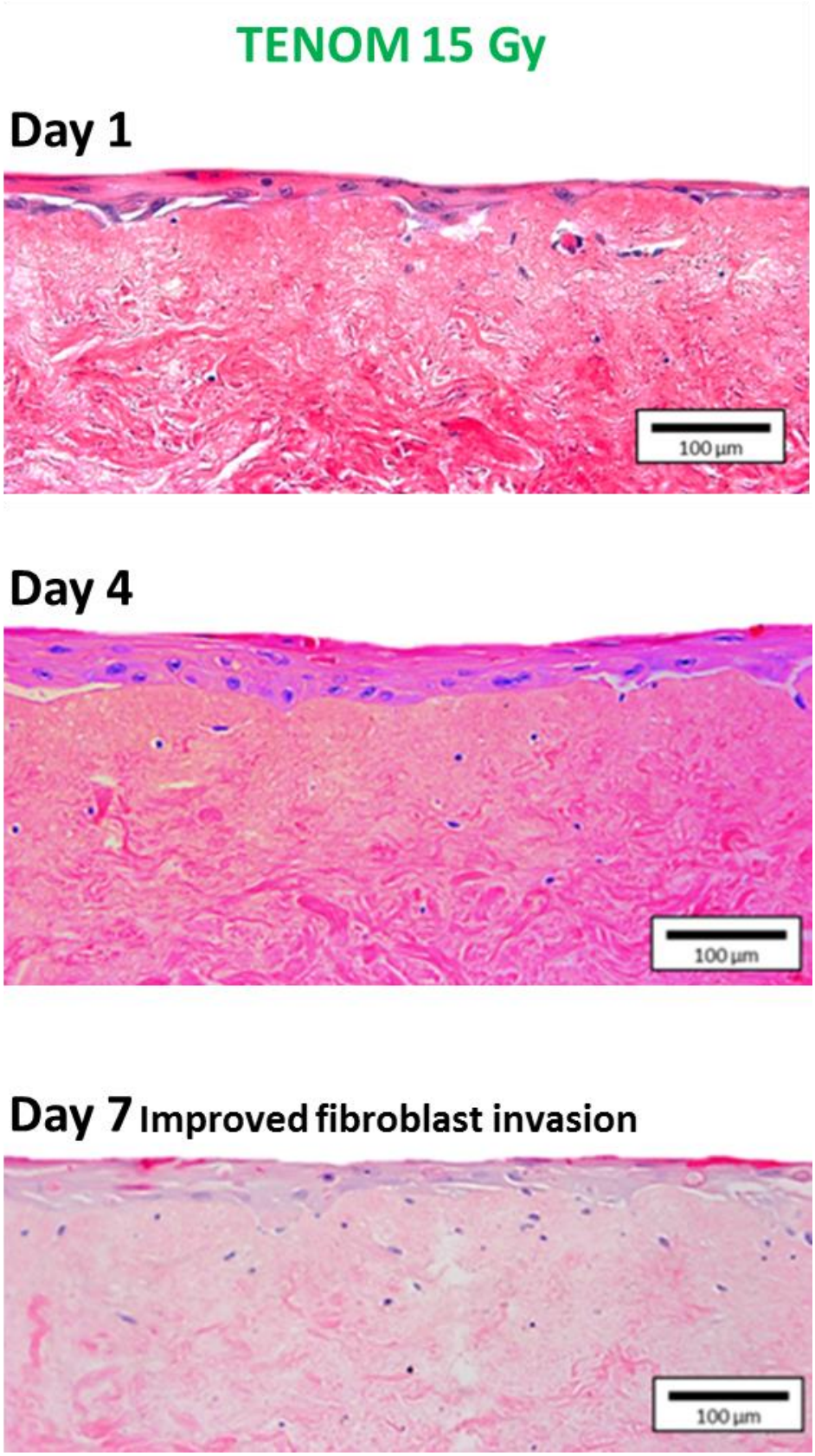

Figure 3. 48 H&E images of tissue engineered normal oral mucosa irradiated with 15 Gy (day 1, 4 and 7).

3.11 Tissue Engineered Cancerous Oral Mucosa

3.11.1 Control models

Cal27 cells were cultured with NOF's on a DED scaffold for 14 days to obtain a 3D tissue engineered Cal27 model. Day 1 H&E images showed epithelial formation of cancer cells which matured significantly at day 4. At day 7, bulbous rete processes, abnormal keratinocyte maturation and a fibroblast populated dermis was seen in these malignant models. The pleomorphism was much more pronounced with prominent hyperchromatic nuclei, basal cell hyperplasia, dyskeratosis and full thickness dysplasia. Focally, epithelial penetration suggests early invasion of OSCC in the connective tissue. Epithelial maturation increased gradually and at day 7 it was showing signs of abnormal thickening as it appears in cancer models (figure 3.49).

3.11.2 Irradiated models

Radiation effects were clearly observed in the tissue engineered cancerous oral mucosa models at day 1, 4 and 7 (figures 3.50 – 3.52). In contrast to the control, epithelial maturation was disturbed by all doses of radiation which inhibited formation of a mature epithelium. In terms of epithelial thickness, 5 Gy models produced a relatively thicker epithelium than the 10 and 15 Gy models. Fibroblast invasion in the connective tissue was also restricted in all the irradiated models. At day 1, epithelium was detached from the connective tissue in the 15 Gy model whereas 5 and 10 Gy models showed the same signs at later days. Epithelia in radiated models were thinner and detached as compared to the control.

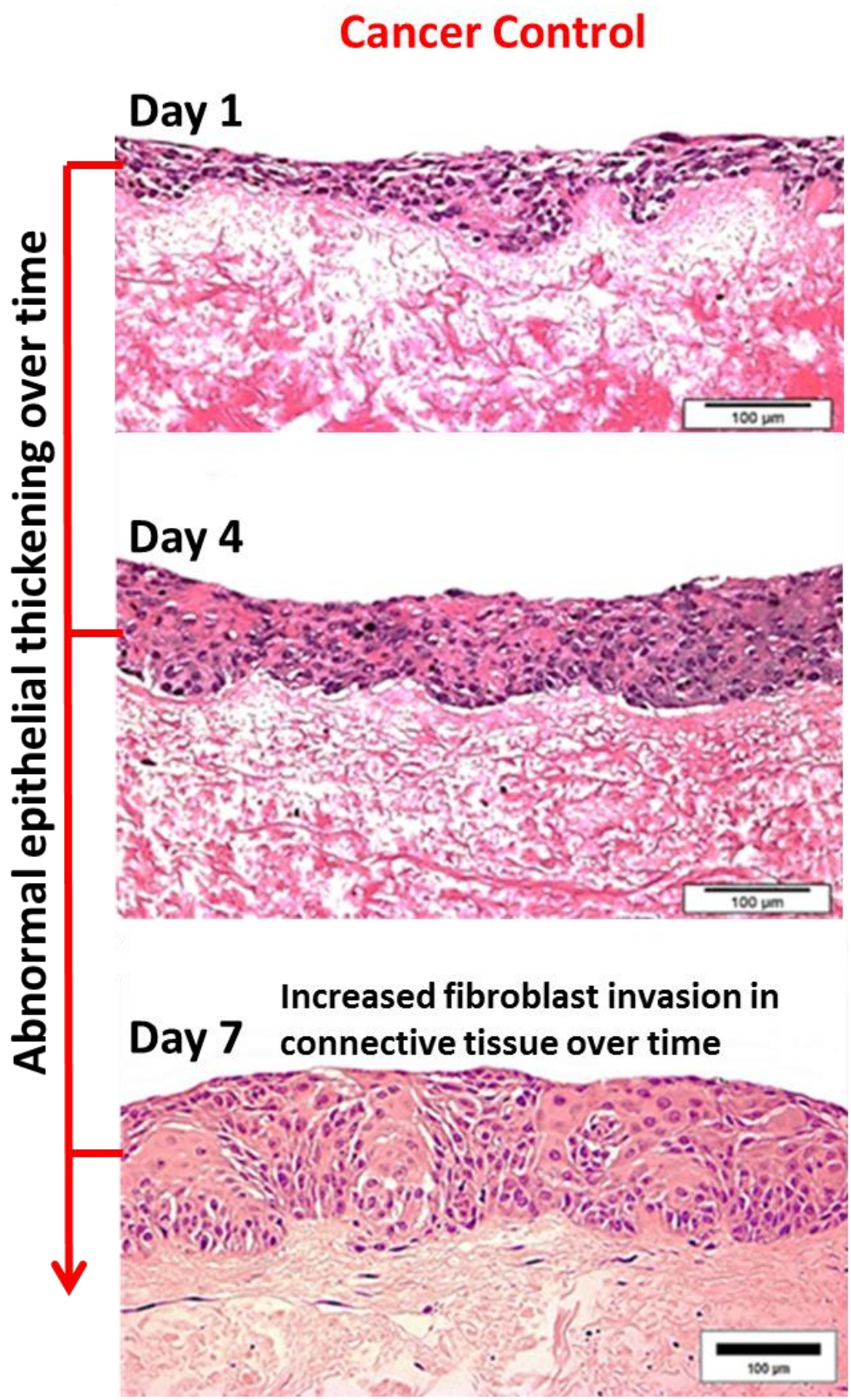

Figure 3. 49 H&E images of controlled tissue engineered cancerous (Cal27) oral mucosa at day 1, 4 and 7.

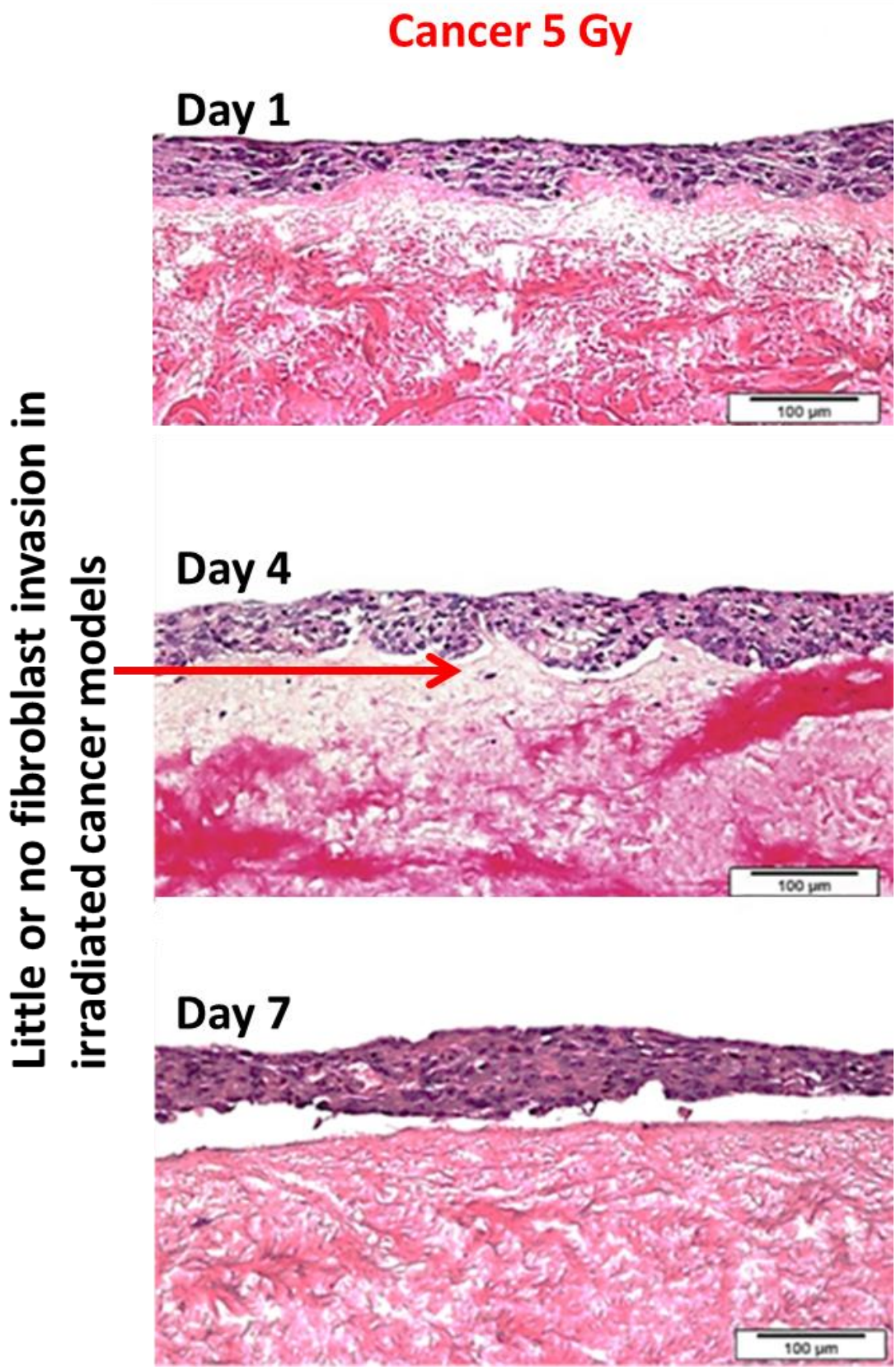

Figure 3. 50 H&E images of tissue engineered cancerous (Cal27) oral mucosa irradiated with 5 Gy (day 1, 4 and 7).

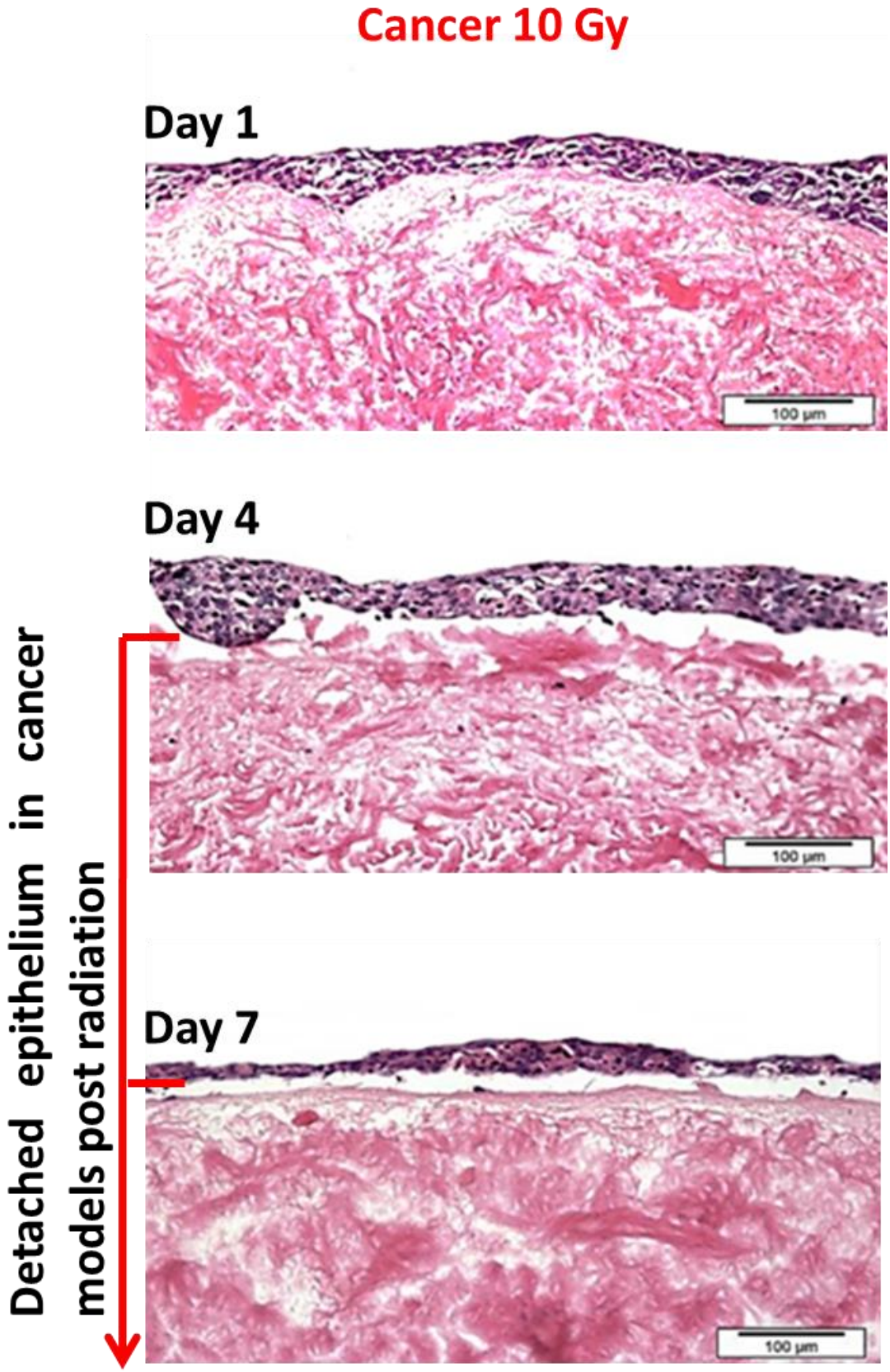

Figure 3. 51 H&E images of tissue engineered cancerous (Cal27) oral mucosa irradiated with 10 Gy (day 1, 4 and 7).

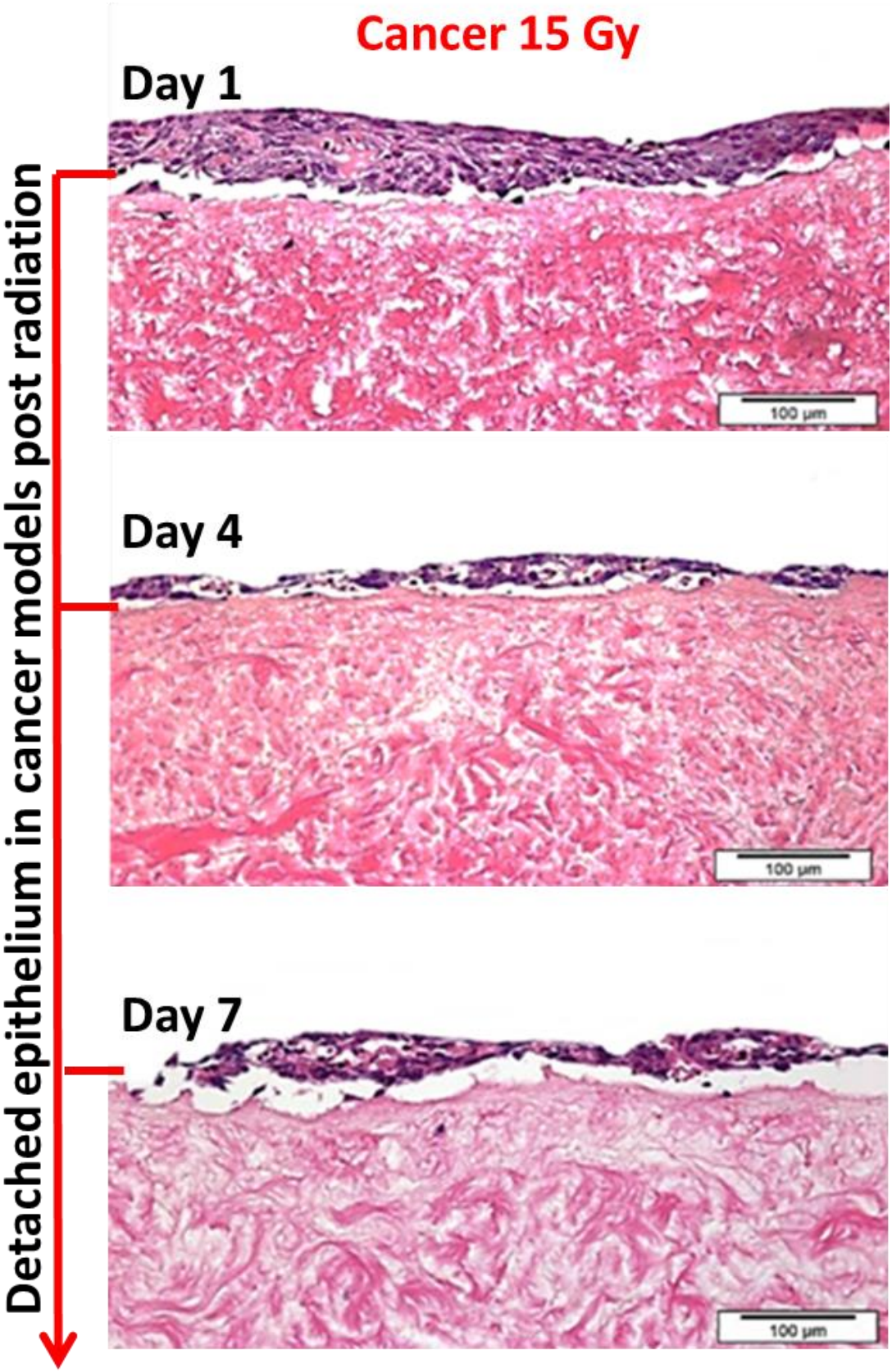

Figure 3. 52 H&E images of tissue engineered cancerous (Cal27) oral mucosa irradiated with 15 Gy (day 1, 4 and 7).

3.12 Raman spectroscopic results

3.12.1 Tissue Engineered Normal Oral Mucosa

TENOM DAY 1

A total of 80 spectra were collected of the 3D tissue engineered normal oral mucosa models at day 1 post irradiation. Average spectra of control along with irradiated models are shown in figure 3.53. Peaks were assigned using spectral data base of tissue engineered normal oral mucosa models presented in table 3.1.

Tryptophan and 621 to 956 cm^{-1} region

The bands present at 621 and 643 cm^{-1} can be assigned to C-C twisting modes of phenylalanine and tyrosine. A weak band was observed at 725 cm^{-1} only in control model can be attributed to ring breathing modes of DNA/RNA bases however in 10 and 15 Gy models this assignment was shifted to at 720 cm^{-1}. Bands present at 759, 1208, 1337 and 1615 cm^{-1} are specific assignments of C-C/C=C stretching modes of tryptophan. These peak intensities have shown variations between control and irradiated models. There is a decrease in tryptophan peak intensity of 15 Gy model whereas increased intensities are seen in 5 and 10 Gy. The band observed at 780 cm^{-1} can be assigned to uracil based ring breathing mode in DNA/RNA which was not observed in 5 Gy model at day 1. The Peak originating at 828 cm^{-1} can be attributed to ring breathing mode of tyrosine, Phosphodiesters and O-P-O stretching of DNA. Band appearing at 852 cm^{-1} can be assigned to proline, hydroxyproline, and ring breathing mode of tyrosine. Band present in all models at 937 cm^{-1} can be attributed to C-C stretch backbone (α-helix conformation of protein).

1002 to 1208 cm^{-1} region

A sharp and intense peak originated at 1002 cm^{-1} in control and irradiated models, which is a typical assignment of symmetric ring breathing mode of phenylalanine. Increased phenylalanine intensities were observed in irradiated models however 15 Gy model showed less intense peak as compared to 5 and 10 Gy. Band appeared at 1031 cm^{-1} can be assigned to CH_3 CH_2 bending modes of collagen and phospholipids, C-H in-plane bending mode of phenylalanine and C-H stretch of proteins. Band present at 1101 cm^{-1} in control and 5 Gy model is an assignment of υ(C-C)-lipids and fatty acids which was shifted to 1102 cm^{-1} and 1103 cm^{-1} in 10 and 15 Gy respectively. A small peak at 1127 cm^{-1} can be assigned to C-C skeletal stretch in lipids which was present in all models. A weak and short band at 1156 cm^{-1} can be attributed to C-C, C-N stretching in proteins, which was present in all models. Weak spectral contribution at 1173 cm^{-1} in all models can be associated to cytosine, guanine or tyrosine (collagen type I). Band appearing at 1208 cm^{-1} is a protein assignment and attributed to phenylalanine, where the least spectral contribution in terms of intensity was observed in 15 Gy model at day 1.

1220 to 1280 cm^{-1} region

Band appearing in this region is a characteristic assignment of proteins in biological tissues which can be attributed to Amide III (protein in α-helix conformation), C-H lipids/amide III collagen assignment and tryptophan. Peak appearing at 1266 cm^{-1} can also be recognised as amide III of collagen.

1317 to 1615 cm^{-1} region

Peaks present at 1317 and 1337 cm^{-1} appeared in all tissue models can be attributed to guanine ring breathing modes of DNA/RNA bases, C-H deformation of proteins and

nucleic acid modes, variations in intensities and shapes were observed between control and irradiated model spectra. The band present at 1448 cm^{-1} in all models can be an assignment of CH_2 bending in proteins. A peak present at 1583 cm^{-1} in control and irradiated models can be attributed to C=C bending mode of phenylalanine (protein assignment). The band at 1605 cm^{-1} can be assigned to tyrosine, ring vibration of phenylalanine or C-C of phenylalanine whereas 1615 cm^{-1} can be attributed to C=C of tyrosine or tryptophan (proteins assignment).

1652 to 1700 cm^{-1} region

A broad and strong band present at 1654 cm^{-1} in control model is a characteristic assignment of proteins in α-helix structure of amide I. The band shift at 1652 cm^{-1} was noticed in the amide I region of irradiated tissue engineered model spectra.

2723 to 3060 cm^{-1} region

A weak band at 2727 cm^{-1} in the control model was observed, which can be assigned to C-H stretching vibrations in lipids, this band was shifted to 2723 cm^{-1} in the irradiated models. A shoulder appeared in control model at 2880 cm^{-1} as compared to peaks in 5, 10 and 15 Gy models**,** which are attributed to CH_2 asymmetric stretch of lipids and proteins. A strong band arising at 2932 cm^{-1} in all models is assigned to C-H vibrations in lipids and proteins as well as CH_2 asymmetric stretch in lipids/fatty acids. CH stretching vibrations were present at band originating at 3060 cm^{-1} in all models.

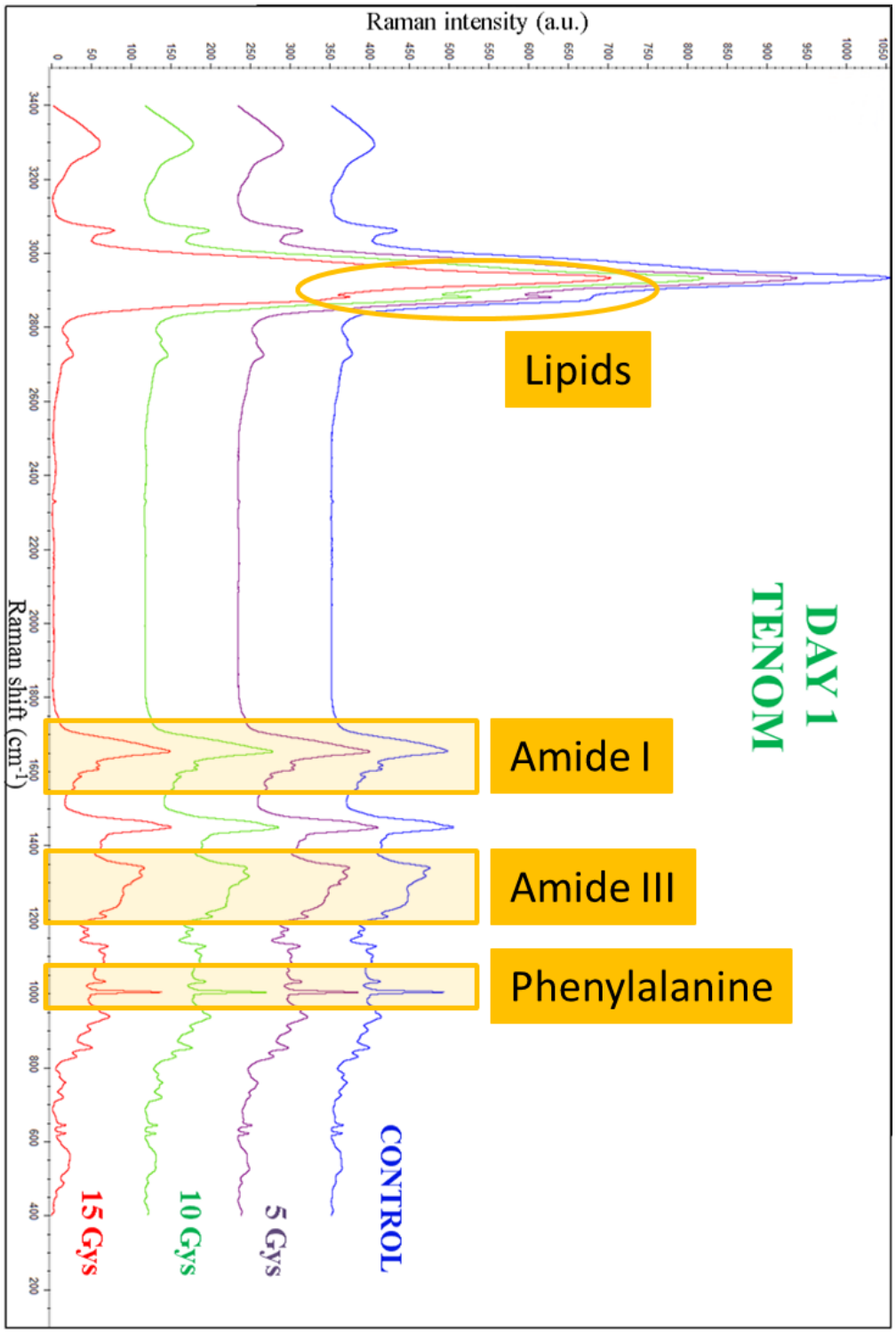

Figure 3. 53 Average spectra of tissue engineered normal oral mucosa (TENOM) at day 1 post radiation, showing control, 5 Gy, 10 Gy and 15 Gy

TENOM DAY 4

A total of 80 spectra were collected at Day 4 post irradiation of TENOM. The models were irradiated with 5, 10 and 15 Gy, average spectra of these models are shown in figure 3.54.

Tryptophan and 621 to 937 cm^{-1} region

The bands present at 621 and 643 cm^{-1} in all models can be attributed to C-C twisting modes of phenylalanine and tyrosine. The peak present at 719 cm^{-1} was only observed in 5 Gy model and can be attributed to symmetric stretch vibration of choline group $N^{+}(CH_3)_3$, characteristic for phospholipids. A weak band was observed at 720 cm^{-1} in control models only and can be attributed to ring breathing modes of DNA/RNA bases however in 10 and 15 Gy models, this assignment was shifted to 725 cm^{-1}. Bands present at 759, 1208, 1337 and 1615 cm^{-1} are specific assignments of C-C/C=C stretching modes of tryptophan. A subtle shift in tryptophan bands of the irradiated models was observed. The band observed at 780 cm^{-1} is a uracil based ring breathing mode in DNA/RNA which was absent in 10 and 15 Gy model at day 4. The Peak originating at 828 cm^{-1} can be attributed to ring breathing mode of tyrosine, Phosphodiesters and O-P-O stretching of DNA, moreover a shift to 830 cm^{-1} was noticed in irradiated models. The band appearing at 852 cm^{-1} can be assigned to proline, hydroxyproline, and ring breathing mode of tyrosine. Bands present in all models at 937 cm^{-1} can be assigned to C-C stretch backbone (α-helix conformation of protein).

1002 to 1208 cm^{-1} region

A sharp and intense peak at 1002 cm^{-1} in control model and at 1003 cm^{-1} in irradiated models is a typical assignment of symmetric ring breathing mode of phenylalanine. The band present at 1031 cm^{-1} can be attributed to CH_3 CH_2 bending modes of collagen and phospholipids, C-H in-plane bending mode of phenylalanine and C-H stretch of

proteins. A weak band arising at 1064 cm^{-1} in the control, 5 and 10 Gy models is an assignment of C-C skeletal stretch of lipids; this peak did not appear in 15 Gy model. 1101 cm^{-1} in control model can be assigned to υ(C-C)-lipids and fatty acids which was shifted to 1104 cm^{-1} in irradiated models. A small peak at 1130 cm^{-1} can be assigned to C-C skeletal stretch and structural changes in phospholipids. A weak and short band at 1156 cm^{-1} can be attributed to C-C, C-N stretching in proteins, which was present in all models. Weak spectral contribution at 1173 cm^{-1} in all models can be associated to cytosine, guanine or tyrosine (collagen type I). Band appearing at 1208 cm^{-1} is a protein assignment and attributed to phenylalanine.

1220 to 1280 cm^{-1} region

Bands appearing in this region are characteristic assignment of proteins which can be associated with Amide III (protein in α-helix conformation), C-H lipids/amide III collagen assignment and tryptophan. Peak at 1266 cm^{-1} can also be recognised as amide III of collagen.

1317 to 1615 cm^{-1} region

Peaks present at 1317 and 1337 cm^{-1} appeared in all the tissue models and can be attributed to guanine ring breathing modes of DNA/RNA bases, C-H deformation of proteins and nucleic acid modes, variations in terms of intensities and shifts were observed between control and irradiated model spectra. The band present at 1448 cm^{-1} was shifted to 1450 cm^{-1} only in the 15 Gy models which can be attributed to CH_2 bending in proteins. A peak present at 1583 cm^{-1} in the control models can be attributed to C=C bending mode of phenylalanine (protein assignment), there was a shift observed at 1585 cm^{-1} in the irradiated models. The band at 1605 cm^{-1} can be an assignment of tyrosine, ring vibration of phenylalanine or C-C of phenylalanine whereas 1615 cm^{-1}

can be attributed to C=C of tyrosine or tryptophan (proteins assignment). At day 4, 1615 was shifted to 1617 cm^{-1} in all irradiated models.

1652 to 1700 cm^{-1} region

A broad and strong band present at 1655 cm^{-1} in control, 5 and 10 Gy models at day 4 can be attributed to proteins in α-helix structure of amide I. Band shift at 1653 cm^{-1} was noticed only in the 15 Gy model.

2725 to 3061 cm^{-1} region

A weak band at 2725 cm^{-1} in the control, 5 and 10 Gy model was observed, which can be assigned to C-H stretching vibrations in lipids, this band was shifted to 2729 cm^{-1} in the 15 Gy model. In control model, peak present at 2880 cm^{-1} can be attributed to CH_2 asymmetric stretch of lipids and proteins, whereas there a shift to 2882 cm^{-1} was observed in the irradiated models. A strong band arising at 2932 cm^{-1} in all models can be assigned to C-H vibrations in lipids and proteins as well as CH_2 asymmetric stretch in lipids/fatty acids. This band was significantly intense in irradiated models as compared to control. CH stretching vibrations were present at band originating at 3061 cm^{-1} in all models.

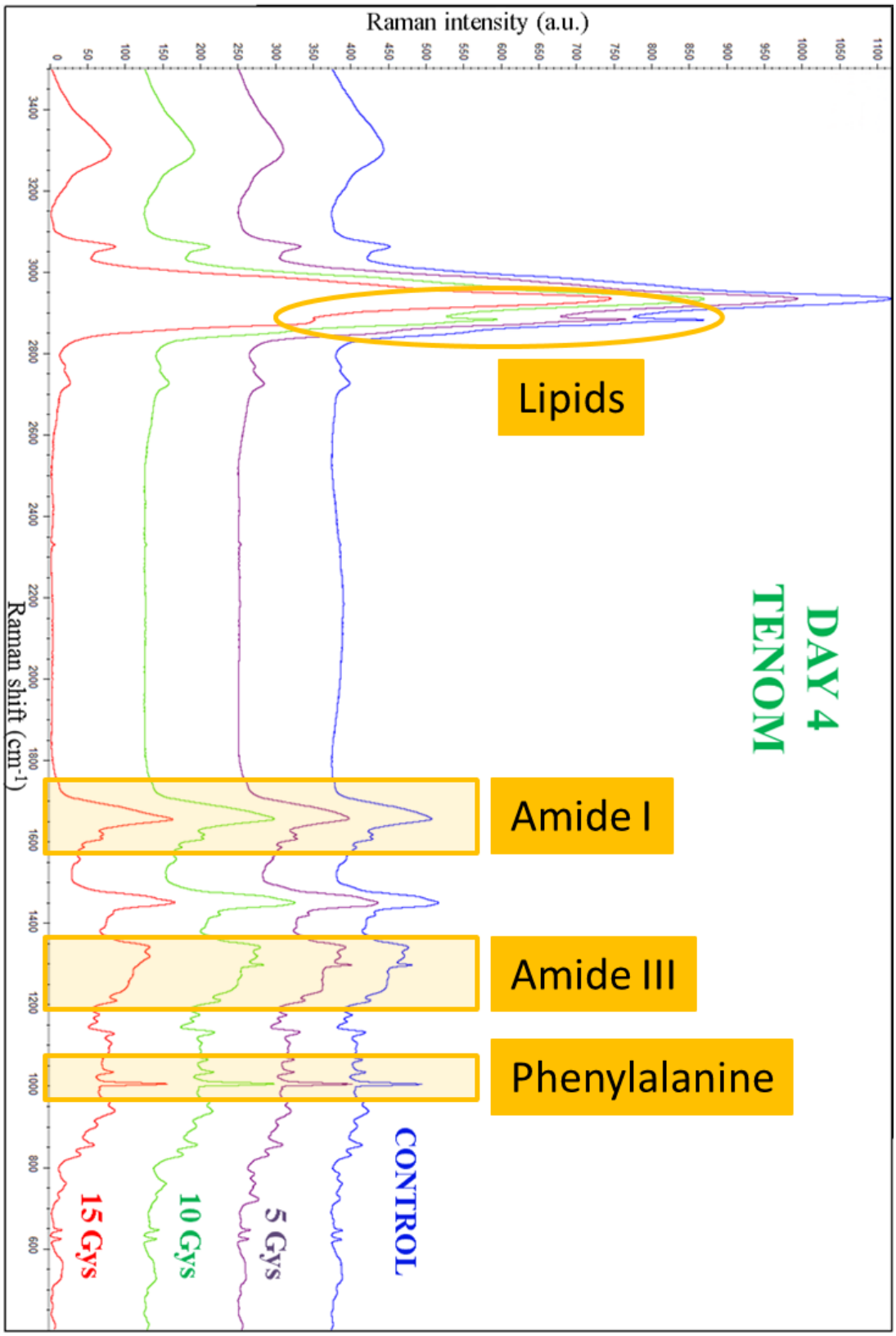

Figure 3. 54 Average spectra of tissue engineered normal oral mucosa (TENOM) at day 4 post radiation, showing control, 5 Gy, 10 Gy and 15 Gy

TENOM DAY 7

A total of 80 spectra were collected at Day 7 post irradiation of 3D TENOM. The model was irradiated with 5, 10 and 15 Gy, average spectra of these models are shown in figure 3.55.

Tryptophan and 621 to 936 cm^{-1} region

Bands present at 621 and 643 cm^{-1} in all models can be attributed to C-C twisting modes of phenylalanine and tyrosine. Bands present at 759, 1208, 1337/9 and 1615 cm^{-1} are specific assignments of C-C/C=C stretching modes of tryptophan. A subtle shift in tryptophan bands of the irradiated models was observed. The band observed at 781 cm^{-1} is a uracil based ring breathing mode in DNA/RNA which were absent in control model at day 7. The Peak originating at 828 cm^{-1} can be attributed to ring breathing mode of tyrosine, Phosphodiesters and O-P-O stretching of DNA, moreover a shift to 830 cm^{-1} was present in irradiated models. Band at 853 cm^{-1} can be assigned to proline, hydroxyproline, and ring breathing mode of tyrosine. The band present at 937 cm^{-1}in all models can be associated with Proline (collagen type I), amino acid side chain vibrations of proline and hydroxyproline, C-C stretch backbone (α-helix conformation of protein/collagen assignment).

1003 to 1208 cm^{-1} region

A sharp and intense peak at 1003 cm^{-1} in the control and irradiated models is a typical assignment of symmetric ring breathing mode of phenylalanine. The band present at 1031 cm^{-1} can be attributed to CH_3 CH_2 bending modes of collagen and phospholipids, C-H in-plane bending mode of phenylalanine and C-H stretch of proteins. At day 7 spectral results showed less variations in peak shift which might suggest that the irradiated tissues are regaining their normal cell metabolism. Peak present at 1156 cm^{-1} was observed in all tissue models which can be attributed to C-C, C-N stretching in

proteins. A weak band arising at 1072 cm^{-1} in all models can be an assignment of υ(C-H), tyrosine (protein assignment). A small peak at 1130 cm^{-1} can be attributed to C-C skeletal stretch and structural changes in phospholipids. A weak and short band at 1156 cm^{-1} can be attributed to C-C, C-N stretching in proteins, which was present in all models. Weak spectral contribution at 1173 cm^{-1} in all models can be associated to cytosine, guanine or tyrosine (collagen type I). A band appearing at 1208 cm^{-1} is a protein assignment and attributed to phenylalanine.

1220 to 1280 cm^{-1} region

This region was highly affected by irradiation as significant spectral changes could be observed at different day intervals. Bands appearing in this region are characteristic assignment of proteins which can be attributed to Amide III (protein in α-helix conformation), C-H lipids/amide III collagen assignment and tryptophan.

1317 to 1615 cm^{-1} region

Peaks present at 1317 and 1337 cm^{-1} appeared in all the tissue models and can be assigned to guanine ring breathing modes of DNA/RNA bases, C-H deformation of proteins and nucleic acid modes. The band present at 1449 cm^{-1} in all models can be attributed to C-H vibrations in lipids/proteins. Peak present at 1585 cm^{-1} can be an assignment of C=C Olefinic stretch (protein assignment). Band present at 1605 cm^{-1} is attributed to tyrosine, ring vibration of phenylalanine or C-C of phenylalanine whereas 1615 cm^{-1} can be assigned to C=C of tyrosine or tryptophan (proteins assignment).

1650 to 1700 cm^{-1} region

A broad and strong band present at 1654 cm^{-1} in control and 10 Gy model at day 7 can be attributed to proteins in α-helix structure of amide I. The band shift at 1653 and 1656 cm^{-1} was noticed in 15 and 5 Gy models respectively.

2726 to 3061 cm^{-1} region

A weak band at 2726 cm^{-1} in control and irradiated models was observed, which can be assigned to C-H stretching vibrations in lipids. In the control models, the peak present at 2881 cm^{-1} can be attributed to CH_2 asymmetric stretch of lipids and proteins, whereas there was a shoulder observed in the irradiated models. A strong band arising at 2933 cm^{-1} in all models can be assigned to C-H vibrations in lipids and proteins as well as CH_2 asymmetric stretch in lipids/fatty acids. CH stretching vibrations were present at band originating at 3060 cm^{-1} in control and 5 Gy models whereas it was shifted to 3016 cm^{-1} in 10 and 15 Gy models.

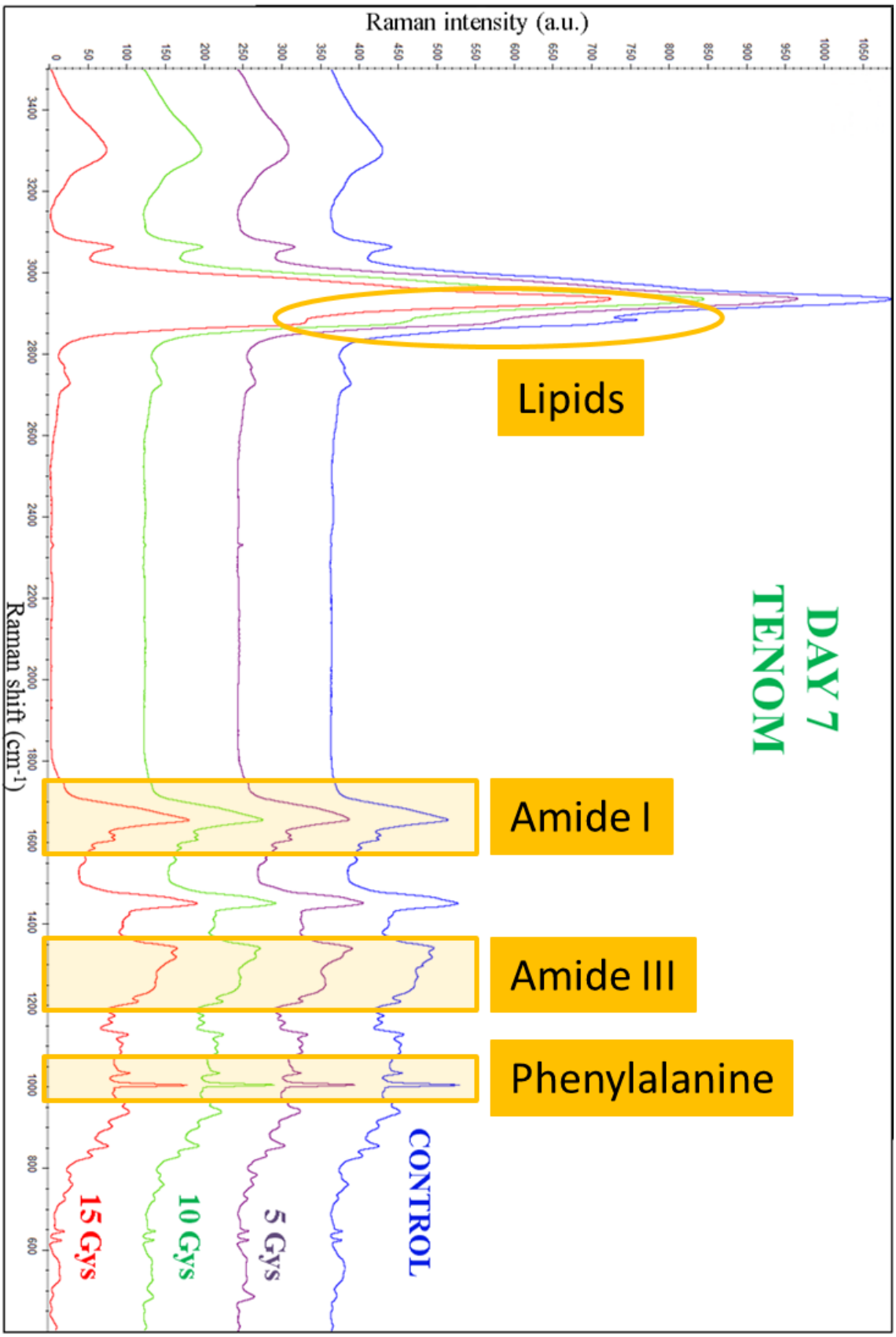

Figure 3. 55 Average spectra of tissue engineered normal oral mucosa (TENOM) at day 7 post radiation, showing control, 5 Gy, 10 Gy and 15 Gy

3.12.2 Tissue Engineered Cancerous Oral Mucosa

Cancer DAY 1

A total of 80 spectra were collected at Day 1 post irradiation of 3D tissue engineered cancerous oral mucosa models using Cal27 cell line. This cancer model was irradiated with 5, 10 and 15 Gy, average spectra of these models are shown in figure 3.56. Peaks were assigned using spectral data base of tissue engineered Cal27 model presented in table 3.1.

Tryptophan and 621 to 958 cm^{-1} region

The bands present at 621 and 643 cm^{-1} can be assigned to C-C twisting modes of phenylalanine and tyrosine; these bands did not appear in the 15 Gy model. A weak band was observed in control, 5 and 10 Gy models at 724 cm^{-1} which can be attributed to ring breathing modes of DNA/RNA bases however in the 15 Gy model, this assignment was observed at 720 cm^{-1}. Peaks present at 759 (control and 10 Gy only), 1208, 1337 (absent in 15 Gy model) and 1615 cm^{-1} (absent in 15 Gy model) are specific assignments of C-C/C=C stretching modes of tryptophan. The band observed at 780 cm^{-1} can be attributed to uracil based ring breathing mode in DNA/RNA which was not present in the 15 Gy model at day 1. The peak originating at 828 cm^{-1} in control, 5 and 10 Gy models was assigned to ring breathing mode of tyrosine, Phosphodiesters and O-P-O stretching of DNA, moreover a shift 815 cm^{-1} was observed in the 15 Gy model. Peak appearing at 853 cm^{-1} was intense in 15 Gy model as compared to the rest of models and was attributed to proline, hydroxyproline, and ring breathing mode of tyrosine. In the 15 Gy model, peak present at 921 cm^{-1} can be assigned to C-C stretch of proline ring. Band arising at 937 cm^{-1} can be assigned to C-C stretch backbone (α-helix conformation of protein), which was only present in the 15 Gy models only.

1002 to 1208 cm^{-1} region

A sharp and intense peak originated at 1002 cm^{-1} in control, 5 and 10 Gy models which is a typical assignment of symmetric ring breathing mode of phenylalanine, in 15 Gy models this peak was shifted to 1003 cm^{-1} with decreased intensity. Band appeared at 1031 cm^{-1} was present in all models which can be assigned to CH_3 CH_2 bending modes of collagen and phospholipids, C-H in-plane bending mode of phenylalanine and C-H stretch of proteins. Spectra of all four models at day 1 showed a weak band appearing at 1096 cm^{-1} which can be attributed to Phosphodioxy groups PO^-_2 in nucleic acids. A small peak at 1127 cm^{-1} can be an assignment of C-C skeletal stretch in lipids which was absent in the 15 Gy model. A weak and short band at 1157 cm^{-1} is attributed to carotenoids, appearing in control, 5 and 10 Gy models only. All models spectra showed weak spectral contribution at 1173 cm^{-1} which can be associated to cytosine, guanine or tyrosine (collagen type I). Band appearing at 1208 cm^{-1} can be a protein assignment and attributed to phenylalanine, where the least spectral contribution in terms of intensity was observed in 15 Gy model.

1246 to 1270 cm^{-1} region

The band appearing in this region is a characteristic assignment of proteins in biological tissues which can be attributed to Amide III (protein in α-helix conformation) and tryptophan. The peak appearing at 1246 cm^{-1} only in 15 Gy model can also be recognised as amide III of collagen furthermore, another peak was also observed in the 15 Gy model at 1267 cm^{-1} which can be attributed to C-H lipids/amide III collagen assignment. In control, 5 and 10 Gy models, band present at 1250 cm^{-1} was attributed to amide III (shifted in 15 Gy).

1317 to 1615 cm^{-1} region

Peaks present at 1317 and 1337 cm^{-1} appeared in all tissue models which were assigned to guanine ring breathing modes of DNA/RNA bases, C-H deformation of proteins and nucleic acid modes, it was observed that the intensities of these peaks decreased from control to 15 Gy tissue model. CH_2 bending in proteins is assigned to the band present at 1448 cm^{-1} in control, 5 and 10 Gy tissue models whereas a shift in this band was observed at 1450 cm^{-1} in 15 Gy model. A peak present at 1583 cm^{-1} was absent in the spectrum of 15 Gy model which can be attributed to C=C bending mode of phenylalanine (protein assignment). The band at 1605 cm^{-1} can be an assignment of tyrosine, ring vibration of phenylalanine or C-C of phenylalanine whereas 1615 cm^{-1} (missing in 15 Gy model) can be attributed to C=C of tyrosine or tryptophan (proteins assignment).

1658 to 1668 cm^{-1} region

A broad and strong band present at 1658 in the control models, 1662 in 5 and 10 Gy and 1668 cm^{-1} in 15 Gy model is a characteristic assignment of proteins in α-helix structure of amide I. A band shift was significantly noticed in the amide I region of control and irradiated tissue engineered model spectra.

2726 to 3061 cm^{-1} region

A weak band at 2725 in 5 Gy model, 2732 in control and 10 Gy model and 2737 cm^{-1} in 15 Gy model was observed, which can be attributed to C-H stretching vibrations in lipids. A shoulder appeared in control and 10 Gy models at 2881 cm^{-1} as compared to a peak in 5 and 15 Gy models**,** which can be assigned to CH_2 asymmetric stretch of lipids and proteins. A strong band arising at 2933 cm^{-1} in the control, 5 and 10 Gy models and shifted to 2940 cm^{-1} in 15 Gy model can be assigned to C-H vibrations in lipids and

proteins as well as CH_2 asymmetric stretch in lipids/fatty acids. CH stretching vibrations were present at band originating at 3061 cm^{-1} in all models except 15 Gy, which showed a shift to 3059 cm^{-1}.

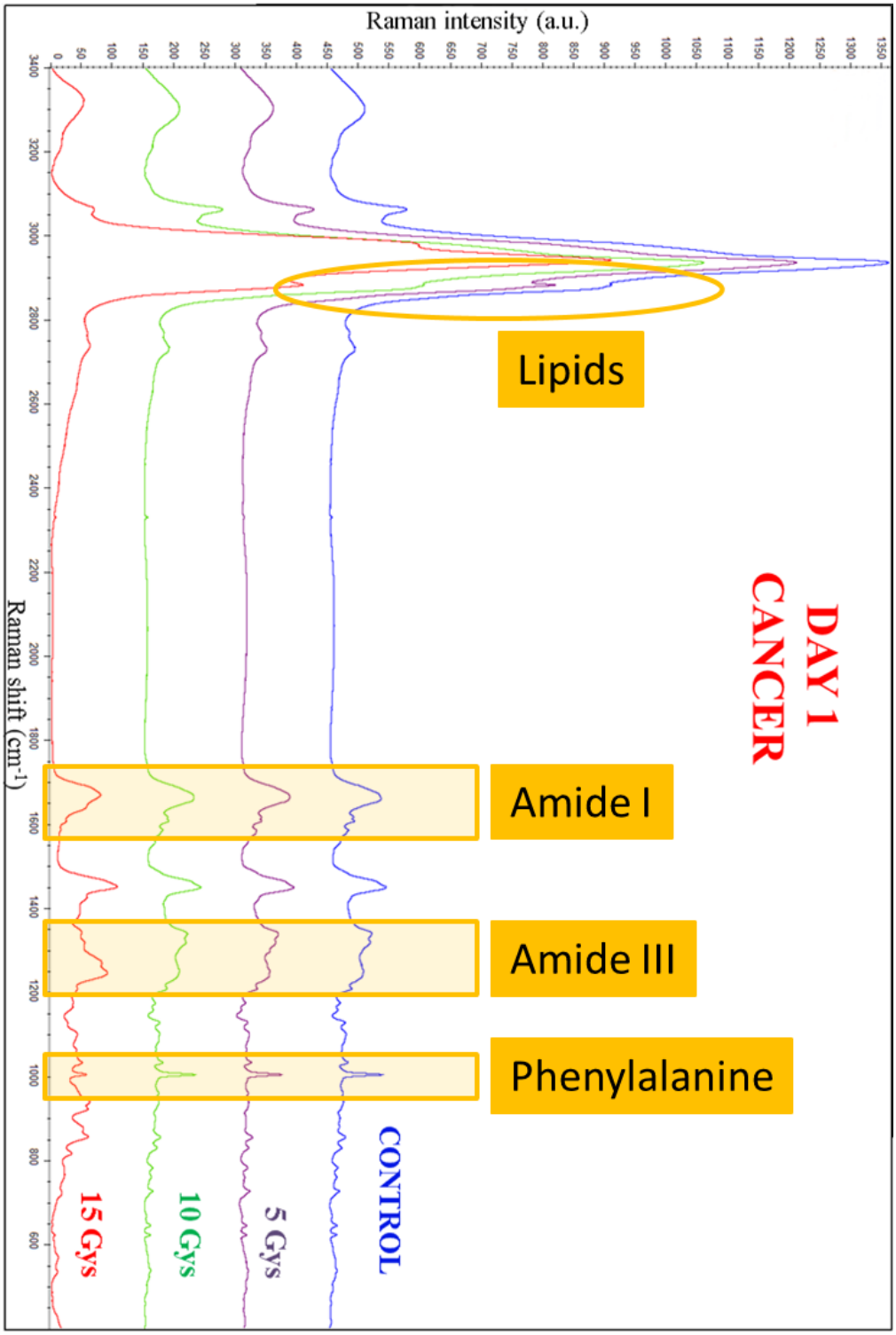

Figure 3. 56 Average spectra of tissue engineered cancerous oral mucosa at day 1 post radiation, showing control, 5 Gy, 10 Gy and 15 Gy

Cancer DAY 4

A total of 80 spectra were collected at Day 4 post irradiation of 3D tissue engineered cancerous oral mucosa models using Cal27 cell line. This cancer model was irradiated with 5 Gy, 10 and 15 Gy, average spectra of these models are shown in figure 3.57.

Tryptophan and 621 to 958 cm^{-1} region

The bands present at 621 and 643 cm^{-1} can be assigned to C-C twisting modes of phenylalanine and tyrosine; these bands did not appear in the 15 Gy model at day 1 post radiation. A weak band was observed in all models at 725 cm^{-1} which can be attributed to ring breathing modes of DNA/RNA bases, spectral differences were visible in this region at day 1. Peaks present at 759 (10 and 15 Gy only), 1208, 1337 and 1615 cm^{-1} are specific assignments of C-C/C=C stretching modes of tryptophan. The band observed at 780 cm^{-1} can be attributed to uracil based ring breathing mode in DNA/RNA which was absent in the 15 Gy model at day 1 however appeared at day 4 spectra. At day 4 the Peak present at 828 cm^{-1} can be assigned to ring breathing mode of tyrosine, Phosphodiesters and O-P-O stretching of DNA, moreover this band was shifted to 815 cm^{-1} in the spectra of 15 Gy model at day 1. The peak appearing at 853 cm^{-1} in the control and irradiated models with variations in peak intensities was attributed to proline, hydroxyproline, and ring breathing mode of tyrosine.

1002 to 1208 cm^{-1} region

Band at 1002 cm^{-1} in the control, 5 and 10 Gy models, is a typical assignment of symmetric ring breathing mode of phenylalanine however this peak was shifted to 1003 cm^{-1} in 15 Gy model. Band appeared at 1031 cm^{-1} was present in all models which can be assigned to CH_3 CH_2 bending modes of collagen and phospholipids, C-H in-plane bending mode of phenylalanine and C-H stretch of proteins. Spectra of all four models showed a weak band appearing at 1096 cm^{-1} which can be attributed to Phosphodioxy

groups PO^-_2 in nucleic acids, 15 Gy model showed the least intense spectral contribution. A small peak at 1127 cm^{-1} can be an assignment of C-C skeletal stretch in lipids which was absent in the 15 Gy model at day 1 but appeared in spectra of day 4 post radiation. A weak and short band at 1157 cm^{-1} can be attributed to carotenoids, only present in 10 and 15 Gy spectra. All models spectra showed weak spectral contribution at 1173 cm^{-1} which can be associated to cytosine, guanine or tyrosine (collagen type I). The band appearing at 1208 cm^{-1} can be a protein assignment and attributed to phenylalanine.

1246 to 1270 cm^{-1} region

The band present in this region represents characteristic protein assignments in biological tissues which can be attributed to Amide III (protein in α-helix conformation) and tryptophan. Band present at 1250 cm^{-1} in all cancer models at day 4 can be attributed to amide III. A lot of variations have been observed in this region with regards to spectra of day 1 and 15 Gy models.

1317 to 1615 cm^{-1} region

Peaks present at 1317 and 1337 cm^{-1} appeared in all tissue models were assigned to guanine ring breathing modes of DNA/RNA bases, C-H deformation of proteins and nucleic acid modes, narrowness and broadness of peaks was present between control and irradiated models suggesting stress on different tissue types. CH_2 bending in proteins can be assigned to the band present at 1448 cm^{-1} in all tissue models. A peak present at 1583 cm^{-1} can be attributed to C=C bending mode of phenylalanine (protein assignment), which was absent in 15 Gy model at day 1 spectra. The band at 1605 cm^{-1} can be assigned to tyrosine, ring vibration of phenylalanine or C-C of phenylalanine whereas 1615 cm^{-1} (absent in 15 Gy model at day 1) is attributed to C=C of tyrosine or tryptophan (proteins assignment).

1656 to 1664 cm^{-1} region

A broad and strong band present at 1664 cm^{-1} in control model, 1662 cm^{-1} in 5 and 10 Gy and 1656 cm^{-1} in 15 Gy model is a characteristic assignment of proteins in α-helix structure of amide I.

2726 to 3061 cm^{-1} region

A weak band at 2726 cm^{-1} in the control, 5 and 15 Gy model, 2732 cm^{-1} in 10 Gy model can be assigned to C-H stretching vibrations in lipids. A shoulder appeared in 10 Gy models at 2881 cm^{-1} as compared to a peak in control, 5 and 15 Gy models**,** which can be assigned to CH_2 asymmetric stretch of lipids and proteins. A strong band arising at 2933 cm^{-1} in all models can be attributed to C-H vibrations in lipids and proteins as well as CH_2 asymmetric stretch in lipids/fatty acids. CH stretching vibrations were present at band originating at 3061 cm^{-1} in all models spectra.

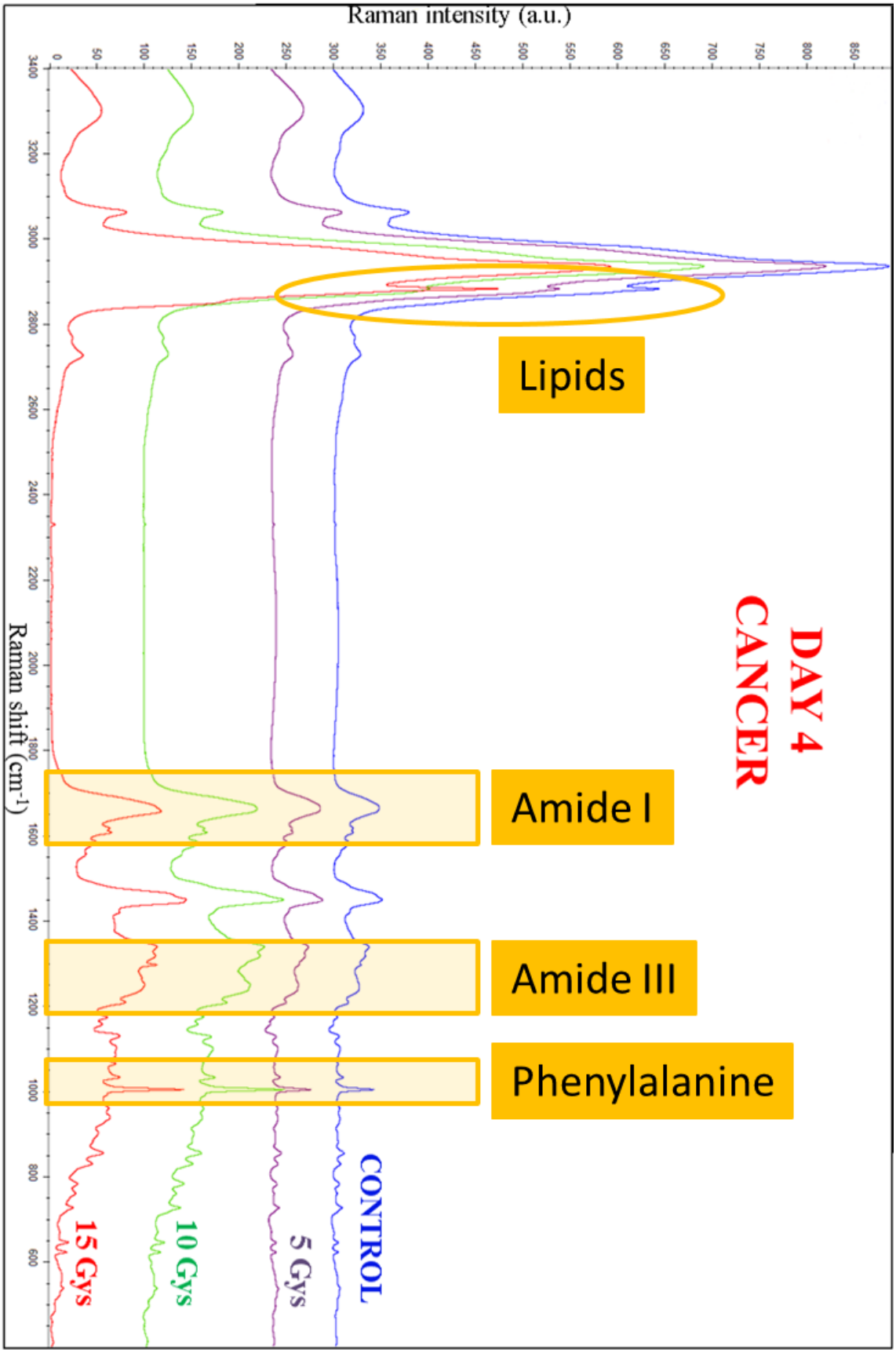

Figure 3. 57 Average spectra of tissue engineered cancerous oral mucosa at day 4 post radiation, showing control, 5 Gy, 10 Gy and 15 Gy

Cancer DAY 7

A total of 80 spectra were collected at Day 7 post irradiation of 3D tissue engineered cancerous oral mucosa models using the Cal27 cell line. This cancer model was irradiated with 5, 10 and 15 Gy, average spectra of these models are shown in figure 3.58.

Tryptophan and 621 to 935 cm^{-1} region

The bands present at 621 and 643 cm^{-1} can be attributed to C-C twisting modes of phenylalanine and tyrosine. A weak band was observed at 725 cm^{-1} which can be assigned to ring breathing modes of DNA/RNA. Peaks present at 759, 1208, 1337 and 1615 cm^{-1} are specific assignments of C-C/C=C stretching modes of tryptophan. It was observed that the tryptophan peaks started to appear in tissue models after 7 days of irradiation however they were absent at day 4 post radiations. Band observed at 780 cm^{-1} can be assigned to uracil based ring breathing mode in DNA/RNA which was not observed in the 15 Gy model at day 1. The peak originating at 828 cm^{-1} can be attributed to ring breathing mode of tyrosine, phosphodiester groups and O-P-O stretching of DNA, this band was not seen in 15 Gy model at day 1 spectra. Band present at 853 cm^{-1} can be attributed to proline, hydroxyproline, and ring breathing mode of tyrosine. Band arising at 935 cm^{-1} can be an assignment of C-C stretching mode of proline and valine and protein backbone (α-helix conformation of protein).

1002 to 1208 cm^{-1} region

A sharp peak at 1002 cm^{-1} in all models is a typical assignment of symmetric ring breathing mode of phenylalanine. The band at 1031 cm^{-1} can be assigned to CH_3 CH_2 bending modes of collagen and phospholipids, C-H in-plane bending mode of phenylalanine and C-H stretch of proteins. Spectra of all models except 5 Gy at day 7 showed a weak band appearing at 1096 cm^{-1} which can be assigned to Phosphodioxy

groups PO^{-}_{2} in nucleic acids. A small peak at 1127 cm^{-1} can be attributed to C-C skeletal stretch in lipids. A weak and short band at 1157 cm^{-1} can be assigned to carotenoids. All models spectra showed weak spectral contribution at 1173 cm^{-1} which can be associated to cytosine, guanine or tyrosine (collagen type I). The band present at 1208 cm^{-1} is a protein assignment and attributed to phenylalanine.

1245 to 1270 cm^{-1} region

Bands present in this region are typical assignments of proteins in biological tissues which can be attributed to Amide III (protein in α-helix conformation) and tryptophan. Peak appearing at 1250 cm^{-1} can be recognised as amide III of collagen, C-H lipids/amide III collagen assignment, amide III (protein assignment).

1317 to 1615 cm^{-1} region

Bands present at 1317 and 1337 cm^{-1} appeared in all tissue models can be assigned to guanine ring breathing modes of DNA/RNA bases, C-H deformation of proteins and nucleic acid modes. CH_2 bending in proteins can be assigned to the band present at 1448 cm^{-1} in all models at day 7 post irradiation. There was a shift in band observed in 15 Gy model at day 1 and 4. A peak present at 1583 cm^{-1} can be attributed to C=C bending mode of phenylalanine (protein assignment), this band was absent in 15 Gy models at day 1. Band at 1605 cm^{-1} can be attributed to tyrosine, ring vibration of phenylalanine or C-C of phenylalanine whereas 1615 cm^{-1} (missing in 15 Gy model at day 1) can be attributed to C=C of tyrosine or tryptophan (proteins assignment).

1658 to 1663 cm^{-1} region

A broad and strong band present at 1658 cm^{-1} in control model, 5 and 15 Gy models is a characteristic assignment of proteins in α-helix structure of amide I. Band shift to 1664 cm^{-1} in 10 Gy model was significantly noticed.

2732 to 3060 cm^{-1} region

A weak band at 2732 cm^{-1} in control model, 2728 cm^{-1} in 5 Gy model, 2726 cm^{-1} in 10 Gy model and 2725 cm^{-1} in 15 Gy model was observed, which can be assigned to C-H stretching vibrations in lipids. A shoulder appeared in control model in contrast to peaks present at 2881 cm^{-1} in irradiated models**,** which can be attributed to CH_2 asymmetric stretch of lipids and proteins. A strong band arising at 2933 cm^{-1} in all models can be attributed to C-H vibrations in lipids and proteins as well as CH_2 asymmetric stretch in lipids/fatty acids. CH stretching vibrations were present at band originating at 3060 cm^{-1} in all models.

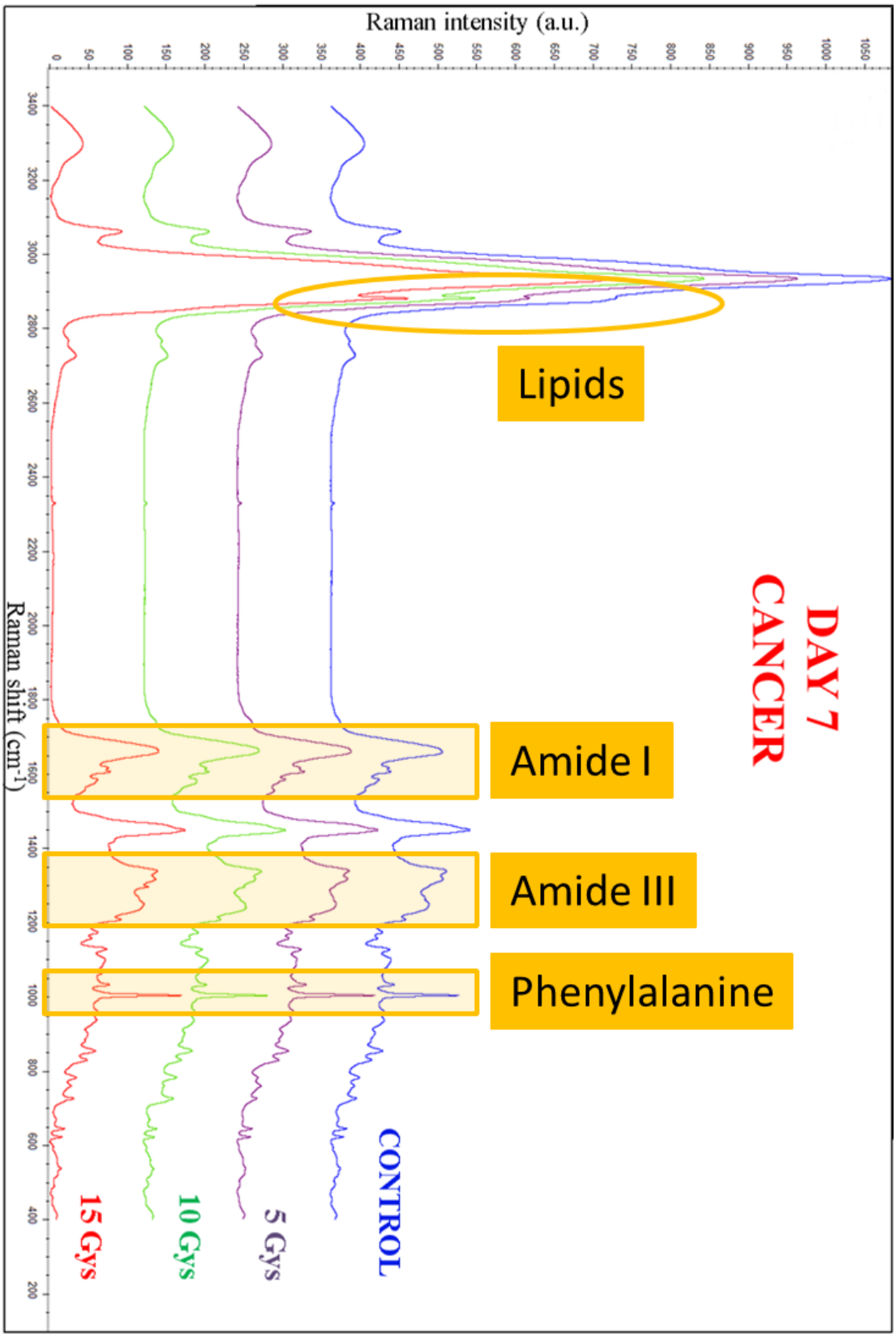

Figure 3. 58 Average spectra of tissue engineered cancerous oral mucosa at day 7 post radiation, showing control, 5 Gy, 10 Gy and 15 Gy

3.13 Peak Height Analysis

Peak height analysis was performed to analyse variations in peak intensities of specific biomolecules such as Phenylalanine (proteins) and DNA (nucleic acid). Analysis was conducted between tissue engineered normal oral mucosa (TENOM) and cancer models. Peak heights of control and irradiated models were evaluated over time i.e. day 1, 4 and 7 post radiations (figure 3.59 and 3.60).

TENOM showed better resistance to radiation as compared to cancer models on these specific biomolecules. Gradual increase in peak intensities of TENOM was observed with increased incubation times whereas cancer models have shown significant decrease in the intensity of these macromolecules. These findings may suggest that phenylalanine (proteins) and DNA (nucleic acid) are seriously damaged by radiation in cancer models however the repair process of these molecules was more stable and consistent in normal mucosa model.

Although the irradiated cancer models have shown increase in intensities of phenylalanine and DNA with the passage of time but it is not as significant as it is in normal mucosa models.

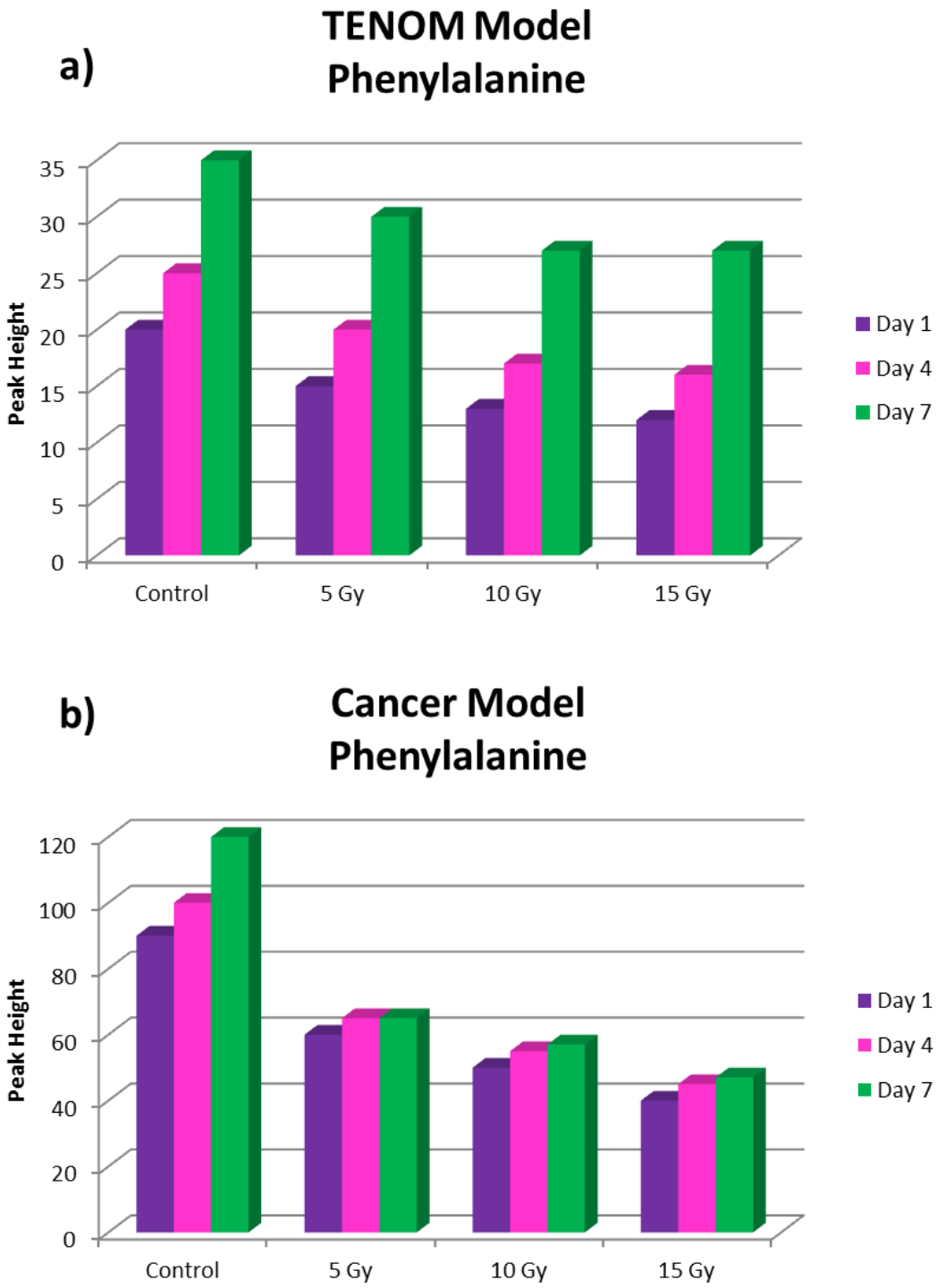

Figure 3. 59 Peak height analysis of Phenylalanine between control and irradiated models at day 1, 4 and 7 post radiation. a) TENOM model b) Cancer model

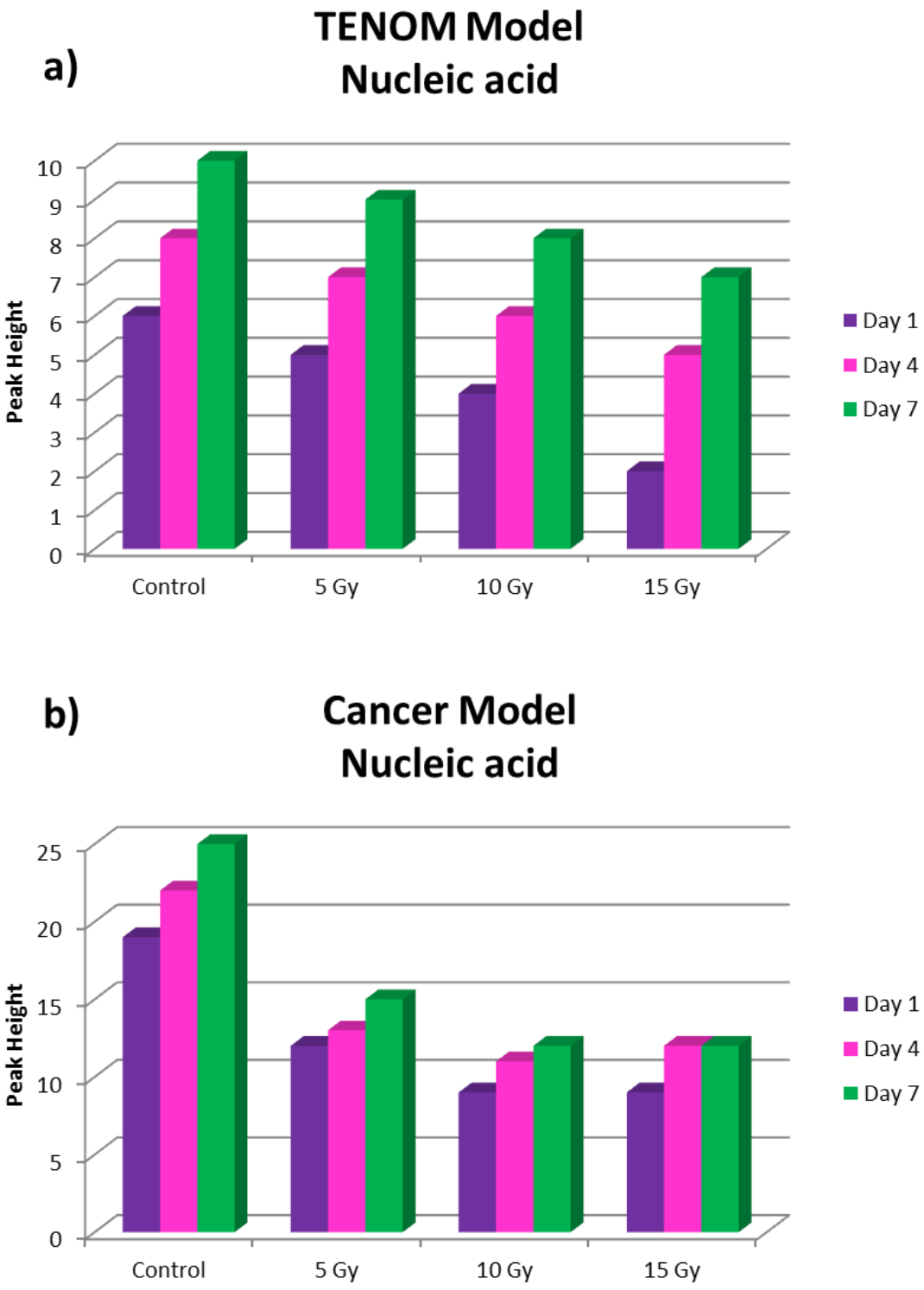

Figure 3. 60 Peak height analysis of nucleic acid between control and irradiated models at day 1, 4 and 7 post radiation. a) TENOM model b) Cancer model

3.14 Multivariate data analysis

Tissue Engineered Normal Oral Mucosa

Principal Component Analysis

In this study principal component analysis (PCA) was used to differentiate between effects of radiations on tissue engineered normal (TENOM) and cancerous (CANCER) oral mucosa on the basis of spectral variances.

PCA was performed over complete spectral range (400 to 3400 cm^{-1}), 2700 to 3100 cm^{-1} (Lipids/proteins), 1550 to 1750 cm^{-1} (amide I), 1200 to 1400 cm^{-1} (amide III) and 800 to 1200 cm^{-1} (DNA/Proteins) region. The comparison was conducted between control, 5, 10 and 15 Gy at Day 1, 4 and 7 post radiations.

TENOM DAY 1

400 to 3400 cm^{-1} (Complete Spectral Range)

PCA results over the complete spectral range showed 87% of variance where clear separation between the control and irradiated group was observed. PC1 distinguished 5 and 10 Gy from the control; moreover the first component also separated 15 Gy from the rest of irradiated models. The second component distinctly separated control from 10 and 15 Gy but a lesser variance was observed with 5 Gy model (figure 3.61a & f).

2700 to 3100 cm^{-1} Region

PCA results over the 2700 to 3100 cm^{-1} spectral range at day 1 post radiation in TENOM showed 95% of variance with clear separation between the control and irradiated models. PC1 separated control and 15 Gy from the rest of radiated models; whereas the second component was able to differentiate control and 5 Gy from 10 and 15 Gy (figure 3.61b & g).

1550 to 1750 cm^{-1} (amide I) Region

At 1550 to 1750 cm^{-1} (amide I) region, PCA results showed 81% of variance where most of control and 5 Gy models were differentiated from 15 Gy however 10 Gy model showed similarities with 5 Gy as well as 15 Gy in PC1. PC2 separated control tissues from irradiated ones in the amide I region where a few of control and 15 Gy models assembling quite close to each other (figure 3.61c & h).

1200 to 1400 cm^{-1} (amide III) Region

Maximum amount of variance (97%) was recorded in the 1200 to 1400 cm^{-1} region referred to as amide III. PCA results at day 1 post radiation have shown intra tissue variations which have resulted in scattered cluster formations (figure 3.61d). PC1 of the amide III region clearly separated 15 Gy from 5 and 10 Gy whereas control tissue showed significant variance within its group. In PC2, 10 Gy distinctly separated from control and 5 Gy whereas few of the 15 Gy models showed less variance with 10 Gy models (figure 3.61d).

800 to 1200 cm^{-1} (DNA/Proteins) Region

The spectral range between 800 to 1200 cm^{-1}, accounts for DNA and proteins such as tryptophan, phenylalanine, tyrosine and proline. The amount of variance recorded in this region was 97%. PC1 discriminated control from 5 and 10 Gy and 15 Gy to a lesser extent. The second component resulted in clear separation of control and 5 Gy with 15 Gy models whereas the 10 Gy model showed equal similarities with 5 and 15 Gy (figure 3.61e & j).

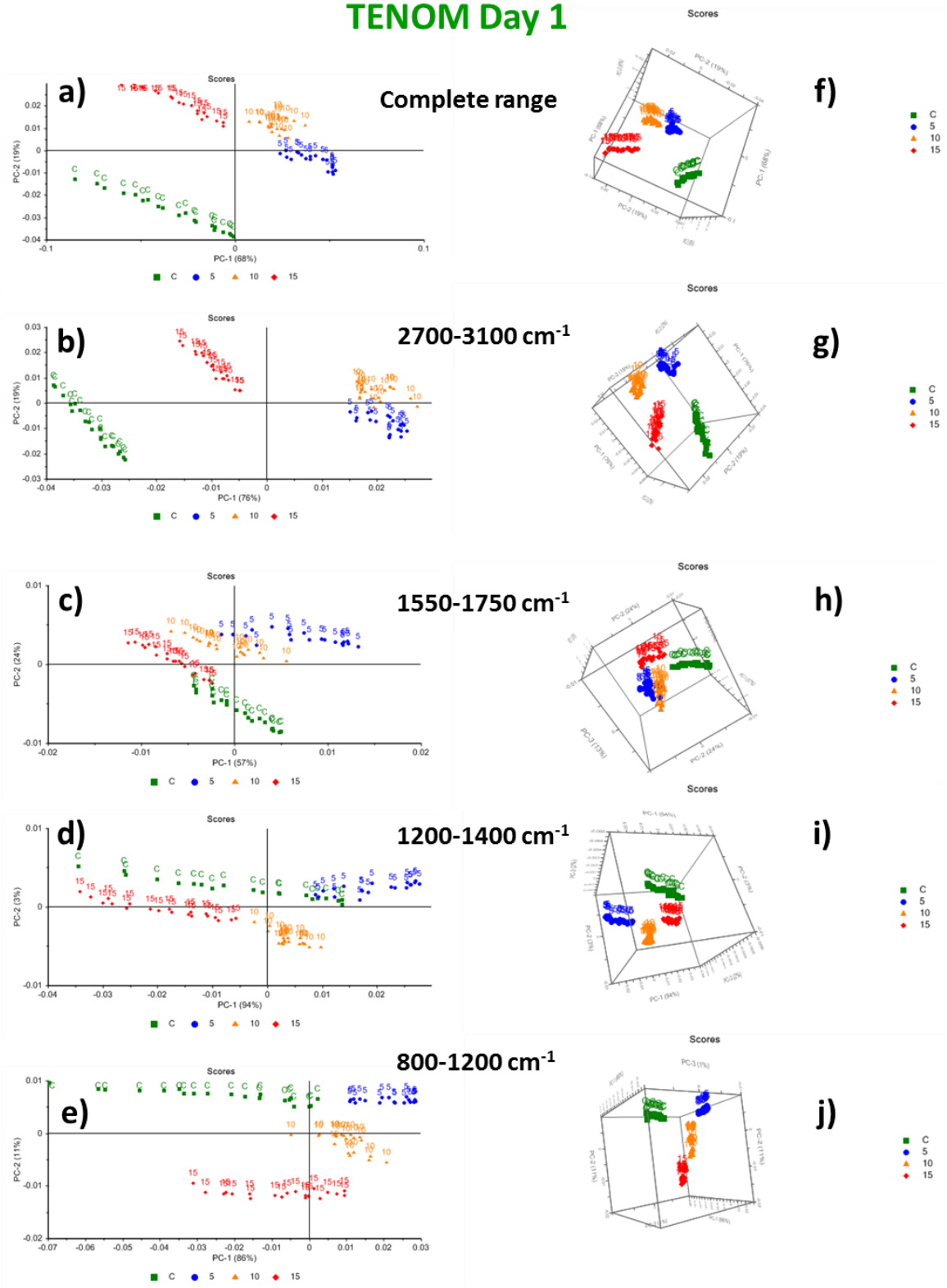

Figure 3. 61 PCA results of TENOM at DAY 1 post radiation. (a-e) 2D plots over complete spectral range, 2700 to 3100 cm-1, 1550 to 1750 cm-1, 1200 to 1400 cm-1 and 800 to 1200 cm-1 region respectively. (f-j) Corresponding 3D plots showing first 3 PC's

TENOM DAY 4

400 to 3400 cm^{-1} (Complete Spectral Range)

At day 4, cluster formation of control and irradiated models was more compact and distinct as compared to day 1. PCA results over the complete spectral range showed 93% of variance in PC1 and PC2 with strong separation between the control and irradiated groups. PC1 showed 73% of variance and distinguished controls from 5, 10 and 15 Gy. The second component distinctly separated 15 Gy models from 5 and 10 Gy as well. It was observed that not only controls were differentiated from the irradiated models but separation between irradiated models was also present (figure 3.62a & f).

2700 to 3100 cm^{-1} Region

PCA results over the 2700 to 3100 cm^{-1} spectral range at day 4 post radiation in TENOM showed 93% of variance with clear separation between the control and irradiated models. PC1 separated 15 Gy from control, 5 and 10 Gy models; whereas the second component was able to differentiate 15 Gy from 5 and 10 Gy as well as controls from 5 and 10 Gy models (figure 3.62b & g).

1550 to 1750 cm^{-1} (amide I) Region

At 1550 to 1750 cm^{-1} (amide I) region, PCA results showed 93% of variance where the first component was able to distinguish controls from all of irradiated models. PC2 completely separated 5 Gy models from the rest of irradiated ones and controls to a slightly lesser extent (figure 3.62c & h).

1200 to 1400 cm^{-1} (amide III) Region

Maximum amount of variance (99%) was recorded in the 1200 to 1400 cm^{-1} region. PC1 of the amide III region clearly separated controls from the rest of irradiated data set and more compact cluster formation is seen. In PC2, again 15 Gy models were differentiated from 5 Gy and to a lesser extent with 10 Gy (figure 3.62d & i).

800 to 1200 cm^{-1} (DNA/Proteins) Region

The amount of variance recorded in this region was 98%. PC1 discriminated control from irradiated models where 5 Gy cluster was observed closest to controls. The second component differentiated 5 and 15 Gy from 10 Gy and control models (figure 3.62e & j).

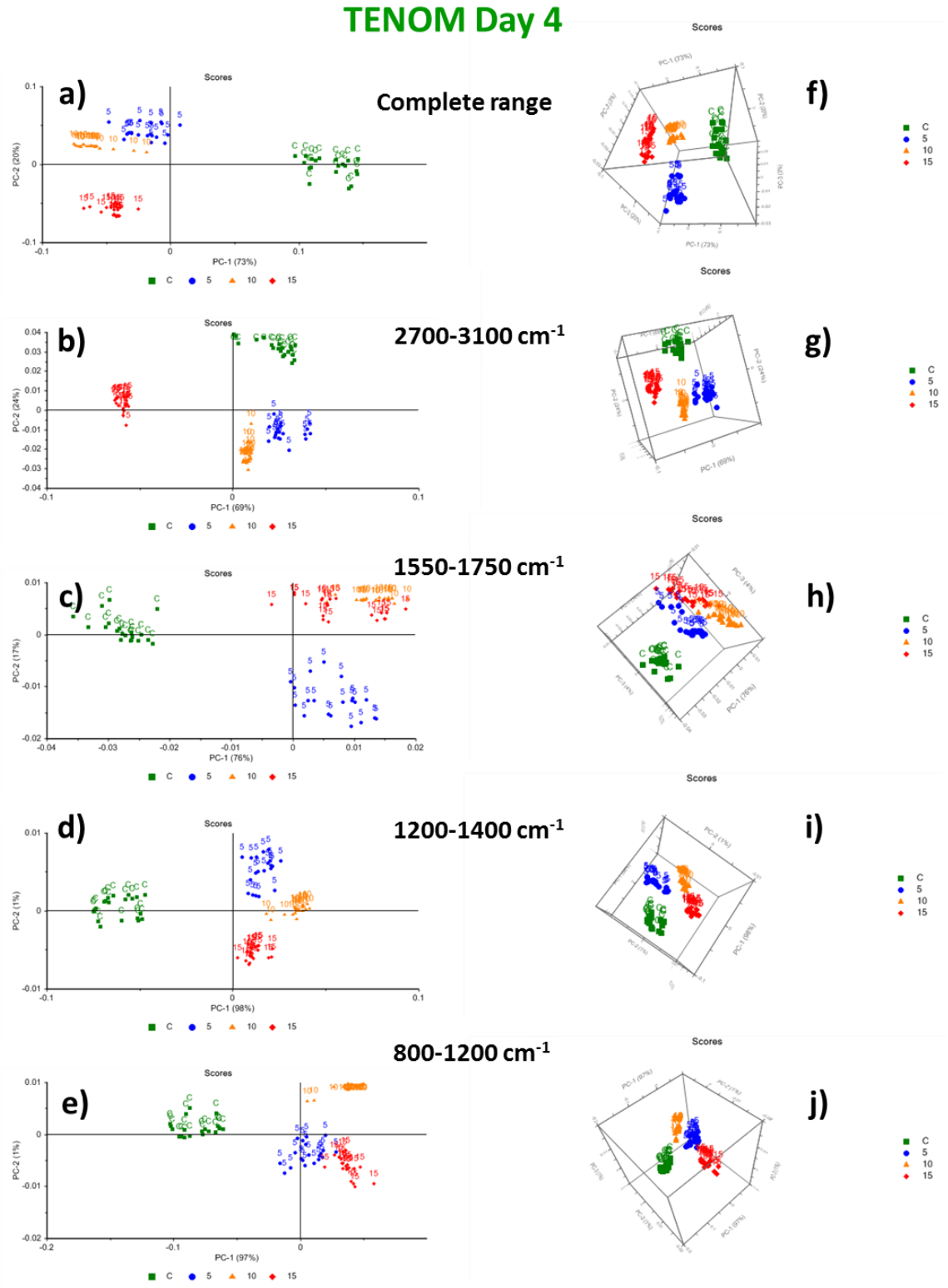

Figure 3. 62 PCA results of TENOM at DAY 4 post radiation. (a-e) 2D plots over complete spectral range, 2700 to 3100 cm-1, 1550 to 1750 cm-1, 1200 to 1400 cm-1 and 800 to 1200 cm-1 region respectively. (f-j) Corresponding 3D plots showing first 3 PC's

TENOM DAY 7

400 to 3400 cm^{-1} (Complete Spectral Range)

At day 7, generally it was seen that 5 Gy and 10 Gy clusters were placed relatively closer to control models. PCA results over the complete spectral range showed 90% of variance where PC1 differentiated controls and 5 Gy models from 15 Gy model. Cluster for 10 Gy showed similarities with both 15 Gy and 5 Gy in PC1. The second component distinctly separated 5 Gy models from control whereas lesser variance was observed amongst irradiated models (figure 3.63a & f).

2700 to 3100 cm^{-1} Region

PCA results over the 2700 to 3100 cm^{-1} spectral range at day 7 post radiation in TENOM showed 95% of variance where PC1 significantly differentiated control models from the irradiated ones. The second component was able to differentiate 5 Gy from 15 Gy however 10 Gy showed equal similarities with both (figure 3.63b & g).

1550 to 1750 cm^{-1} (amide I) Region

The amide 1 region showed interesting trend in cluster formation where 5 and 10 Gy moved closer to control at day 7. The first component differentiated 15 Gy from the rest of models whereas in PC2 5Gy was separated from irradiated and control models (figure 3.63c & h).

1200 to 1400 cm^{-1} (amide III) Region

In comparison to the amide I region, similar pattern was observed in amide III compartment where 5 and 10 Gy clusters moved close to control in the first component and 15 Gy was separated from them. In PC2, 15 Gy model was differentiated from 5 Gy and to a lesser extent with 10 Gy (figure 3.63d & i).

800 to 1200 cm^{-1} (DNA/Proteins) Region

The amount of variance recorded in this region was 98%. PC1 separated control and 5 Gy from 15 Gy, moreover, 10 Gy cluster was formed very close to control as well as possessed similarities with 15 Gy. PC2 differentiated 5 and 15 Gy from 10 Gy and control models where control cluster formation was near to 5 Gy (figure 3.63e & j).

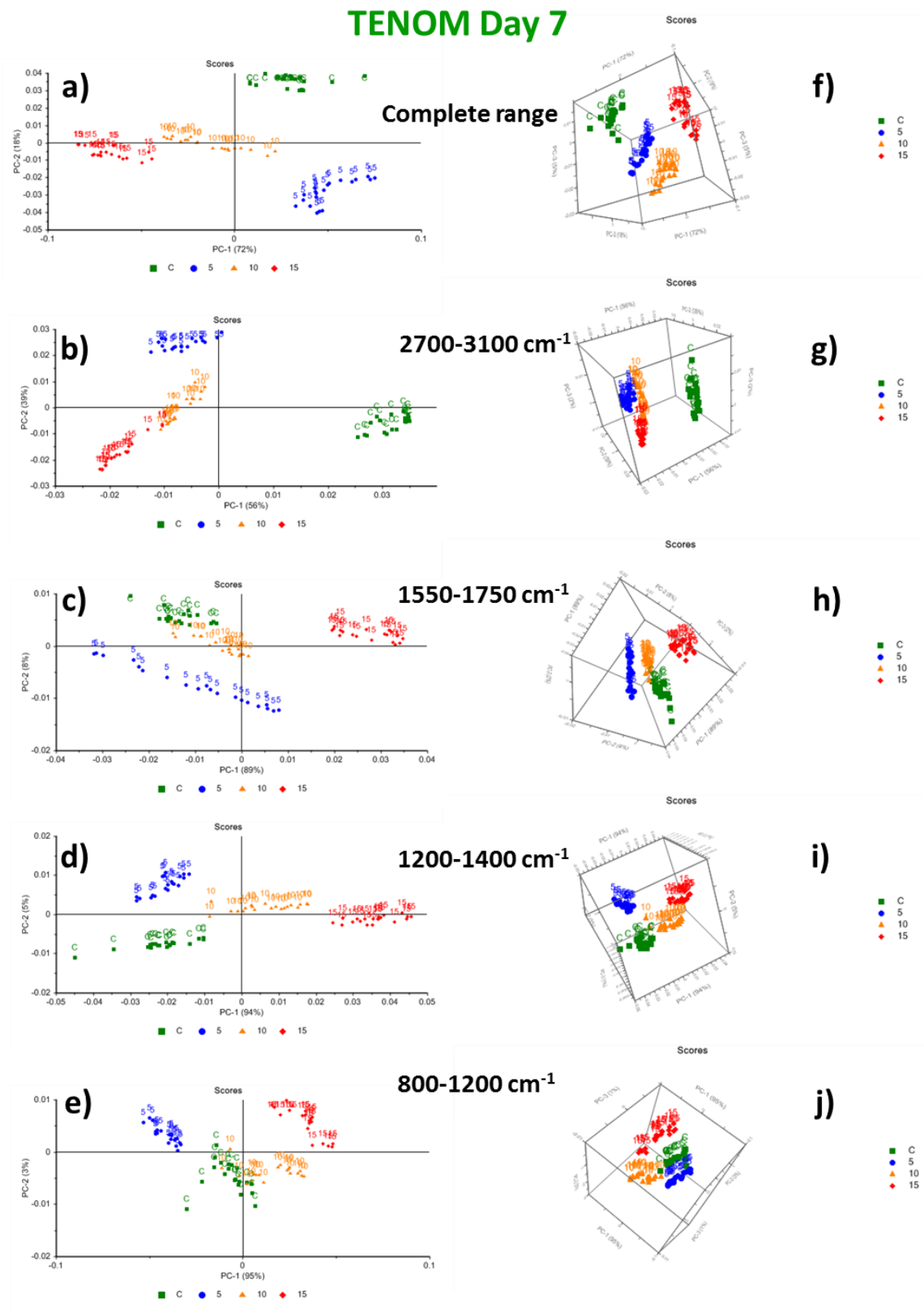

Figure 3. 63 PCA results of TENOM at DAY 7 post radiation. (a-e) 2D plots over complete spectral range, 2700 to 3100 cm-1, 1550 to 1750 cm-1, 1200 to 1400 cm-1 and 800 to 1200 cm-1 region respectively. (f-j) Corresponding 3D plots showing first 3 PC's

Tissue Engineered Cancerous Oral Mucosa

CANCER DAY 1

400 to 3400 cm^{-1} (Complete Spectral Range)

At day 1, over the complete spectral range in cancer models it was seen that control and 5 Gy models were differentiated by 10 and 15 Gy in the first component. The second component distinctly separated 15 Gy model from the rest of radiated models as well as control (figure 3.64a & f).

2700 to 3100 cm^{-1} Region

PCA results over the 2700 to 3100 cm^{-1} spectral range at day 7 in cancer models showed that control and 5 Gy models were differentiated from the rest of irradiated models in PC1. The second component showed differentiation between irradiated models (figure 3.64b & g).

1550 to 1750 cm^{-1} (amide I) Region

PCA results at amide 1 region showed a different behaviour of cluster formations. In contrast to the high wavenumber region, the control model was clearly discriminated from the irradiated ones. The first component differentiated control and 5 Gy from the rest of models whereas in PC2, 5Gy was separated from control as well as 10 Gy model (figure 3.64c & h).

1200 to 1400 cm^{-1} (amide III) Region

In consideration to the amide I region, similar arrangement of clusters was observed in amide III compartment where the first component differentiated control from 5 and 10 Gy and at the same time 15 Gy from the rest of irradiated models. In PC2, 10 and 15 Gy models were differentiated from control and 5 Gy (figure 3.64d & i).

800 to 1200 cm^{-1} Region

The amount of variance recorded in this region was 98%. PC1 differentiated control and 15 Gy from the other two radiated models however, in PC2 the control models were completely differentiated by irradiated models (figure 3.64e & j).

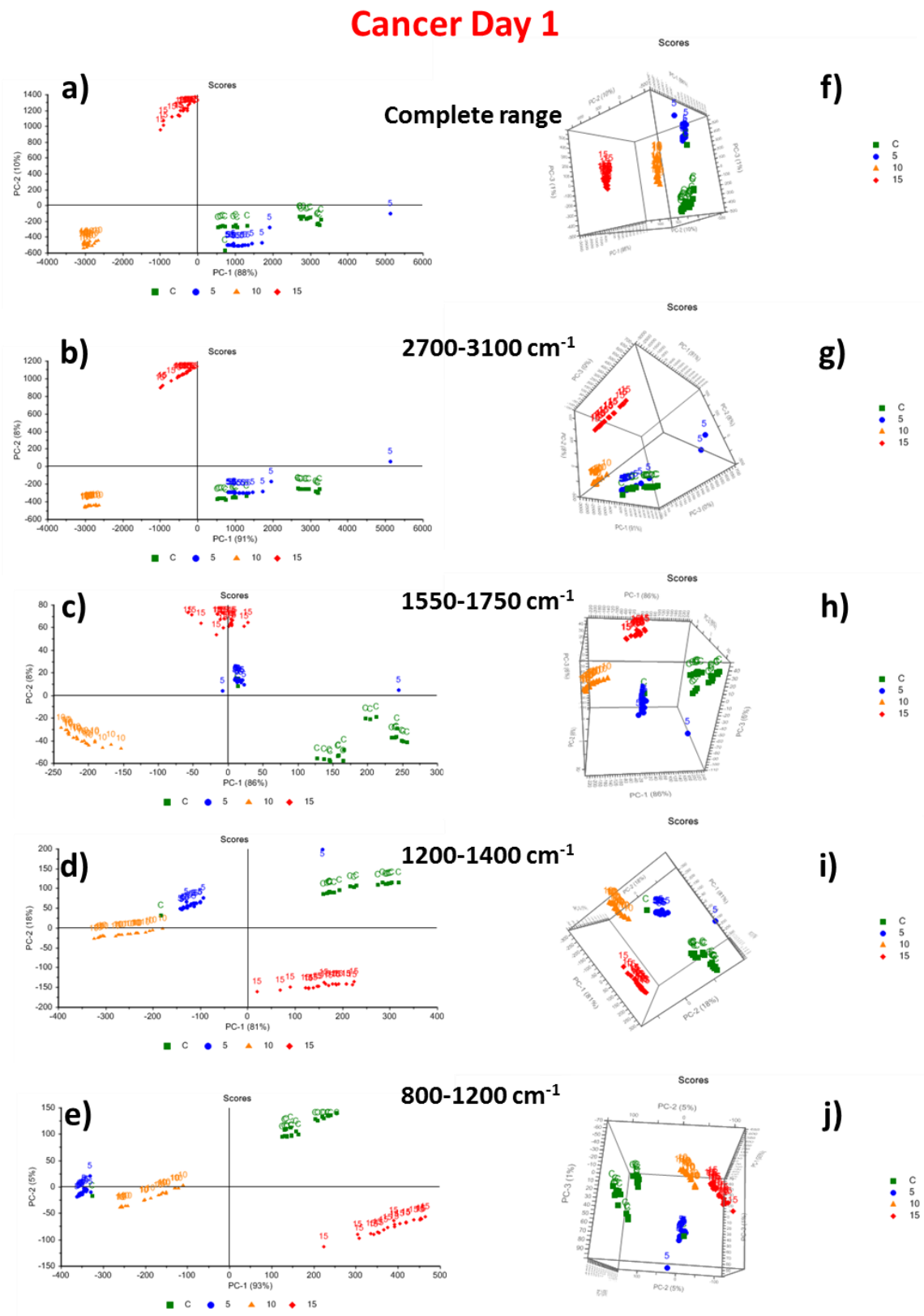

Figure 3. 64 PCA results of T.E cancer model at DAY 1 post radiation. (a-e) 2D plots over complete spectral range, 2700 to 3100 cm-1, 1550 to 1750 cm-1, 1200 to 1400 cm-1 and 800 to 1200 cm-1 region respectively. (f-j) Corresponding 3D plots showing first 3 PC's

CANCER DAY 4

400 to 3400 cm^{-1} (Complete Spectral Range)

PCA results over the complete spectral range at day 4 in cancer models showed that in PC1 control and 5 Gy models were placed very close to each other and differentiated from 10 and 15 Gy. The second component was able to separate 10 Gy model from 15 Gy significantly however control was discriminated from 5 Gy model to a lesser extent (figure 3.65a & f).

2700 to 3100 cm^{-1} Region

PCA results over the 2700 to 3100 cm^{-1} spectral range at day 4 were consistent with complete spectral range. Similar trends were observed where PC1 differentiated control and 5 Gy from the rest of irradiated models and in PC2, 10 and 15 Gy models were differentiated from one another. The distinct feature observed at day 4 post radiation was that the 5 Gy model had moved fairly close to control (figure 3.65b & g).

1550 to 1750 cm^{-1} (amide I) Region

The first component differentiated control and 5 Gy from the rest of models whereas in PC2 5Gy was separated from control as well as 15 Gy model (figure 3.65c & h).

1200 to 1400 cm^{-1} (amide III) Region

In amide III region the first component distinguished control and 5 Gy from 10 and 15 Gy. In PC2, lesser differentiation was seen between control and 5 Gy, however 10 and 15 Gy models were clearly separated from one another (figure 3.65d & i).

800 to 1200 cm^{-1} Region

The amount of variance recorded in this region was 99%. Control and 5 Gy clusters were closely packed in this region and differentiation could hardly be seen. In PC1, 10 and 15 Gy models were differentiated from control and 5 Gy whereas in PC2, 15 Gy model was separated from the rest of models including control (figure 3.65e & j).

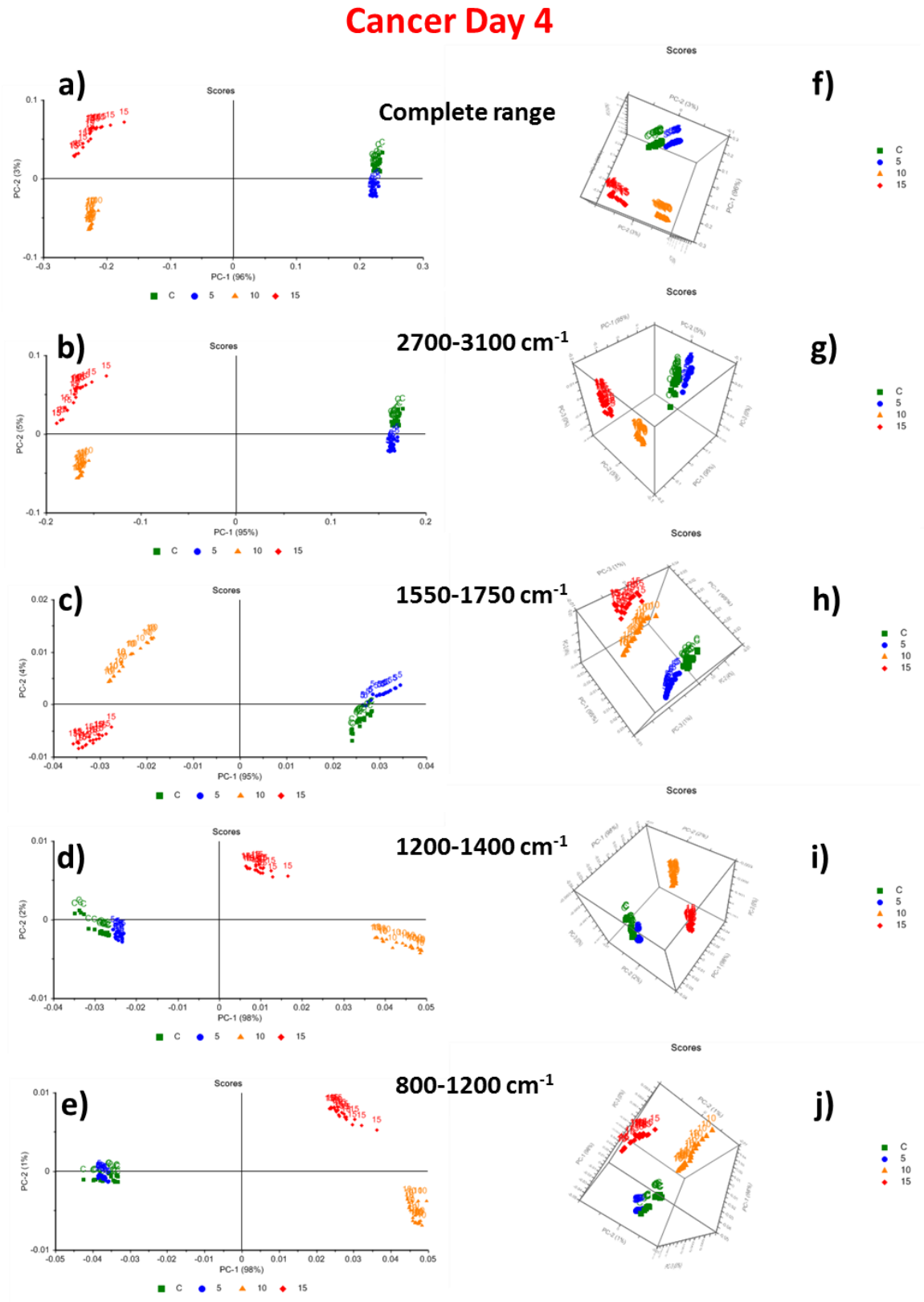

Figure 3. 65 PCA results of T.E cancer model at DAY 4 post radiation. (a-e) 2D plots over complete spectral range, 2700 to 3100 cm-1, 1550 to 1750 cm-1, 1200 to 1400 cm-1 and 800 to 1200 cm-1 region respectively. (f-j) Corresponding 3D plots showing first 3 PC's

Cancer DAY 7

400 to 3400 cm^{-1} (Complete Spectral Range)

PCA results over the complete spectral range at day 7 in cancer models showed that the irradiated models had moved towards the control as they have started to regain cancerous properties with the passage of time. The cluster formation was not as condensed as it was at day 1 and day 4 which may suggest increased biochemical activities at cellular level. PC1 showed clear separation of 15 Gy model with control and 5 Gy where 10 Gy showed similarities towards both control and 15 Gy. The second component was only able to separate 10 Gy model from 15 Gy but to a lesser extent as compared to day 4 (figure 3.66a & f).

2700 to 3100 cm^{-1} Region

In this region, the first component differentiated control and 5 Gy from 15 Gy model whereas 10 Gy cluster was placed in between them showing more similarities with control model. Lesser variations were observed in PC2 where 10 Gy model was separated from the rest to a lesser extent as compared to day 1 and 4 (figure 3.66b & g).

1550 to 1750 cm^{-1} (amide I) Region

A different pattern and cluster arrangement was observed in the amide I region at day 7 where all groups were closely placed and mixed to one another suggesting highest metabolic rate (figure 3.66c & h).

1200 to 1400 cm^{-1} (amide III) Region

In the amide III region, PC1 differentiated 15 Gy model from the rest but to a lesser extent from 10 Gy. The relatively scattered cluster formation showed transformation of irradiated models towards control. PC2 could only differentiate 10 Gy from 5 Gy model significantly (figure 3.66d & i).

800 to 1200 cm^{-1} Region

The amount of variance recorded in this region was 90%. Control and 5 Gy models were closely packed and differentiation could hardly be seen amongst them. In PC1, 10 and 15 Gy models were differentiated from control and 5 Gy but the trend was observed that they are moving towards control. In PC2, 10 Gy model was separated from the rest of models including control (figure 3.66e & j).

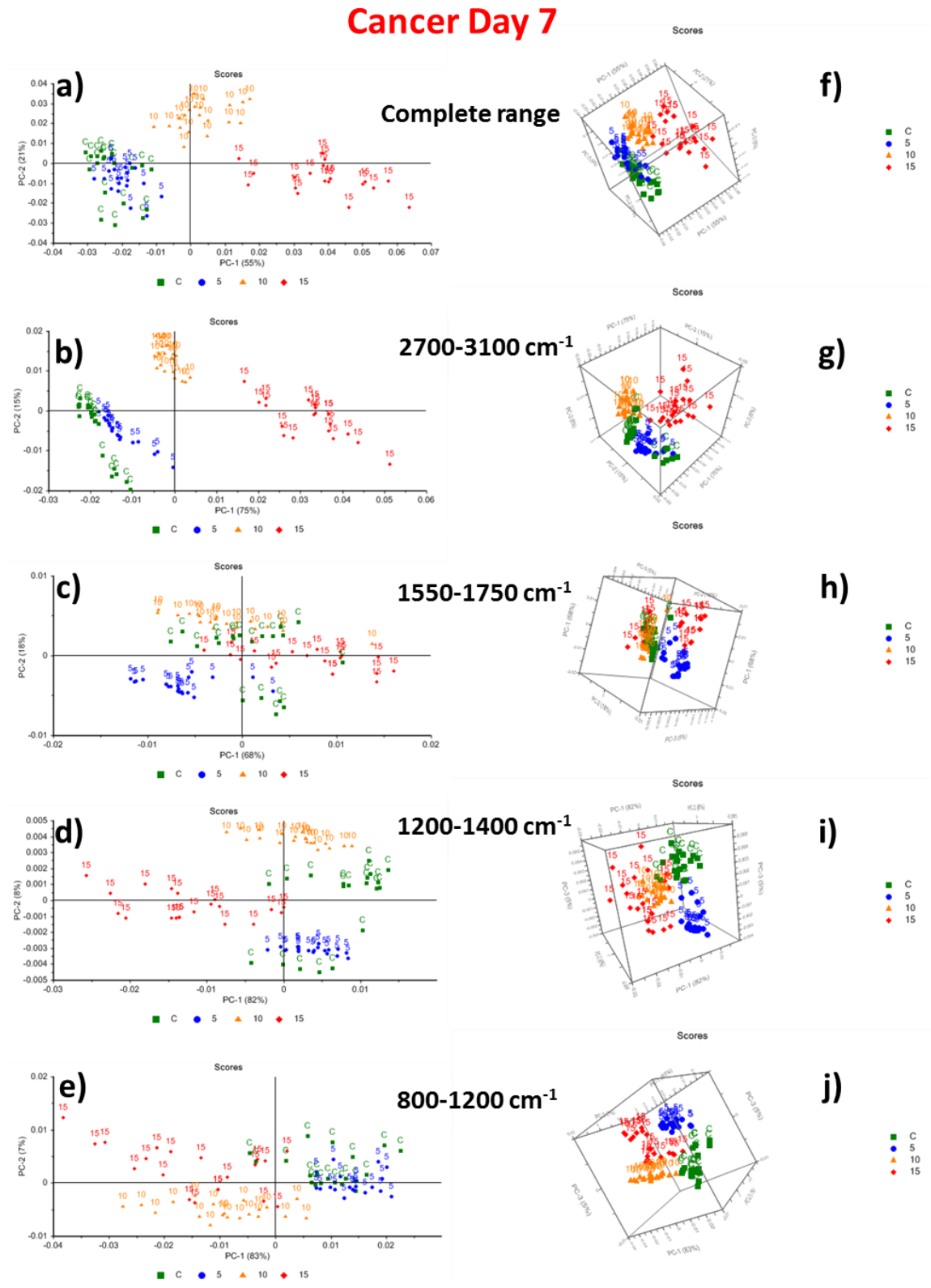

Figure 3. 66 PCA results of T.E cancer model at DAY 7 post radiation. (a-e) 2D plots over complete spectral range, 2700 to 3100 cm-1, 1550 to 1750 cm-1, 1200 to 1400 cm-1 and 800 to 1200 cm-1 region respectively. (f-j) Corresponding 3D plots showing first 3 PC's

Cluster Analysis

Tissue Engineered Normal Oral Mucosa

DAY 1 Post Radiation

Figure 3.67a shows cluster classification of control, 5, 10 and 15 Gy models over the complete spectral range at day 1. Two main branches are formed; one exclusively contains control model and 15 Gy model whereas the second primarily possesses 5 Gy and 10 Gy models. Maximum intra tissue variability is observed within the control model, which is also divided in to two sub groups but within the same branch.

DAY 4 Post Radiation

At day 4, cluster analysis of control and irradiated models showed two distinct branches, one primarily had control models whereas the second branch possessed all irradiated models (figure 3.67b). Better classification was observed in terms of grouping control and irradiated models. The second branch having irradiated models showed that the 5 Gy models were distant to 15 Gy as compared to 10 Gy.

DAY 7 Post Radiation

At day 7, again two distinct branches were formed; one having control and 5 Gy models whereas the second branch possessed 10 and 15 Gy models (figure 3.67c). Day 7 classification showed better understanding of biochemical activities and maturity within the cells. 5 Gy model was grouped closest to control whereas 15 Gy models were the most distant.

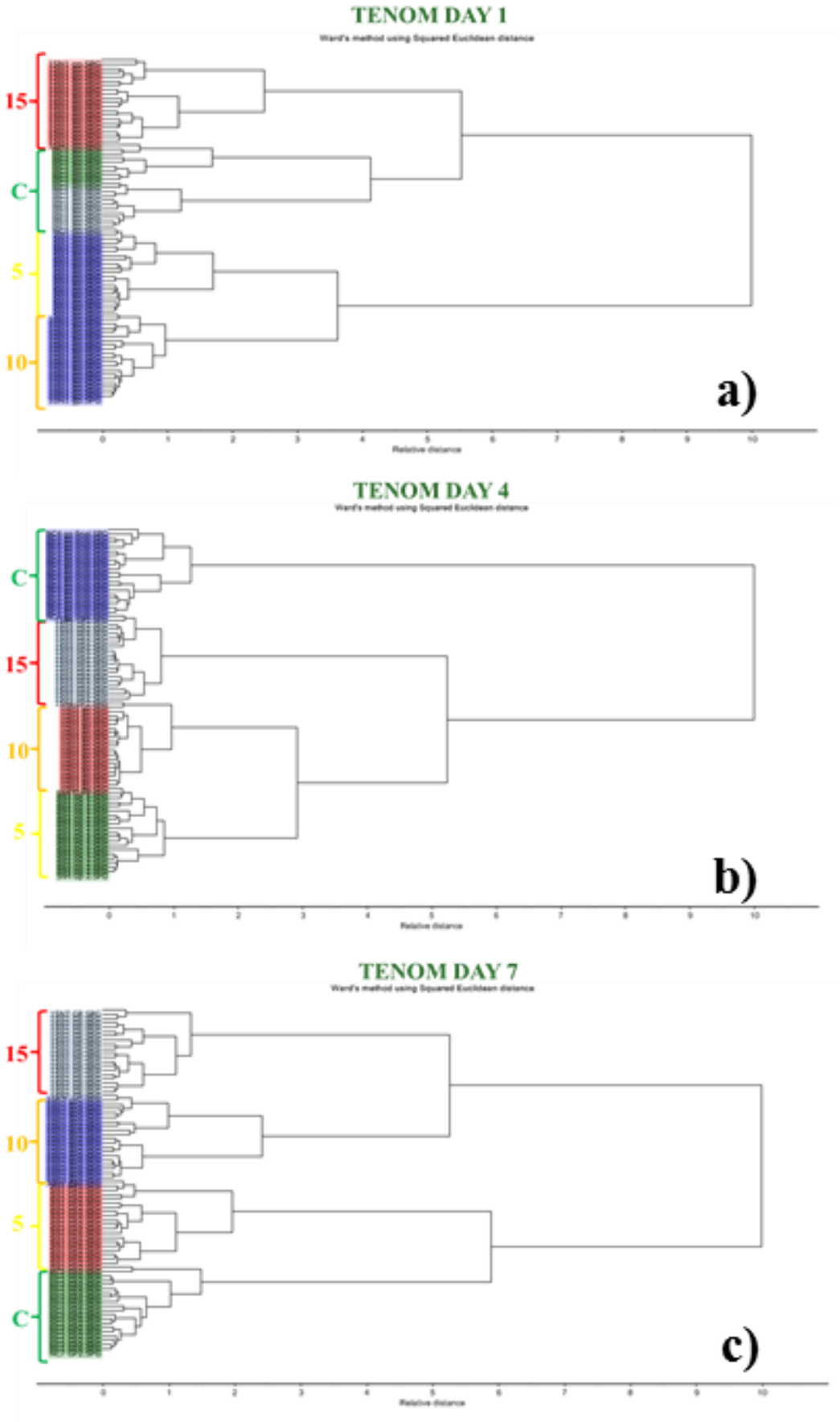

Figure 3. 67 Dendogram showing classification of TENOM model between control, 5, 10 and 15 Gy at (a) Day 1, (b) Day 4 and (c) Day 7 post radiation

Tissue Engineered Cancerous Oral Mucosa

DAY 1 Post Radiation

Figure 3.68a shows cluster classifications of the control, 5, 10 and 15 Gy models over the complete spectral range. Two main branches are formed; one exclusively contains 15 Gy models whereas the second possesses control, 5 Gy and 10 Gy models. Control models are the most distant from 15 Gy suggesting that this is an effects caused by the highest dose of radiation.

DAY 4 Post Radiation

At day 4, cluster analysis of control and irradiated models showed two distinct branches, one primarily had the control and 5 Gy models whereas the second branch possessed 10 and 15 Gy models (figure 3.68b). An interesting trend was observed where 5 Gy models had come close to the control models which might be suggesting that cancerous activities resuming within cells.

DAY 7 Post Radiation

Cluster analysis at day 7 showed a different result as compared to day 1 and 4 where control model was placed close to 15 Gy and in the same branch as well (figure 3.68c). Relative distance within one model type was increased which propose intra tissue variations which might be as a result of increased metabolic activities in cancer cells day 7 post radiation. The dendogram shows that the 5 Gy models were placed very close to the control, suggesting similarities with cancer tissue at day 7.

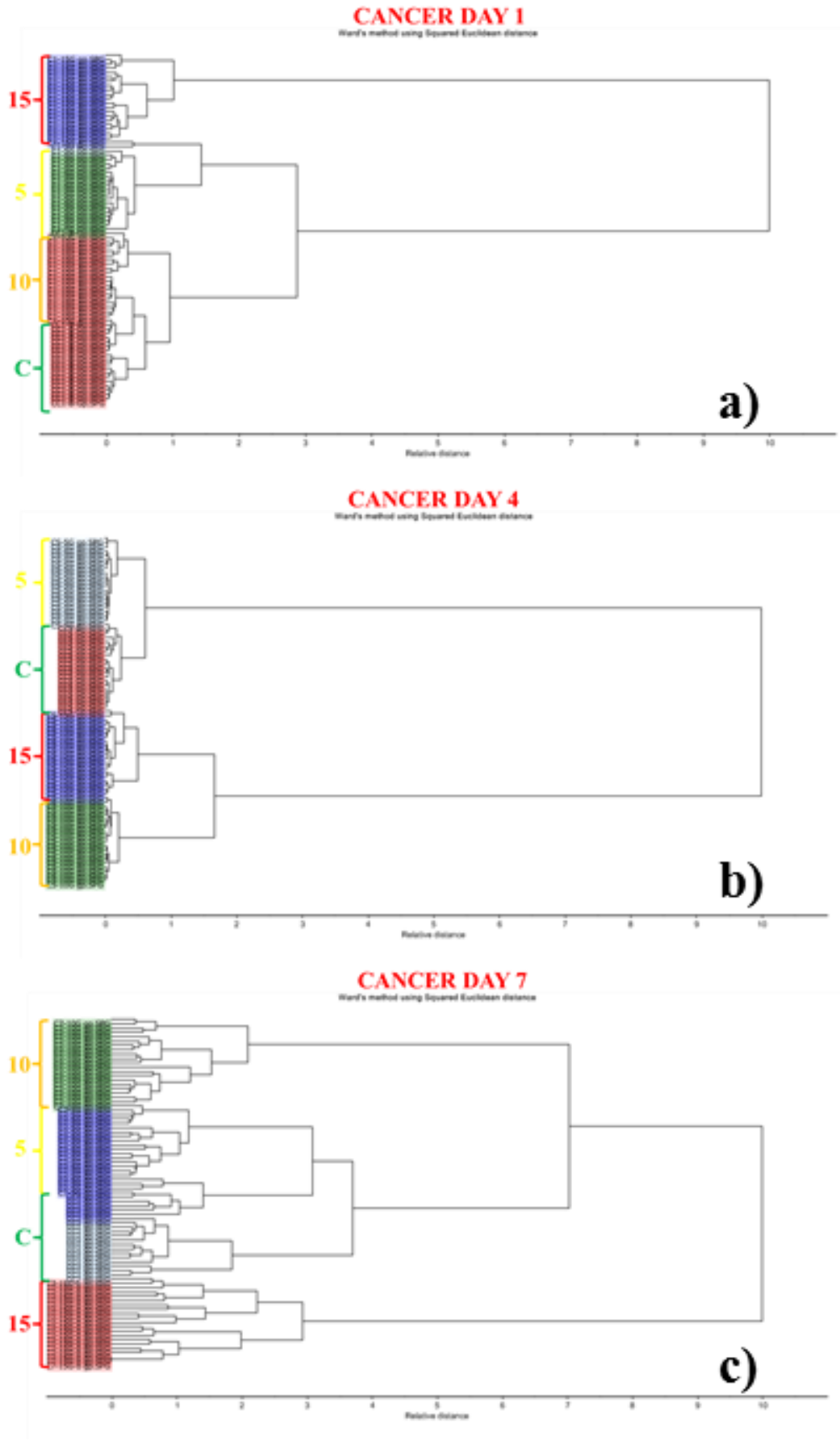

Figure 3. 68 Dendogram showing classification of cancer model between control, 5, 10 and 15 Gy at (a) Day 1, (b) Day 4 and (c) Day 7 post radiation

3.15 Discussion (Section 3 – Irradiated Tissue Engineered Models)

Radiotherapy is one of the primary treatment options along with surgical interventions and chemotherapy for head and neck cancers. Its effectiveness relies on the radiosensitivity of tumours, host conditions or stage of the tumour and injury caused to normal tissue as a result of therapy (Ou et al., 2012). To understand tumour radiosensitivity it is important to evaluate molecular level alterations caused by irradiations (Feng et al., 2010). Obtaining patient material has always been a challenge therefore *in vitro* experiments have been performed to collect radiobiological data. Animal testing is a common practice but in this case it is hard to co relate irradiation effects observed in a non-human environment along with radiotherapy outcomes in patients (Matthews et al., 2011a).

In cancer treatments radiotherapy is second only to surgery, where the rate is 68% surgery, 28% radiotherapy and 4% chemotherapy. Currently cancer cells are exposed to small and precise doses of radiation at different time intervals using high technology irradiation equipment. There is not much known about the post irradiation molecular mechanism and cell metabolism which leads to cell death. In head and neck tumour treatments, one of the major complications with radiotherapy, chemotherapy and bone marrow transplant is oral mucositis. Clinically, patients may present mild to severe painful ulcers which restrict food intake to an extent that feeding tube is administered (Trotti et al., 2003, Colley et al., 2013).

The aim of this experiment was to investigate irradiation effects on tissue engineered normal and cancerous oral mucosa using Raman spectroscopy. There is not much known about biochemical pathways which are involved with radiotherapy therefore there is a need to understand the molecular changes occurring in respect to lipids, proteins and nucleic acids. Tissue engineered models were constructed and irradiated for investigations which offered more relevant physiological environment.

Histologically, we observed alterations in the cells and decreased epithelial thickening with increasing radiation doses. Cell nuclei appeared to be smaller in size showing signs of pyknosis indicating chromatin condensation taking place in the nucleus as a result of necrosis in response to radiation (Kumar V et al., 2007)). In contrast to irradiated models, H&E images of control normal oral mucosa revealed stratified epithelium gradually increasing from 1 cell thick to approximately 10 cells thickness at day 7. Similarly, abnormal epithelial maturation was observed in control cancer models suggesting aggressive cell proliferation and increased metabolic activities as compared to radiation exposed models.

Raman investigations in this study have discovered some significant biochemical changes associated with radiation. These alterations were associated with lipids, proteins and nucleic acid present in tissues. Varying intensities of these molecules were observed with different radiation doses as well as incubation times. These differences in intensities indicate the effects of radiations in the tissues post radiation and during incubation. When exposed to radiations, the mechanism of cell death or damage is initiated which is associated with double strand breaking of DNA whereas during incubation the process of DNA damage repair is activated (Chen and Nirodi, 2007, Szumiel, 2006). Similarly, the spectral variances in proteins that we observed may also indicate that radiations influence the process of protein synthesis hence disturbing the mechanism of cell proliferation (Liu et al., 2006, Yasser et al., 2014).

Spectral data revealed noteworthy variations in the nucleic acid compartments both in normal and cancerous oral mucosa models. Shift in peak positioning of ring breathing mode of DNA/RNA from 725 cm^{-1} to 720 cm^{-1} in irradiated models suggest severe conformational changes taking place at cellular level. DNA associated spectral alterations were also observed at 828 cm^{-1} (Phosphodiesters and O-P-O stretching of

DNA) and amide III region which consists of proteins (amino acids) as well as nucleic acids. Spectral results varied with different doses of radiation both in terms of peak positioning and change in intensity. Once the cells or tissues are exposed to ionisation radiation, highly reactive hydroxyl ions, superoxide and organic radicals are quickly formed to react with oxygen hence producing reactive oxygen species such as H_2O_2 and organic peroxides. Further, these reactive species chemically bind with DNA which causes damage (Chen and Nirodi, 2007, Quintiliani, 1986). This chemical interaction of reactive species with biological macro molecules like nucleic acids results in ionisation or chemical breakage, which ultimately alters their molecular structure and effect metabolism (Ou et al., 2012, Spitz et al., 2004).

Severe effects of radiation are observed with doses over 6 Gy (Ou et al., 2012), similar pattern is observed in our work where the 15 Gy cancer models showed significant structural change in the amide III region and DNA macromolecule. Double strand breaks are known to be the most harmful lesions caused by radiation exposure which may lead to translocation and incompetence of chromosomes resulting in apoptosis, gene inactivation or cell arrest (Sancar et al., 2004, Rakhorst et al., 2006). Radiations directly or indirectly as a result of reactive oxygen species that damages DNA which ultimately causes injury to epidermis as we have seen in H&E stained images of tissue engineered irradiated models (Rakhorst et al., 2006). Different responses in peak intensities associated with nucleic acid were observed, a significant decrease was observed in models irradiated to 15 Gy however in contrast, an increase in intensity was seen in models exposed to 5 and 10 Gy. This spectral behaviour may suggest that severe conformational changes were present with the highest dose of radiation and nucleic acid resistance or response to radiation was restored in models with lesser dosages. Human immune system offers a reactive mechanism against any stimulus however this mechanism cannot be explained when investigating *in vitro* tissue engineered models.

A repair process is triggered in the human system to rescue damaged DNA as a result of radiation exposure. A nuclear protein, such as poly(ADP-ribose) polymerase-1 (PARP1) is one of these proteins responsible for various cellular activities for instance DNA replication, repair and transcription. PARP1 plays a vital role in DNA repair and is immediately activated in response to radiation. PARP1 has the capability to identify DNA strand breaks and direct repair enzymes to the effected location (Villani et al., 2013, Bouchard et al., 2003, Dantzer et al., 1999). The increased intensities of DNA associated bands might suggest that the repair mechanism is initiated in response to radiation. Significant variation that we observed was in day 1 cancer models where there was a major change in amide III region specifically DNA peak which showed decrease in intensity when exposed to 15 Gy suggesting severe conformational effects. However the spectra of 5 and 10 Gy models showed different characteristic suggesting resistance of cancer cells and activation of DNA repair process by nuclear proteins. Incubation period helped to stabilise the repair mechanism as we observed in the spectra of day 4 and 7 of both normal and cancer tissue engineered models. Spectral features of irradiated models resembled the control model spectra with the passage of time, suggesting effects of incubation and viability of cells post radiation.

PCA results have also demonstrated similar features where in day 1 of both normal and cancer mucosa models, separation between control and irradiated samples could be monitored. Cluster formation was improved with increasing incubation times which might suggest that initially at day 1 the models were more heterogenic in nature. PCA results of amide III region (1200 to 1400 cm^{-1}) at day 4 in normal mucosa model, which contains information regarding nucleic acids along with proteins clearly separated control from irradiated models. With respect to incubation time, we observed that at day 4 and 7, irradiated normal model clusters started to group themselves closer to control which might suggest increasing metabolic activities in the cells and progression of DNA

repair mechanisms. These observations indicate the sensitivity of the technique to identify biochemical changes not only associated with irradiation but with increasing incubation times as well. These cluster arrangements of control and irradiated models at day 1, 4 and 7 may also support the fact that DNA damage is caused by radiations as part of the treatment and at the same time the repair mechanism is activated by nuclear proteins which may have eventually enhanced cell proliferation.

Phenylalanine is an essential amino acid which plays a significant part in cell metabolism (Ou et al., 2012, Feng et al., 2010, Thomas, 1999). There is less known about the effects of irradiation on these macromolecules, our results have shown fluctuation in intensity of phenylalanine band (ring breathing mode) typically present at 1002 cm^{-1}. These variations were not only as a result of radiation but increased incubation time also contributed towards it. Day 1 cancer model (15 Gy) spectra showed significant decrease in phenylalanine peak which gradually increases at day 4 and 7. This indicates that the quantity of aromatic amino acids and α-helix protein structures increases however β-sheet and random coil protein structures decreases with incubation time. Similar spectral features were observed with tryptophan and tyrosine, earlier studies have demonstrated that radiations and post radiation incubation times influence protein structures in terms of degradation and synthesis respectively (Tapio and Jacob, 2007). These structural changes may suggest that cell survival activities are initiated by oxidative stress caused by radiations hence leading to denaturing or breakage of structural proteins into free amino acids (Dröge, 2002). Our results can be correlated to these findings; day 1 spectral data shows severe effects of 15 Gy on cancer model specifically on nucleic acid and protein compartments. This observation supports the fact that degradation is taking place immediately after exposure to higher dose of radiation however less intense spectral variances were observed with 5 and 10 Gy. Normal and cancer models showed different spectral features in response to increasing

doses of radiation at day 1 specifically. This may advise that complex nature of cancer models react differently to specific amounts of doses (Andraka et al., 2012).

Spectral data of day 4 and 7 in both normal and cancer models have shown an increase in amino acids which may suggest the activation of protein synthesis mechanisms as a result of cell damage due to radiation. Our results demonstrate that with radiation there is an increase in the α-helix protein structure which might indicate the production of specific repair proteins responsible for cell survival (Matthews et al., 2011b). PCA results of the finger print region (800 to 1800 cm^{-1}) at day 4 in normal mucosa model, clearly separates control from irradiated models whereas in cancer models it is difficult to separate 5 Gy from control as they group themselves very close to one another. At day 4 and 7, irradiated clusters started to group themselves closer to control proposing increased metabolic activities in the cells and activation of repair protein mechanisms. Peak height analysis of phenylalanine and DNA macromolecule suggests that normal tissue has recovered better than cancer over time.

Substantial change in peak intensity at 2880 cm^{-1} was recorded, which is a typical assignment of CH_2 asymmetric stretch of lipids in biological tissues. Spectra of normal and cancer mucosa models possess varied spectral features in this region. An increase or decrease in the intensity of these bands indicates the concentration or amount of lipids present in the tissues. Valuable evidence can be obtained regarding lipid peroxidation assessments from high wavenumber region of the Raman spectra. As we discussed earlier that radiations significantly damage DNA, moreover free radicals formed as a result of radiations seriously target lipid membranes as well. This process leads to lipid peroxidation caused by free radicals such as super peroxide $(O_2)^-$ and hydroxyl radical $(OH)^-$ as well as hydrogen peroxide (H_2O_2) as a reactive molecule. Hydrogen peroxide and oxygen have the potential to damage nearly all molecules present in cells and eventually lead to consequences like lipid peroxidation, DNA alterations and abnormal

cell proliferation (Mahendra R Patait, 2011). The polyunsaturated fatty acids are attacked by these reactive oxygen species which begin a self-propagating chain reaction. This process of lipids destruction extremely effects cell viability despite the presence of natural antioxidant defence mechanism (Mylonas and Kouretas, 1999). The concentration of unsaturated fatty acids varies in the cells with exposure to different doses of radiations and incubation periods hence leading to variations in peak positioning and intensities. Lipid saturation may also be evaluated through spectroscopic means which may lead to potential Raman markers for lipid metabolism. The variations observed in the lipid vibrations (-CH_3, -CH_2 and -CH=CH-) of Raman spectra may suggest differences in lipid metabolism which may be useful in understanding radio therapeutic effects with different doses and time periods during treatment. In normal mucosa model, peak attributed to CH_2 asymmetric stretch of lipids at 2880 cm^{-1} was absent in control model as compared to irradiated ones however a significant increase in this peak was observed at day 4 which may suggest severe conformational changes taking place as a result of radiation and with increased incubation time the cellular response is changing. These changes may indicate the initial effects of lipid peroxidation in this instance at day 1 and further at day 4 and 7 reactive mechanisms are taking place as part of cellular recovery.

A strong band at 2933 cm^{-1} in the cancer control, 5 and 10 Gy models at day 1 showed a significant shift in the 15 Gy models to 2940 cm^{-1}. This shows variations in the CH stretching vibrations of lipids and may suggest severe effects of 15 Gy on this region in biological tissues. With the passage of time, at day 4 and 7 this peak was shifted back towards the control, 5 and 10 Gy. This might propose that cell death did not occur when exposed to 15 Gy as signs of recovery were observed at day 4 and 7. This shows the importance of the technique to sense subtle differences which can identify or monitor radiation effects at different doses and time points at cellular level.

PCA results over the lipid region successfully differentiated the control from irradiated models as well as separation within different doses of radiation. These results may suggest that $\nu(CH_2)$ symmetric and asymmetric vibrations of lipids (2880 cm^{-1}) and C-H, CH_2 symmetric vibrations of lipids and proteins (2932, 2937, 2940 and 3060 cm^{-1}) have contributed in distinguishing between these control and irradiated tissue types (Koljenović et al., 2005, Movasaghi et al., 2012, Rehman et al., 2007, Sigurdsson et al., 2004). Though PCA performed over the complete spectral range has shown encouraging differentiation between tissue types but further analysing narrow spectral bands such as lipid and finger print regions have helped us to identify specific molecules which have contributed in these separations. Post radiation incubation time has shown significant changes in formation of these clusters. Day 1 PCA plots of normal and cancer models show loosely formed clusters as compared to day 4 and 7 which may suggest severe effects of radiations as well as immature epithelia. An interesting trend was observed in the lipid region of normal and cancer models that even at day 7 separations between control and irradiated clusters was maintained to some extent. In contrast, the finger print region of cancer models at day 7 showed that irradiated models are mixing well with control models which might suggest that the metabolic activities are taking place more efficiently. This may also suggest that radiation has more effect in the high wavenumber region (lipids) in terms of controlling cellular activities.

Cluster Analysis grouped different tissue types independently and also measured the amount of variation present within one group. In normal oral mucosa models, the control tissue was divided into two branches at day 1 which might suggest the amount of inner group variability in that tissue. Day 1 post radiation means that the sample was fixed after 7 days of air liquid interface whereas day 7 post radiation is 14 days of air liquid interface. This might suggest that at day 1 the epithelium is not completely

mature and is in process of several metabolic activities which have led to this heterogeneity. As the incubation period increases the trend changes, day 4 completely separates the control in one branch with the irradiated in another branch. Throughout our statistical data sets we have observed that day 4 shows the maximum separation between control and irradiated groups. At day 7 we observed two main branches where one contained controls and 5 Gy models and the second have 10 and 15 Gy models. This variation may propose that radiation effects are maximum at day 4 and repair mechanisms are activated at day 7 hence promoting cell proliferations.

Radiation exposure to cancer models presented different behaviour in cluster analysis as compared to normal mucosa models. The different trends that we observed were; 15 Gy model was completely isolated in a separate branch at day 1 and there was significant increase in inner group variability at day 7 in all models. Day 4 and 7 data may suggest that aggressive metabolic response of cancer models as compared to normal however peak height analysis of specific biomolecules like phenylalanine and DNA suggest that normal tissue has the tendency to recover better than cancer. 5 Gy model was grouped with control in one branch at day 4 which might suggest that cell proliferation was aggressive in lesser dose of radiation.

3.16 Summary of irradiated tissue engineered models

- In this study for the first time, 3D Tissue engineered models of normal and cancerous oral mucosa were irradiated to 5, 10 and 15 Gy for Raman spectroscopic analysis.
- Visual inspection of the spectral data disclosed differences in the lipid, proteins and nucleic acid regions.
- On the basis of biochemical differences, chemometric analysis was able to successfully differentiate between control and irradiated models.
- Raman not only isolated controls from irradiated models but it has also demonstrated sensitivity to pick biochemical changes associated with incubation time.
- Our data suggests that DNA, proteins and lipids undergo severe radiation effects however with increased incubation time there are signs of repair mechanism in the cells.
- Lipid region has shown promising PCA results which may suggest that they have the potential to be used as Raman markers in future.
- Chemometric analysis has helped us understand radiosensitivity of the cells. Cancer cells have shown more heterogeneity after day 4 post radiation whereas peak height analysis of phenylalanine and DNA macromolecules suggest that normal tissue has recovered better than cancer.
- DNA and protein regions have indicated quick response in order to trigger the repair mechanism from day 4 onwards.
- This shows the importance of these 3D models which can be extremely useful in understanding biochemical pathways.

Chapter 4

4.1 Conclusions

This work has for the first time demonstrated Raman spectroscopic investigations carried out on 3D tissue engineered oral mucosa models. Three different studies were conducted to explore the potential of Raman spectroscopy in terms of optical diagnosis and surveillance of tissues undergoing radiotherapy, which is one of the commonly used treatment option for oral cancer. The conclusions drawn from these studies are detailed below.

3D Tissue Engineered Oral Mucosa Models

It is valuable to understand the pathogenesis of cancer in order to diagnose the disease at an early stage. Human tissue is scarce therefore these *in vitro* models provide an opportunity to analyse biological/biochemical pathways in all conditions histologically as well as spectroscopically. Adjacent sections of each tissue were cut in two thicknesses for H&E staining (5 µm) for histological analysis and unstained sections (20 µm) for Raman analysis.

Spectroscopic studies can be challenging when wax embedded tissues are analysed. Improper removal of wax from tissues can hinder vital biochemical information therefore it was required to establish a de-wax procedure before Raman analysis. A standard de-wax protocol was established in order to completely remove wax from 20 µm thick tissue sections so that pure biological information is obtained from Raman spectral data (Mian et al., 2014).

Good quality Raman spectrum was acquired in 2 minutes and 30 seconds. The oral cavity is an easily accessible region therefore the time needed to acquire Raman spectrum in the clinic for a point-of-care, real-time diagnostic is realistic. By reducing

both the number of accumulations and exposure times, spectrum collection time could be significantly reduced. This ability of a Raman spectrometer suggests promising future of the technique where it can be utilized in clinical set ups.

Raman spectra of normal, dysplastic (D19, D20 and DOK) and cancer (Cal27, SCC4 and FaDu) models revealed significant spectral variances associated with lipids, proteins and nucleic acids. Generally broader peaks of amide I and III were observed in dysplastic and cancer models as compared to normal which indicates dominancy and alteration of protein structures. Tryptophan and phenylalanine demonstrated an increase in peak intensities in dysplastic and cancer models, showing that these amino acids are more abundant in these tissues. The lipid (high wavenumber) region showed a peak shift in DOK which separated it from normal, dysplastic and cancer models. These molecules have shown promising potential to be used as Raman markers to identify normal and abnormal tissues.

Raman spectroscopy demonstrated its sensitivity to differentiate between HNSCC models of different anatomical origins. Clinically this could be quite useful not only in identification of anatomical site of the tumour but in detecting tumour margins which may assist surgeons to perform guided tissue biopsy procedures.

Chemometric analysis (PCA, CA and LDA) successfully differentiated between the three types of tissue engineered oral mucosa models. More importantly subtypes of dysplasia (D19, D20 and DOK) and cancer (Cal27, SCC4 and FaDu) were also identified. Supervised tissue classification (LDA) showed 100% sensitivity and specificity when classifying subtypes. This shows that Raman spectroscopy is more sensitive in identifying subtypes of dysplastic and cancer models as compared to the whole group. Successful demonstration of discriminating subtypes of dysplastic and cancer models may suggest that this technique along with chemometric tools has a

future in clinical diagnostics to determine different grades (mild, moderate and severe) of pathological tissues.

Patient Biopsy Work

Different anatomical locations within the oral cavity have variances in their spectral data, therefore to achieve controlled and comparable results only tongue tissue specimens were selected for this part of the study.

Visual comparison of average spectra of normal, dysplasia and cancer tissues showed significant differences in lipid, protein and DNA profiles. Cancer tissue spectra generated broader peaks of amide I and III which indicated denatured and strained protein and DNA structures. Increased intensities were observed in phenylalanine, tryptophan, nucleic acids, amide I and amide II as the tissue changed its state from normal to dysplasia and then cancer. On the basis of these biochemical differences cancer tissue spectra could be easily differentiated from normal and dysplasia. It is encouraging to isolate cancer from dysplasia because this could play a vital role in surveillance of suspected lesions without frequent surgical interventions.

LDA achieved a sensitivity of more than 95% between normal and cancerous oral tissues. Promising results were obtained between dysplasia and cancer as well with over 80% of sensitivity, which suggests that RS has a promising future in clinical settings for surveillance of dysplasia and early detection of cancer.

Irradiation Work

Radiotherapy is one of the treatment options available for oral cancer. Despite advancements in treatment regimes radiotherapy leads to a number of side effects therefore it is necessary to understand the biological and biochemical pathways which are associated with tissue radio-sensitivity. The study of irradiated tissues *in vivo* is not

plausible and therefore it is ideal to investigate biochemical changes taking place in *in vitro* models. 3D Tissue engineered models of normal and cancerous oral mucosa were irradiated with 5, 10 and 15 Gy and investigated by Raman spectroscopy. 480 high quality Raman spectra were collected at day 1, 4 and 7 post radiation for spectral and chemometric analysis.

Visual analysis of the spectral data showed that radiation had primarily targeted amide I, III and lipid regions of normal and cancer models of tissue engineered oral mucosa. Variations in peak intensity and positioning were observed with different doses of radiation at day 1, 4 and 7. Incubation time is crucial because it allows the cells to react and proceed with metabolic activities in response to radiation. Fluctuation in intensity of phenylalanine and nucleic acid peaks was observed with increased incubation time. Amide III region showed increased metabolic activities at day 4 and 7 post radiation therefore cancer cells showed more aggressive behaviour at these time points. These specific molecules can be useful in monitoring cellular response of patients during radiotherapy.

PCA and CA not only differentiated between control and irradiated models but they were also able to discriminate between different doses of radiations i.e. 5, 10 and 15 Gy. PCA showed distinct clusters of control and irradiated models at day 1 however with increased incubation time irradiated clusters tend to come closer to control. PCA cluster formation showed that DNA and proteins have responded quicker in order to trigger the repair mechanism from day 4 onwards hence suggesting that these molecules may be more radio-resistant. The ability of Raman spectroscopy along with multivariate data analysis techniques can be extremely useful to detect radio-sensitive and radio-resistant behaviours of tissues undergoing treatment.

4.2 Future Work

There is a need to introduce an optical diagnostic technique in clinical set ups which can image tissues *in vivo* and is capable of detecting cancer at an early stage. Despite advancements in currently used diagnostic options such as CT and MRI scans, they have limitations to acquire biochemical information from tissues. Raman spectroscopy has shown promising results and may serve the purpose well as it holds the benefit of being non-invasive, non-destructive and a real time technique. Low percentage of dysplastic oral lesions proceed to cancer which makes it difficult to monitor such suspected cases histologically, therefore Raman spectroscopy may help in non-invasive surveillance of dysplastic tissues and eventually offering early diagnosis. These advantages of Raman spectroscopy would certainly be an asset to oncologists, surgeons and specialist pathologists. This PhD work demonstrates the abilities of Raman spectroscopy to identify biochemical changes associated with normal and abnormal tissues as well as control and irradiated tissue engineered oral mucosa constructs which can be of diagnostic and therapeutic significance.

- In future studies it would be valuable to increase the number of patient biopsies and perform spectroscopic investigations on various anatomical locations within oral cavity which would widen the data set and explore further biochemical information.
- It has been illustrated in this work that Raman spectroscopy is extremely sensitive to identify subtypes of dysplasia and cancer therefore if would be beneficial to investigate different grades of dysplasia which would certainly help in early cancer diagnosis.
- Raman spectroscopy offers a range of lasers with different wavelengths and penetration powers. Depth profiling of oral mucosa could be performed to assess underlying soft tissue in both normal and pathological conditions. It would be

ideal to determine laser penetration depths in oral epithelia with various lasers and establish a suitable parameter for *in vivo* practice. This protocol could assist surgeons while performing complete tumour removals and restrict chances of post-operative metastasis.

- This work demonstrated effects of radiation on tissue engineered models of normal and cancerous oral mucosa, it would be very useful to induce chemotherapeutic drugs to these models and spectroscopically investigate tissue behaviour over incubation time. These *in vitro* models will allow better understanding of drug tissue interaction and aid in further pharmaceutical developments.

The work undertaken in this PhD has contributed significantly to the generation of a spectral database essential to implement Raman spectroscopy in clinical *in vivo* trials. This certainly would be a step forward towards early, non-invasive and real time diagnosis of oral cancer. Since the oral cavity is an easily accessible region fiber optic probes attached to the Raman system could investigate the oral mucosa and obtain biochemical information within seconds. This *in vivo* clinical setting would be suitable to monitor dysplastic lesions non-invasively overtime in order to detect any cancerous changes. Moreover Raman *in vivo* system may also be utilised to screen patients undergoing radio- or chemotherapy. This may assist in controlled dose/drug induction and reduce the number of associated side effects. Promising screening outcomes of patients undergoing treatments may guide radiologists and pharmacists to develop therapeutics and eventually improve prognosis for patients.

References

ABDUL, S., BROWN, B. H., MILNES, P. & TIDY, J. A. 2006. The use of electrical impedance spectroscopy in the detection of cervical intraepithelial neoplasia. *International Journal of Gynecological Cancer,* 16, 1823-1832.

ALFANO, R. R., TATA, D. B., CORDERO, J., TOMASHEFSKY, P., LONGO, F. W. & ALFANO, M. A. 1984. LASER-INDUCED FLUORESCENCE SPECTROSCOPY FROM NATIVE CANCEROUS AND NORMAL TISSUE. *Ieee Journal of Quantum Electronics,* 20, 1507-1511.

ANA PAULA OLIVEIRA, RENATA ANDRADE BITAR, LANDULFO SILVEIRA JR., RENATO AMARO ZÂNGARO & MARTIN., A. A. 2006. Near-Infrared Raman Spectroscopy for Oral Carcinoma Diagnosis. *Photomedicine and Laser Surgery.,* 24, 348-353.

ANDRAKA, N., GONZALEZ-VELASCO, J., CELEIRO, J., ARRONDO, J. L. R. & BILBAO, P. 2012. An infrared microspectroscopy 2DCOS study of the effect of radiation on normal and cancer cells. *Vibrational Spectroscopy,* 60, 189-192.

ANDRUS, P. G. 2006. Cancer monitoring by FTIR spectroscopy. *Technology in cancer research & treatment* 5, 157-167.

ARGIRIS, A., KARAMOUZIS, M. V., RABEN, D. & FERRIS, R. L. 2008. Head and neck cancer. *Lancet,* 371, 1695-709.

ATALA, A., BAUER, S. B., SOKER, S., YOO, J. J. & RETIK, A. B. 2007. Tissue-engineered autologous bladders for patients needing cystoplasty. *Journal of Urology,* 177, 66-66.

AYALA, A., MUNOZ, M. F. & ARGUELLES, S. 2014. Lipid Peroxidation: Production, Metabolism and Signalling Mechanisms of Malondialdehyde and 4-Hydroxy-2-Nonenal. *Journal of Oxidative Medicine and Cellular Longevity,* 2014, 31.

BAKLANOVA, N. I., KOLESOV, B. A. & ZIMA, T. M. 2007. Raman study of yttria-stabilized zirconia interfacial coatings on Nicalon (TM) fiber. *Journal of the European Ceramic Society,* 27, 165-171.

BANYAY, M., SARKAR, M. & GRÄSLUND, A. 2003. A library of IR bands of nucleic acids in solution. *Biophysical Chemistry,* 104, 477-488.

BAO, L., YAN, H., MAHURIN SHANNON, M., GU, B. & DAI, S. 2006. Surface-Enhanced Raman Scattering of Uranyl-Humic Complexes Using a Silver-Doped Sol-Gel Substrate. *Nuclear Waste Management.* American Chemical Society.

BARR, H., DIX, T. & STONE, N. 1998. Optical spectroscopy for the early diagnosis of gastrointestinal malignancy. *Lasers in Medical Science,* 13, 3-13.

BEEBE, K. R. & KOWALSKI, B. R. 1987. AN INTRODUCTION TO MULTIVARIATE CALIBRATION AND ANALYSIS. *Analytical Chemistry,* 59, A1007-&.

BELJEBBAR, A., DUKIC, S., AMHARREF, N. & MANFAIT, M. 2010. Ex vivo and in vivo diagnosis of C6 glioblastoma development by Raman spectroscopy coupled to a microprobe. *Analytical and Bioanalytical Chemistry,* 398, 477-487.

BERGHOLT, M. S., ZHENG, W. & HUANG, Z. 2012. Characterizing variability in in vivo Raman spectroscopic properties of different anatomical sites of normal tissue in the oral cavity. *Journal of Raman Spectroscopy,* 43, 255-262.

BHARGAVA, S., CHAPPLE, C. R., BULLOCK, A. J., LAYTON, C. & MACNEIL, S. 2004. Tissue-engineered buccal mucosa for substitution urethroplasty. *BJU Int.*, 93(6), 807-11.

BHARGAVA, S., PATTERSON, J. M., INMAN, R. D., MACNEIL, S. & CHAPPLE, C. R. 2008. Tissue-Engineered Buccal Mucosa Urethroplasty—Clinical Outcomes. *European Urology*, 53, 1263-1271.

BIGIO, I. J. & BOWN, S. G. 2004. Spectroscopic sensing of cancer and cancer therapy - Current status of translational research. *Cancer Biology & Therapy*, 3, 259-267.

BIGIO IJ, M. J. 1997. Ultraviolet and visible spectroscopies for tissue diagnostics: fluorescence spectroscopy and elastic-scattering spectroscopy. . *Phys Med Biol,* 42, 803–14.

BINOY, J., ABRAHAM, J. P., JOE, I. H., JAYAKUMAR, V. S., PETTIT, G. R. & NIELSEN, O. F. 2004. NIR-FT Raman and FT-IR spectral studies and ab initio calculations of the anti-cancer drug combretastatin-A4. *Journal of Raman Spectroscopy,* 35, 939-946.

BIRD, B., MILJKOVIC, M., ROMEO, M. J., SMITH, J., STONE, N., GEORGE, M. W. & DIEM, M. 2008. Infrared micro-spectral imaging: distinction of tissue types in axillary lymph node histology. *BMC clinical pathology,* 8, 8-8.

BODANESE, B., SILVEIRA, L., JR., ALBERTINI, R., ZANGARO, R. A. & TAVARES PACHECO, M. T. 2010. Differentiating Normal and Basal Cell Carcinoma Human Skin Tissues In Vitro Using Dispersive Raman Spectroscopy: A Comparison Between Principal Components Analysis and Simplified Biochemical Models. *Photomedicine and Laser Surgery,* 28, S119-S127.

BOUCHARD, V. J., ROULEAU, M. & POIRIER, G. G. 2003. PARP-1, a determinant of cell survival in response to DNA damage. *Experimental Hematology,* 31, 446-454.

BROWN, L. M. 2005. Epidemiology of alcohol-associated cancers. *Alcohol,* 35, 161-168.

CALS, F. L. J., BAKKER SCHUT, T. C., KOLJENOVIĆ, S., PUPPELS, G. J. & DE JONG, R. J. B. 2013. Method development: Raman spectroscopy-based histopathology of oral mucosa. *Journal of Raman Spectroscopy,* 44, 963-972.

CHAI, W. L., MOHARAMZADEH, K., BROOK, I. M., EMANUELSSON, L., PALMQUIST, A. & VAN NOORTT, R. 2010. Development of a Novel Model for the Investigation of Implant-Soft Tissue Interface. *Journal of Periodontology,* 81, 1187-1195.

CHAKRABARTI RN, D. K., SIKDAR S., GHOSH K 1991. Smokeless tobacco and premalignant and malignant lesions of the oral cavity. *Indian J Med Sci.,,* 45, 273-5.

CHAKRABARTY, K. H., DAWSON, R. A., HARRIS, P., LAYTON, C., BABU, M., GOULD, L., PHILLIPS, J., LEIGH, I., GREEN, C., FREEDLANDER, E. & MAC NEIL, S. 1999. Development of autologous human dermal-epidermal composites based on sterilized human allodermis for clinical use. *British Journal of Dermatology,* 141, 811-823.

CHANG, X. J., YANG, C. C., HSU, W. S., XU, W. Z. & SHIH, T. S. 1983. SERUM AND ERYTHROCYTE AMINO-ACID PATTERN - STUDIES ON MAJOR BURN CASES. *Burns,* 9, 240-248.

CHEN, D. J. & NIRODI, C. S. 2007. The epidermal growth factor receptor: A role in repair of radiation-induced DNA damage. *Clinical Cancer Research,* 13, 6555-6560.

CHENG, W.-T., LIU, M.-T., LIU, H.-N. & LIN, S.-Y. 2005. Micro-Raman spectroscopy used to identify and grade human skin pilomatrixoma. *Microscopy Research and Technique,* 68, 75-79.

CHOO-SMITH, L. P., EDWARDS, H. G. M., ENDTZ, H. P., KROS, J. M., HEULE, F., BARR, H., ROBINSON, J. S., BRUINING, H. A. & PUPPELS, G. J. 2002. Medical applications of Raman spectroscopy: From proof of principle to clinical implementation. *Biopolymers,* 67, 1-9.

CI, Y. X., GAO, T. Y., FENG, J. & GUO, Z. Q. 1999. Fourier Transform Infrared Spectroscopic Characterization of Human Breast Tissue: Implications for Breast Cancer Diagnosis. *Applied Spectroscopy,* 53, 312-315.

CLARK, R. J. H. & HESTER, R. E. 1993. *Biomolecular spectroscopy,* Chicago, USA, John Wiley & Son Ltd.

COLLEY, H. E., EVES, P. C., PINNOCK, A., THORNHILL, M. H. & MURDOCH, C. 2013. Tissue-engineered oral mucosa to study radiotherapy-induced oral mucositis. *International Journal of Radiation Biology,* 89, 907-914.

COLLEY, H. E., HEARNDEN, V., JONES, A. V., WEINREB, P. H., VIOLETTE, S. M., MACNEIL, S., THORNHILL, M. H. & MURDOCH, C. 2011. Development of tissue-engineered models of oral dysplasia and early invasive oral squamous cell carcinoma. *Br J Cancer,* 105, 1582-1592.

CONROY, J., RYDER, A. G., LEGER, M. N., HENNESSEY, K. & MADDEN, M. G. 2005. Qualitative and quantitative analysis of chlorinated solvents using Raman spectroscopy and machine learning. Opto-Ireland 2005 Conference, 2005

Apr 05-06 2005 Dublin, IRELAND. 131-142.

CROW, P., BARRASS, B., KENDALL, C., HART-PRIETO, M., WRIGHT, M., PERSAD, R. & STONE, N. 2005. The use of Raman spectroscopy to differentiate between different prostatic adenocarcinoma cell lines. *Br J Cancer,* 92, 2166-2170.

CURADO, M. P., EDWARDS, B., SHIN, H. R., FERLAY, J., HEANUE, M., BOYLE, P. & STORM, H. 2009. *IARC. Cancer incidence in five continents volume IX* [Online]. Available: http://www.dep.iarc.fr.

D.L. JEANMAIRE & DUYNE, R. P. V. 1977. Surface Raman Spectroelectrochemistry Part I. Heterocyclic, Aromatic, and Aliphatic Amines Adsorbed on the Anodized Silver Electrode. *Electroanalytical Chemistry,* 84, 1-20.

DANTZER, F., SCHREIBER, V., NIEDERGANG, C., TRUCCO, C., FLATTER, E., RUBIA, G. D. L., OLIVER, J., ROLLI, V., MÉNISSIER-DE MURCIA, J. & DE MURCIA, G. 1999. Involvement of poly(ADP-ribose) polymerase in base excision repair. *Biochimie,* 81, 69-75.

DAS, R. S. & AGRAWAL, Y. K. 2011. Raman spectroscopy: Recent advancements, techniques and applications. *Vibrational Spectroscopy,* 57, 163-176.

DE GELDER, J., DE GUSSEM, K., VANDENABEELE, P. & MOENS, L. 2007. Reference database of Raman spectra of biological molecules. *Journal of Raman Spectroscopy,* 38, 1133-1147.

DEBERARDINIS, R. J., SAYED, N., DITSWORTH, D. & THOMPSON, C. B. 2008. Brick by brick: metabolism and tumor cell growth. *Current opinion in genetics & development,* 18, 54-61.

DESHMUKH, A., SINGH, S. P., CHATURVEDI, P. & KRISHNA, C. M. 2011a. Raman spectroscopy of normal oral buccal mucosa tissues: study on intact and incised biopsies. *Journal of Biomedical Optics,* 16.

DESHMUKH, A., SINGH, S. P., CHATURVEDI, P. & KRISHNA, C. M. 2011b. Raman spectroscopy of normal oral buccal mucosa tissues: study on intact and incised biopsies. *Journal of Biomedical Optics,* 16, 127004-12700410.

DEVPURA, S., THAKUR, J. S., SETHI, S., NAIK, V. M. & NAIK, R. 2011. Diagnosis of head and neck squamous cell carcinoma using Raman spectroscopy: tongue tissues. *Journal of Raman Spectroscopy*, n/a-n/a.

DONFACK, P., REHDERS, M., BRIX, K., BOUKAMP, P. & MATERNY, A. 2010. Micro Raman spectroscopy for monitoring alterations between human skin keratinocytes HaCaT and their tumorigenic derivatives A5RT3—toward a Raman characterization of a skin carcinoma model. *Journal of Raman Spectroscopy,* 41, 16-26.

DOWNES, A., MOURAS, R., BAGNANINCHI, P. & ELFICK, A. 2011. Raman spectroscopy and CARS microscopy of stem cells and their derivatives. *Journal of Raman Spectroscopy,* 42, 1864-1870.

DRÖGE, W. 2002. Free Radicals in the Physiological Control of Cell Function. *Physiological Reviews,* 82, 47-95.

DUKOR, R. K. 2006. Vibrational Spectroscopy in the Detection of Cancer. *Handbook of Vibrational Spectroscopy.* John Wiley & Sons, Ltd.

DUONG, H. S., LE, A. D., ZHANG, Q. Z. & MESSADI, D. V. 2005. A novel 3-dimensional culture system as an in vitro model for studying oral cancer cell invasion. *International Journal of Experimental Pathology,* 86, 365-374.

EDWARDS, H. G. M., VILLAR, S. E. J., PARNELL, J., COCKELL, C. S. & LEE, P. 2005. Raman spectroscopic analysis of cyanobacterial gypsum halotrophs and relevance for sulfate deposits on Mars. *Analyst,* 130, 917-923.

EL-DIASTY, F. 2011. Coherent anti-Stokes Raman scattering: Spectroscopy and microscopy. *Vibrational Spectroscopy,* 55, 1-37.

EL-MOFT Y SK, L. D. 2003. Prevalence of human papillomavirus type 16 DNA in squamous cell carcinoma of the palatine tonsil, and not the oral cavity, in young patients:a distinct clinicopathologic and molecular disease entity. *Am J Surg Pathol,* 27, 1463–1470.

FAOLÁIN, E. Ó., HUNTER, M. B., BYRNE, J. M., KELEHAN, P., LAMBKIN, H. A., BYRNE, H. J. & LYNG, F. M. 2005. Raman Spectroscopic Evaluation of Efficacy of Current Paraffin Wax Section Dewaxing Agents. *Journal of Histochemistry & Cytochemistry,* 53, 121-129.

FARQUHARSON, S., SHENDE, C., INSCORE, F. E., MAKSYMIUK, P. & GIFT, A. 2005. Analysis of 5-fluorouracil in saliva using surface-enhanced Raman spectroscopy. *Journal of Raman Spectroscopy,* 36, 208-212.

FAULDS, K., SMITH, W. E. & GRAHAM, D. 2003. Evaluation of Surface-Enhanced Resonance Raman Scattering for Quantitative DNA Analysis. *Analytical Chemistry,* 76, 412-417.

FENG, X.-P., YI, H., LI, M.-Y., LI, X.-H., YI, B., ZHANG, P.-F., LI, C., PENG, F., TANG, C.-E., LI, J.-L., CHEN, Z.-C. & XIAO, Z.-Q. 2010. Identification of Biomarkers for Predicting Nasopharyngeal Carcinoma Response to Radiotherapy by Proteomics. *Cancer Research,* 70, 3450-3462.

FRANK, C. J., MCCREERY, R. L. & REDD, D. C. 1995. Raman spectroscopy of normal and diseased human breast tissues. *Anal Chem,* 67, 777-83.

FROST, R. L., EDWARDS, H. G. M., DUONG, L., KLOPROGGE, J. T. & MARTENS, W. N. 2002. Raman spectroscopic and SEM study of cinnabar from Herod's palace and its likely origin. *Analyst,* 127, 293-296.

FUKUYAMA, Y., YOSHIDA, S., YANAGISAWA, S. & SHIMIZU, M. 1999. A study on the differences between oral squamous cell carcinomas and normal oral mucosas measured by Fourier transform infrared spectroscopy. *Biospectroscopy,* 5, 117-126.

GNIADECKA, M., WULF, H. C., NYMARK MORTENSEN, N., FAURSKOV NIELSEN, O. & CHRISTENSEN, D. H. 1997. Diagnosis of Basal Cell Carcinoma by Raman Spectroscopy. *Journal of Raman Spectroscopy,* 28, 125-129.

GRUBISHA, D. S., LIPERT, R. J., PARK, H. Y., DRISKELL, J. & PORTER, M. D. 2003. Femtomolar detection of prostate-specific antigen: An immunoassay based on surface-enhanced Raman scattering and immunogold labels. *Analytical Chemistry,* 75, 5936-5943.

GUZE, K., PAWLUK, H. C., SHORT, M., ZENG, H., LORCH, J., NORRIS, C. & SONIS, S. 2014. Pilot study: Raman spectroscopy in differentiating premalignant and malignant oral lesions from normal mucosa and benign lesions in humans. *Head & Neck,* n/a-n/a.

GUZE, K., SHORT, M., SONIS, S., KARIMBUX, N., CHAN, J. & ZENG, H. 2009. Parameters defining the potential applicability of Raman spectroscopy as a diagnostic tool for oral disease. *Journal of Biomedical Optics,* 14, 014016-014016-9.

HAKA, A. S., SHAFER-PELTIER, K. E., FITZMAURICE, M., CROWE, J., DASARI, R. R. & FELD, M. S. 2005. Diagnosing breast cancer by using Raman spectroscopy. *Proceedings of the National Academy of Sciences of the United States of America,* 102, 12371-12376.

HAKA, A. S., VOLYNSKAYA, Z., GARDECKI, J. A., NAZEMI, J., LYONS, J., HICKS, D., FITZMAURICE, M., DASARI, R. R., CROWE, J. P. & FELD, M. S. 2006. In vivo Margin Assessment during Partial Mastectomy Breast Surgery Using Raman Spectroscopy[?Q1:

Running head: Raman Margin Assessment at Partial Mastectomy. Short title OK?Q1]. *Cancer Research,* 66, 3317-3322.

HANLON EB, M. R., KOO TW, SHAFER KE, MOTZ JT, FITZMAURICE M, KRAMER JR, ITZKAN I, DASARI RR, FELD MS. 2000. Prospects for in vivo Raman spectroscopy. *Physics in medicine and biology,* 45(2).

HARRIS, A. T., RENNIE, A., WAQAR-UDDIN, H., WHEATLEY, S. R., GHOSH, S. K., MARTIN-HIRSCH, D. P., FISHER, S. E., HIGH, A. S., KIRKHAM, J. & UPILE, T. 2010, 2:26. Raman spectroscopy in head and neck cancer. *Head and Neck Oncology,* 2:26.

HAYNES, C. L., ADAM D. MCFARLAND & DUYNE, R. P. V. 2005. Surface-enhanced Raman spectroscopy. *Analytical Chemistry,* 77, 338-A.

HEIMANN, T., COHEN, R., SZPORN, A. & GIL, J. 1991. Correlation of nuclear morphometry and DNA ploidy in rectal cancer. *Diseases of the Colon & Rectum,* 34, 449-454.

HENDRA P., C. JONES & G. WARNER 1991. *Fourier Transform Raman Spectroscopy, Instrumentation and Applications,* New York, Ellis Harwood.

HERRMANN K & G., N. 2003. Epstein-Barr virus-associated carcinomas; facts and fiction. *J Pathol,* 199, 140–145.

HUANG, Y.-S., KARASHIMA, T., YAMAMOTO, M. & HAMAGUCHI, H.-O. 2005. Molecular-Level Investigation of the Structure, Transformation, and Bioactivity of Single Living Fission Yeast Cells by Time- and Space-Resolved Raman Spectroscopy. *Biochemistry,* 44, 10009-10019.

HUANG, Z., MCWILLIAMS, A., LUI, H., MCLEAN, D. I., LAM, S. & ZENG, H. 2003a. Near-infrared Raman spectroscopy for optical diagnosis of lung cancer. *International Journal of Cancer,* 107, 1047-1052.

HUANG, Z. W., MCWILLIAMS, A., LUI, H., MCLEAN, D. I., LAM, S. & ZENG, H. S. 2003b. Near-infrared Raman spectroscopy for optical diagnosis of lung cancer. *International Journal of Cancer,* 107, 1047-1052.

HWANG, M. S., CHO, S., CHUNG, H. & WOO, Y. A. 2005. Nondestructive determination of the ambroxol content in tablets by Raman spectroscopy. *Journal of Pharmaceutical and Biomedical Analysis,* 38, 210-215.

IU. REHMAN, Z. MOVASAGHI & REHMAN, S. 2012. *Vibrational Spectroscopy for Tissue Analysis,* Boca Raton, Florida, United States., Taylor and Francis Group.

JAMES W. CHAN, DOUGLAS S. TAYLOR, THEODORE ZWERDLING, STEPHEN M. LANE, KO IHARA & HUSER, T. 2006. Micro-Raman Spectroscopy Detects Individual Neoplastic and Normal Hematopoietic Cells. *Biophys J.* , 15, 648–656.

JEMAL, A., BRAY, F., CENTER, M. M., FERLAY, J., WARD, E. & FORMAN, D. 2011. Global cancer statistics. *CA Cancer J Clin,* 61, 69-90.

JESS, P. R. T., GARCÉS-CHÁVEZ, V., SMITH, D., MAZILU, M., PATERSON, L., RICHES, A., HERRINGTON, C. S., SIBBETT, W. & DHOLAKIA, K. 2006. Dual beam fibre trap for Raman micro-spectroscopy of single cells. *Optics Express,* 14, 5779-5791.

JIANG, L., JI, N., ZHOU, Y., LI, J., LIU, X., WANG, Z., CHEN, Q. & ZENG, X. 2009. CAL 27 is an oral adenosquamous carcinoma cell line. *Oral Oncology,* 45, e204-e207.

K.TEH, S., W.ZHENG, Y.HO, K., M.TEH, G.YEOH, K. & Z.HUANG 2008. Diagnostic potential of near-infrared Raman spectroscopy in the stomach: differentiating dysplasia from normal tissue. *British Journal of Cancer,* 98, 457–465.

KALYAN KUMAR, K., CHOWDARY, M. V. P., MATHEW, S., RAO, L., MURALI KRISHNA, C. & KURIEN, J. 2008. Raman spectroscopic diagnosis of breast cancers: evaluation of models. *Journal of Raman Spectroscopy,* 39, 1276-1282.

KAUR H.S. 2006. *Instrumental Methods of Chemical Analysis,* Meerut,India. , Pragati Prakashan.

KEEREWEER, S., KERREBIJN, J., VAN DRIEL, P., XIE, B., KAIJZEL, E., SNOEKS, T., QUE, I., HUTTEMAN, M., VAN DER VORST, J., MIEOG, J., VAHRMEIJER, A., VAN DE VELDE, C., BAATENBURG DE JONG, R. & LÖWIK, C. 2011. Optical Image-guided Surgery—Where Do We Stand? *Molecular Imaging and Biology,* 13, 199-207.

KELLER, M. D., KANTER, E. M., LIEBER, C. A., MAJUMDER, S. K., HUTCHINGS, J., ELLIS, D. L., BEAVEN, R. B., STONE, N. & MAHADEVAN-JANSEN, A. 2008. Detecting temporal and spatial effects of epithelial cancers with Raman spectroscopy. *Disease Markers,* 25, 323-337.

KELLY, J. G., TREVISAN, J., SCOTT, A. D., CARMICHAEL, P. L., POLLOCK, H. M., MARTIN-HIRSCH, P. L. & MARTIN, F. L. 2011. Biospectroscopy to metabolically profile biomolecular structure: a multistage approach linking computational analysis with biomarkers. *Journal of Proteome Research,* 10, 1437-1448.

KENDALL, C., HUTCHINGS, J., BARR, H., SHEPHERD, N. & STONE, N. 2011. Exploiting the diagnostic potential of biomolecular fingerprinting with vibrational spectroscopy. *Faraday Discussions,* 149, 279-290.

KENDALL, C., ISABELLE, M., BAZANT-HEGEMARK, F., HUTCHINGS, J., ORR, L., BABRAH, J., BAKER, R. & STONE, N. 2009. Vibrational spectroscopy: a clinical tool for cancer diagnostics. *Analyst,* 134, 1029-1045.

KENDALL, C., STONE, N., SHEPHERD, N., GEBOES, K., WARREN, B., BENNETT, R. & BARR, H. 2003. Raman spectroscopy, a potential tool for the objective identification and classification of neoplasia in Barrett's oesophagus. *The Journal of Pathology,* 200, 602-609.

KIRSCH, M., SCHACKERT, G., SALZER, R. & KRAFFT, C. 2010. Raman spectroscopic imaging for in vivo detection of cerebral brain metastases. *Analytical and Bioanalytical Chemistry,* 398, 1707-1713.

KNUCHEL, R., HOFSTADTER, F., JENKINS, W. E. A. & MASTERS, J. R. W. 1989. SENSITIVITIES OF MONOLAYERS AND SPHEROIDS OF THE HUMAN BLADDER-CANCER CELL-LINE MGH-U1 TO THE DRUGS USED FOR INTRAVESICAL CHEMOTHERAPY. *Cancer Research,* 49, 1397-1401.

KOLJENOVIĆ, S., SCHUT, T. B., VINCENT, A., KROS, J. M. & PUPPELS, G. J. 2005. Detection of Meningioma in Dura Mater by Raman Spectroscopy. *Analytical Chemistry,* 77, 7958-7965.

KONOROV, S. O., GLOVER, C. H., PIRET, J. M., BRYAN, J., SCHULZE, H. G., BLADES, M. W. & TURNER, R. F. B. 2007. In Situ Analysis of Living Embryonic Stem Cells by Coherent Anti-Stokes Raman Microscopy. *Analytical Chemistry,* 79, 7221-7225.

KRAFFT, C., NEUDERT, L., SIMAT, T. & SALZER, R. 2005. Near infrared Raman spectra of human brain lipids. *Spectrochimica Acta Part A: Molecular and Biomolecular Spectroscopy,* 61, 1529-1535.

KRAFFT, C., STEINER, G., BELEITES, C. & SALZER, R. 2009. Disease recognition by infrared and Raman spectroscopy. *Journal of Biophotonics,* 2, 13-28.

KRISHNA, C. M., SOCKALINGUM, G. D., KURIEN, J., RAO, L., VENTEO, L., PLUOT, M., MANFAIT, M. & KARTHA, V. B. 2004. Micro-Raman Spectroscopy for Optical Pathology of Oral Squamous Cell Carcinoma. *Appl. Spectrosc.,* 58, 1128-1135.

KRISHNA, C. M., SOCKALINGUM, G. D., VADHIRAJA, B. A., MAHEEDHAR, K., RAO, A. C. K., RAO, L., VENTEO, L., PLUOT, M., FERNANDES, D. J., VIDYASAGAR, M. S., KARTHA, V. B. & MANFAIT, M. 2007. Vibrational spectroscopy studies of formalin-fixed cervix tissues. *Biopolymers,* 85, 214-221.

KRISHNAN, R. S. & SHANKAR, R. K. 1981. RAMAN EFFECT - HISTORY OF THE DISCOVERY. *Journal of Raman Spectroscopy,* 10, 1-8.

KUDELSKI, A. 2008. Analytical applications of Raman spectroscopy. *Talanta,* 76, 1-8.

KUJAN, O., DESAI, M., SARGENT, A., BAILEY, A., TURNER, A. & SLOAN, P. 2006a. Potential applications of oral brush cytology with liquid-based technology: Results from a cohort of normal oral mucosa. *Oral Oncology,* 42, 810-818.

KUJAN, O., KHATTAB, A., OLIVER, R. J., ROBERTS, S. A., THAKKER, N. & SLOAN, P. 2007. Why oral histopathology suffers inter-observer variability on grading oral epithelial dysplasia: An attempt to understand the sources of variation. *Oral Oncology,* 43, 224-231.

KUJAN, O., OLIVER, R. J., KHATTAB, A., ROBERTS, S. A., THAKKER, N. & SLOAN, P. 2006b. Evaluation of a new binary system of grading oral epithelial dysplasia for prediction of malignant transformation. *Oral oncology,* 42, 987-993.

KUMAR V, ABBAS A, NELSON F & R., M. 2007). *Robbins Basic Pathology,* Philadelphia, PA, USA., Saunders, Elsevier Inc.

LAKSHMI, R. J., KARTHA, V. B., MURALI KRISHNA, C., R. SOLOMON, J. G., ULLAS, G. & UMA DEVI, P. 2002. Tissue Raman Spectroscopy for the Study of Radiation Damage: Brain Irradiation of Mice. *Radiation Research,* 157, 175-182.

LARRAONA-PUY, GHITA, A., ZOLADEK, A., PERKINS, W., VARMA, S., LEACH, I. H., KOLOYDENKO, A. A., WILLIAMS, H. & NOTINGHER, I. 2011. Discrimination between basal cell carcinoma and hair follicles in skin tissue sections by Raman micro-Spectroscopy. *Journal of Molecular Structure,* 993, 57-61.

LARRAONA-PUY, M., GHITA, A., ZOLADEK, A., PERKINS, W., VARMA, S., LEACH, I. H., KOLOYDENKO, A. A., WILLIAMS, H. & NOTINGHER, I. 2009. Development of Raman microspectroscopy for automated detection and imaging of basal cell carcinoma. *Journal of biomedical optics,* 14, 054031.

LASKA, J. & WIDLARZ, J. 2005. Spectroscopic and structural characterization of low molecular weight fractions of polyaniline. *Polymer,* 46, 1485-1495.

LAU, D. P., HUANG, Z., LUI, H., MAN, C. S., BEREAN, K., MORRISON, M. D. & ZENG, H. 2003. Raman spectroscopy for optical diagnosis in normal and cancerous tissue of the nasopharynx—preliminary findings. *Lasers in Surgery and Medicine,* 32, 210-214.

LEE, Y.-C. A., MARRON, M., BENHAMOU, S., BOUCHARDY, C., AHRENS, W., POHLABELN, H., LAGIOU, P., TRICHOPOULOS, D., AGUDO, A., CASTELLSAGUE, X., BENCKO, V., HOLCATOVA, I., KJAERHEIM, K., MERLETTI, F., RICHIARDI, L., MACFARLANE, G. J., MACFARLANE, T. V., TALAMINI, R., BARZAN, L., CANOVA, C., SIMONATO, L., CONWAY, D. I., MCKINNEY, P. A., LOWRY, R. J., SNEDDON, L., ZNAOR, A., HEALY, C. M., MCCARTAN, B. E., BRENNAN, P. & HASHIBE, M. 2009. Active and involuntary tobacco smoking and upper aerodigestive tract cancer risks in a multicenter case-control study. *Cancer Epidemiol Biomarkers Prev.,* 18, 3353-61.

LI, Y., WEN, Z.-N., LI, L.-J., LI, M.-L., GAO, N. & GUO, Y.-Z. 2010. Research on the Raman spectral character and diagnostic value of squamous cell carcinoma of oral mucosa. *Journal of Raman Spectroscopy,* 41, 142-147.

LIEBER, C. A., MAJUMDER, S. K., ELLIS, D. L., BILLHEIMER, D. D. & MAHADEVAN-JANSEN, A. 2008. In vivo nonmelanoma skin cancer diagnosis using Raman microspectroscopy. *Lasers in Surgery and Medicine,* 40, 461-467.

LIU, X. F., XIA, Y. F., LI, M. Z., WANG, H. M., HE, Y. X., ZHENG, M. L., YANG, H. L. & HUANG, W. L. 2006. The effect of p21 antisense oligodeoxynucleotides on the radiosensitivity of nasopharyngeal carcinoma cells with normal p53 function. *Cell Biology International,* 30, 283-287.

LOPEZ, E. P.-M., MORAL, R. M.-D., MARTINEZ-GARCIA, C., ZANETTI, R., ROSSO, S., SERRANO, S., ANEIROS, J., JIMENEZ-PUENTE, A. & REDOND, M. 2003. Lifestyles, environmental and phenotypic factors associated with lip cancer : a case–control study in southern Spain. *British Journal of Cancer,* 88, 1702-170.

LUO, L. Z., WERNER, K. M., GOLLIN, S. M. & SAUNDERS, W. S. 2004. Cigarette smoke induces anaphase bridges and genomic imbalances in normal cells. *Mutat Res.,* 554, 375-85.

LYANDRES, O., SHAH, N. C., YONZON, C. R., WALSH, J. T., GLUCKSBERG, M. R. & VAN DUYNE, R. P. 2005. Real-time glucose sensing by surface-enhanced Raman spectroscopy in bovine plasma facilitated by a mixed decanethiol/mercaptohexanol partition layer. *Analytical Chemistry,* 77, 6134-6139.

LYNG, F. M., FAOLÁIN, E. Ó., CONROY, J., MEADE, A. D., KNIEF, P., DUFFY, B., HUNTER, M. B., BYRNE, J. M., KELEHAN, P. & BYRNE, H. J. 2007. Vibrational spectroscopy for cervical cancer pathology, from biochemical analysis to diagnostic tool. *Experimental and Molecular Pathology,* 82, 121-129.

MACKENZIE, I. C. & FUSENIG, N. E. 1983. REGENERATION OF ORGANIZED EPITHELIAL STRUCTURE. *Journal of Investigative Dermatology,* 81, S189-S194.

MACNEIL, S. 2007. Progress and opportunities for tissue-engineered skin. *Nature,* 445, 874-880.

MAHADEVAN-JANSEN, A., MITCHELL, M. F., RAMANUJAM, N., MALPICA, A., THOMSEN, S., UTZINGER, U. & RICHARDS-KORTUM, R. 1998. Near-infrared Raman spectroscopy for in vitro detection of cervical precancers. *Photochemistry and Photobiology,* 68, 123-132.

MAHADEVAN-JANSEN, A. & RICHARDS-KORTUM, R. R. 1996. Raman spectroscopy for the detection of cancers and precancers. *Journal of Biomedical Optics,* 1, 31-70.

MAHENDRA R PATAIT, R. N. M., SHRUTI KHANZODE 2011. Estimation of Serum Lipid Peroxides Before and After Radiotherapy in Oral Squamous Cell Carcinoma Patients *Journal of Indian Academy of Oral Medicine and Radiology.*

MALINI, R., VENKATAKRISHNA, K., KURIEN, J., M. PAI, K., RAO, L., KARTHA, V. B. & KRISHNA, C. M. 2006. Discrimination of normal, inflammatory, premalignant, and malignant oral tissue: A Raman spectroscopy study. *Biopolymers,* 81, 179-193.

MATTHEWS, Q., BROLO, A. G., LUM, J., DUAN, X. & JIRASEK, A. 2011a. Raman spectroscopy of single human tumour cells exposed to ionizing radiation in vitro. *Physics in Medicine and Biology,* 56, 19-38.

MATTHEWS, Q., JIRASEK, A., LUM, J. J. & BROLO, A. G. 2011b. Biochemical signatures of in vitro radiation response in human lung, breast and prostate tumour cells observed with Raman spectroscopy. *Physics in Medicine and Biology,* 56, 6839-6855.

MAZUREK, S. & SZOSTAK, R. 2006. Quantitative determination of diclofenac sodium and aminophylline in injection solutions by FT-Raman spectroscopy. *Journal of Pharmaceutical and Biomedical Analysis,* 40, 1235-1242.

MCCREERY R.L. 2000 *Raman Spectroscopy for Chemical Analysis,* New York, John Wiley.

MCGREGOR, F., MUNTONI, A., FLEMING, J., BROWN, J., FELIX, D. H., MACDONALD, D. G., PARKINSON, E. K. & HARRISON, P. R. 2002. Molecular Changes Associated with Oral Dysplasia Progression and Acquisition of Immortality: Potential for Its Reversal by 5-Azacytidine. *Cancer Research,* 62, 4757-4766.

MCGREGOR, F., WAGNER, E., FELIX, D., SOUTAR, D., PARKINSON, K. & HARRISON, P. R. 1997. Inappropriate Retinoic Acid Receptor-β Expression in Oral Dysplasias: Correlation with Acquisition of the Immortal Phenotype. *Cancer Research,* 57, 3886-3889.

MIAN, S. A., COLLEY, H. E., THORNHILL, M. H. & REHMAN, I. U. 2014. Development of a Dewaxing Protocol for Tissue-Engineered Models of the Oral Mucosa Used for Raman Spectroscopic Analysis. *Applied Spectroscopy Reviews,* 49, 614-617.

MICHAEL B. FENN, PETROS XANTHOPOULOS, GEORGIOS PYRGIOTAKIS, STEPHEN R. GROBMYER, PANOSM. PARDALOS & HENCH, L. L. 2011 Raman Spectroscopy for Clinical Oncology. *Advances in Optical Technologies,* 2011, 20

MILLS, A. D. & MORRIS, L. 1999. From basic cell biology to cancer screening. *Trends in Cell Biology,* 9, 418.

MILLS, S. E. 2004. *Histology for Pathologists,* Philadelphia, USA., Lippincott Williams & Wilkins

MOHARAMZADEH, K., BROOK, I. M., SCUTT, A. M., THORNHILL, M. H. & VAN NOOYT, R. 2008. Mucotoxicity of dental composite resins on a tissue-engineered human oral mucosal model. *Journal of Dentistry,* 36, 331-336.

MOHARAMZADEH, K., BROOK, I. M., VAN NOORT, R., SCUTT, A. M. & THORNHILL, M. H. 2007. Tissue-engineered oral mucosa: a review of the scientific literature. *Journal of Dental Research,* 86, 115-124.

MOHARAMZADEH, K., FRANKLIN, K. L., BROOK, I. M. & VAN NOORT, R. 2009. Biologic Assessment of Antiseptic Mouthwashes Using a Three-Dimensional Human Oral Mucosal Model. *Journal of Periodontology,* 80, 769-775.

MOVASAGHI, Z., REHMAN, S. & REHMAN, I. U. 2007. Raman spectroscopy of biological tissues. *Applied Spectroscopy Reviews,* 42, 493-541.

MOVASAGHI, Z., REHMAN, S. & REHMAN, I. U. 2012. Raman Spectroscopy Can Detect and Monitor Cancer at Cellular Level: Analysis of Resistant and Sensitive Subtypes of Testicular Cancer Cell Lines. *Applied Spectroscopy Reviews,* 47, 571-581.

MOVASAGHI, Z., REHMAN, S. & REHMAN, I. U. 2013. *Vibrational spectroscopy for tissue analysis,* Boca Raton, CRC Press.

MULLER, M. G., VALDEZ, T. A., GEORGAKOUDI, I., BACKMAN, V., FUENTES, C., KABANI, S., LAVER, N., WANG, Z. M., BOONE, C. W., DASARI, R. R., SHAPSHAY, S. M. & FELD, M. S. 2003. Spectroscopic detection and evaluation of morphologic and biochemical changes in early human oral carcinoma. *Cancer,* 97, 1681-1692.

MURALI KRISHNA, C., G.D. SOCKALINGUM, JACOB KURIEN, LAKSHMI RAO, L. VENTEO, M. PLUOT, M. MANFAIT & KARTHA, V. B. 2004. Micro-Raman Spectroscopy for Optical Pathology of Oral Squamous Cell Carcinoma. *Applied Spectroscopy,* Vol. 58, 1128-1135.

MURALI KRISHNA, C., SOCKALINGUM, G. D., VIDYASAGAR, M. S., MANFAIT, M., FERNANADES, D. J., VADHIRAJA, B. M. & MAHEEDHAR, K. 2008. An overview on applications of optical spectroscopy in cervical cancers. *J Cancer Res Ther,* 4, 26-36.

MURDOCH, C., BROWN, B. H., HEARNDEN, V., SPEIGHT, P. M., D'APICE, K., HEGARTY, A. M., TIDY, J. A., HEALEY, T. J., HIGHFIELD, P. E. & THORNHILL, M. H. 2014. Use of electrical impedance spectroscopy to detect malignant and potentially malignant oral lesions. *International Journal of Nanomedicine,* 9, 4521-4532.

MYERS, A. B. 1997. Resonance Raman Intensity Analysis of Excited-State Dynamics. *Accounts of Chemical Research,* 30, 519-527.

MYLONAS, C. & KOURETAS, D. 1999. Lipid peroxidation and tissue damage. *In vivo (Athens, Greece),* 13, 295-309.

N. D. MAGEE , R. J. BEATTIE , R. GRAY , M. IMRIE , M. ENNIS , J. MCGARVEY & ELBORN, J. S. 2010. Raman Spectroscopy Analysis Of Induced Sputum In Lung Cancer. *American Journal of Respiratory and Critical Care,* 181Article ID A3492.

NAUGLER, C. 2008. Brush biopsy sampling of oral lesions. *Canadian Family Physician,* 54, 194-194.

NIEDOBITEK, G., HERBST, H. & YOUNG, L. 1993. Epstein-Barr virus and carcinomas. *International Journal of Clinical & Laboratory Research,* 23, 17-24.

NOTINGHER, I., GREEN, C., DYER, C., PERKINS, E., HOPKINS, N., LINDSAY, C. & HENCH, L. L. 2004a. Discrimination between ricin and sulphur mustard toxicity in vitro using Raman spectroscopy. *Journal of The Royal Society Interface,* 1, 79-90.

NOTINGHER, I., GREEN, C., DYER, C., PERKINS, E., HOPKINS, N., LINDSAY, C. & HENCH, L. L. 2004b. Discrimination between ricin and sulphur mustard toxicity in vitro using Raman spectroscopy. *Journal of the Royal Society Interface,* 1.

OLD, O. J., FULLWOOD, L. M., SCOTT, R., LLOYD, G. R., ALMOND, L. M., SHEPHERD, N. A., STONE, N., BARR, H. & KENDALL, C. 2014. Vibrational spectroscopy for cancer diagnostics. *Analytical Methods,* 6, 3901-3917.

OLIVO, M., BHUVANESWARI, R. & KEOGH, I. 2011. Advances in Bio-Optical Imaging for the Diagnosis of Early Oral Cancer. *Pharmaceutics*.

OLLENSCHLÄGER, G., JANSEN, S., SCHINDLER, J., RASOKAT, H., SCHRAPPE-BÄCHER, M. & ROTH, E. 1988. Plasma amino acid pattern of patients with HIV infection. *Clinical Chemistry,* 34, 1787-1789.

OU, L., CHEN, Y., HUANG, Y., SU, Y., LIN, D., ZOU, C. & LEI, J. 2012. Analysis of protein from nasopharyngeal carcinoma cell line CNE2 irradiated by X-ray using Raman spectroscopy. *Spectroscopy-an International Journal,* 27, 1-7.

PALLUA, J. D., PEZZEI, C., ZELGER, B., SCHAEFER, G., BITTNER, L. K., HUCK-PEZZEI, V. A., SCHOENBICHLER, S. A., HAHN, H., KLOSS-BRANDSTAETTER, A., KLOSS, F., BONN, G. K. & HUCK, C. W. 2012. Fourier transform infrared imaging analysis in discrimination studies of squamous cell carcinoma. *Analyst,* 137, 3965-3974.

PARKER, F. S. 1983. *Applications of Infrared, Raman and Resonance Raman spectroscopy in Biochemistry*, New York, USA., Plenum Press, New York, USA.

PARKER, S. F. & TOOKE, P. B. 1997. The effect of apodisation and finite resolution on Fourier transform infrared and Raman spectra. *Spectrochimica Acta Part A: Molecular and Biomolecular Spectroscopy,* 53, 2245-2252.

PARKIN, D. M., BRAY, F., FERLAY, J. & PISANI, P. 2005. Global cancer statistics, 2002. *CA Cancer J Clin,* 55, 74-108.

PETIBOIS, C. & DÉLÉRIS, G. 2006. Chemical mapping of tumor progression by FT-IR imaging: towards molecular histopathology. *Trends in Biotechnology,* 24, 455-462.

PETRY, R., SCHMITT, M. & POPP, J. 2003. Raman Spectroscopy - A prospective tool in the life sciences. *Chemphyschem,* 4, 14-30.

PICHARDO-MOLINA, J., FRAUSTO-REYES, C., BARBOSA-GARCÍA, O., HUERTA-FRANCO, R., GONZÁLEZ-TRUJILLO, J., RAMÍREZ-ALVARADO, C., GUTIÉRREZ-JUÁREZ, G. & MEDINA-GUTIÉRREZ, C. 2007. Raman spectroscopy and multivariate analysis of serum samples from breast cancer patients. *Lasers in Medical Science,* 22, 229-236.

POH, C. F., NG, S. P., WILLIAMS, P. M., ZHANG, L., LARONDE, D. M., LANE, P., MACAULAY, C. & ROSIN, M. P. 2007. Direct fluorescence visualization of clinically occult

high-risk oral premalignant disease using a simple hand-held device. *Head and Neck-Journal for the Sciences and Specialties of the Head and Neck,* 29, 71-76.

PUPPELS, G. J., GARRITSEN, H. S., SEGERS-NOLTEN, G. M., DE MUL, F. F. & GREVE, J. 1991. Raman microspectroscopic approach to the study of human granulocytes. *Biophysical journal,* 60, 1046-1056.

QUINTAS, G., GARRIGUES, S. & DE LA GUARDIA, M. 2004. FT-Raman spectrometry determination of Malathion in pesticide formulations. *Talanta,* 63, 345-350.

QUINTILIANI, M. 1986. The Oxygen Effect in Radiation Inactivation of DNA and Enzymes. *International Journal of Radiation Biology,* 50, 573-594.

RAKHORST, H. A., TRA, W. M. W., POSTHUMUS-VAN SLUIJS, S. T., HOVIUS, S. E. R., LEVENDAG, P. C., KANAAR, R. & HOFER, S. O. P. 2006. Quantitative analysis of radiation-induced DNA break repair in a cultured oral mucosal model. *Tissue Engineering,* 12, 3395-3403.

RAM, S. & SIAR, C. H. 2005. Chemiluminescence as a diagnostic aid in the detection of oral cancer and potentially malignant epithelial lesions. *International Journal of Oral and Maxillofacial Surgery,* 34, 521-527.

RAMAN, C. V. & KRISHNAN, K. S. 1928. A New Type of Secondary Radiation. *Nature,* 121.

RASTOGI, V., PURI, N., MISHRA, S., ARORA, S., KAUR, G. & YADAV, L. 2013. An insight to oral epithelial dysplasia. *Int J Head Neck Surg.,* 4, 74-82.

RATH, T., ROTH, E., KEIDL, R. & MEISSL, G. 1987. PHENYLALANINE - TOTAL AMINO-ACID RATIO IN 45 BURN PATIENTS. *Scandinavian Journal of Plastic and Reconstructive Surgery and Hand Surgery,* 21, 297-300.

REHMAN, S., MOVASAGHI, Z., TUCKER, A. T., JOEL, S. P., DARR, J. A., RUBAN, A. V. & REHMAN, I. U. 2007. Raman spectroscopic analysis of breast cancer tissues: identifying differences between normal, invasive ductal carcinoma and ductal carcinoma in situ of the breast tissue. *Journal of Raman Spectroscopy,* 38, 1345-1351.

REICHART, P. 2001. Identification of risk groups for oral precancer and cancer and preventive measures. *Clinical Oral Investigations,* 5, 207-213.

ROBBINS, S. L., COTRAN, R. S. & KUMAR, V. 1994 *Pathologic Basis of Disease,* Philadelphia, USA, W. B. Saunders

ROBERT, B. 2009. Resonance Raman spectroscopy. *Photosynthesis Research,* 101, 147-155.

ROBICHAUX-VIEHOEVER, A., KANTER, E., SHAPPELL, H., BILLHEIMER, D., JONES III, H. & MAHADEVAN-JANSEN, A. 2007. Characterization of Raman Spectra Measured in Vivo for the Detection of Cervical Dysplasia. *Appl. Spectrosc.,* 61, 986-993.

ROTH, E., ZOCH, G., SCHULZ, F., KARNER, J., MUHLBACHER, F., HAMILTON, G., MAURITZ, W., SPORN, P. & FUNOVICS, J. 1985. AMINO-ACID CONCENTRATIONS IN PLASMA AND SKELETAL-MUSCLE OF PATIENTS WITH ACUTE HEMORRHAGIC NECROTIZING PANCREATITIS. *Clinical Chemistry,* 31, 1305-1309.

RUBAN, A. V., BERERA, R., ILIOAIA, C., VAN STOKKUM, I. H. M., KENNIS, J. T. M., PASCAL, A. A., VAN AMERONGEN, H., ROBERT, B., HORTON, P. & VAN GRONDELLE, R. 2007. Identification of a mechanism of photoprotective energy dissipation in higher plants. *Nature,* 450, 575-U22.

RUIZ-CHICA, A. J., MEDINA, M. A., SÁNCHEZ-JIMÉNEZ, F. & RAMÍREZ, F. J. 2004. On the interpretation of Raman spectra of 1-aminooxy-spermine/DNA complexes. *Nucleic Acids Research,* 32, 579-589.

S.A.J. DRUET & TARAN, J. P. E. 1981. CARS Spectroscopy. *Progress in Quantum Electronics,* 7, 1-72.

SACRISTAN, J., REINECKE, H., MIJANGOS, C., SPELLS, S. & YARWOD, J. 2002. Surface modification of polystyrene films. Depth profiling and mapping by Raman microscopy. *Macromolecular Chemistry and Physics,* 203, 678-685.

SAHU, A., SAWANT, S., MAMGAIN, H. & KRISHNA, C. M. 2013. Raman spectroscopy of serum: an exploratory study for detection of oral cancers. *Analyst,* 138, 4161-4174.

SALAMAT-MILLER, N., CHITTCHANG, M. & JOHNSTON, T. P. 2005. The use of mucoadhesive polymers in buccal drug delivery. *Advanced Drug Delivery Reviews,* 57, 1666-1691.

SANCAR, A., LINDSEY-BOLTZ, L. A., ÜNSAL-KAÇMAZ, K. & LINN, S. 2004. MOLECULAR MECHANISMS OF MAMMALIAN DNA REPAIR AND THE DNA DAMAGE CHECKPOINTS. *Annual Review of Biochemistry,* 73, 39-85.

SEBALLOS, L., ZHANG, J. & SUTPHEN, R. 2005. Surface-enhanced Raman scattering detection of lysophosphatidic acid. *Analytical and Bioanalytical Chemistry,* 383, 763-767.

SEITZ, H., PÖSCHL, G. & SIMANOWSKI, U. 1998. Alcohol and Cancer. *Recent Developments in Alcoholism.* Springer US.

SEITZ HK & PM., S. 2002. *Ethanol toxicity and nutritional status. Nutritional toxicology.*, Cotsones, F. N. and McKay, M.A., eds, ppl 122-154. Taylor and Francis, London, New York.

SHAFER-PELTIER, K. E., HAKA, A. S., FITZMAURICE, M., CROWE, J., MYLES, J., DASARI, R. R. & FELD, M. S. 2002. Raman microspectroscopic model of human breast tissue: implications for breast cancer diagnosis in vivo. *Journal of Raman Spectroscopy,* 33, 552-563.

SHAH, N. C., LYANDRES, O., YONZON, C. R., ZHANG, X. & DUYNE, R. P. V. 2007. Surface-Enhanced Raman Sensing: Glucose and Anthrax. *New Approaches in Biomedical Spectroscopy.* American Chemical Society.

SHARWANI, A., JERJES, W., SALIH, V., SWINSON, B., BIGIO, I. J., EL-MAAYTAH, M. & HOPPER, C. 2006. Assessment of oral premalignancy using elastic scattering spectroscopy. *Oral Oncology,* 42, 343-349.

SHAW, R. A. & MANTSCH, H. H. 1999. Vibrational biospectroscopy: from plants to animals to humans. A historical perspective. *Journal of Molecular Structure,* 481, 1-13.

SHETTY G, K. C., SHEPHERD N, STONE N, BARR H. 2006. Raman spectroscopy: elucidation of biochemical changes in carcinogenesis of oesophagus. *British Journal of Cancer,* 94.

SHIN, D. M., VORAVUD, N., RO, J. Y., LEE, J. S., HONG, W. K. & HITTELMAN, W. N. 1993. SEQUENTIAL INCREASES IN PROLIFERATING CELL NUCLEAR ANTIGEN EXPRESSION IN HEAD AND NECK TUMORIGENESIS - A POTENTIAL BIOMARKER. *Journal of the National Cancer Institute,* 85, 971-978.

SHIU, M.-N. C., TH-H February 2004 Impact of betel quid, tobacco and alcohol on three-stage disease natural history of oral leukoplakia and cancer: implication for prevention of oral cancer. *European Journal of Cancer Prevention,* 13, 39-45.

SHORT, K. W., CARPENTER, S., FREYER, J. P. & MOURANT, J. R. 2005. Raman spectroscopy detects biochemical changes due to proliferation in mammalian cell cultures. *Biophysical Journal,* 88, 4274-4288.

SIGURDSSON, S., PHILIPSEN, P. A., HANSEN, L. K., LARSEN, J., GNIADECKA, M. & WULF, H. C. 2004. Detection of skin cancer by classification of Raman spectra. *Biomedical Engineering, IEEE Transactions on,* 51, 1784-1793.

SINGH, S. P., DESHMUKH, A., CHATURVEDI, P. & KRISHNA, C. M. 2012a. In vivo Raman spectroscopic identification of premalignant lesions in oral buccal mucosa. *Journal of Biomedical Optics,* 17.

SINGH, S. P., DESHMUKH, A., CHATURVEDI, P. & MURALI KRISHNA, C. 2012b. In vivo Raman spectroscopic identification of premalignant lesions in oral buccal mucosa. *Journal of Biomedical Optics,* 17, 1050021-1050029.

SINGH, S. P., SAHU, A., DESHMUKH, A., CHATURVEDI, P. & KRISHNA, C. M. 2013. In vivo Raman spectroscopy of oral buccal mucosa: a study on malignancy associated changes (MAC)/cancer field effects (CFE). *Analyst,* 138, 4175-4182.

SPEIGHT, P. M. 2007. Update on oral epithelial dysplasia and progression to cancer. *Head and neck pathology,* 1, 61-6.

SPITZ, D., AZZAM, E., JIAN LI, J. & GIUS, D. 2004. Metabolic oxidation/reduction reactions and cellular responses to ionizing radiation: A unifying concept in stress response biology. *Cancer and Metastasis Reviews,* 23, 311-322.

SRIDHARAN, G. & SHANKAR, A. A. 2012. Toluidine blue: A review of its chemistry and clinical utility. *Journal of oral and maxillofacial pathology : JOMFP,* 16, 251-5.

STEFANUTO, P., DOUCET, J.-C. & ROBERTSON, C. 2014. Delays in treatment of oral cancer: a review of the current literature. *Oral Surgery, Oral Medicine, Oral Pathology and Oral Radiology,* 117, 424-429.

STONE, N., KENDALL, C., CHANDRATREYA, N., SHEPHERD, N. & BARR, H. 2002. Near-infrared Raman spectroscopy for detection and classification of gastrointestinal disease. Conference on Biomedical Vibrational Spectroscopy II, 2002

Jan 19-20 2002a San Jose, Ca. 117-126.

STONE, N., KENDALL, C., SHEPHERD, N., CROW, P. & BARR, H. 2002b. Near-infrared Raman spectroscopy for the classification of epithelial pre-cancers and cancers. *Journal of Raman Spectroscopy,* 33, 564-573.

STONE, N., KENDALL, C., SMITH, J., CROW, P. & BARR, H. 2004. Raman spectroscopy for identification of epithelial cancers. *Faraday Discussions,* 126, 141-157.

STONE, N., STAVROULAKI, P., KENDALL, C., BIRCHALL, M. & BARR, H. 2000. Raman spectroscopy for early detection of laryngeal malignancy: Preliminary results. *Laryngoscope,* 110, 1756-1763.

SU, L., SUN, Y., CHEN, Y., CHEN, P., SHEN, A., WANG, X., JIA, J., ZHAO, Y., ZHOU, X. & HU, J. 2012a. Raman spectral properties of squamous cell carcinoma of oral tissues and cells. *Laser Physics,* 22, 311-316.

SU, L., SUN, Y. F., CHEN, Y., CHEN, P., SHEN, A. G., WANG, X. H., JIA, J., ZHAO, Y. F., ZHOU, X. D. & HU, J. M. 2012b. Raman spectral properties of squamous cell carcinoma of oral tissues and cells. *Laser Physics,* 22, 311-316.

SUN, T.-P., CHING, C. T.-S., CHENG, C.-S., HUANG, S.-H., CHEN, Y.-J., HSIAO, C.-S., CHANG, C.-H., HUANG, S.-Y., SHIEH, H.-L., LIU, W.-H., LIU, C.-M. & CHEN, C.-Y. 2010. The use of bioimpedance in the detection/screening of tongue cancer. *Cancer Epidemiology,* 34, 207-211.

SWINSON, B., JERJES, W., EL-MAAYTAH, M., NORRIS, P. & HOPPER, C. 2006. Optical techniques in diagnosis of head and neck malignancy. *Oral Oncology,* 42, 221-228.

SZUMIEL, I. 2006. Epidermal growth factor receptor and DNA double strand break repair: The cell's self-defence. *Cellular Signalling,* 18, 1537-1548.

TANKIEWICZ, A., DZIEMIAŃCZYK, D., BUCZKO, P., SZARMACH, I. J., GRABOWSKA, S. Z. & PAWLAK, D. 2006. Tryptophan and its metabolites in patients with oral squamous cell carcinoma: preliminary study. *Advances in medical sciences,* 51 Suppl 1, 221-224.

TAPIO, S. & JACOB, V. 2007. Radioadaptive response revisited. *Radiation and Environmental Biophysics,* 46, 1-12.

TEH, S. K., ZHENG, W., HO, K. Y., TEH, M., YEOH, K. G. & HUANG, Z. 2008. Diagnostic potential of near-infrared Raman spectroscopy in the stomach: differentiating dysplasia from normal tissue. *Br J Cancer,* 98, 457-65.

TEH, S. K., ZHENG, W., HO, K. Y., TEH, M., YEOH, K. G. & HUANG, Z. 2010. Near-infrared Raman spectroscopy for early diagnosis and typing of adenocarcinoma in the stomach. *British Journal of Surgery,* 97, 550-557.

THOMAS, G. J. 1999. RAMAN SPECTROSCOPY OF PROTEIN AND NUCLEIC ACID ASSEMBLIES. *Annual Review of Biophysics and Biomolecular Structure,* 28, 1-27.

THOMAS, J., BUZZINI, P., MASSONNET, G., REEDY, B. & ROUX, C. 2005. Raman spectroscopy and the forensic analysis of black/grey and blue cotton fibres - Part 1. Investigation of the effects of varying laser wavelength. *Forensic Science International,* 152, 189-197.

TOMAR, S. L. 2003. Trends and patterns of tobacco use in the United States. *Am J Med Sci.,* 326(4), 248-54.

TROTTI, A., BELLM, L. A., EPSTEIN, J. B., FRAME, D., FUCHS, H. J., GWEDE, C. K., KOMAROFF, E., NALYSNYK, L. & ZILBERBERG, M. D. 2003. Mucositis incidence,

severity and associated outcomes in patients with head and neck cancer receiving radiotherapy with or without chemotherapy: a systematic literature review. *Radiotherapy and Oncology,* 66, 253-262.

UPILE T, JERJES W, BETZ CS, EL MAAYTAH M, WRIGHT A & C., H. 2007. Optical diagnostic techniques in the head and neck. . *Dental Update,* 34, 410-2, 415-6, 419-20

UTZINGER, U., HEINTZELMAN, D. L., MAHADEVAN-JANSEN, A., MALPICA, A., FOLLEN, M. & RICHARDS-KORTUM, R. 2001. Near-infrared Raman spectroscopy for in vivo detection of cervical precancers. *Applied Spectroscopy,* 55, 955-959.

VENKATAKRISHNA, K., JACOB KURIEN, KEERTHILATHA M. PAI, MANNA VALIATHAN, NIRMALA NAGESH KUMAR, C. MURALI KRISHNA, G. ULLAS & KARTHA, V. B. 2001. Optical pathology of oral tissue: A Raman spectroscopy diagnostic method. *Curr Sci,* 80, 101-105.

VILLANI, P., FRESEGNA, A. M., RANALDI, R., ELEUTERI, P., PARIS, L., PACCHIEROTTI, F. & CORDELLI, E. 2013. X-Ray Induced DNA Damage and Repair in Germ Cells of PARP1(-/-) Male Mice. *International Journal of Molecular Sciences,* 14, 18078-18092.

WANG, L. & MIZAIKOFF, B. 2008. Application of multivariate data-analysis techniques to biomedical diagnostics based on mid-infrared spectroscopy. *Analytical and Bioanalytical Chemistry,* 391, 1641-1654.

WARD, K. R., BARBEE, R. W., REYNOLDS, P. S., TORRES FILHO, I. P., TIBA, M. H., TORRES, L., PITTMAN, R. N. & TERNER, J. 2007. Oxygenation monitoring of tissue vasculature by resonance Raman spectroscopy. *Analytical Chemistry,* 79, 1514-1518.

WARNAKULASURIYA, S., REIBEL, J., BOUQUOT, J. & DABELSTEEN, E. 2008. Oral epithelial dysplasia classification systems: predictive value, utility, weaknesses and scope for improvement. *Journal of Oral Pathology & Medicine,* 37, 127-133.

WARNAKULASURIYA, S., SUTHERLAND, G. & SCULLY, C. 2005. Tobacco, oral cancer, and treatment of dependence. *Oral Oncology,* 41, 244-260.

WEIBENBACHER, N., LENDL, B., FRANK, J., WANZENBÖCK, H. D., MIZAIKOFF, B. & KELLNER, R. 1997. Continuous surface enhanced Raman spectroscopy for the detection of trace organic pollutants in aqueous systems. *Journal of Molecular Structure,* 410–411, 539-542.

WILDER-SMITH, P., LEE, K., GUO, S., ZHANG, J., OSANN, K., CHEN, Z. & MESSADI, D. 2009. In Vivo Diagnosis of Oral Dysplasia and Malignancy Using Optical Coherence Tomography: Preliminary Studies in 50 Patients. *Lasers in Surgery and Medicine,* 41, 353-357.

WILLARD, H. H., MERRITT, L. L. J. & DEAN, J. A. 1949. Instrumental Methods of Analyses. *Soil Science,* 67.

WU, H., VOLPONI, J. V., OLIVER, A. E., PARIKH, A. N., SIMMONS, B. A. & SINGH, S. 2011. In vivo lipidomics using single-cell Raman spectroscopy. *Proc Natl Acad Sci U S A.,* 108, 3809-14.

YANG, Y., LIU, C. H., SAVAGE, H. E., SCHANTZ, S. P. & ALFANO, R. R. Optical fluorescence and Raman biopsy of squamous cell carcinoma from the head and neck. 1998. 68-71.

YASSER, M., SHAIKH, R., CHILAKAPATI, M. K. & TENI, T. 2014. Raman spectroscopic study of radioresistant oral cancer sublines established by fractionated ionizing radiation. *PloS one,* 9, e97777-e97777.

YI-YONG, T., AI-GUO, S., JING-WEI, Z., NAN, W., LIANG, F., QIAO-FENG, W., YONG, Y. & JI-MING, H. Design of auto-classifying system and its application in Raman spectroscopy diagnosis of gastric carcinoma. Machine Learning and Cybernetics, 2003 International Conference on, 2-5 Nov. 2003 2003. 1360-1363 Vol.3.

ZENG, H., MCWILLIAMS, A. & LAM, S. 2004. Optical spectroscopy and imaging for early lung cancer detection: a review. *Photodiagnosis and Photodynamic Therapy*, 1, 111-122.

ZHANG, X., YIN, H., COOPER, J. & HASWELL, S. 2008. Characterization of cellular chemical dynamics using combined microfluidic and Raman techniques. *Analytical and Bioanalytical Chemistry,* 390, 833-840.

ZININ, P. V., MISRA, A., KAMEMOTO, L., YU, Q., HU, N. & SHARMA, S. K. 2010. Visible, near-infrared, and ultraviolet laser-excited Raman spectroscopy of the monocytes/macrophages (U937) cells. *Journal of Raman Spectroscopy,* 41, 268-274.

ZOU, Y. & GUO, Z. 2003. A review of electrical impedance techniques for breast cancer detection. *Medical Engineering & Physics,* 25, 79-90.

Appendix

Publications

- Development of a Dewaxing Protocol for Tissue-Engineered Models of the Oral Mucosa Used for Raman Spectroscopic Analysis. **Mian S. A.**, Colley, H. E., Thornhill, M. H. & Rehman, I. U. Applied Spectroscopy Reviews, 49, 614-617, 2014.
- Synthesis and In-Vitro Analysis of Degradative Resistance of a Novel Bioactive Composite. Abdul Samad Khan, **Mian Salman Aziz**, Deepen Paul, Ferranti Wong, and Ihtesham Ur Rehman. Journal of Bionanoscience Vol.2, 1–12, 2008.

Submitted manuscript

- Raman spectroscopic analysis of tissue engineered normal, dysplastic and cancerous oral mucosa. **Salman A. Mian**, Helen. E. Colley, Muhammad S. Ullah, Ceyla Yorucu and Ihtesham U. Rehman.

Manuscripts in progress

- Raman spectroscopy in Oral Cancer diagnosis. ‘’Review Article’’. **S. A. Mian**, Abdul S. Khan, Helen E. Colley & Ihtesham U. Rehman.
- Investigation of irradiation effects on tissue engineered oral mucosa using Raman spectroscopy. **S. A. Mian**, Helen E. Colley & Ihtesham U. Rehman.
- Raman spectroscopic evaluation of normal, dysplastic and cancerous oral mucosa **S. A. Mian**, Helen E. Colley & Ihtesham U. Rehman.

Poster presentations

- 11-12 June 2012: Medical school annual research meeting, University of Sheffield.
- 4-7 November 2012: 8th NCRI Cancer Conference, Liverpool, UK.
- 22-03- 2013: Sheffield Cancer Research Centre, Inaugural Cancer Research Forum.
- 20-05-2014: 2nd Year poster competition, Department of materials science and engineering, University of Sheffield.

Conferences and seminars

- 22-05-2012: Faculty of Engineering RIET Day, University of Sheffield.
- 22-04-2012: 1 Day Internal Research Student Conference, University of Sheffield.
- Weekly seminars of Research Skills and Communication.
- Weekly Research in Progress seminars at Kroto Research Institute.
- Weekly Journal club presentations at the School of Clinical Dentistry, University of Sheffield.
- 4-7 November 2012: 8th NCRI Cancer Conference, Liverpool, UK.
- 16-05-2013: Materials science seminar at Thermo Scientific headquarters in Hemel Hempstead over Raman spectroscopy and its applications.
- 14-02-2014: Symposium on Advanced Single Cell Biotechnology at University of Sheffield.

Internship at Philips Research

Marie Curie Fellow (1st June 2014 till 30th November 2014) on the project of Understanding Interactions of Human Tissue with Medical Devices (UNITISS) at High Tech Campus, Philips Research, Eindhoven.

I was primarily involved in the Department of Oral Health Care and carried out research on multiple projects related to chemical agent driven dental plaque reduction and spectroscopic mapping of bovine teeth before and after teeth whitening procedures.

I have a bachelor's degree in Dental Surgery and this exposure to industry proved to be extremely beneficial for my professional development. I have always enjoyed this multidisciplinary environment where I have this liberty to explore both clinical and research oriented angles of a project.

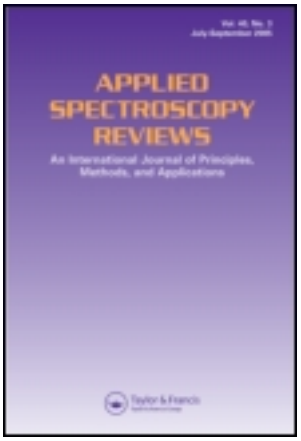

Applied Spectroscopy Reviews
Publication details, including instructions for authors and subscription information:
http://www.tandfonline.com/loi/laps20

Development of a Dewaxing Protocol for Tissue-Engineered Models of the Oral Mucosa Used for Raman Spectroscopic Analysis

Salman A. Mian[ab], Helen E. Colley[b], Martin H. Thornhill[b] & Ihtesham u. Rehman[a]

[a] Department of Materials Science and Engineering, University of Sheffield, Sheffield, UK

[b] School of Clinical Dentistry, University of Sheffield, Sheffield, UK

Accepted author version posted online: 17 Jan 2014.Published online: 24 Apr 2014.

To cite this article: Salman A. Mian, Helen E. Colley, Martin H. Thornhill & Ihtesham u. Rehman (2014) Development of a Dewaxing Protocol for Tissue-Engineered Models of the Oral Mucosa Used for Raman Spectroscopic Analysis, Applied Spectroscopy Reviews, 49:8, 614-617, DOI: 10.1080/05704928.2014.882348

To link to this article: http://dx.doi.org/10.1080/05704928.2014.882348

Applied Spectroscopy Reviews, 49:614–617, 2014

ISSN: 0570-4928 print / 1520-569X online
DOI: 10.1080/05704928.2014.882348

Taylor & Francis
Taylor & Francis Group

Development of a Dewaxing Protocol for Tissue-Engineered Models of the Oral Mucosa Used for Raman Spectroscopic Analysis

SALMAN A. MIAN,[1,2] HELEN E. COLLEY,[2] MARTIN H. THORNHILL,[2] AND IHTESHAM U. REHMAN[1]

[1]Department of Materials Science and Engineering, University of Sheffield, Sheffield, UK
[2]School of Clinical Dentistry, University of Sheffield, Sheffield, UK

Abstract: *We demonstrate that wax-embedded models of tissue-engineered oral mucosa can be effectively dewaxed using xylene for Raman spectroscopic analysis. Tissue sections of 20 μm thickness were cut and mounted onto glass slides. Sections were placed in xylene for increasing lengths from 2 to 45 min. Acquired Raman spectra revealed the wax contribution in the fingerprint region until 28-min treatment in xylene. Good quality and wax-free spectra were recorded at 30, 35, 40, and 45 min in xylene with no significant differences among them. It is essential to collect uncontaminated Raman spectra in order to achieve authentic results because the fingerprint region of biological tissues holds extremely vital information that is of diagnostic significance in cancer.*

Keywords: Dewaxing protocol, oral mucosa, Raman spectroscopy, analytical, sample preparations, biological

Introduction

Raman spectroscopy has recently emerged as a promising tool in biomedical applications. The advantages of the technique, including that it is noninvasive and allows real-time detection, have attracted attention in cancer diagnosis (1). Raman spectra collected from a biological tissue provide information about the chemical composition as well as molecular conformation (2). Contamination with dust particles or wax as a result of inappropriate dewaxing affects the spectrum, leading to false information and discouraging results. Because wax contributes to the fingerprint region of the spectra, it interferes with amide I, keratin, nucleic acid, and amide III compartments and prevents their expression (3), which has the most sensitive information in biological tissues. Therefore, in spectroscopic studies it is extremely important to completely eliminate wax in order to acquire comprehensive expression of vital components that are of diagnostic significance.

Address correspondence to Dr. Ihtesham ur Rehman, Reader in Biomedical Materials, Department of Materials Science and Engineering, The Kroto Research Institute, University of Sheffield, North Campus, Broad Lane, Sheffield S3 7HQ, UK. E-mail: i.u.rehman@sheffield.ac.uk

Color versions of one or more of the figures in the article can be found online at www.tandfonline.com/laps.

This study was designed to establish a standard protocol for dewaxing tissue sections using xylene in order to eliminate the residual wax contribution from Raman spectra.

Experimental Procedures

Tissue Section Preparation

Tissue-engineered models of the oral mucosa were prepared, fixed, and paraffin embedded as previously described (4). Twenty-micrometer tissue sections were cut using a Leica RM2235 microtome (Leica Microsystems, Milton Keynes, UK) with S35 microtome blades (Feather, Osaka, Japan) and mounted on to microscope glass slides (CellPath Ltd., Newtown, UK). Mounted sections were oven dried for 30 min at 60°C. For wax removal the slides were placed in xylene for increasing lengths of time (2–45 min). Xylene treatment was followed by dehydration of the tissue sections in 50, 70, and 100% ethanol for 5 min each as well as to eliminate xylene from the tissue sections. Eighteen sections were prepared for Raman analysis and the experiment was performed in duplicate.

Raman Spectroscopic Measurements

Spectra were acquired using a DXR Raman microscope (Thermo Electron Scientific Instruments LLC, Madison, WI) fitted with a 532-nm diode-pumped solid state laser with a laser power of 10 mW. The microscope was equipped with an X50 long-working-distance objective lens. The confocal aperture of the system was set to 50 μm pinhole and estimated spectral and spatial resolutions were 5 cm^{-1} and 0.6 μm, respectively. Scattered light was detected using a CCD detector with an average 2 cm^{-1} per CCD pixel element. The scattered Raman signal was measured over a complete spectral range (50–3500 cm^{-1}), whereas only the fingerprint region (500–1800 cm^{-1}) was analyzed. Exposure time was set to 30 s and five sample exposures were accumulated to improve the signal-to-noise ratio. The spectra obtained were analyzed and processed using OMNIC Atlμs Software Suite (Thermo Electron Scientific Instruments LLC). The units of spectroscopic intensities are arbitrary units (a.u.); the baseline of each spectrum is only relevant to relative intensity; therefore, the spectra were offset to enhance clarity.

Results and Discussion

A microscope glass slide can contribute to the Raman spectrum when thin tissue sections (less than 10–15 μm) are mounted and it influences the fingerprint region. The strong Raman signal from glass may obstruct spectral peaks from the tissue sample. Hence, it was necessary to mount 20-μm-thick tissue sections on the glass slide to obtain spectra free from the glass background.

Distinctive Raman contributions are observed in the spectrum of paraffin wax at 1063, 1133, 1296, and 1441 cm^{-1} (Figure 1). These are typical assignments of C-C (carbon–carbon) stretching and CH_2 and CH_3 deformation (3, 5, 6). Figure 2 shows a sequence of spectra after wax removal in xylene for increasing lengths of time (2–30 min).

Wax contributions at 1063, 1133, 1296, and 1441 cm^{-1} are clearly observed in the spectra of tissue sections kept in xylene from 2 to 28 min, which are attributed to CC skeletal stretch, CC stretch, CH_2 deformation, and CH_2 deformation, respectively. These spectral contributions from residual wax mask the tissue molecules emanating from the

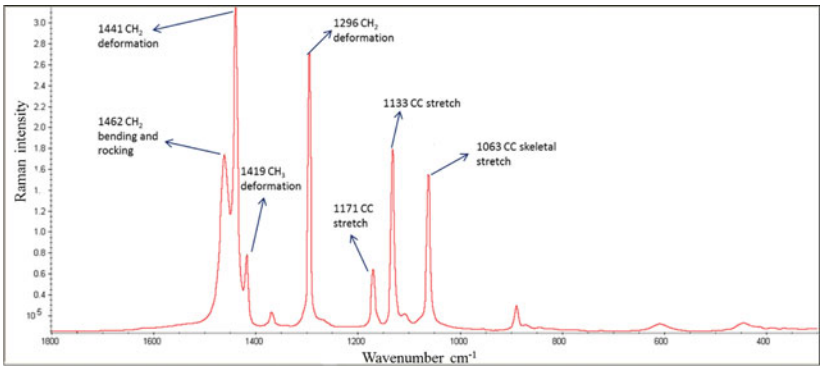

Figure 1. Raman spectrum of pure paraffin wax.

fingerprint region holding biochemical information regarding the state of tissues. These peaks show variations in intensities, which gradually decrease as the tissue is kept in xylene from 2 to 28 min. A phenylalanine contribution at 1002 cm^{-1} is expressed in the spectrum of the tissue section kept in xylene for 30 min, which was absent in the pure wax spectrum (Figure 2). Complete removal of wax is essential to achieve spectral contributions from amide I, keratin, amide III, nucleic acid (DNA), and phenylalanine. These regions were hindered in the spectra of tissues kept in xylene for up to 28 min, whereas their expressions were recorded clearly in the spectrum analyzed after 30 min in xylene.

Raman spectra were also acquired from tissue sections kept in xylene for 35, 40, and 45 min to observe any further variations. No differences from the 30-min spectrum were observed (data not shown).

Wax contamination in Raman spectra obstructs the information regarding chemical composition in biological tissues. Therefore, it is extremely important to eliminate wax in order to achieve accurate results.

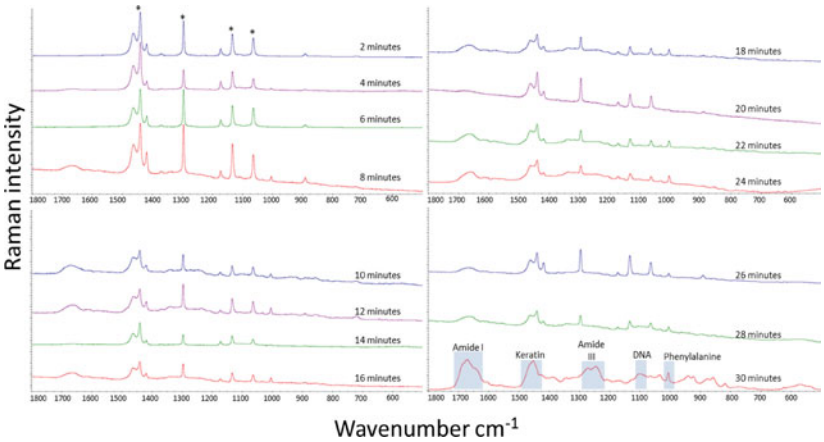

Figure 2. Raman spectra of 20-μm tissue sections after dewaxing in xylene for increasing lengths of time (2–30 min).

Conclusion

In this study, we have demonstrated that to completely eliminate wax contamination from 20-μm-thick tissue sections, a 30-min immersion in xylene is essential. After this time period, no spectral peaks associated with wax were observed in the spectrum of the tissue-engineered oral mucosa.

References

1. Lloyd, G.R., Orr, L.E., Christie-Brown, J., McCarthy, K., Rose, S., Thomas, M., and Stone, N. (2013) Discrimination between benign, primary and secondary malignancies in lymph nodes from the head and neck utilising Raman spectroscopy and multivariate analysis. *Analyst*, 138 (14): 3900–3908.
2. Movasaghi, Z., Rehman, S., and Rehman, I.U. (2007) Raman spectroscopy of biological tissues. *Appl. Spectros. Rev.*, 42 (5): 493–541.
3. Faoláin, E.Ó., Hunter, M.B., Byrne, J.M., Kelehan, P., Lambkin, H.A., Byrne, H.J., and Lyng, F.M. (2005) Raman spectroscopic evaluation of efficacy of current paraffin wax section dewaxing agents. *J. Histochem. Cytochem.*, 53 (1): 121–129.
4. Colley, H.E., Hearnden, V., Jones, A.V., Weinreb, P.H., Violette, S.M., MacNeil, S., Thornhill, M.H., and Murdoch, C. (2011) Development of tissue-engineered models of oral dysplasia and early invasive oral squamous cell carcinoma. *Br. J. Cancer*, 105 (10): 1582–1592.
5. Barry, B.W., Edwards, H.G.M., and Williams, A.C. (1992) Fourier transform Raman and infrared vibrational study of human skin: Assignment of spectral bands. *J. Raman Spectros.*, 23 (11): 641–645.
6. Lakshmi, R.J., Kartha, V.B., Murali Krishna, C., Solomon, J.G.R., Ullas, G., and Uma Devi, P. (2002) Tissue Raman spectroscopy for the study of radiation damage: Brain irradiation of mice. *Radiat. Res.*, 157 (2): 175–182.

Health Research Authority

National Research Ethics Service

NRES Committee Yorkshire & The Humber - Sheffield

HRA NRES Centre Manchester
Barlow House
3rd Floor
4 Minshull Street
Manchester
M1 3DZ

Tel: 0161 625 7832
Fax: 0161 625 7299

25 June 2014

Dr Helen Colley
Lecturer in Oral Science
School of Clinical Dentistry
Academic Unit of Oral & Maxillofacial Pathology,
University of Sheffield
19 Claremont Crescent
Sheffield
S10 2TA

Dear Dr Colley

Study title:	**Development of tissue engineered models of the oral mucosa for the in vitro study of oral mucosal disease and oral mucosal responses.**
REC reference:	**09/H1308/66**
Protocol number:	**N/A**
EudraCT number:	**N/A**
Amendment number:	**One**
Amendment date:	**05 June 2014**
IRAS project ID:	**9603**

The above amendment was reviewed by the Sub-Committee in correspondence.

Ethical opinion

Approval was sought for the following changes:

- A change of Chief Investigator from Professor Martin Thornhill to Dr Helen Colley.
- To continue to collect new samples for laboratory use.
- To change the research title.
- A change to the cell culture method.
- For a Consent Form to be used for this study.
- Documents were revised to ensure they are up to date.

The members of the Committee taking part in the review gave a favourable ethical opinion of the amendment on the basis described in the notice of amendment form and supporting documentation.

The Committee strongly recommended that typographical errors in the Participant Information Sheet are corrected.

Approved documents

The documents reviewed and approved at the meeting were:

Document	*Version*	*Date*
Evidence of Sponsor insurance or indemnity (non NHS Sponsors only) [University of Sheffield]		27 February 2014
Notice of Substantial Amendment (non-CTIMP) [Amendment 1]		13 May 2014
Other [Changes to IRAS form]		
Other [Summary of changes]		
Other [Signed IRAS D1 declaration]		06 June 2014
Participant consent form	1	13 May 2014
Participant information sheet (PIS) [clean]	4.0	13 May 2014
Research protocol or project proposal [clean]	2	13 May 2014
Summary CV for Chief Investigator (CI) [Dr Helen E Colley]		

Membership of the Committee

The members of the Committee who took part in the review are listed on the attached sheet.

R&D approval

All investigators and research collaborators in the NHS should notify the R&D office for the relevant NHS care organisation of this amendment and check whether it affects R&D approval of the research.

Statement of compliance

The Committee is constituted in accordance with the Governance Arrangements for Research Ethics Committees and complies fully with the Standard Operating Procedures for Research Ethics Committees in the UK.

We are pleased to welcome researchers and R & D staff at our NRES committee members' training days – see details at http://www.hra.nhs.uk/hra-training/

09/H1308/66: Please quote this number on all correspondence

Yours sincerely

On behalf of
Professor Basil Sharrack
Chair

E-mail: nrescommittee.yorkandhumber-sheffield@nhs.net

Enclosures: List of names and professions of members who took part in the review

Copy to: Professor Martin Thornhill
University of Sheffield

Dr Dipak Patel

NRES Committee Yorkshire & The Humber - Sheffield

Attendance at Sub-Committee of the REC meeting

Committee Members:

Name	*Profession*	*Present*	*Notes*
Mr Pete Laud	Statistical Consultant	Yes	
Professor Basil Sharrack	Consultant Neurologist	Yes	

Also in attendance:

Name	*Position (or reason for attending)*
Miss Helen Penistone	REC Manager

Ref: STH15753/NT/GK

Sheffield Teaching Hospitals NHS
NHS Foundation Trust

13 September 2013

Dr Keith Hunter
School of Clinical Dentistry
University of Sheffield
Claremont Crescent
Sheffield
S10 2TA

Dear Dr Hunter,

Non-Substantial Amendment
Letter of Continued NHS Permission

STH ref:	**15753**
NIHR CSP ref:	**NA**
REC ref:	**08/S0709/70**
MHRA ref:	**CTA no.: NA** **EudraCT no.: NA**
Study title:	**Biomarkers in Head and neck cancer and precancer: a pilot study for candidate biomarkers**
Principal Investigator:	**Dr Keith Hunter, UoS**
Sponsor:	**Sheffield Teaching Hospitals NHS Foundation Trust**
Funder:	**Unfunded**
Amendment ref:	**Minor Am 06 – Ext of study end date until July 2015**

Thank you for submitting the following documents:

Document	*Version/date*
West of Scotland Research Ethics Service – Acknowledgement of Minor Amendment	10 Jul 13
West of Scotland Research Ethics Service – Acknowledgement of Annual Report	10 Jul 13

These have been reviewed by the Research Department who have no objection to the amendment and can confirm continued NHS permission for the study at STH.

Yours sincerely,

Professor S Heller
Director of R&D, Sheffield Teaching Hospitals NHS Foundation Trust
Telephone +44 (0) 114 22 65934
Fax +44 (0) 114 22 65937